AD719867

FINAL SCIENTIFIC REPORT

NUMERICAL STUDIES OF PLANETARY

CIRCULATIONS IN A MODEL ATMOSPHERE

1 August 1967 — 28 Feb. 1970

A. HUSS

DEPARTMENT OF METEOROLOGY
HEBREW UNIVERSITY
JERUSALEM, ISRAEL

DDC

MAR 9 1971

C

FINAL SCIENTIFIC REPORT

NUMERICAL STUDIES OF PLANETARY

CIRCULATIONS IN A MODEL ATMOSPHERE

1 August 1967 — 28 Feb. 1970

A. HUSS

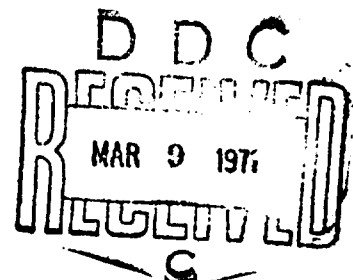DEPARTMENT OF METEOROLOGY
HEBREW UNIVERSITY
JERUSALEM, ISRAEL

Distribution of this document
is unlimited

CONTENTS

GENERAL CIRCULATION EXPERIMENTS
WITH A TWO LEVEL PRIMITIVE EQUATIONS MODEL

by

Eliahu Doron and Abraham Huss

Abstract

A modified version of the primitive equations model proposed by
Mintz and Arakawa was integrated in order to obtain circulation patterns in
a zonal strip. A hydrologic cycle was included and its influence on the develop-
ing circulation was investigated. In the first integration not including release
of latent heat a more or less symmetric circulation developed, with a jet stream
characteristic of summer conditions at the central latitude. The strength and
distribution of the meridional circulation was also quite characteristic of summer
in the real atmosphere. In the second integration, including the water vapor
cycle, the development was more vigorous and higher amplitudes of the geo-
potential were reached. The surface pressure gradients were also more pro-
nounced and were close to those observed in the southern hemisphere in summer.
The resulting precipitation and evaporation amounts were much too low, so that
although an improvement in the direction towards a more realistic simulation of
the atmosphere is observed in the second integration, this improvement is not
very marked.

INTRODUCTION

The experiments described in the following are part of a series, carried out in order to assess the effect of the hydrologic cycle on the development of the general circulation of the atmosphere. They are a direct continuation of research carried out along the same lines with a quasi-geostrophic model (Huss and Doron, 1967). From the results of this earlier set of experiments tentative conclusions were drawn as to the effect of the release of latent heat. The question, as to whether these effects are real physical phenomena or merely derived from the specific mathematical formulation of the model, could not be answered with certainty. One way of overcoming this difficulty is to try to simulate the same effects with a different model. For such a comparison it is necessary to apply both models to the same domain and to include the same physical parameters, as far as possible.

A first step in this direction was made in the following experiments. The model chosen was essentially the two level, primitive equations model developed by Mintz and Arakawa (Langlois and Kwok 1969). As this model covers laterally the whole globe and vertically only the troposphere, certain modifications were required. These included the application of a different vertical coordinate and the formulation of boundary conditions appropriate for the zonal strip chosen for the quasi-geostrophic model. In addition the original definition of heat sources and sinks was abandoned and the formulation of the quasi-geostrophic case was used. Finally, all the effects due to the curvature of the globe were neglected and the equations were applied to a plane strip, as in the previous model.

General Aspects of the Model

In order to investigate further the influence of the introduction of water vapor and release of latent heat on the general circulation, a second more advanced model was used. The model chosen was basically the two level primitive equations model developed by Mintz and Arakawa (Langlois and Kwok, 1968). Certain modifications, which will be listed below, were necessary in order to apply it to the same domain chosen for the previous experiments. Thus the vertical coordinate had to be modified. Furthermore, the introduction of lateral "walls" as boundaries necessitated the introduction of suitable boundary conditions and an appropriate definition of a corresponding finite difference scheme. No attempt was made of mapping and the equations were applied to a plane. Finally the original formulation of heat sources and sinks was abandoned and a simple heating function was employed, similar to the one used in the previous model. Thus, using also similar initial conditions, the results of the two models might be compared The main advantage of the present model is the removal of the quasi-geostrophic restriction imposed on the previous model. A second advantage would be that orographic effects could be introduced in a straightforward way - but this was not done in the following experiments. As in the previous model two levels were used in the vertical, and they were fixed in such a way as to be as close as possible to the levels used previously In the original model the humidity field was carried by the lower level only. In the present experiments, water vapor was carried explicitly at two levels. It was not expected, however, that this would lead to any marked improvements, as the amount of water at the upper level must be at least one order of magnitude smaller than the amount

at the lower level. Thus the release of latent heat at the upper level will have only a small effect. It was expected however, that this modification would improve the mechanism of water vapor transports in the atmosphere. The experience gained may be of help in the treatment of the distribution of other materials in the atmosphere, such as radioactive substances.

Governing equations and integral constraints

Making use of the x, y, τ, t coordinate system introduced by Phillips (1957) the thermo-hydrodynamic equations may be written in the form:

$$\frac{\partial v}{\partial t} + v \cdot \nabla v + \dot\sigma \frac{\partial v}{\partial \sigma} + f k \times v + \nabla \phi - \frac{\sigma}{\pi} \frac{\partial \phi}{\partial \sigma} + F = 0 , \tag{1}$$

$$\frac{\partial \phi}{\partial \sigma} + \frac{R T}{\sigma} = 0 , \tag{2}$$

$$\frac{\partial \pi}{\partial t} + \nabla \cdot \pi v + \frac{\partial}{\partial \sigma} (\pi \dot\sigma) = 0 , \tag{3}$$

$$\frac{\partial \Theta}{\partial t} + v \cdot \nabla \Theta + \dot\sigma \frac{\partial \Theta}{\partial \sigma} - \frac{Q}{c_p} \left(\frac{\pi \sigma}{P_o} \right)^{R/c_p} = 0 , \tag{4}$$

$$\Theta - T \left(\frac{P_o}{\pi \sigma} \right)^{R/c_p} = 0 , \tag{5}$$

where:

$\vee$ - Horizontal wind vector,

f - $2\Omega \sin \varphi$ - Coriolis parameter,

$\Bbbk$ - Vertical unit vector,

ϕ - Geopotential,

Θ - Potential temperature ,

$\overline{}$ - Temperature ,

R - Gas constant for dry air ,

C_p - Specific heat at constant pressure,

P_o - 100 cb ,

π - Surface pressure ,

σ - $\dfrac{p}{\pi}$, The vertical coordinate,

Q - Diabatic heating per unit mass,

F - Frictional force .

Eqs. (1) and (4) may be written in the flux form by multiplying them by π and adding (3) multiplied by $\vee$ and Θ respectively. The result is:

$$\frac{\partial}{\partial t}(\pi \vee) + \nabla \cdot (\pi \vee \vee) + \frac{\partial}{\partial \sigma}(\pi \dot{\sigma} \vee) + \pi f \Bbbk \times \vee - \frac{\partial}{\partial \sigma}(\sigma \phi)\nabla \pi \qquad (6)$$
$$+ \nabla \cdot \pi \phi = 0 ,$$

$$\frac{\partial}{\partial t}(\pi \Theta) + \nabla \cdot (\pi \Theta \vee) + \frac{\partial}{\partial \sigma}(\pi \dot{\sigma} \Theta) - \frac{\pi Q}{c_p}\left(\frac{\pi \sigma}{P_o}\right)^{R/c_p} = 0 . \qquad (7)$$

By substituting the temperature for the potential temperature, eq. (7) becomes:

$$\frac{\partial}{\partial t}(\pi T) + \nabla \cdot (\pi T \psi) + \frac{\partial}{\partial \sigma}(\pi T \dot\sigma) + \frac{\pi R T \dot\sigma}{\sigma c_p} + \tag{8}$$

$$\frac{R T}{c_p}\left(\frac{\partial \pi}{\partial t} - \psi \cdot \nabla \pi\right) - \frac{\pi Q}{c_p} = 0.$$

In the absence of frictional forces and diabatic heat sources the total energy $\overline{\frac{1}{2}\pi \psi^2 + \pi c_p T}$, the mass-averaged potential temperature $\overline{\pi \Theta}$, and the mass averaged second moment of the potential temperature $\overline{\frac{1}{2}\pi \Theta^2}$ should be conserved. Following Mintz and Arakawa our aim is to construct a two level model involving a vertical finite difference scheme, which will maintain the above mentioned constraints. As the derivation and the final results are somewhat different from the one given by Mintz and Arakawa, they will be discussed in the following.

The levels $\sigma = 0$, 1/4, 1/2, 3/4, 1 will be denoted by subscripts 0, 1, 2, 3, 4, respectively. Equations (3), (6), (8), will be applied at levels 1 and 3. Applying eq. (3) at both levels and assuming:

$$\frac{\partial}{\partial \sigma}(\pi \dot\sigma)_1 = 2\pi(\dot\sigma_2 - \dot\sigma_0) = 2\pi \dot\sigma_2,$$

$$\frac{\partial}{\partial \sigma}(\pi \dot\sigma)_3 = 2\pi(\dot\sigma_4 - \dot\sigma_2) = -2\pi \dot\sigma_2,$$

with the boundary condition $\dot\sigma_0 = \dot\sigma_4 = 0$ the result is :

$$\frac{\partial \pi}{\partial t} + \nabla \cdot (\pi \psi_1) + 2\pi \dot\sigma_2 = 0,$$

$$\frac{\partial \pi}{\partial t} + \nabla \cdot (\pi \psi_3) - 2\pi \dot\sigma_2 = 0. \tag{9}$$

By adding eqs. (9) we obtain:

$$\frac{\partial \pi}{\partial t} = -\frac{1}{2} \nabla \cdot \left[\pi (\mathbf{v}_1 + \mathbf{v}_3) \right] , \tag{10}$$

and by substracting we obtain:

$$\dot{\sigma}_2 = - \frac{1}{4\pi} \nabla \cdot \left[\pi (\mathbf{v}_1 - \mathbf{v}_3) \right] . \tag{11}$$

Next we write the last term of eq. (1) in the form:

$$- \frac{\sigma}{\pi} \frac{\partial \phi}{\partial \sigma} \nabla \pi = - \frac{\nabla \pi}{\pi} \left[\frac{\partial}{\partial \sigma} (\phi \sigma) - \phi \right] ,$$

and applying eq. (1) at both levels the result is:

$$\frac{\partial \mathbf{v}_1}{\partial t} + \mathbf{v}_1 \cdot \nabla \mathbf{v}_1 + \dot{\sigma}_2 (\mathbf{v}_3 - \mathbf{v}_1) + f \mathbf{k} \times \mathbf{v}_1 + \nabla \phi_1 + \frac{\nabla \pi}{\pi} (\phi_1 - \phi_2) = 0 ,$$

$$\frac{\partial \mathbf{v}_3}{\partial t} + \mathbf{v}_3 \cdot \nabla \mathbf{v}_3 + \dot{\sigma}_2 (\mathbf{v}_3 - \mathbf{v}_1) + f \mathbf{k} \times \mathbf{v}_3 + \nabla \phi_3 + \frac{\nabla \pi}{\pi} (\phi_3 + \phi_2) = 0 . \tag{12}$$

The terms $\dot{\sigma}_2 (\mathbf{v}_3 - \mathbf{v}_1)$ in eqs. (12) are derived by interpolating $\dot{\sigma}$ at both levels in the form: $\dot{\sigma}_1 = \frac{\dot{\sigma}_2}{2}$ and $\dot{\sigma}_3 = \frac{\sigma_2}{2}$ and by taking forward differencing for $\frac{\partial \mathbf{v}}{\partial \sigma}$ at level 1 and backward differencing at level 3.

Multiplying eqs. (12) by $\pi \mathbf{v}_1$ and $\pi \mathbf{v}_3$ respectively: and eqs. (9) by $\frac{1}{2} \mathbf{v}_1^2$ and $\frac{1}{2} \mathbf{v}_3^2$ respectively, and adding, we obtain·

$$\frac{\partial}{\partial t}\left(\tfrac{1}{2}\pi v_1^2\right) + \nabla\cdot\left(\tfrac{1}{2}\pi v_1^2 \, v_1\right) + \pi\dot\sigma_2 \, v_1\cdot v_3 + \pi v_1\cdot\nabla\phi_1 + (\phi_1-\phi_2)\, v_1\cdot\nabla\pi = 0,$$

$$\frac{\partial}{\partial t}\left(\tfrac{1}{2}\pi v_3^2\right) + \nabla\cdot\left(\tfrac{1}{2}\pi v_3^2 \, v_3\right) - \pi\dot\sigma_2 \, v_1\cdot v_3 + \pi v_3\cdot\nabla\phi_3 + (\phi_2+\phi_3)\, v_3\cdot\nabla\pi = 0.$$

(13)

The fourth terms in eqs. (13) can be written in the form (using eq. (9)):

$$\pi v_1\cdot\nabla\phi_1 = \nabla\cdot(\pi\phi_1 v_1) - \phi_1\nabla\cdot(\pi v_1) = \nabla\cdot(\pi\phi_1 v_1) + \phi_1\left(\frac{\partial\pi}{\partial t} + 2\pi\dot\sigma_2\right),$$

$$\pi v_3\cdot\nabla\phi_3 = \nabla\cdot(\pi\phi_3 v_3) - \phi_3\nabla\cdot(\pi v_3) = \nabla\cdot(\pi\phi_3 v_3) + \phi_3\left(\frac{\partial\pi}{\partial t} - 2\pi\dot\sigma_2\right).$$

Applying this to eq. (13) the result is :

$$\frac{\partial}{\partial t}\left(\tfrac{1}{2}\pi v_1^2\right) + \nabla\cdot\left[\pi v_1\left(\tfrac{1}{2}v_1^2 + \phi_1\right)\right] + \left(v_1\cdot v_3 + 2\phi_2\right)\pi\dot\sigma_2 + \phi_2\frac{\partial\pi}{\partial t} =$$
$$= (\phi_2-\phi_1)\left(\frac{\partial\pi}{\partial t} + v_1\cdot\nabla\pi + 2\pi\dot\sigma_2\right),$$

$$\frac{\partial}{\partial t}\left(\tfrac{1}{2}\pi v_3^2\right) + \nabla\cdot\left[\pi v_3\left(\tfrac{1}{2}v_3^2 + \phi_3\right)\right] - \left(v_1\cdot v_3 + 2\phi_2\right)\pi\dot\sigma_2 - \phi_2\frac{\partial\pi}{\partial t} =$$
$$= -(\phi_2+\phi_3)\left(\frac{\partial\pi}{\partial t} + v_3\cdot\nabla\pi\right) + (\phi_3-\phi_2)2\pi\dot\sigma_2.$$

(14)

Adding eqs. (14) and integrating over the horizontal extent of the domain we get:

$$\frac{\partial}{\partial t}\overline{\left[\tfrac{1}{2}\pi(v_1^2 + v_3^2)\right]} = -\overline{(\phi_3+\phi_1)\frac{\partial\pi}{\partial t}} + \overline{\phi_2(v_1-v_3)\cdot\nabla\pi}$$
$$- \overline{(\phi_1-\phi_3)2\pi\dot\sigma_2} - \overline{\phi_1 v_1\cdot\nabla\pi} - \overline{\phi_3 v_3\cdot\nabla\pi},$$

(15)

where $(\overbrace{\qquad})$ denotes horizontal averaging.

Eq. (15) is the finite difference analogue of the kinetic energy equation, when integrated over the domain

We now write eq. (7) at both levels in the form:

$$\frac{\partial}{\partial t}(\pi \Theta_1) + \nabla \cdot (\pi \Theta_1 v_1) + 2\pi \Theta_2 \dot{\sigma}_2 = 0,$$

$$\frac{\partial}{\partial t}(\pi \Theta_3) + \nabla \cdot (\pi \Theta_3 v_3) - 2\pi \Theta_2 \dot{\sigma}_2 = 0; \qquad (16)$$

adding eq. (16) and integrating horizontally over the domain :

$$\frac{\partial}{\partial t}\overbrace{[\pi(\Theta_1 + \Theta_3)]} = 0. \qquad (17)$$

Eq. (17) is the finite difference analogue of the potential temperature average, so that this constraint is satisfied.

Adding $2\pi \dot{\sigma}_2 T_2 \left(\frac{P_0}{P_1}\right)^{R/c_p}$ and $-2\pi \dot{\sigma}_2 T_2 \left(\frac{P_0}{P_3}\right)^{R/c_p}$ to eqs. (16) respectively and dividing them by $c_p \left(\frac{P_0}{P_1}\right)^{R/c_p}$ and $c_p \left(\frac{P_0}{P_3}\right)^{R/c_p}$ respectively we obtain :

$$\frac{\partial}{\partial t}(\pi c_p T_1) + \nabla \cdot (\pi c_p T_1 v_1) + 2\pi \dot{\sigma}_2 c_p T_2 - c_p \pi \Theta_1 \frac{\partial}{\partial t}\left[\left(\frac{P_1}{P_0}\right)\right]^{R/c_p}$$

$$- c_p \pi \Theta_1 v_1 \cdot \nabla \left[\left(\frac{P_1}{P_0}\right)^{R/c_p}\right] = 2\pi \dot{\sigma}_2 c_p \left[T_2 - \left(\frac{P_1}{P_0}\right)^{R/c_p} \Theta_2\right],$$

$$\frac{\partial}{\partial t}(\pi c_p T_3) + \nabla \cdot (\pi c_p T_3 v_3) - 2\pi \dot{\sigma}_2 c_p T_2 - c_p \pi \Theta_2 \frac{\partial}{\partial t}\left[\left(\frac{P_2}{P_0}\right)^{R/c_p}\right] \quad (18)$$

$$- c_p \pi \Theta_3 v_3 \cdot \nabla \left[\left(\frac{P_3}{P_0}\right)^{R/c_p}\right] = 2\pi \dot{\sigma}_2 c_p \left[\left(\frac{P_3}{P_0}\right)^{R/c_p} \Theta_2 - T_2\right].$$

Now,

$$\frac{\partial}{\partial t}\left[\left(\frac{p_1}{p_0}\right)^{R/c_p}\right] = \frac{R}{c_p}\, p_0^{-R/c_p}\, p_1^{-R/c_p-1}\, \frac{\partial p_1}{\partial t} = \frac{R}{c_p p_1}\left(\frac{p_1}{p_0}\right)^{R/c_p}\frac{\partial \pi}{\partial t} = \frac{R\,T_1}{c_p\,\pi\,\Theta_1}\frac{\partial \pi}{\partial t} ,$$

so that

$$-c_p \pi \Theta_1 \frac{\partial}{\partial t}\left[\left(\frac{p_1}{p_0}\right)^{R/c_p}\right] = -R T_1\, \frac{\partial \pi}{\partial t} ;$$

in the same way:

$$c_p \pi \Theta_3 \frac{\partial}{\partial t}\left[\left(\frac{p_3}{p_0}\right)^{R/c_p}\right] = -R T_3\, \frac{\partial \pi}{\partial t} ,$$

$$-c_p \pi \Theta_1\, \mathbf{v}_1 \cdot \nabla\left[\left(\frac{p_1}{p_0}\right)^{R/c_p}\right] = -R T_1\, \mathbf{v}_1 \cdot \nabla \pi ,$$

$$-c_p \pi \Theta_3\, \mathbf{v}_3 \cdot \nabla\left[\left(\frac{p_3}{p_0}\right)^{R/c_p}\right] = -R T_3\, \mathbf{v}_3 \cdot \nabla \pi ,$$

Applying these results to eqs. (18)   the result is:

$$\frac{\partial}{\partial t}\left(\pi c_p T_1\right) + \nabla \cdot \left(\pi c_p T_1 \mathbf{v}_1\right) + 2\pi \dot{\sigma}_2 c_p T_2 - R T_1\left(\frac{\partial \pi}{\partial t} + \mathbf{v}_1 \cdot \nabla \pi\right) =$$
$$= 2\pi \dot{\sigma}_2 c_p T_2\left[1 - \left(\tfrac{1}{2}\right)^{R/c_p}\right] ,$$

$$\frac{\partial}{\partial t}\left(\pi c_p T_3\right) + \nabla \cdot \left(\pi c_p T_3 \mathbf{v}_3\right) - 2\pi \dot{\sigma}_2 c_p T_2 - R T_3\left(\frac{\partial \pi}{\partial t} + \mathbf{v}_3 \cdot \nabla \pi\right) =$$
$$= 2\pi \dot{\sigma}_2 c_p T_2\left[\left(\tfrac{3}{2}\right)^{R/c_p} - 1\right] . \qquad (19)$$

Finally adding the four equations (14) and (19) and integrating over the domain the result is:

$$\frac{\partial}{\partial t}\left[\pi\left(c_p T_1 + c_p T_3 + \frac{1}{2}v_1^2 + \frac{1}{2}v_3^2\right)\right] = \left(RT_1 + \phi_2 - \phi_1\right)\left(\frac{\partial \pi}{\partial t} + v_1 \cdot \nabla \pi\right)$$

$$+ \left(RT_3 + \phi_2 - \phi_3\right)\left(\frac{\partial \pi}{\partial t} + v_3 \nabla \pi\right) + 2\pi\dot\sigma_2\left[\phi_3 - \phi_1 + c_p T_2\left\{\left(\frac{3}{2}\right)^{R/c_p} - \left(\frac{1}{2}\right)^{R/c_p}\right\}\right] \tag{20}$$

Eq. (20) is the finite difference analogue of the total energy equation.

In order to maintain kinetic energy conservation no matter what the values of π, $\dot\sigma_2$ and v are, we must require:

$$RT_1 = \phi_1 - \phi_2 ,$$

$$RT_3 = \phi_2 + \phi_3 ,$$

$$c_p T_2 \left[\left(\frac{3}{2}\right)^{R/c_p} - \left(\frac{1}{2}\right)^{R/c_p}\right] = \phi_1 - \phi_3 . \tag{21}$$

Eqs. (21) represent the finite difference form of the hydrostatic equation. Turning to eqs. (16) and writing them in the form:

$$\pi\left(\frac{\partial \Theta_1}{\partial t} + v_1 \cdot \nabla \Theta_1\right) + \Theta_1\left[\frac{\partial \pi}{\partial t} + \nabla \cdot (\pi v_1)\right] + 2\pi\dot\sigma_2 \Theta_2 = 0 ,$$

$$\pi\left(\frac{\partial \Theta_3}{\partial t} + v_3 \cdot \nabla \Theta_3\right) + \Theta_3\left[\frac{\partial \pi}{\partial t} + \nabla \cdot (\pi v_3)\right] - 2\pi\dot\sigma_2 \Theta_2 = 0 , \tag{22}$$

and using (9), we obtain.

$$\frac{\partial \Theta_1}{\partial t} + v_1 \cdot \nabla \Theta_1 + 2\dot\sigma_2\left(\Theta_2 - \Theta_1\right) = 0 ,$$

$$\frac{\partial \Theta_3}{\partial t} + v_3 \cdot \nabla \Theta_3 + 2\dot\sigma_2\left(\Theta_3 - \Theta_2\right) = 0 . \tag{23}$$

Multiplying eqs. (23) by $\pi \Theta_1$ and $\pi \Theta_2$ respectively,

$$\frac{\partial}{\partial t}\left(\tfrac{1}{2}\pi\Theta_1^2\right) + \nabla\cdot\left(\tfrac{1}{2}\pi\Theta_1^2\, v_1\right) + 2\pi\dot\sigma_2\,\Theta_1\left(\Theta_2 - \tfrac{1}{2}\Theta_1\right) = 0,$$

$$\frac{\partial}{\partial t}\left(\tfrac{1}{2}\pi\Theta_3^2\right) + \nabla\cdot\left(\tfrac{1}{2}\pi\Theta_3^2\, v_3\right) - 2\pi\dot\sigma_2\,\Theta_3\left(\Theta_2 - \tfrac{1}{2}\Theta_3\right) = 0. \tag{24}$$

Adding eqs (24) and integrating over the domain:

$$\frac{\partial}{\partial t}\widetilde{\left[\tfrac{1}{2}\pi\left(\Theta_1^2+\Theta_3^2\right)\right]} = 2\pi\dot\sigma_2\,\widetilde{\left[\Theta_2\left(\Theta_1-\Theta_3\right)-\tfrac{1}{2}\left(\Theta_1^2-\Theta_3^2\right)\right]}, \tag{25}$$

Equation (25) is the finite difference analogue of the second moment of the potential temperature equation.

In order to maintain the constraint for an arbitrary value of $\dot\sigma_2$ and π we thus must have:

$$\Theta_2 = \tfrac{1}{2}\frac{\Theta_1^2 - \Theta_3^2}{\Theta_1 - \Theta_3} = \tfrac{1}{2}\left(\Theta_1 + \Theta_3\right), \tag{26}$$

and for the temperature at level 2 we obtain:

$$T_2 = \tfrac{1}{2}\left[2^{R/c_p}\,T_1 + \left(\tfrac{2}{3}\right)^{R/c_p}T_3\right]. \tag{27}$$

Defining:
$$\alpha = \frac{c_p}{2}\,2^{R/c_p}\left[\left(\tfrac{3}{2}\right)^{R/c_p} - \left(\tfrac{1}{2}\right)^{R/c_p}\right],$$

$$\beta = \frac{c_p}{2}\left(\tfrac{2}{3}\right)^{R/c_p}\left[\left(\tfrac{3}{2}\right)^{R/c_p} - \left(\tfrac{1}{2}\right)^{R/c_p}\right]$$

and solving eqs. (21) and (27) we obtain:

$$\phi = \frac{1}{2}\left[(\Omega+\alpha)T_1 + (\Omega+\beta)T_3\right],$$

$$\phi_2 = \frac{1}{2}\left[(\alpha-\Omega)T_1 + (\beta+\Omega)T_3\right],$$

(28)

$$\phi_3 = \frac{1}{2}\left[(\Omega-\alpha)T_1 + (\Omega-\beta)T_3\right].$$

We are now in a position to sum up the equations of the model under adiabatic and frictionless conditions:

$$\frac{\partial}{\partial t}(\pi u_1) + \nabla\cdot(\pi u_1 v_1) + \pi(u_1+u_3)\dot{\sigma}_2 - \pi\beta v_1 + \frac{\partial}{\partial x}(\pi\phi_1) + (\Omega T_1 - \phi_1)\frac{\partial\pi}{\partial x} = 0, \qquad \text{I}$$

$$\frac{\partial}{\partial t}(\pi u_3) + \nabla\cdot(\pi u_3 v_3) - \pi(u_1+u_3)\dot{\sigma}_2 - \pi\beta v_3 + \frac{\partial}{\partial x}(\pi\phi_3) + (\Omega T_3 - \phi_3)\frac{\partial\pi}{\partial x} = 0, \qquad \text{II}$$

$$\frac{\partial}{\partial t}(\pi v_1) + \nabla\cdot(\pi v_1 v_1) + \pi(v_1+v_3)\dot{\sigma}_2 + \pi\beta u_1 + \frac{\partial}{\partial y}(\pi\phi_1) + (\Omega T_1 - \phi_1)\frac{\partial\pi}{\partial y} = 0, \qquad \text{III}$$

$$\frac{\partial}{\partial t}(\pi v_3) + \nabla\cdot(\pi v_3 v_3) - \pi(v_1+v_3)\dot{\sigma}_2 + \pi\beta u_3 + \frac{\partial}{\partial y}(\pi\phi_3) + (\Omega T_3 - \phi_3)\frac{\partial\pi}{\partial y} = 0, \qquad \text{IV}$$

$$\frac{\partial}{\partial t}(\pi T_1) + \nabla\cdot(\pi T_1 v_1) - \frac{\Omega T_1}{c_p}\left(\frac{\partial\pi}{\partial t} + v_1\cdot\nabla\pi\right) + 2\pi\dot{\sigma}_2\left(\tfrac{1}{2}\right)^{R/c_p} T_2 = 0, \qquad \text{V}$$

$$\frac{\partial}{\partial t}(\pi T_3) + \nabla\cdot(\pi T_3 v_3) - \frac{\Omega T_3}{c_p}\left(\frac{\partial\pi}{\partial t} + v_3\cdot\nabla\pi\right) - 2\pi\dot{\sigma}_2\left(\tfrac{3}{2}\right)^{R/c_p} T_2 = 0, \qquad \text{VI}$$

$$\frac{\partial \pi}{\partial t} = -\frac{1}{2} \nabla \cdot \left[\pi (v_1 + v_3) \right] = -\nabla \cdot (\pi v_1) - 2\pi \dot{\sigma}_2 = -\nabla \cdot (\pi v_3) + 2\pi \dot{\sigma}_2, \quad \text{VII}$$

$$\dot{\sigma}_2 = -\frac{1}{4\pi} \nabla \cdot \left[\pi (v_1 - v_3) \right], \quad \text{VIII}$$

$$T_2 = \frac{1}{2} \left[2^{R/c_p} T_1 + \left(\frac{2}{3} \right)^{R/c_p} T_3 \right]. \quad \text{IX}$$

Equations I - IX and the 3 equations (28) thus complete the system of the model equations.

FRICTIONAL TERMS, EDDY DIFFUSION TERMS AND DIABATIC HEATING

As the vertical diffusion terms and the surface friction were essentially modelled in the same way as sugg   by Mintz and Arakawa, their derivations will be   omitted here. The only difference worth mentioning, is that in the case of the surface stress the dependence on surface density was omitted, i. e. it was made to depend only on the surface wind and on the pressure.   The surface wind was extrapolated linearly from the winds at the two reference levels.   The inclusion of changes in surface density, amounting to no more than 10%, would not make the surface stress any more accurate, and would take up more computer time. The horizontal diffusion terms were made proportional to the Laplacian of the diffused quantity, with the same constant of proportionality for momentum sensible heat and water vapor.

As mentioned above, the original formulation of heat sources and sinks was completely abandoned. As in the quasi-geostrophic model the only heat sources taken into account were sensible heat flux from the lower boundary and release of latent heat   The only sinks were radiation losses to space and downward flux to the surface. The sensible heat flux was made proportional to the temperature difference between air and ocean. Assuming, as we did before, a standard atmosphere lapse rate between the lower reference level and the surface, the air temperature at the lower boundary became proportional to T_3.   The heat flux enters the lowest layer only, this being an additional aspect which differs   from the previous model. The radiation losses were calculated in the same way and were made equal at both levels

ENERGY TRANSFORMATIONS

As already mentioned above, the average kinetic energy per unit column is given by:

$$\overline{K} = \frac{\pi}{4g} \overline{(v_1^2 + v_3^2)}.$$

Multiplying eqs. I-IV by u_1, u_3, v_1, v_3 respectively and adding eq VII multiplied by $\frac{1}{2}u_1^2, \frac{1}{2}u_3^2, \frac{1}{2}v_1^2, \frac{1}{2}v_3^2$ respectively, we obtain:

$$\frac{\partial}{\partial t}\left[\frac{1}{2}\pi(v_1^2 + v_3^2)\right] = -\nabla \cdot \left[\frac{\pi v_1^2}{2} v_1\right] - \nabla \cdot \left[\frac{\pi v_3^2}{2} v_3\right]$$
$$-\pi v_1 \cdot \nabla \phi_1 - \pi v_3 \cdot \nabla \phi_3 - RT_1 v_1 \cdot \nabla \pi - RT_3 v_3 \cdot \nabla \pi. \quad (29)$$

Integrating over the horizontal extent of the domain:

$$\frac{\partial \overline{K}}{\partial t} = -\overline{\frac{\pi}{2g}(v_1 \cdot \nabla \phi_1 + v_3 \cdot \nabla \phi_3)} - \frac{1}{2g}\overline{(RT_1 v_1 + RT_3 v_3) \cdot \nabla \pi}. \quad (30)$$

In the absence of frictional losses the right hand side represents the transformation of potential into kinetic energy:

$$[P, K] = -\frac{1}{2g}\overline{\left[\pi(v_1 \cdot \nabla \phi_1 + v_3 \cdot \nabla \phi_3) + (RT_1 v_1 + RT_3 v_3) \cdot \nabla \pi\right]}. \quad (31)$$

Frictional losses are divided into two parts, one due to vertical diffusion of momentum and one due to horizontal diffusion. These losses represent the

energy which is transformed into the kinetic energy of small - scale eddies not resolved by the model. For these two transformations we obtain:

$$\left[K, F_v \right] = -\overline{\frac{\pi}{2g} (v_1 \cdot F_1 + v_3 \cdot F_3)},$$

$$\left[K, A \right] = \frac{c}{2g} \overline{\left[v_1 \cdot \nabla^2(\pi v_1) + v_3 \cdot \nabla^2(\pi v_3) \right]}, \tag{32}$$

c being the eddy diffusion constant, where F_1 and F_2 are given by (Langlois 1968):

$$F_1 = -B(v_1 - v_3)/\pi^2,$$

$$F_3 = B(v_1 - v_3)/\pi^2 - D|v_4| v_4/\pi, \tag{33}$$

B and D are constants.

With this definition of F_1 and F_2 the final result becomes:

$$\left[K, F_v \right] = \frac{B}{2g} \frac{(v_1 - v_3)^2}{\pi} + \frac{D}{2g} |v_4| v_4 \cdot v_3, \tag{34}$$

with v_4 given by:

$$v_4 = \tfrac{1}{2}(3 v_3 - v_1).$$

THE HUMIDITY FIELD

As in the previous model the variable chosen to represent the humidity field was the specific humidity, q. The prognostic equation for the specific humidity was written in the form:

$$\frac{\partial}{\partial t}(\pi q) + \nabla \cdot (\pi q v) + \frac{\partial}{\partial \sigma}(\pi q \dot\sigma) + \pi(C - E) - A \nabla^2(\pi q) = C, \tag{35}$$

where :

E - Specific humidity gain through evaporation,

C - Specific humidity loss through precipitation,

A - Eddy diffusion coefficient.

The formulation of the evaporation and precipitation mechanism adopted in the previous model was retained also for the present model, except that the amount of water vapor added through evaporation was allowed to enter the lower layer only. Thus the assumption of constant relative humidity with height was dropped and no instantaneous adjustment of the humidity distribution through evaporation and precipitation was required. As seen from the equation, no vertical diffusion of water vapor was introduced at this stage. Adopting the same vertical differencing as for temperature, we get the two prognostic equations at the two levels:

$$\frac{\partial}{\partial t}(\pi q_1) + \nabla \cdot (\pi q_1 v_1) + 2\pi \dot{\sigma}_2 q_2 + \pi C_1 - A \nabla^2 (\pi q_1) = 0,$$

$$\frac{\partial}{\partial t}(\pi q_3) + \nabla \cdot (\pi q_3 v_3) - 2\pi \dot{\sigma}_2 q_2 + \pi (C_3 - E_3) - A \nabla^2 (\pi q_3) = C, \qquad (36)$$

q_2 was estimated as a weighted average of q_1 and q_3. Assuming that the humidity is distributed according to a σ^3 law, as in the previous model, we obtain:

$$q_1 = \left(\frac{1}{2}\right)^3 q_2,$$

$$q_3 = \left(\frac{3}{2}\right)^3 q_2.$$

with $\qquad c_2 = A\, q_{r_1} + B\, q_3 \,, \qquad\qquad A + B = 1 \,.$

Thus $\qquad q_{r_2} = .73\, c_{r_1} + .27\, q_3 \,.$

Experience obtained from a 3-level model involving, among other aspects, the concentration of radon as a time-dependent variable, showed that the poor resolution in the vertical, with the assumed time step may lead to negative values of the concentration. This was due to the fact that on the average the concentration at the intermediate level was about five times larger than that in the upper level and about three times smaller than that in the lower level when linear interpolation was used for q_r . The vertical advection process was thus overestimated at the upper level and underestimated at the lower level. To overcome this difficulty a weighted average was used. The results show that this was quite adequate and the relative humidity never went below about 30%

BOUNDARY AND INITIAL CONDITIONS

As mentioned above, the equations were applied to the same domain as in the previous experiments. Thus we require cyclic continuity on the eastern boundaries. On the northern and southern boundaries the following boundary conditions were chosen :

(1) $\qquad v_N = v_S = 0$

(2) $\qquad \dfrac{\partial}{\partial y}(\pi v)_N = \dfrac{\partial}{\partial y}(\pi v)_S = \dfrac{\partial}{\partial y}(\pi u)_N = \dfrac{\partial}{\partial y}(\pi u)_S = 0$

(3) $\qquad \dfrac{\partial}{\partial y}(\pi T)_N = \dfrac{\partial}{\partial y}(\pi T)_S = 0 \,.$

Condition (1) ensures that no mass leaves the domain through advection
Condition (2) and (3) ensure that there is no diffusion of momentum or

of heat through the lateral boundaries.

The initial conditions were generated in the following way :

First the ocean surface temperature was assumed to be constant with longitude and to vary linearly from $27^{\circ}C$ at $j = 1$ to $-25^{\circ}C$ at $j = 14$, with a gradient of $4^{\circ}C$ per grid interval. Next it was assumed that the air surface temperature was equal to the ocean temperature, so that initially no sensible heat entered the model atmosphere from the lower boundary. The surface pressure was assumed to be constant everywhere, and equal to the standard pressure of 1013 mb. Next the temperature at level 3 was calculated from the surface temperature by assuming a standard atmosphere lapse rate between the surface and level 3. The upper level temperatures were assumed to vary linearly from $232^{\circ}A$ at $j = 1$ to $219^{\circ}A$ at $j = 14$, with a gradient of 1° per grid interval. From the temperatures at both levels the geopotentials at both levels were calculated. At this stage a perturbation was superimposed on the zonally averaged geopotentials of the following form , $\phi = \phi_0 + A \sin \frac{\pi Y}{Y} \sin \frac{2\pi x}{X}$, where Y and X are the lengths of the domain in the y and x direction respectively. The amplitude chosen was the same as in the previous model. Next the temperatures were corrected to correspond to the perturbed geopotentials Finally the winds were assumed to be initially geostrophic and were calculated from the geopotentials.

The Arakawa finite difference scheme was retained in all the equations. The grid interval used was the same as in the previous model, but the time interval was reduced to 10 minutes to ensure mathematical stability of the integration. The time derivative was approximated by the Matsuno scheme.

FINITE DIFFERENCE SHCEME AND BOUNDARY CONDITIONS

As mentioned above the same domain chosen for the previous experiments was retained. It contained 15 grid points in the x and y directions respectively. The staggered grid configuration proposed by Arakawa was used. As it was thought advisable to write the finite difference equations in a formulation which would allow a straightforward application to the computer program, the different variables at the four different points were assigned the same indices (see Figure below).

Defining (with the upper index denoting the level):

$$U_{i,j} = \frac{1}{4\Delta s}(u_{i,j} + u_{i,j+1})(\pi_{i,j} + \pi_{i-1,j}),$$

$$V_{i,j} = \frac{1}{4\Delta s}(v_{i,j} + v_{i+1,j})(\pi_{i,j} + \pi_{i,j-1}),$$

$$S_{i,j} = \pi_{i,j}\,\sigma_{i,j}^2,$$

(37)

the finite difference form of eq. VII becomes:

$$\frac{\partial}{\partial t}(\pi_{i,j}) = \frac{1}{2}\left[U_{i,j}^1 + U_{i,j}^2 - U_{i+1,j}^1 - U_{i+1,j}^3 \right.$$
$$\left. + V_{i,j}^1 + V_{i,j}^2 - V_{i,j+1}^1 - V_{i,j+1}^2 \right],$$

(38)

and eq. VIII becomes:

$$S_{i,j} = \frac{1}{4}\left[u_{i,j}^{1} - u_{i,j}^{2} - u_{i+1,j}^{1} + u_{i+1,j}^{2}\right.$$

$$\left. + v_{i,j}^{1} - v_{i,j}^{2} - v_{i,j+1}^{1} + v_{i,j+1}^{2}\right]. \tag{39}$$

The boundary conditions for the last two eqs. become:

$$v_{i,1}^{\kappa} = v_{i,15}^{\kappa} = 0,$$

for every i and k , where k denotes the level.

The last condition ensures conservation of mass in the form:

$$\sum_{i,j} \nabla_{i,j} \cdot (\pi v) = 0.$$

Next we turn to the divergence terms in eqs. I - VI. They are written in the form:

$$\nabla \cdot (\pi x v)_{i,j} = \frac{1}{8}\left[\frac{2}{3}(u_{i,j} + u_{i+1,j} + u_{i+1,j-1} + u_{i,j-1})(x_{i,j} + x_{i+1,j})\right.$$

$$-\frac{2}{3}(u_{i,j} + u_{i,j-1} + u_{i-1,j} + u_{i-1,j-1})(x_{i,j} + x_{i-1,j})$$

$$+\frac{2}{3}(v_{i-1,j+1} + v_{i,j+1} + v_{i-1,j} + v_{i,j})(x_{i,j} + x_{i,j+1})$$

$$-\frac{2}{3}(v_{i-1,j} + v_{i,j} + v_{i-1,j-1} + v_{i,j-1})(x_{i,j} + x_{i,j-1})$$

$$+\frac{1}{3}(u_{i,j} + u_{i+1,j} + v_{i,j} + v_{i,j+1})(x_{i,j} + x_{i+1,j+1})$$

$$+\frac{1}{3}(u_{i,j-1} + u_{i+1,j-1} - v_{i,j} - v_{i,j-1})(x_{i,j} + x_{i+1,i-1})$$

$$-\frac{1}{3}(u_{i,j} + u_{i-1,j} - v_{i-1,j} - v_{i-1,j+1})(x_{i,j} + x_{i-1,j+1})$$

$$-\frac{1}{3}(u_{i,j-1} + u_{i-1,j-1} + v_{i-1,j} + v_{i-1,j-1})(x_{i,j} + x_{i-1,i-1})\right] \tag{40}$$

With x denoting either u or v.

To ensure the condition $\int_S \nabla \cdot (\pi \times \vee) \, d\circ = 0$ the following formulation is used near the boundaries:

$$\tfrac{1}{2} \nabla \cdot (\pi u \vee)_{i,1} = \tfrac{1}{8 \Delta s} \Big[\pi_{i,1} (u_{i,1} + u_{i+1,1})(u_{i,1} + u_{i+1,1})$$

$$- \pi_{i-1,1}(u_{i,1} + u_{i-1,1})(u_{i,1} + u_{i-1,1}) \Big] + \tfrac{1}{8} \Big[\tfrac{2}{3}(v_{i,2} + v_{i-1,2})(u_{i,1} + u_{i,2})$$

$$+ \tfrac{1}{3} v_{i,2}(u_{i,1} + u_{i+1,2}) + \tfrac{1}{3} v_{i-1,2}(u_{i,1} + u_{i-1,2}) \Big],$$

$$\tfrac{1}{2} \nabla \cdot (\pi u \vee)_{i,15} = \tfrac{1}{8 \Delta s} \Big[\pi_{i,14}(u_{i,15} + u_{i+1,15})(u_{i,15} + u_{i+1,15})$$

$$- \pi_{i-1,14}(u_{i,15} + u_{i-1,15})(u_{i,15} + u_{i-1,15}) \Big] - \tfrac{1}{8} \Big[\tfrac{2}{3}(v_{i,14} + v_{i-1,14})(u_{i,15} + u_{i,14})$$

$$+ \tfrac{1}{3} v_{i,14}(u_{i,15} + u_{i+1,14}) + \tfrac{1}{3} v_{i-1,14}(u_{i,15} + u_{i-1,14}) \Big]. \tag{41}$$

The $\vee$ equations are treated in a different way as with v = 0 on the boundaries, the equations are not applied there. This requires a different formulation of the scheme at a distance of one grid interval from the boundary, in the form.

$$\nabla \cdot (\pi \vee \vee)_{i,2} = \tfrac{1}{8} \Big[\tfrac{5}{6} (u_{i,2} + u_{i+1,2} + u_{i+1,1} + u_{i,1})(v_{i,2} + v_{i+1,2})$$

$$- \tfrac{5}{6} (u_{i,2} + u_{i,1} + u_{i-1,2} + u_{i-1,1})(v_{i,2} + v_{i-1,2})$$

$$+ \tfrac{2}{3} (v_{i-1,2} + v_{i,3} + v_{i-1,2} + v_{i,2})(v_{i,2} + v_{i,3})$$

$$+ \tfrac{1}{3} (u_{i,2} + u_{i+1,2} + v_{i,2} + v_{i,3})(v_{i,2} + v_{i+1,3})$$

$$- \tfrac{1}{3} (u_{i,2} + u_{i-1,2} - v_{i-1,2} - v_{i-1,3})(v_{i,2} + v_{i-1,3}) \Big],$$

$$\nabla\cdot(\pi v \, \mathbf{v})_{i,14} = \frac{1}{3}\left[\frac{5}{6}\left(U_{i,14} + U_{i+1,14} + U_{i,13} + U_{i+1,13}\right)\left(v_{i,14} + v_{i+1,14}\right)\right.$$

$$-\frac{5}{6}\left(U_{i,14} + U_{i,13} + U_{i-1,14} + U_{i-1,13}\right)\left(v_{i,14} + v_{i-1,14}\right)$$

$$-\frac{2}{3}\left(V_{i,14} + V_{i-1,14} + V_{i,13} + V_{i-1,13}\right)\left(v_{i,14} + v_{i,13}\right)$$

$$+\frac{1}{3}\left(U_{i,13} + U_{i+1,13} - V_{i,14} - V_{i,13}\right)\left(v_{i,14} + v_{i+1,13}\right)$$

$$\left.-\frac{1}{3}\left(U_{i,13} + U_{i-1,13} + V_{i-1,14} + V_{i-1,13}\right)\left(v_{i,14} + v_{i-1,13}\right)\right]. \quad (42)$$

The application of this scheme ensures conservation of momentum in the flux terms. Whether it also conserves energy does not appear to be certain, but it is expected that even if it does not, the error will be very small, particularly when a more extensive domain with more grid points will be used.

The vertical flux terms in eqs. I - IV are written in the form:

$$\left[\pi\left(x^1 + x^3\right)\dot{\sigma}^2\right]_{i,j} =$$

$$= \frac{1}{4}\left(x^1_{i,j} + x^3_{i,j}\right)\left(S_{i,j} + S_{i-1,j} + S_{i,j-1} + S_{i-1,j-1}\right), \quad (43)$$

with X denoting either u or v.

The coriolis parameter f is defined at the same points as u and v so that:

$$(\pi f u)_{i,j} = \frac{1}{4}\left(\pi_{i,j} + \pi_{i-1,j} + \pi_{i,j-1} + \pi_{i-1,j-1}\right) f_{i,j} \, u_{i,j} \, ,$$

$$(\pi f v)_{i,j} = \frac{1}{4}\left(\pi_{i,j} + \pi_{i-1,j} + \pi_{i,j-1} + \pi_{i-1,j-1}\right) f_{i,j} \, v_{i,j} \, . \quad (44)$$

In the u equation on the boundaries it is of course omitted, by virtue of the condition v = 0, so that this presents no problem as far as conservation of energy is concerned.

Next we write:

$$\frac{\partial}{\partial x}(\pi\phi)_{i,j} \;=\;$$

$$= \frac{1}{2\Delta s}\left(\pi_{i,j}\,\phi_{i,j} + \pi_{i,j-1}\,\phi_{i,j-1} - \pi_{i-1,j}\,\phi_{i-1,j} - \pi_{i-1,j-1}\,\phi_{i-1,j-1}\right),$$

$$\frac{\partial}{\partial y}(\pi\phi)_{i,j} \;=\;$$

$$= \frac{1}{2\Delta s}\left(\pi_{i,j}\,\phi_{i,j} + \pi_{i-1,j}\,\phi_{i-1,j} - \pi_{i,j-1}\,\phi_{i,j-1} - \pi_{i-1,j-1}\,\phi_{i-1,j-1}\right), \quad (45)$$

and finally:

$$\left[(RT-\phi)\frac{\partial\pi}{\partial x}\right]_{i,j} = \frac{1}{4\Delta s}\Big[(RT_{i,j}-\phi_{i,j}+RT_{i-1,j}-\phi_{i-1,j})(\pi_{i,j}-\pi_{i-1,j})$$

$$+ (RT_{i,j-1}-\phi_{i,j-1}+RT_{i-1,j-1}-\phi_{i-1,j-1})(\pi_{i,j-1}-\pi_{i-1,j-1})\Big],$$

$$\left[(RT-\phi)\frac{\partial\pi}{\partial y}\right]_{i,j} = \frac{1}{4\Delta s}\Big[(RT_{i,j}-\phi_{i,j}+RT_{i,j-1}-\phi_{i,j-1})(\pi_{i,j}-\pi_{i,j-1})$$

$$+ (RT_{i-1,j}-\phi_{i-1,j}+RT_{i-1,j-1}-\phi_{i-1,j-1})(\pi_{i-1,j}-\pi_{i-1,j-1})\Big]. \quad (46)$$

On the boundaries we write in the u equations, using the condition $\frac{\partial}{\partial y}(\pi\phi)=0$,

$$\frac{\partial}{\partial x}(\pi\phi)_{i,1} = \frac{1}{\Delta s}\left(\pi_{i,1}\,\phi_{i,1} - \pi_{i-1,1}\,\phi_{i-1,1}\right),$$

$$\frac{\partial}{\partial x}(\pi\phi)_{i,15} = \frac{1}{\Delta s}\left(\pi_{i,14}\,\phi_{i,14} - \pi_{i-1,14}\,\phi_{i-1,14}\right),$$

$$\left[(RT-\phi)\frac{\partial\pi}{\partial x}\right]_{i,1} =$$

$$= \frac{1}{2\Delta s}\left[(RT_{i,1}-\phi_{i,1}+RT_{i-1,1}-\phi_{i-1,1})(\pi_{i,1}-\pi_{i-1,1})\right],$$

$$\left[(RT-\phi)\frac{\partial\pi}{\partial x}\right]_{i,15} =$$

$$= \frac{1}{2\Delta s}\left[(RT_{i,14}-\phi_{i,14}+RT_{i-1,14}-\phi_{i-1,14})(\pi_{i,14}-\pi_{i-1,14})\right] (47)$$

Next we write:

$$\frac{\partial}{\partial x}(\pi\phi)_{i,j} =$$

$$= \frac{1}{2\Delta s}\left(\pi_{i,j}\phi_{i,j} + \pi_{i,j-1}\phi_{i,j-1} - \pi_{i-1,j}\phi_{i-1,j} - \pi_{i-1,j-1}\phi_{i-1,j-1}\right),$$

$$\frac{\partial}{\partial y}(\pi\phi)_{i,j} =$$

$$= \frac{1}{2\Delta s}\left(\pi_{i,j}\phi_{i,j} + \pi_{i-1,j}\phi_{i-1,j} - \pi_{i,j-1}\phi_{i,j-1} - \pi_{i-1,j-1}\phi_{i-1,j-1}\right), \quad (45)$$

and finally:

$$\left[(RT-\phi)\frac{\partial\pi}{\partial x}\right]_{i,j} = \frac{1}{4\Delta s}\left[(RT_{i,j}-\phi_{i,j}+RT_{i-1,j}-\phi_{i-1,j})(\pi_{i,j}-\pi_{i-1,j})\right.$$

$$\left. + (RT_{i,j-1}-\phi_{i,j-1}+RT_{i-1,j-1}-\phi_{i-1,j-1})(\pi_{i,j-1}-\pi_{i-1,j-1})\right],$$

$$\left[(RT-\phi)\frac{\partial\pi}{\partial y}\right]_{i,j} = \frac{1}{4\Delta s}\left[(RT_{i,j}-\phi_{i,j}+RT_{i,j-1}-\phi_{i,j-1})(\pi_{i,j}-\pi_{i,j-1})\right.$$

$$\left. + (RT_{i-1,j}-\phi_{i-1,j}+RT_{i-1,j-1}-\phi_{i-1,j-1})(\pi_{i-1,j}-\pi_{i-1,j-1})\right]. \quad (46)$$

On the boundaries we write in the u equations, using the condition $\frac{\partial}{\partial y}(\pi\phi) = 0$:

$$\frac{\partial}{\partial x}(\pi\phi)_{i,1} = \frac{1}{\Delta s}\left(\pi_{i,1}\phi_{i,1} - \pi_{i-1,1}\phi_{i-1,1}\right),$$

$$\frac{\partial}{\partial x}(\pi\phi)_{i,15} = \frac{1}{\Delta s}\left(\pi_{i,14}\phi_{i,14} - \pi_{i-1,14}\phi_{i-1,14}\right),$$

$$\left[(RT-\phi)\frac{\partial\pi}{\partial x}\right]_{i,1} =$$

$$= \frac{1}{2\Delta s}\left[(RT_{i,1}-\phi_{i,1}+RT_{i-1,1}-\phi_{i-1,1})(\pi_{i,1}-\pi_{i-1,1})\right],$$

$$\left[(RT-\phi)\frac{\partial\pi}{\partial x}\right]_{i,15} =$$

$$= \frac{1}{2\Delta s}\left[(RT_{i,14}-\phi_{i,14}+RT_{i-1,14}-\phi_{i-1,14})(\pi_{i,14}-\pi_{i-1,14})\right]. \quad (47)$$

These formulations ensure that no momentum is generated by the diffusion terms.

The vertical diffusion and surface friction terms present no problem as they only involve quantities defined at the same grid point.

Now we turn to eqs. V and VI:

The horizontal flux terms are written in the form:

$$\nabla \cdot (\pi T v)_{i,j} = \frac{1}{2} \Big[u_{i+1,j} (T_{i,j} + T_{i+1,j}) - u_{i,j} (T_{i,j} + T_{i-1,j})$$
$$+ V_{i,j+1} (T_{i,j} + T_{i,j+1}) - V_{i,j} (T_{i,j} + T_{i,j-1}) \Big] . \tag{53}$$

With $V_{i,1} = V_{i,15} = 0$, this definition is valid also for the flux terms near the boundaries so that at $j = 1$ the fourth term is omitted, and at $j = 14$ the third term is omitted.

For the vertical flux terms we first substitute for T_2 its value from eq. IX, so that:

$$\Big[2\pi \dot\sigma^2 \left(\tfrac{3}{2}\right)^{R/c_p} T_2 \Big]_{i,j} = S_{i,j} \left(3^{R/c_p} T_{i,j}^1 + T_{i,j}^3 \right),$$
$$\Big[2\pi \dot\sigma^2 \left(\tfrac{1}{2}\right)^{R/c_p} T_2 \Big]_{i,j} = S_{i,j} \left(T_{i,j}^1 + \left(\tfrac{1}{3}\right)^{R/c_p} T_{i,j}^3 \right) . \tag{54}$$

The third terms in eqs. V and VI present no problem and they are written as:

$$\Big[\frac{RT}{c_p} \frac{\partial \pi}{\partial t} \Big]_{i,j} = \frac{R T_{i,j}}{c_p} \left(\frac{\partial \pi}{\partial t} \right)_{i,j} , \tag{55}$$

with the definition of $\left(\frac{\partial \pi}{\partial t} \right)_{i,j}$ given by (38).

Special care must be taken with the remaining term, $\frac{R}{c_p} T v \cdot \nabla \pi$. This term represents part of the energy transformation from potential energy

into kinetic energy. Thus if total energy is to be conserved, it should have the same form as the corresponding term in the kinetic energy equation, which is defined at a different grid point. To overcome this difficulty the total energy is defined at the points where T is defined. The kinetic energy is then calculated as an average of its values at the four surrounding u points.

Thus the calculation of the terms $RT\psi \cdot \nabla\pi$ proceeds in the following way: first it is defined at the points where u is defined, by using the definition of the terms $\left[RT\frac{\partial\pi}{\partial x}\right]_{i,j}$ and $\left[RT\frac{\partial\pi}{\partial y}\right]_{i,j}$ in eqs. I - VI.

Next we define:

$$\left[RTu\frac{\partial\pi}{\partial x}\right]_{i,j} = u_{i,j}\left[RT\frac{\partial\pi}{\partial x}\right]_{i,j} ,$$

$$\left[RTv\frac{\partial\pi}{\partial y}\right]_{i,j} = v_{i,j}\left[RT\frac{\partial\pi}{\partial y}\right]_{i,j} . \tag{56}$$

Finally the value of this term at the points where T is defined is calculated as an average of its values at the four surrounding u and v points. This procedure presents no special problems near the boundaries as $RTv\frac{\partial\pi}{\partial y} = 0$ on the boundaries and $RTu\frac{\partial\pi}{\partial x}$ has already been defined there.

It remains now only to define the time differencing scheme. For this purpose we use the definition of $(\pi u)_{i,j}$ and $(\pi v)_{i,j}$ given by (48) and (51) and also define:

$$\left(\pi T\right)_{i,j} = \pi_{i,j} \ T_{i,j} . \tag{57}$$

For the time differencing the so-called Matsuno scheme is used in the following way:

Given the equation : $\quad \frac{\partial x}{\partial t} = \rho(\alpha_1, \alpha_2, \cdots, \alpha_n)$ $\hspace{2cm}$ (58)

the first step is an ordinary forward difference scheme of the form:

$$x^{*\,t+1} = x^t + \Delta t\, \rho(\alpha_1^t, \alpha_2^t, \cdots, \alpha_n^t)\,, \hspace{2cm} (59)$$

and the second step is :

$$x^{t+1} = x^t + \Delta t\, \rho(\alpha_1^{*\,t+1}, \alpha_2^{*\,t+1}, \cdots, \alpha_n^{*\,t+1})\,, \hspace{1.5cm} (60)$$

The two equations (28) for $\phi^1_{i,j}$ and $\phi^3_{i,j}$ are calculated at each point by:

$$\phi^1_{i,j} = \frac{1}{2}\left[(\Omega+\alpha)\,T^1_{i,j} + (\Omega+\beta)\,T^3_{i,j}\right],$$

$$\phi^3_{i,j} = \frac{1}{2}\left[(\Omega-\alpha)\,T^1_{i,j} + (\Omega-\beta)\,T^1_{i,j}\right], \hspace{1.5cm} (61)$$

The third of the equations (28) for ϕ^2 has already been used to transform the last terms of the eqs. I - IV, so that ϕ^2 does not appear explicitly in the program.

Analysis of results

Two integrations were performed. The integration not involving release of latent heat will be referred to as Experiment I, and the experiment in which water vapor is carried as Experiment II. In Experiment I the model equations were integrated for a period of 37 days, and the integration was discontinued when a quasi-steady state was attained and no new information could be gained by prolonging the integration. Consequently emphasis will be placed in the following on the conditions prevailing on the last days of the integration.

The early stages of development were characterized by a rapid growth of the amplitude of the disturbance at both levels, similar to the development observed in the quasi-geostrophic model (Huss 1967) referred to above. It is worth while mentioning that this growth stopped on the third day and a decrease in amplitude was observed between the third and seventh days (Fig. 1). Afterwards the amplitudes started to grow again until they reached their steady state value on about the 20th day. The temporary decrease in amplitude was observed in all the experiments with the quasi-geostrophic model, though starting at a later date, i.e. on the 12th day. It thus appears that a tendency towards the development of an index cycle is observed in all experiments. This tendency, however, is damped, in most cases, as the integration is continued. The reason for this damping is not clear from the results. It might be due to the very crude formulation of the surface friction and vertical diffusion terms, which were expected to have a damping effect. On the other hand it might also be due to the finite difference formulation of the model equations, as some difference schemes are known to have marked damping effects.

In the quasi-geostrophic experiment involving water vapor, a marked index cycle developed, which was not damped until the end of the integration on the 67th day. Thus it seems that in the models strong differential heating is required in order to maintain the index cycle and counteract the

damping effect, whatever its origin may be. In the present case the values of the sensible heat flux in the south were lower than in the previous experiments and thus the index cycle appears to have been damped very fast.

In addition, the present model contains lateral eddy diffusion terms, which have a damping effect and thus it was expected that more pronounced differential heating would be required in order to maintain the index cycle. The values of the amplitudes of the geopotential waves reached towards the end of the integration were about half of the corresponding values obtained in the quasi-geostrophic case. This result was expected and is a consequence of the summer conditions imposed on the model.

The mean zonal wind distribution (Fig. 2) is characterized by a maximum westerly flow at the upper level at the central latitude and easterlies at lower levels near the boundaries. However the intensity of the jet was weaker than in the quasi-geostrophic model. The maximum value obtained was about 25 m sec^{-1} which is characteristic for summer conditions in the real atmosphere. Summer conditions were obtained in the model by reducing the surface temperature meridional gradients from 4.5° per grid interval, in the quasi-geostrophic case, to 4° per grid interval in the present case. This of course leads to a much weaker thermal wind and thus to a weaker jet. Thus, with a proper choice of the surface temperature gradient it is possible, even with the crude heating function assumed in the model, to simulate either winter or summer conditions at least as far as temperature and wind conditions are concerned. One undesirable result was the appearance of stronger easterlies near the northern boundary as compared with the belt of easterlies in the south. This seems to be a result of the assumption of a constant coriolis parameter, whereas in the quasi-geostrophic case this strong restriction is partly offset by assuming a non vanishing β term in the vorticity equation. This restriction is not an inherent aspect of the present model, as a variable coriolis parameter can easily be introduced. In that respect the present results are only of a preliminary nature

and a variable coriolis parameter will be introduced in future experiments.

A schematic presentation of the mean meridional circulation is shown in Fig. 7. The qualitative picture agrees quite well with the one observed in nature, with two direct cells in the northern and southern parts of the region and an indirect cell in the middle. The southern Hadley cell is of course too small compared with the corresponding Hadley cell in the real atmosphere, probably due to the presence of a "wall" as the southern boundary.

Its northern edge is situated at the right location at about 30°N and the corresponding meridional and vertical wind speeds have the correct magnitude, appropriate for summer conditions (Mintz and Lang 1955). The central indirect cell is also too small in its latitudinal extent and its northern edge is situated too far to the south, thus contributing to an incerease in the size of the northern direct cell. This again seems to be a result of the assumption of a constant coriolis parameter together with the restriction of the integration to a small domain. Thus it appears that, with the shortcomings mentioned above, the summertime mean meridional circulation is reasonably well simulated by the model.

The mean zonal surface pressure is presented in Fig. 8. Again as noted in the case of some other variables, the qualitative distribution is quite realistic. Thus the tropical low pressure belt, the subtropical high pressure belt, the low of the mid latitudes and the polar highs are simulated quite well in the correct latitudes. However, the pressure difference between the low and high pressure belts is too large, if compared to conditions prevailing in the northern hemisphere and too small if compared to those in the southern hemisphere. In the northern hemisphere of the real atmosphere the pressure distribution is very much affected by the ocean continent contrasts, as most of the land masses are concentrated there. This effect is smoothed out when zonal averages are computed, making the mean meridional pressure gradients much smaller than those of the southern hemisphere.

It should be noted here that the initial surface pressure was chosen to correspond to the mean pressure at sea level observed in the atmosphere. With the exclusion of the mountians in the model, this means that the model contains more mass than the real atmosphere. This is expected to lead to exaggerated values for the fluxes of momentum, heat and water vapor. One way of overcoming this difficulty is by assuming an initial surface pressure corresponding to the real mass of the atmosphere as done by Smagorinsky (1965). However, this was not done in the present experiments.

The variation with time of the total kinetic energy is given in Fig. 5. As with the amplitude of the geopotentials, traces of an index cycle are observed at the early stages of the integration. Starting on the 15th day a constant decrease of kinetic energy is observed, lasting until the end of the integration. As mentioned above, an instantaneous heat balance was imposed on the model, so that there was no net heating or cooling of the whole atmosphere. The energy losses due to surface friction and vertical and lateral diffusion could not be replenished from any other sources. It was thus expected that the total energy in the model would decrease with time, thus limiting the validity of the prediction for a long period. The observed decrease in kinetic energy from the 15th to the 37th day was about 100 Kj. m^{-2} which was about 4% of the total kinetic energy. This again motivated the decision to discontinue the integration before this effect became too serious. The total kinetic energy at the end of the integration was about 2200 Kj m^{-2}. This value is somewhat higher than the average values obtained by Oort (1964) but lies within the limits of error quoted in his paper. This high value could be explained by the fact that we had too much mass in the model and these high values were obtained even though the wind velocities were quite realistic.

Evidence of the damping of the index cycle is most clearly observed in the values of the transformation of potential energy into kinetic energy,

as a function of time (Fig. 4). A series of oscillations is observed with a period of about 7 days, and a decreasing amplitude as the integration preoceeds, until total damping of the oscillation takes place at the end of the experiment. The value of the $[\rho, \omega]$ transformation on the last day was about 130 Kj. m^{-2} day^{-1}, which is smaller by a factor of two as compared with the value presented by Oort (1964). The kinetic energy losses due to lateral eddy diffusion were rather low, and never exceeded 15 Kj. m^{-2} day^{-1}.

A comparison of the kinetic energy changes computed from values on two consecutive days, with the energy changes computed from the energy transformations, reveals a difference of the order of 10 Kj. $m^{-2}day^{-1}$. With the care taken in the model to ensure conservation of energy, it was concluded that this difference could be attributed only to the deficiency (from the point of view of energy conservation) of the time scheme employed in the model. Inspecting the daily energy changes in the model we observe that this fictitious energy loss accounts for about 10% of the change. The cumulative effects might thus be quite serious, in the long run. Combining the kinetic energy losses due to all three effects, we obtain a value of 155 Kj $m^{-2}day^{-1}$ for the total kinetic energy sink, as compared to a value of about 200 Kj. $m^{-2}day^{-1}$ obtained by Oort.

We thus conclude that the energy cycle obtained in the model was somewhat too weak, a fact which is consistent with the damping effect observed. The dominant kinetic energy losses were caused by the surface friction and the vertical eddy diffusion. The losses due to lateral diffusion were an order of magnitude smaller. This differs markedly from the results obtained by Smagorinsky (1965) where the lateral diffusion accounted for a loss of about twice as much as the vertical diffusion. Oorts results do not give seperate values for these two effects for the atmosphere so it could not be decided which of the results is closer to reality, though from the results given by Phillips (1956), it appears that both effects should have the same order of magnitude.

Next we turn our attention to the heat balance components (Fig. 6).
The net heating had a marked maximum at $j = 3$ with a value of about 0.1 Kj m^{-2}
sec^{-1} and a minimum at $j = 12$ with a value of about -0.08 Kj m^{-2} sec^{-1}. Qual-
itatively this agrees quite well with the distribution given by Rasool and Prabhakara
(1965), for the summer season in both hemispheres. The maximum heating in
August in the northern hemisphere is located at about 15°N with a value of about
0.15 Kj m^{-2} sec^{-1}; Our maximum thus lies too far to the north and the values are
somewhat too low. The minimum on the other hand is located too far south. This
seems to be a result of the choice of a too small domain and the effect of the "walls".
The gradients of differential heating obtained are thus quite realistic, which is
surprising with the simple heating function employed in the model. The southern
"wall" however seems to arrest the heating processes there, and thus in the south-
ern part of the region the gradients of heating are exaggerated as there is almost
no heating near the boundary. As a result of this the total excess of heating in the
southern region over the northern region is much too low and consequently the
heat transport to the north is also too small. The present experiment carries no
water vapor, which is expected to account for a large part of the heating in the
south and thus we conclude that the inclusion of this process is essential for a
correct distribution of heat sources and sinks in the model.

The radiational losses obtained were rather low compared with
values obtained by Astling and Horn (1964), from Tiros II measurements. The
satellite data contained of course the total outgoing long wave radiation and thus
included also that part coming from the lower surface through the atmospheric
"window". Nevertheless the low values obtained in the model have a marked effect
on the distribution of the heating with height, making the lower level heating at least
an order of magnitude stronger than the upper level heating. This is in contrast to
the previous model where the heating was distributed evenly in the column. The
situation in the atmosphere probably lies between these two extremes.

Inspecting the poleward flux of zonal momentum at both levels
the following distribution is observed: strong poleward fluxes appear at the upper
level in the southern part of the region, with a maximum value of 8.9 $m^2 sec^{-2}$
at $j = 6$. Maximum southward fluxes at the upper level with a value of 13.9 m^2
sec^{-2} were observed at $j = 10$. These values are low, compared to the summer
values obtained by Holopainen (1967). The northern maximum is situated too far
south as a result of the southward shift of the edge of the central indirect merid-
ional cell, commented on above.

The mean zonal poleward heat transport, on the other hand, shows
a better qualitative agreement with the situation in the real atmosphere, as pre-
sented by Rasool and Prabhakara (1965). Thus a small region of southward fluxes
appears near the southern boundary, at $j = 1$ and 2. Further north, northward
fluxes prevail, reaching a maximum value at $j = 7$ and then decreasing until
southward fluxes are encountered again at $j = 15$. The values presented in the
paper referred to above, were computed for latitude circles, so that with the
different length of each latitude circle in the atmosphere, as compared to our
planar zonal strip, actual comparison of values is difficult. As the upper level
temperatures obtained in the model are somewhat too high and the meridional wind
components have the right magnitude, it appears that the values obtained for the
poleward flux of heat are somewhat too high.

Experiment II

The second experiment, with the model including a water vapor
cycle and release of latent heat, was continued for a period of 32 days. As before,
a quasi-steady state was attained and further integration seemed pointless. As it
is desired to assess the influence of the release of latent heat on the development of
the circulation patterns, the water-vapor budget will be discussed first and the
discussion of synoptic manifestation will follow later.

The choice of a smaller meridional gradient of the sea surface temperatures led of course to lower air temperatures in the southern part of the region, as compared with the previous model. Consequently the water vapor in the south, where most of the humidity is expected to be concentrated, was much lower in the present case. For example, the amount of preceipitable water per unit column at $j = 1$ was about 37 mm in the pres nt case. as compared to 47 mm at the same latitude in the previous model. This, of course, had a marked effect on the precipitation and evaporation in the south The distribution with latitude of the mean zonal relative humidity, on the other hand, was similar to that obtained in the previous experiments. (Fig. 9). Thus a maximum in the relative humidity appeared at the southern boundary, a minimum at $j = 5$ and a second maximum close to the northern boundary of the region.

As in the previous model, the meridional gradient of relative humidity was exaggerated, as the relative humidities in the south and in the north were too high, and the relative humidity in the dry belt was too low, compared to the values presented by Haurwitz and Austin (1944)

Thus it seems that the shortcomings of the humidity distribution in the present experiment result from too low temperatures in the south. This can easily be corrected in future experiments designed to simulate summer conditions by assuming a higher average sea surface temperature, while retaining the same meridional gradients. This will not change the initial gradients of the geopotentials, and the same initial wind distribution will also be retained, while, on the other hand higher values for the specific humidity will be obtained throughout the region.

The inspection of the zonally averaged distribution of the precipitation and evaporation amounts reveals the same shortcomings. While the qualitative distribtution is essentially correct, with two precipitation maxima,

one at the southern wall and the other somewhat to the north of the central latitude and an evaporation maximum at j = 3 - the total amounts are much too low. Moreover, the southern maximum in precipitation is lower than the mid-latitude maximum, contrary to the situation in the atmosphere, where the tropical maximum is dominant, especially during summer. The same effect was observed also in the previous model and is due to the presence of the southern boundary wall and to the exclusion of the tropical regions.

The excess of precipitation over evaporation, which determines in the real atmosphere the net release of latent heat, has in the model a maximum positive value at about j = 11 and a maximum negative value at j = 3. In the model, however, this variable does not determine the net release of latent heat, as it was assumed that the amount of heat needed for evaporation is drawn from the ocean, which is assumed to have an infinite heat capacity, and not from the atmosphere. Therefore the net release of latent heat is always positive in the model. This agrees with the results obtained by Rasool and Prabhakara (1965) for the summer season in both hemispheres. In the atmosphere this means that there exists an appreciable transport of latent heat between the two hemispheres, an effect which cannot be in a model simulating only a part of one hemisphere.

In conclusion it may be stated that though the qualitative distribution of the elements of the water vapor cycle was simulated quite well, the various mechmisms were underestimated. Consequently, it should be expected that the total effect of the release of latent heat on the circulation pattern in the model would not be very marked.

Bearing this result in mind, we now turn our attention to the synoptic manife ˙˙tions.

The mean zonal flow on the last day of the integration is presented in Fig. 3. The only difference from the result of experiment I is

the appearance of stronger easterlies in the north and weaker (almost vanish-
ing) easterlies in the south. This undesirable feature is even more pronounced
in the present experiment. It is thus concluded that a variable coriolis para-
meter is essential for obtaining more realistic circulation patterns, even in
models not containing tropical regions. This could be seen even in some ex-
periments with the quasi-geostrophic model where the β term has been drop-
ped (Huss 1964).

The rate of growth of the amplitudes of the geopotential distur-
bance (Fig. 1), on the other hand, became much more rapid when precipitation
strated on the fifth day. Thus a value of about 130 g. p. m. was reached at the
upper level on the tenth day, as compared to a value of 100 g. p. m. on the same
day in the previous experiment. The amplitude remained higher in the present
experiment during the whole period of integration - although at the end of the
period the difference was not very marked and amounted only to about 10 g. p. m.
at the upper level. The damping of the index cycle also proceeded at a some-
what slower rate, supporting our contention that stronger heating might sustain
the index cycle.

Evidence of a slower damping is observed also in the changes
with time of the total kinetic energy (Fig. 5) At the early stages a marked
increase in the kinetic energy was observed right after precipitation started,
and at least three appreciable oscillations were observed before total damping
took place and the energy started to decrease continuously, as it did in the pre-
vious experiment. The period of oscillation remained the same, i. e. about 7
days.

The energy cycle on the other hand was much more pronounced
than in experiment I. Thus a very rapid increase in both the $[P, K]$ trans-
formation and the $[K, F]$ transformation was observed after the start of precip-
itation. The $[P, K]$ transformation reached a value of about 140 Kj m^{-2} day^{-1} on

the third day as compared to a value of about 90 Kj m^{-2}day^{-1} on the same day in experiment I. The $[P_iK]$ transformation oscillated between high and low values until the end of the integration, with a larger amplitude than in experiment I However, the oscillations were still very weak and are hardly characteristic of the index cycle oscillations observed in nature. The average value of the transformation of potential into kinetic energy was about 160 Kj m^{-2}day^{-1}. This value is still somewhat too low, compared with the values presented by Oort (1964). It might thus be concluded that a more realistic distribution of the water vapor cycle elements would have an even greater effect toward increasing the energy cycle elements and would bring them closer to the observed values

An inspection of the heat balance components (Fig. 6) reveals that the net heating in the southern part of the region was almost the same as in experiment I, and the only effect of the release of latent heat there was to somewhat reduce the gradients of differential heating. In the northern regions where the precipitation maximum was located, the effect was more pronounced. The release of latent heat in the north resulted in the direct heating of the lower level As a result the temperature difference between the atmosphere and ocean surface increased, leading to higher values of cooling due to the sensible heat flux from the atmosphere into the ocean. Thus the net result of the release of latent heat in the north was to increase the net cooling, instead of reducing it. The maximum value of net cooling was about 0.13 Kj m^{-2}sec^{-1} as compared to a value of about 0.08 Kj m^{-2}sec^{-1} obtained in experiment I. As the amount of heating in the south was the same in both experiments we conclude that the differential heating was larger in the present experiment, a fact which accounts for the higher amplitudes observed and the slower damping of the index cycle.

The surface pressure distribution was also qualitatively the same as in the first experiment, with the low and high pressure belts located at the same latitudes. The meridional gradients of the surface pressure, however,

were somewhat larger than in the first experiment. The distribution was thus
closer to the situation in the southern hemisphere, so that as far as surface
pressure is concerned the inclusion of the hydrologic cycle leads to an
improvement.

CONCLUSION

Reviewing the results of the last two experiments, as compared with the results of the experiments with the quasi-geostrophic model, the following conclusions may be drawn·

The main qualitative features of the general circulation were simulated quite well in all experiments. These features include the meridional circulation consisting of three cells, the central jet stream, and the more or less adequately simulated mean zonal flow. In fact, these features were obtained in some models even without the introduction of diabatic heating. On the other hand, it has to be remembered that the initial distributions of the geopotential and temperature fields were already quite close to the observed distributions, at least as far as zonal averages are concerned. It thus seems that the maintenance of the general circulation, at least for relatively short periods, is not very much influenced by the heating function employed. On the other hand the generation of the features mentioned above, starting from an isothermal atmosphere at rest, would depend very much on the heating. We thus conclude that even a simple model with a simple heating function might be useful for certain purposes. For example, such a model might be used to get a rough estimate for the concentration with latitude of radioactive fallout from an atomic explosion. For predictions of changes in the general circulation, such as the index cycle or the seasonal variations, it appears that the inclusion of a realistic heating function is essential. In that respect it seems that the inclusion of the hydrologic cycle goes quite a way towards making the heating function more realistic. In addition it provides useful information about large scale precipitation areas..

One essential factor left out in the experiment was the ocean-continent contrast. This factor must be included in actual forecasts of changes in the general circulation as the zonal distributions of the various field variables affecting the weather were of course not simulated at all by our models.

REFERENCES

Astling, E. G. and L H Horn, 1964: Some Geographical Variations of Terrestial Radiation Measured by TIROS II, J. Atm. Sc. 21, 30-34.

Haurwitz, B., and J.M. Austin, 1944: Climatology, N.Y., Mc-Graw Hill.

Holopainen, E. D., 1967: On the Mean Meridional Circulation and the Flux of Angular Momentum over the Northern Hemisphere. Tellus 19, 1-13.

Huss, A., 1964: The effect of Variable Coriolis Parameter in a Planetary Circulation Generated by a Two-Parameter Quasi-Geostrophic Model. J. Atm. Sc. 21, 507-512.

Huss, A. and E. Doron, 1967: Planetary Circulation Obtained by Means of Two-Level Quasi-Geostrophic Models with Various Formulations of Diabatic Heating. Final Scientific Report - Numerical Studies of Planetary Circulations in a Model Atmosphere, Grant AF EOAR 65-89

Langlois, W. E. and H. C. W. Kwok, 1969: Description of the Mintz-Arakawa Numerical General Circulation Model. Numerical Simulation of Weather and Climate. Tech. Rep. No 3, U. C. L. A. Departement of Meteorology.

Mintz, Y. and J. Lang , 1955: A Model of the Mean Meridional Circulation Final Report, AF 19 (122) - 48. General Circulation Project, U. C. L. A. paper VI.

Oort, A. H., 1964: On Estimates of the Atmospheric Energy Cycle. Mon. Wea. Rev. 92, 483-493.

Phillips, N.A., 1956: The General Circulation of the Atmosphere:
A Numerical Experiment. Quart. J.R. Met. Soc. 82, 123-164.

Phillips, N A., 1957: A Coordinate System Having Some Special Advantages for Numerical Forecasting. J. of Met. 14, 184-185.

Rasool, S.I. and C. Prabhakara, 1965: Heat Budget of the Southern Hemisphere. Problems of Atmospheric Circulation. Editors: R.V. Garcia and T.F. Malone. 76-92.

Smagorinsky, J., S. Manabe and J. L. Holloway, Jr., 1965: Numerical Results From a Nine-Level General Circulation Model. Mon. Wea. Rev. 93, 727-768.

AMPLITUDE OF GEOPOTENTIAL WAVE AT CENTRAL LATITUDE IN g.p.m
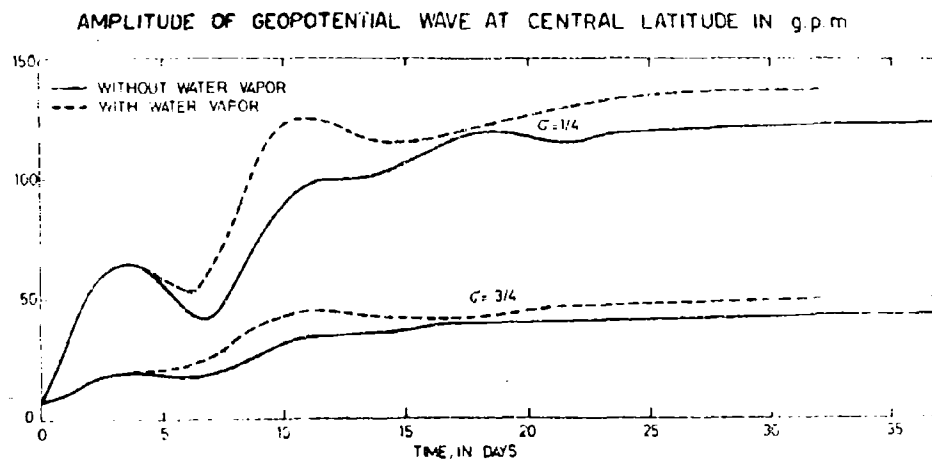
Fig. 1. Amplitude of first harmonic of geopotential at
both levels in g. p. m. Experiments I and II

MEAN ZONAL FLOW IN m sec^{-1} ON 36th DAY
RUN WITHOUT WATER VAPOR
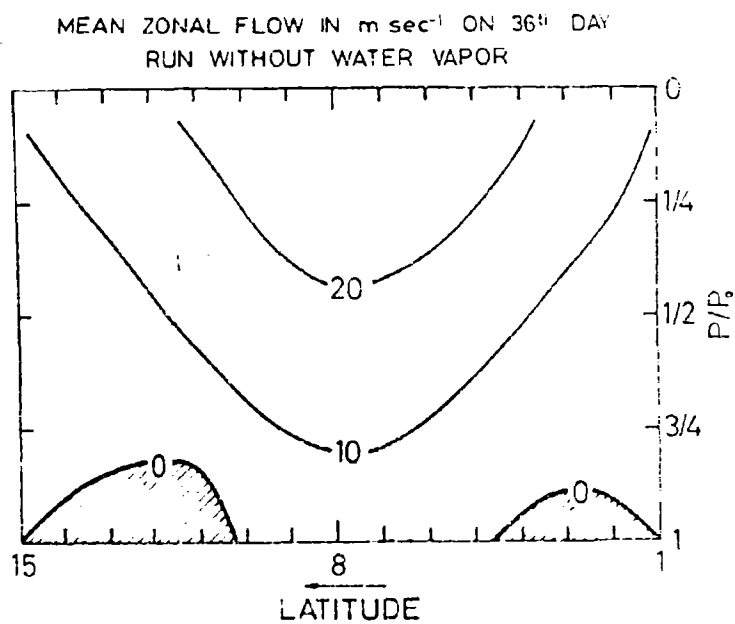
Fig. 2. Mean zonal flow on 36th day. Experiment I

MEAN ZONAL FLOW IN m sec⁻¹ ON 32ᴺᴰ DAY
RUN WITH WATER VAPOR
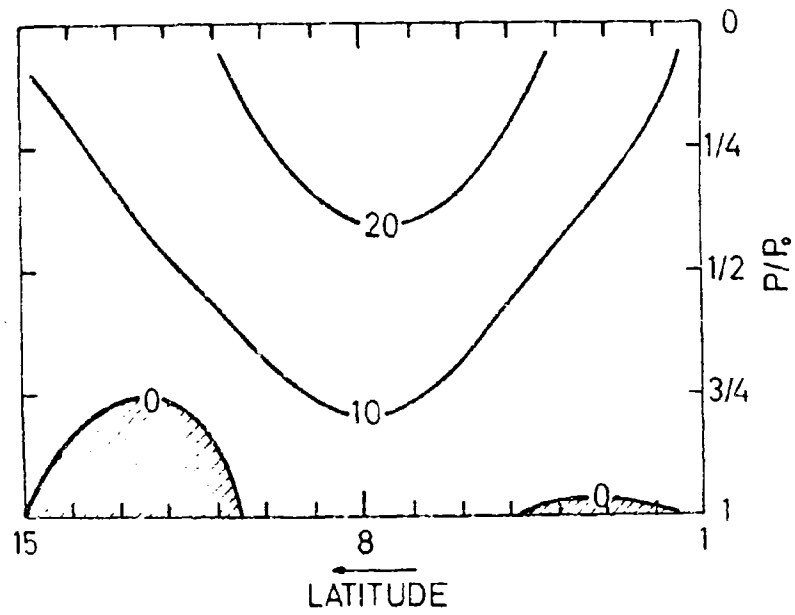
Fig. 3. Mean zonal flow on 32nd day. Experiment II

AREA AVERAGED KINETIC ENERGY TRANSFORMATIONS IN $kj\ m^{-2} day^{-1}$
RUN WITHOUT WATER VAPOR

TIME, IN DAYS

AREA AVERAGED KINETIC ENERGY TRANSFORMATIONS IN $kj\ m^{-2} day^{-1}$
RUN WITH WATER VAPOR

TIME, IN DAYS
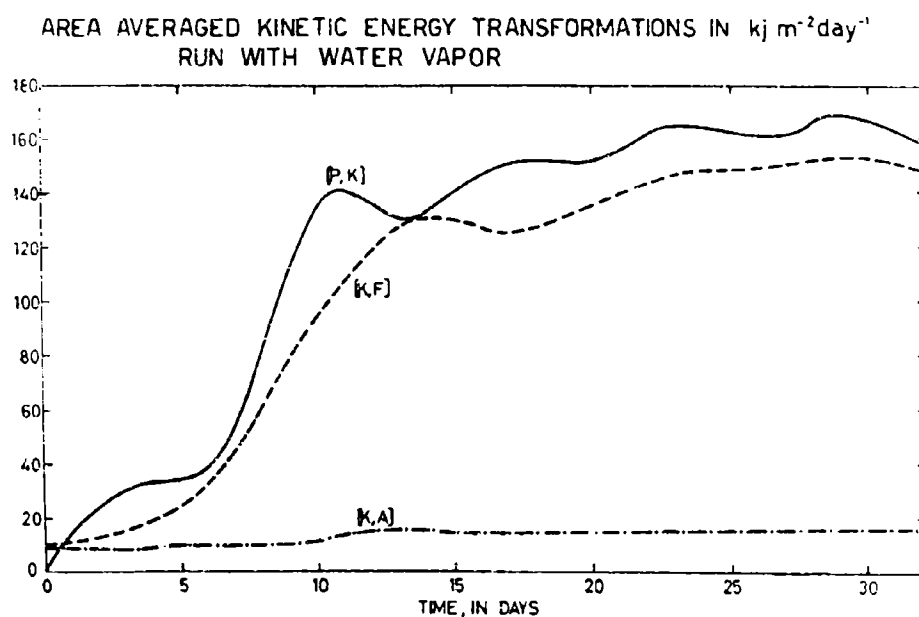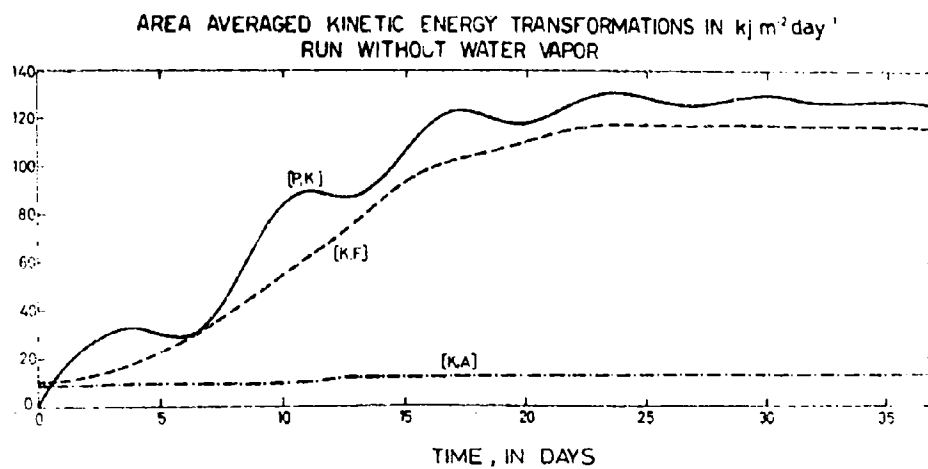
Fig. 4. Mean kinetic energy transformations. $[P, K]$ = transformation of potential into kinetic energy, $[K, F]$ = transformation of kinetic energy into surface friction. $[K, A]$ = transformation of kinetic energy into eddy diffusion. Experiments I and II

AREA AVERAGED KINETIC ENERGY PER UNIT COLUMN IN $kj\ m^{-2}$
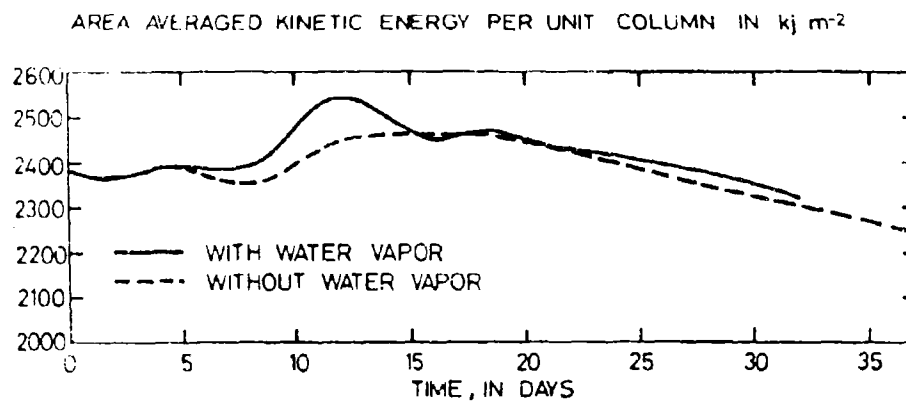
Fig. 5. Area averaged kinetic energy. Experiments I and II

ZONALLY AVERAGED HEAT BALANCE COMPONENTS
ON 36th DAY IN kj m⁻² sec⁻¹ x 10²
RUN WITHOUT WATER VAPOR

Q_S – SENSIBLE HEAT
Q_R – RADIATION LOSSES
Q_N – NET HEATING
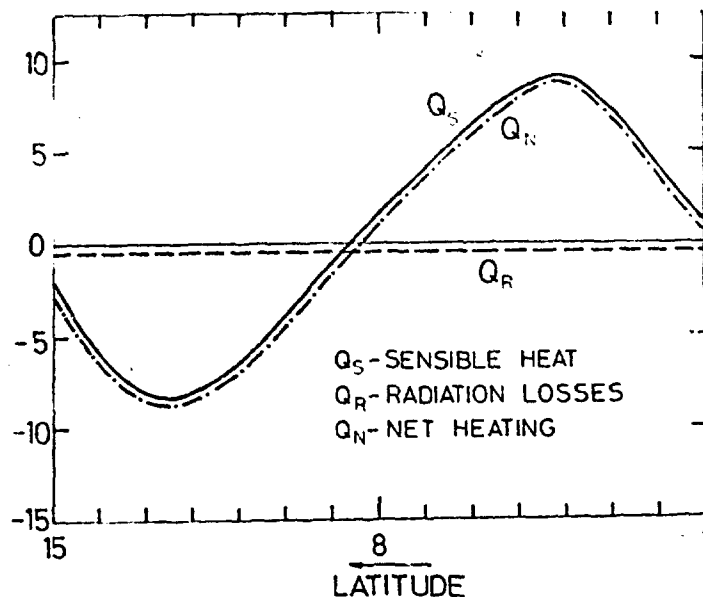
ZONALLY AVERAGED HEAT BALANCE COMPONENTS
ON 32ND DAY IN kj m⁻² sec⁻¹ x 10²
RUN WITH WATER VAPOR

Q_S – SENSIBLE HEAT
Q_P – LATENT HEAT
Q_R – RADIATION LOSSES
Q_N – NET HEATING
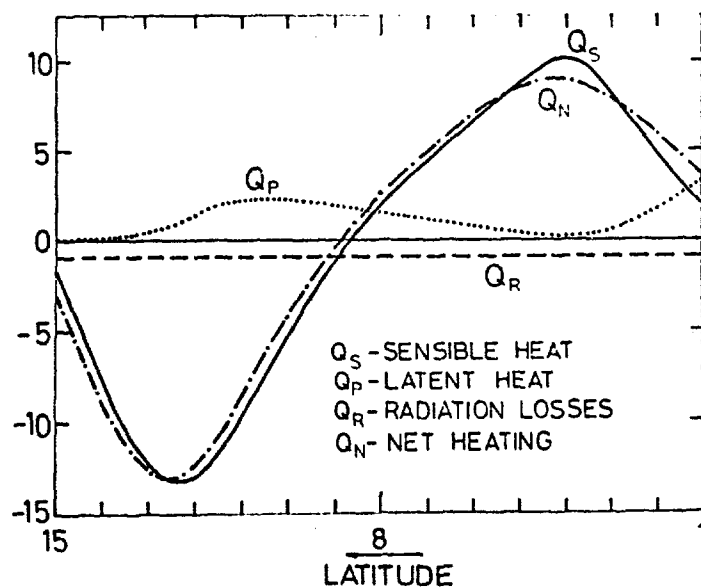
Fig. 6. Heat balance components. Experiments I and II

SCHEMATIC MERIDIONAL CIRCULATION ON 32ND DAY
RUN WITHOUT WATER VAPOR
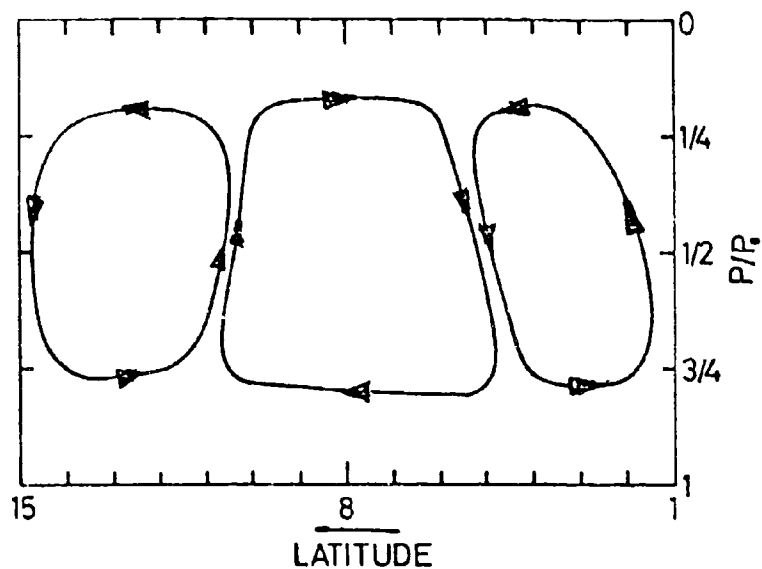
Fig. 7. Schematic meridional circulation. Experiment I

MEAN ZONAL SURFACE PRESSURE ON
LAST DAY OF RUN IN mb

WITHOUT WATER VAPOR
WITH WATER VAPOR
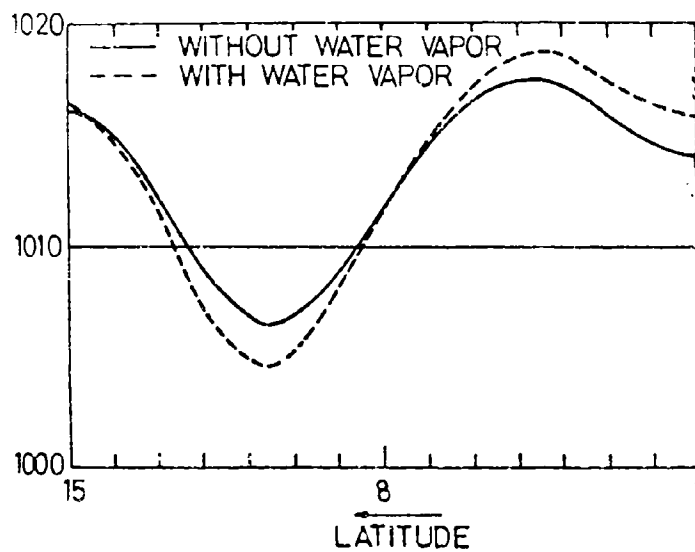
Fig. 8. Mean zonal surface pressure. Experiments I and II

MEAN ZONAL RELATIVE HUMIDITY IN % ON 32ND DAY
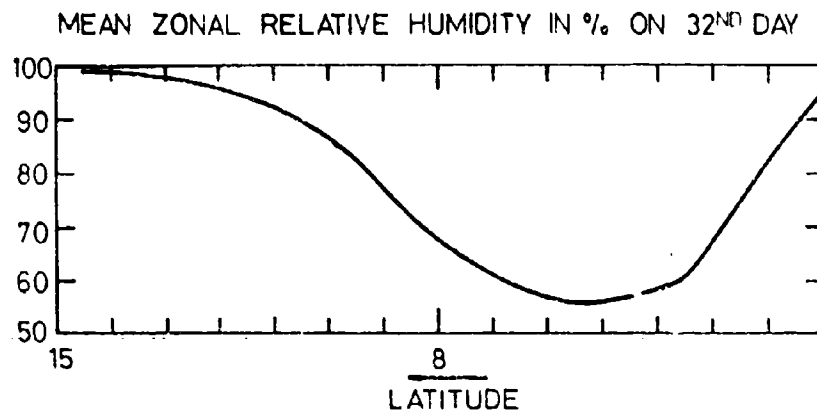
Fig. 9. Mean zonal relative humidity. Experiment II

MEAN ZONAL PRECIPITATION AND EVAPORATION
ON 32ND DAY IN mm
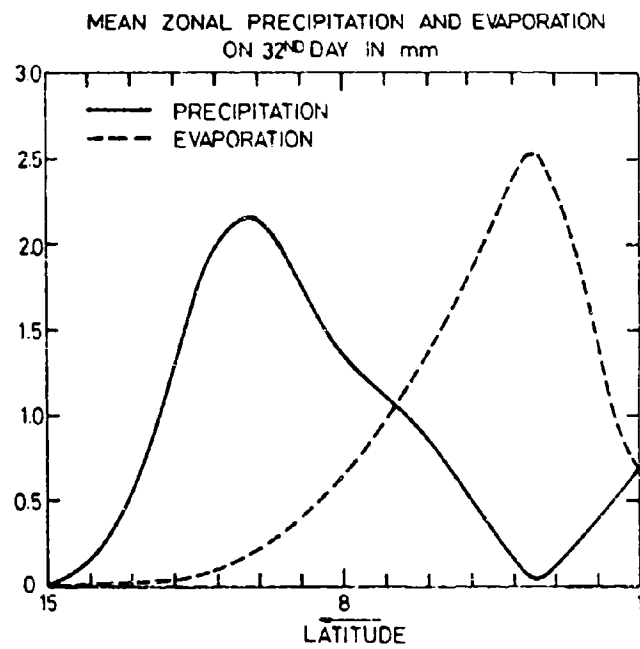
Fig. 10 Mean zonal evaporation and precipitation. Experiment II

INCLUSION OF LATERAL VISCOSITY
AND THE APPLICATION OF A MATSUNO SCHEME
IN A TWO LEVEL MODEL OF THE
GENERAL CIRCULATION OF THE ATMOSPHERE

b y

A. HUSS and M. NAVON

A b s t r a c t

Equations of a two level quasi-hydrostatic and quasi-geostrophic model, have been numerically integrated in order to study the evolution of general circulation patterns.

A lateral friction term was included in a model whose main features are described by Huss (1967).

The eddy viscosity coefficient was assumed to be constant. Two different integrations were performed. The first one involving an integration of 42 days was based on a model which did not include water vapor.

In the second experiment which was integrated for 65 days a humidity distribution was introduced and the lateral friction term was also included.

The calculated distributions of the field variables were compared with the results obtained in the 1967 report mentioned above and with actual distributions based on real data. In both the experiments a considerable smoothing of the various field variables was obtained and considerable differences were observed, compared to the previous experiments.

In the second experiment the smoothing destroyed the
pronounced index cycle which appeared in a previous experiment.

In the third experiment, the Matsuno time differencing
scheme was introduced instead of the leap-frog scheme, while
no lateral friction was included.

The numerical integration was carried for 62 days. A
smoothing, similar to that obtained in the first two experiments
was observed, but with a more realistic distribution of the
field variables.

INTRODUCTION

a) The Lateral Friction Term

Defining an eddy as a parcel of atmospheric air capable of retaining some measure of individuality and moving as a separate entity in the surrounding fluid - we shall take the eddy instead of the molecule as the fundamental part - so that entities such as eddy-viscosity or eddy-conductivity will be the macroscopic counterpart of the molecular viscosity and conductivity.

It is obvious that any finite-difference description cannot describe explicitly those scales of motions which are too small compared to the grid size.

The energy in the numerical models tends to accumulate in the shorter wave range since it cannot cascade to sufficiently small scales and dissipate by molecular viscosity.

Eddy diffusion terms are thus used in order to keep the energy of the short waves small - and to prevent computational instability.

Under the influence of the lateral eddy diffusion the shorter the wavelength of the perturbation, the more pronounced is the smoothing effect.

Yet the shortcoming of such procedures is that, when

integrations are made with lateral friction terms - solutions
appear to be too smooth if large enough diffusion coefficients
are employed to give computational stability and to filter
small scale perturbations.

b) Review of numerical values adopted for the lateral friction
coefficient

Approximating the turbulent stress terms after Boussinesq
(1877) by analogy with viscous stresses we obtain:

$$ - u'v' = K \frac{\partial \bar{v}}{\partial x} \quad ; \quad -u'u' = K \frac{\partial \bar{u}}{\partial x} $$

$\left(\overline{\quad\quad} \right)$ denoting averaging, u, v being components of velocity
in the horizontal plane and K defined as the lateral friction
coefficient. Very little is known about the value of K. Most
authors assume K to be a constant; others allow it to vary
with time, height etc.

Defant (1921) in discussing his "large Austausch process"
found:

$$ K = A_v = 8 \cdot 10^{10} cm^2 sec^{-1} $$

Richardson (1926) found an empirical law appropriate
for estimating the dispersion of clusters in the atmosphere.
This involved an eddy diffusion coefficient depending on the
size of the eddies (or clusters):

$$ K = 0.2 \, l^{4/3} $$

For instance, if we take l to be equal to the grid spacing adopted in our model :

$$l = \Delta x = 400 \, Km. = 4 \cdot 10^7 cm.$$

We obtain :

$$K = 0.2 \cdot 4 \cdot 10^{28/3} = 0.8 \cdot 10^9 \cdot 10^{1/3} \cong 1.7 \cdot 10^9 \, cm^2 \cdot sec^{-1} = 1.7 \cdot 10^5 m^2 \cdot sec^{-1}$$

Since the first formulation, Richardson's law received some theoretical justification from Kolmogoroff's similarity hypothesis and Batchelor (1950)'s work.

Leith (1961), in a general circulation experiment, took a value of $K = 10^6 \, m^2 \cdot sec^{-1}$ and carried his experiment for seven months.

Malkus and Witt (1959) used Richardson's relation for a small scale convection experiment with $K = 0.5 \, m^2 \cdot sec^{-1}$.

Smagorinsky (1958) uses an eddy diffusion coefficient varying with space and time of the form:

$$K = (kl)^2 [D] , \quad k = \frac{1}{4} \qquad l = \text{grid spacing}$$

$[D]$ = two dimensional deformation tensor.

K increases for smaller scale variations and for larger velocity amplitudes. He justified the choice of such a coefficient by similarity considerations applied to wind tunnel experiments.

Lilly (1962) used a similar coefficient, which also depended on static stability.

In a numerical experiment dealing with diffusion and

fallout of stratospheric radioactive materials Davidson, Friend and Seitz (1966, Tellus) used:

$$A = K'_{\shortparallel} = K = 3 \cdot 10^{9} cm^{2}. sec^{-1} = 3 \cdot 10^{5} m^{2}. sec^{-1}.$$

Phillips in his well known general circulation experiment (1956) took $A = 10^{5}$ m^{2}/sec, Matsumoto (1960) in a 5 level geostrophic model assumed the same value.

Machta (1955) assuming Fickian diffusion of the dust cloud of radioactive debris from atomic explosions found:

$$K = A = 0.5 \cdot 10^{5} m^{2}. sec^{-1}.$$

On the other hand Sutton, (1953) and Priestly by assuming turbulent regimes (free and forced convection) arrive at values of $K = 10^{6} - 10^{4}$ cm^{2} sec^{-1} and the same value results from Taylor's statistical considerations.

Koo-Tchen-Chao shows an equivalence between the smoothing method defined by: $\qquad \zeta^{*} = \zeta + k \nabla^{2} \zeta$
and the introduction of the lateral eddy viscosity term,

ζ - being the relative vorticity, ∇^{2} - finite difference Laplacian , k - the smoothing coefficient.

He obtained:

$$k = \frac{A \, \Delta t}{(\Delta s)^{2}}$$

Δt - the time step

Δs - the grid spacing

A - the eddy viscosity coefficient

Dobs (1956) assumed $A = 7.10^8$ cm^{2}sed^{-1} . When

$\Delta S = 300$ km $\qquad \Delta t = 24$ hr $\qquad k = 1$.

Sigryggsen assumed $A = 2.10^{10}$ cm^{2}sec^{-1}

$\Delta S = 300$ km $\qquad \Delta t = 12$ hr and thus $k = \frac{1}{4}$.

With $\Delta t = 1$ hr, $k = 1/13$ $\qquad \Delta S = 300$ km we get

from the above relation: $A = 5.10^9$ cm^{2}sec^{-1}.

In an asymptotic development of the diffusion in the
Ekman Layer, Csanady (1969) obtained a formula which gives
an eddy diffusion coefficient of 10^5m^{2}sec^{-1}. His formula is:

$$K_{eff} = \frac{4-\pi}{8} \cdot \frac{u_g^2}{f} = \frac{0.146}{f} \cdot u_g^2 \cong 10^5 m^2 sec^{-1} ; \quad u_g = 15 m.sec^{-1}, f = 10^{-4} sec^{-1}$$

It is now generally accepted that A varies between
10^9 cm^{2}sec^{-1} and 10^5 cm^{2}sec^{-1}.

Governing equations

The model's equations and the boundary conditions will
refer to the 0,250, 500, 750 and 1000 mb levels which will be
denoted by subscripts 0,1,2,3,4 respectively.

The quasi-geostrophic assumption is implied. The basic
dependent variables are the stream function at the two levels
250 mb and 750 mb, denoted ψ_1 , and ψ_3 . Because of the
quasi-geostrophic assumptions they are related to the geo-
potential by means of :

$$(1) \quad \psi = \frac{\phi}{f_m}$$

for mean-coriolis parameter $= f_m$.

From the stream-functions, the non-divergent component of velocities is obtained:

$$\mathbf{V}_g = k \times \nabla \psi$$

k = unit vector along p-axis

∇ = horizontal del operator on a pressure surface surface

The vorticity ζ is given by: $\zeta = \nabla^2 \psi$

The continuity equation is:

$$(2) \qquad \nabla \mathbf{V} = - \frac{\partial \omega}{\partial p}$$

ω - vertical   p- velocity.

Through the hydrostatic relation T can be obtained from the stream-function:

$$(3) \qquad \frac{\partial \phi}{\partial p} = - \frac{RT}{P} = f_m \frac{\partial \psi}{\partial p} \qquad\qquad R \text{ gas constant}$$

The 2 prognostic equations are written in terms of potential vorticities, denoted q_1 and q_3.

The thermodynamic energy equations can be written:

$$(4) \qquad \frac{\partial \phi}{\partial p} \frac{H}{C_p T} = \frac{\partial}{\partial t} \frac{\partial \phi}{\partial p} + \mathbf{V}.\nabla \frac{\partial \phi}{\partial p} \cdot \frac{\partial \ln \theta}{\partial p}$$

θ - potential temperature.

H - the heat added to unit mass in unit time.

C_p - specific heat at constant pressure.

The static stability

$$(5) \qquad \sigma = \frac{\partial \phi}{\partial p} \; \frac{\partial \ln \theta}{\partial p}$$

is assumed to be a function of pressure only.

Dividing (4) by f_m and introducing (5) and (3) we obtain:

$$(6) \quad \frac{\partial}{\partial t} \cdot \frac{\partial \psi}{\partial p} + V \cdot \nabla \frac{\partial \psi}{\partial p} + \frac{\omega \sigma}{f_m} = - \frac{R}{f_m \cdot C_p} \; \frac{H}{p} .$$

Introducing a finite difference approximation of $\frac{\partial \psi}{\partial p}$ by centred differences between p_1 and p_3 and multiplying by P_2 we obtain:

$$(7) \quad \frac{\partial}{\partial t} (\psi_1 - \psi_3) = - V \cdot \nabla (\psi_1 - \psi_3) + \frac{\sigma_2 \, p_2 \, \omega_2}{f_m} + \frac{R}{f_m \, C_p} H_2 .$$

H_2 is now separated into a general adiabatic term H_{2a} and a term due to diffusion:

$$(8) \qquad H_2 = H_{2a} + H_{2d},$$

with

$$(9) \qquad H_{2d} = \frac{C_p \cdot f_m}{R} A_T \nabla^2 (\psi_1 - \psi_3),$$

where A_T is the lateral eddy diffusion coefficient for sensible heat; thus H_{2d} is proportional to the Laplacian of the temperature at 500 mbs.

Equation (7) assumes the form:

$$(10) \quad \frac{\partial}{\partial t}\left(\psi_1 - \psi_3\right) = -V_2 \cdot \nabla\left(\psi_1 - \psi_3\right) + \frac{\sigma_2 \, p_2 \, \omega_2}{f_m} + \frac{R}{f_m \cdot C_p} H_{2a} + A_T \nabla^2\left(\psi_1 - \psi_3\right).$$

In the equations of motion both surface friction and lateral viscosity are incorporated.

The frictional stress τ due to the presence of a lower boundary, is assumed to vary according to:

$$(11) \quad \tau = C(p)\, k_m \, V_4$$

with:

$$(12) \quad C(p) = \frac{p^2}{p_4^2} .$$

Thus the vorticity equations at the two levels p_1 and p_2 will be:

$$(13) \quad \frac{\partial \zeta_1}{\partial t} = -V_1 \cdot \nabla \zeta_1 - V_1 \beta + f_m\left(\frac{\partial \omega}{\partial p}\right)_1 - g\, k_m\left(\frac{\partial C}{\partial p}\right)_1 \zeta_4 + A_V \nabla^2 \zeta_1$$

$$\frac{\partial \zeta_3}{\partial t} = -V_3 \cdot \nabla \zeta_3 - V_3 \beta + f_m\left(\frac{\partial \omega}{\partial p}\right)_3 - g\, k_m\left(\frac{\partial C}{\partial p}\right)_3 \zeta_4 + A_V \nabla^2 \zeta_3 ,$$

A_V - lateral eddy viscosity coefficient.

β - mean Rossby parameter - 1.6×10^{11} $m^{-1} sec^{-1}$,

g - acceleration of gravity - 9.81 m sec^{-2}.

The vertical velocities in (13) are eliminated by substituting centered differences for $\frac{\partial \omega}{\partial p}$ with the assumption of the boundary conditions $\omega_0 = \omega_4 = 0$ and substituting for ω_2 from the thermodynamic energy equation :

$$(14) \quad \omega_2 = \frac{f_m}{\sigma_2 \, p_2}\left[\frac{\partial}{\partial t}\left(\psi_1 - \psi_3\right) + V_2 \nabla\left(\psi_1 - \psi_3\right) - \frac{R}{f_m \, C_p} H_{2a} - A_T \nabla^2\left(\psi_1 - \psi_3\right)\right].$$

We assume:

$$(15) \quad A_v = A_T = 10^5 \, m^2 sec^{-1}.$$

Thus, we obtain the final form of the prognostic equations in terms of q_1 and q_3:

$$(16) \quad \frac{\partial q_1}{\partial t} = -V_1 \cdot \nabla q_1 - V_1 \beta - g k_m \left(\frac{\partial c}{\partial p}\right)_1 \gamma_4 - \frac{\lambda H_2}{f_m C_p} + A \nabla^2 q_1$$

$$\frac{\partial q_3}{\partial t} = -V_3 \cdot \nabla q_3 - V_3 \beta - g k_m \left(\frac{\partial c}{\partial p}\right)_3 \gamma_4 + \frac{\lambda H_2}{f_m C_p} + A \nabla^2 q_3$$

with

$$(17) \quad q_1 = \zeta_1 - \lambda (\psi_1 - \psi_3)$$

$$q_3 = \zeta_3 + \lambda (\psi_1 - \psi_3) \quad .$$

$$\lambda = \frac{1}{C} \frac{f_m^2}{P_2^2} = 1.26 \times 10^{-12} m^{-2}$$

In deriving (15) and (16) we assumed

$$V_2 = \frac{\psi_1 + \psi_3}{2}$$

consequently

$$V_2 \cdot \nabla (\psi_1 - \psi_3) = V_1 \cdot \nabla (\psi_1 - \psi_3) = V_3 \cdot \nabla (\psi_1 - \psi_3)$$

(b) The diabatic heating due to influx of sensible heat from the bottom of the region.

The diabatic heating in the model is exactly the same as assumed by Huss (1967).

The amount of heat entering unit column through its lower boundary situated at 1000 mb, Q_s is made proportional to

the temperature difference between the surface and the air just above, and to the geostrophic wind:

$$(18) \quad Q_s = A_s |v_4| (T_g - T_4)$$

T_g - the prescribed surface temperature

T_4 - air temperature at 1000mb

$|v_4|$ - 1000 mb wind speed

A_s - a constant.

T_g - is constant with time and T_4 was extrapolated from the temperature at the 500 mb level.

$$(19) \quad T_2 = \frac{f_m}{R(\ln p_3 - \ln p_1)} (\psi_1 - \psi_3).$$

Assuming a standard atmosphere lapse-rate between the 500 mb level and the lower boundary:

$$(20) \quad T_4 = T_2 \left(\frac{p_4}{p_2}\right)^{0.19} = 1.141 T_2$$

Similarly we obtain the stream function at 1000 mb level

$$(20a) \quad \psi_4 = \psi_3 - 9.17 \times 10^5 T_2$$

and the geostrophic surface winds

$$(20b) \quad |v_4| = |\nabla \psi_4|$$

From (18), (20), (20b) we obtain the value of Q_s. Assuming Q to be evenly and distributed throughout the whole column of air:

$$(21) \quad H_{2s} = H_s = \frac{2}{p_4} \cdot Q_s .$$

Release of latent heat was introduced in the second experiment.
The net outgoing radiation was assumed to be constant over the
whole region and an instantaneous heat balance was maintained
at each moment of the integration's time. In the first experiment,
due to the symmetry features of the initial conditions and
the structure of the model, this resulted in zero net out-
going radiation. In the second experiment, due to the
introduction of the humidity field and the release of latent
heat, the symmetry was lost and the outgoing radiation did
not vanish.

DEVELOPMENT OF THE ω EQUATION TAKING INTO ACCOUNT
THE EFFECTS OF LATERAL EDDY VISCOSITY AND THE
LATERAL EDDY DIFFUSION COEFFICIENT FOR HEAT

We obtain by substracting 16 (b) from 16 (a)

$$(22) \quad \frac{\partial}{\partial t}(q_1 - q_3) = J(\psi_1, q_1) + J(\psi_3, q_3) - \beta(v_1 - v_3) - g k_m \left[\left(\frac{\partial c}{\partial p}\right)_1 - \left(\frac{\partial c}{\partial p}\right)_3 \right] \nabla^2 \psi_4 - \frac{2\lambda R}{f \cdot c_p} H_{2a} + A \nabla^2 (q_1 - q_3)$$

which may be rewritten in the form

$$(23) \quad \frac{\partial}{\partial t} \nabla^2 (\psi_1 - \psi_3) - 2\lambda \frac{\partial}{\partial t}(\psi_1 - \psi_3) = J(q_1, \psi_1) - J(q_3, \psi_3) - \beta(v_1 - v_3) - g k_m \left[\left(\frac{\partial c}{\partial p}\right)_1 - \left(\frac{\partial c}{\partial p}\right)_3 \right] \nabla^2 \psi_4 - \frac{2\lambda R}{f c_p} H_{2a} + A \nabla^2 q_1 - A \nabla^2 q_3 .$$

Substituting for $2\lambda \frac{\partial}{\partial t}(\psi_1 - \psi_3)$ from the thermo-
dynamic energy equation, i.e. Eq. 10:

$$\frac{\partial}{\partial t} \nabla^2 (\psi_1 - \psi_3) = 2\lambda J(\psi_1, \psi_3) + \frac{2\lambda\sigma}{f} p_2 \omega_2 + \frac{2\lambda R}{f c_p} H_{2a} +$$

(24)
$$+ 2\lambda A \nabla^2 (\psi_1 - \psi_3) + J(q_1, \psi_1) - J(q_3, \psi_3) - \beta(v_1 - v_3) -$$

$$- g k_m \left[\left(\frac{\partial c}{\partial p}\right)_1 - \left(\frac{\partial c}{\partial p}\right)_3 \right] \nabla^2 \psi_4 - \frac{2\lambda R}{f c_p} H_{2a} + A \nabla^2 q_1 - A \nabla^2 q_3$$

Taking the Laplacian of Eq. 10 yields:

(25)
$$\frac{\partial}{\partial t} \nabla^2 (\psi_1 - \psi_3) = \nabla^2 J(\psi_1, \psi_3) + \frac{\sigma p_2}{g} \nabla^2 \omega_2 + \frac{R}{f c_p} \nabla^2 H_{2a} + A \nabla^2 (z_1 - z_3)$$

Subtracting (25) from (24) we obtain:

(26)
$$0 = 2\lambda J(\psi_1, \psi_3) + 2\lambda\sigma p_2 \omega_2 + 2\lambda A \nabla^2 (\psi_1 - \psi_3) + J(q_1, \psi_1) -$$

$$- J(q_3, \psi_3) - \beta(v_1 - v_3) - g k_m \left[\left(\frac{\partial c}{\partial p}\right)_1 - \left(\frac{\partial c}{\partial p}\right)_3 \right] \nabla^2 \psi_4 + A \nabla^2 q_1 -$$

$$- A \nabla^2 q_3 - \nabla^2 J(\psi_1, \psi_3) - \frac{\sigma p_2}{f} \nabla^2 \omega_2 - \frac{R}{f c_p} \nabla^2 H_{2a} - A \nabla^2 z_1 + A \nabla^2 z_3$$

It is easily seen that the terms involving A cancel each other.

Thus, the effects of lateral eddy viscosity and lateral eddy diffusion of heat do not change the ω -equation, provided we assume that the coefficients are equal:

$$A_v = A_T = A = 10^5 m^2 sec^{-1} \quad .$$

Thus, we obtain the ω-equation in the form:

$$(27) \quad \nabla^2 \omega_2 - 2\lambda\omega_2 = \frac{\Delta p_2}{g}\left[J(q_1, \psi_1) - J(q_3, \psi_3) - \beta(v_1 - v_3) + 2\lambda J(\psi_1, \psi_3) - \right.$$

$$\left. - \nabla^2 J(\psi_1, \psi_3) - \frac{R}{f\,c_p}\nabla^2 H_{2a} - g\,k_m\left(\left(\frac{\partial c}{\partial p}\right)_1 - \left(\frac{\partial c}{\partial p}\right)_3\right)\nabla^2 \psi_4 \right]$$

A similar expression was used by Matsumoto (1960) in his 5-level quasi-geostrophic model.

Boundary conditions and initial conditions

The region of integration extends from $x = 0$ to $x = X$ and from $y = 0$ to $y = Y$. The following averages are defined:

$$\left(\widetilde{} \right) = \frac{1}{x} \int_0^x (\quad) dx \; ; \; \left(\overline{} \right) = \frac{1}{y} \int_0^y (\quad) dy$$

The following boundary conditions were applied in the two experiments:

Cyclical continuity of field variables in the x-direction, i.e. if α denotes a variable:

(28) $\alpha(x) = \alpha(0)$

$V_N = V_S = 0$, S and N being the southern and northern boundaries respectively. With our geostrophic assumption, the stream function will, therefore, be constant along each of the boundaries.

(29) $\left(\frac{\widetilde{\partial \psi}}{\partial y} \right)_N = \left(\frac{\widetilde{\partial \psi}}{\partial y} \right)_S = 0$

(30) $\left(\frac{\partial q}{\partial x} \right)_N = \left(\frac{\partial q}{\partial x} \right)_S = 0$

(31) $\left(\frac{\widetilde{\partial}}{\partial y} \right)_N = \left(\frac{\widetilde{\partial q}}{\partial y} \right)_S = 0$

In order to obtain a single valued solution, a single value of the stream-function at some grid point is specified arbitrarily (conditions (30) and (31) have to be modified in

a finite difference formulation to ensure conservation of potential vorticity at each level). The addition of the lateral friction term does not interfere in the conservation of potential vorticity at each level.

$$(32) \quad A \int_0^x \int_0^y \nabla^2 q_{i,3} \, dx \, dy = 0$$

According to (17) and the boundary conditions (28) and (29):

$$(33) \quad \int_0^x \int_0^Y (q_1 + q_3) \, dx \, dy = 0$$

Thus the total potential vorticity must be conserved, and care must be taken that this condition be satisfied in the finite difference formulation. In the lateral friction term the conventional 4 point Laplacian was used at all internal points.

On the boundaries we write:

$$(34) \quad \frac{1}{2} q_{i,0} = \frac{1}{(\Delta s)^2}(q_{i,1} - q_0); \quad \frac{1}{2} q_{i,z} = \frac{1}{(\Delta s)^2}(q_z - q_{i,z-1})$$

The remaining terms were approximated by finite difference schemes as described in the report mentioned above. Thus the scheme for calculating the new values of the potential vorticity on the boundaries becomes:

$$(35) \quad \frac{1}{2} \frac{\partial}{\partial t} q_{i,0} = \frac{1}{2} J_{i,0}(\psi, 3) - g k_m \frac{\partial c}{\partial p} \frac{1}{(\Delta s)^2}(\psi_{i,1} - \psi_0) \pm \frac{1}{2} \lambda \frac{g}{p_4} \frac{R}{f_m c_p} Q_{i,0} +$$
$$+ A \frac{1}{(\Delta s)^2}(q_{i,1} - q_0)$$

$$\frac{1}{2} \frac{\partial}{\partial t} q_{i,z} = \frac{1}{2} J_{i,z}(\psi, 3) - g k_m \frac{\partial c}{\partial p} \frac{1}{(\Delta s)^2}(\psi_{i,z} - \psi_{i,z-1}) \mp \frac{1}{2} \lambda \frac{g}{p_4} \frac{R}{f_m c_p} Q_{i,z} +$$
$$+ A \frac{1}{(\Delta s)^2}(q_z - q_{i,z-1})$$

Initial conditions

The prescribed surface temperature, constant with time, varies linearly in the y direction with a gradient of 4.5^O per grid interval. The temperature was assumed to be constant along the x direction, and had a value of 274° K at the central latitude. Initially Tg = T4 and from the prescribed surface temperatures the initial temperature at 500 mb was obtained as described above. The stream function at 1000 mb is initially assumed to vanish. From (20a) we obtain ψ_3 and from (19) we obtain ψ_1 .

An identical perturbation is superimposed on the zonal distribution obtained in this way both at p_1 and at p_3, having sinusoidal shape with a wavelength of 6216 Km in the x-direction and an amplitude of $8.6 \times 10^5 m^2$/sec at the central latitude, decreasing sinusoidally towards 0 at the southern and northern boundaries. The numbers of grid points in both x and y direction was 15, including boundary points.

The grid spacing was $\Delta S = 444$ km, the time step being $\Delta t = 1$ hour.

Energy transformations

An insight into the energetics of our system will be provided by the energy transformations.

The area averages of the various energy components will be denoted by $\overline{K}$, K', $\overline{P}$ and P' respectively, lower indices denoting the corresponding pressure levels.

If α is any field variable (scalar or vector) we will write: $\alpha = \overline{\alpha} + \alpha'$

where ( )' denotes the deviations from the zonal mean.

We shall start with the vorticity equation at the 250 mb level (the procedure for the 750 mb level being identical).

$$(36) \quad \frac{\partial \zeta_1}{\partial t} = -V_1 \nabla \zeta_1 - V_1 \beta + f_m \frac{\omega_2}{p_2} - g k_m \left(\frac{\partial C}{\partial p}\right)_1 \zeta_4 + A \nabla^2 \zeta_1 .$$

Averaging zonally we obtain:

$$(37) \quad \frac{\partial \tilde{\zeta}_1}{\partial t} = \widetilde{V_1' \nabla \zeta_1'} + \frac{f_m \tilde{\omega}_2}{p_2} - g k_m \left(\frac{\partial C}{\partial p}\right)_1 \tilde{\zeta}_4 + A \nabla^2 \tilde{\zeta}_1$$

The term $-V_1 \beta$ vanishes because of the geostrophic approximation and cyclical continuity.

By multiplying (37) by $\tilde{\psi}_1$ and integrating the product over the total area of the pressure surface, we obtain the rate of change of the kinetic energy of the zonal flow.

Only the lateral friction term will be treated here, other terms having already been treated in a previous report.

The term resulting from lateral viscosity is:

$$(38) \quad A \iint \tilde{\psi}_1 \nabla^2 \tilde{\zeta}_1 \, d\sigma = A L \int \tilde{\psi}_1 \frac{\partial^2}{\partial y^2} (\tilde{\zeta}_1) \, dy$$

where L, is the domain's length in the x direction.

Integrating by parts, and applying the boundary condition, this term becomes

$$(39) \quad -A\int \tilde{\zeta}_1^2 \, d\sigma$$

Thus, including all terms:

$$(40) \quad \frac{\partial}{\partial t} \frac{1}{2} \overline{\tilde{u}}_1^2 = -\tilde{u}_1 \frac{\partial}{\partial y}\overline{(u_1' v_1')} - \frac{f_m}{p_2}\overline{\tilde{\psi}_1 \tilde{\omega}_2} - g\, k_m\left(\frac{\partial c}{\partial p}\right)_1 \tilde{u}_1 \tilde{u}_4 - A\tilde{\zeta}_1^2$$

and the rate of change of the kinetic energy of the zonal flow in a pressure interval of $1 cb$ becomes:

$$(41) \quad \frac{\partial}{\partial t}\overline{K}_1 = \frac{\partial}{\partial t}\frac{1}{g}\overline{\tilde{u}}_1^2 = -\frac{1}{g}\tilde{u}_1\frac{\partial}{\partial y}\overline{(u_1' v_1')} - \frac{f_m}{p_2 g}\overline{\tilde{\psi}_1 \tilde{\omega}_2} -$$
$$- k_m\left(\frac{\partial c}{\partial p}\right)_1 \overline{\tilde{u}_1 \tilde{u}_4} - \frac{A}{g}\overline{\tilde{\zeta}_1^2} .$$

And similarly at the 750 mb level:

$$(42) \quad \frac{\partial}{\partial t}\overline{K}_3 = \frac{\partial}{\partial t}\frac{1}{g}\overline{\tilde{u}}_3^2 = -\frac{1}{g}\tilde{u}_3\frac{\partial}{\partial y}\overline{(u_3' v_3')} - \frac{f_m}{p_2 g}\overline{\tilde{\psi}_3 \tilde{\omega}_2} -$$
$$- k_m\left(\frac{\partial c}{\partial p}\right)_3 \overline{\tilde{u}_3 \tilde{u}_4} - \frac{A}{g}\overline{\tilde{\zeta}_3^2} .$$

If we take the two levels to be representative of the upper and lower half of the model atmosphere respectively, the rate of change of the zonal kinetic energy will be given by:

$$(43) \quad \frac{\partial \overline{K}}{\partial t} = \frac{p_4}{2}\frac{\partial}{\partial t}\left(\overline{K}_1 + \overline{K}_3\right)$$

and the corresponding average per unit pressure interval:

$$(44) \quad \frac{\partial}{\partial t}\left(\bar{\bar{K}}\right) = \frac{1}{2}\frac{\partial}{\partial t}\left(\tilde{K}_1 + \tilde{K}_3\right)$$

A similar procedure is employed to obtain the rate of change of the zonally averaged potential energy. We begin by zonally averaging the thermodynamic energy equation:

$$(45) \quad \frac{\partial}{\partial t}\left(\tilde{\psi}_1 - \tilde{\psi}_3\right) = -v'_{1,3}\cdot\nabla(\psi'_1 - \psi'_3) + \frac{\sigma_2 p_2}{f'_m}\,\tilde{\omega}_2 + \frac{R}{f_m c_p}H_{2a} + A\frac{\partial^2}{\partial y^2}\left(\tilde{\psi}_1 - \tilde{\psi}_3\right)$$

Multiplying it by $\left(\tilde{\psi}_1 - \tilde{\psi}_3\right)$ and integrating over x and y we obtain:

$$(46) \quad \frac{\partial}{\partial t}\,\frac{1}{2}\overline{\left(\tilde{\psi}_1 - \tilde{\psi}_3\right)} = \overline{v'_1\,\tilde{\psi}'_3\left(\tilde{u}_1 - \tilde{u}_3\right)} + \frac{\sigma_2 p_2}{f_m}\,\tilde{\omega}_2\overline{\left(\tilde{\psi}_1 - \tilde{\psi}_3\right)} +$$
$$+ \frac{R}{f_m c_p}\,\tilde{H}_{2a}\overline{\left(\tilde{\psi}_1 - \tilde{\psi}_3\right)} - A\left[\overline{\frac{\partial}{\partial y}\left(\tilde{\psi}_1 - \tilde{\psi}_3\right)}\right]^2$$

Multiplying by $\dfrac{f_m^{\,2}}{\sigma_2 p_2 g} = \dfrac{\lambda p_2}{g}$ we obtain the rate of change of the zonally averaged potential energy per unit column:

$$(47) \quad \frac{\partial P}{\partial t} = \frac{f_m^{\,2}}{\sigma_2 p_2 g}\overline{v'_1\,\psi'_3\left(\tilde{u}_1 - \tilde{u}_3\right)} + \frac{f_m}{p}\,\tilde{\omega}_2\overline{\left(\tilde{\psi}_1 - \tilde{\psi}_3\right)} + \frac{R}{c_p}\,\frac{f_m}{\sigma_2 p_2 g}\overline{\tilde{H}_2\left(\tilde{\psi}_1 - \tilde{\psi}_3\right)} -$$
$$- A\,\frac{f_m^{\,2}}{\sigma_2 p_2 g}\left[\overline{\frac{\partial}{\partial y}\left(\tilde{\psi}_1 - \tilde{\psi}_3\right)}\right]^2$$

The vorticity equation for the eddies is obtained by subtracting (36) from (37):

$$(48) \quad \nabla^2\frac{\partial \psi'_1}{\partial t} = -v_1\cdot\nabla(\zeta_1 + f) + v'_1\cdot\nabla\zeta'_1 + \frac{f_m\,\omega'_2}{p_2} - g k_m\left(\frac{\partial c}{\partial p}\right)_1\zeta'_4 + A\nabla^2\zeta'_1$$

The rate of change of the mean kinetic energy of the eddies is obtained by multiplying (48) by ψ_i' and integrating the products over x and y. For the lateral eddy-viscosity term we have after integration by parts, and application of the boundary conditions:

$$(49) \quad A \int \psi_i' \nabla^2 \zeta_i' \, d\sigma = -A \int (\zeta_i')^2 \, d\sigma$$

Finally we obtain:

$$(50) \quad \frac{\partial}{\partial t} K_i' = \frac{\partial}{\partial t} \frac{1}{g} \overline{\frac{\nabla \widetilde{\psi_i'}^2}{2}} = \frac{1}{g} \widetilde{u}_1 \overline{\frac{\partial}{\partial y}(\widetilde{u_i' v_i'})} - \frac{f_m}{g P_2} \overline{\psi_i' \omega_2'} - k_m \left(\frac{\partial c}{\partial p}\right)_1 \overline{v_i' v_4'} - \frac{A}{g}(\overline{\zeta_i'})^2$$

And similarly for the 750 mb level. As above:

$$(51) \quad \frac{\partial}{\partial t} K' = \frac{p_4}{2} \frac{\partial}{\partial t}(K_1' + K_3')$$

For deriving the rate of change of the potential energy of the eddies, we subtract (45) from the energy equation:

$$(52) \quad \frac{\partial}{\partial t}(\psi_i' - \psi_3') = -V_{1,3} \cdot \nabla(\psi_i - \psi_3) + \overline{V_{1,3} \cdot \nabla(\psi_i' - \psi_3')} + \frac{\sigma_2 P_2 \omega_2'}{f_m} + \frac{R}{f_m C_p} H_{2a}' + A\nabla^2(\psi_i' - \psi_3')$$

Multiplying (52) by $(\psi_i' - \psi_3')$ and integrating we obtain:

$$(53) \quad \frac{\partial P'}{\partial t} = \frac{\partial}{\partial t} \frac{f_m^2}{\sigma_2 P_2 g} \frac{1}{2} \overline{(\psi_i' - \psi_3')^2} = -\frac{f_m^2}{\sigma_2 P_2 g} \overline{\widetilde{V_i \psi_3'}(\widetilde{u}_1 - \widetilde{u}_3)} +$$
$$+ \frac{f_m}{g} \overline{\omega_2'(\psi_i' - \psi_3')} + \frac{R}{C_p} \frac{f_m}{\sigma_2 P_2 g} \overline{H_{2a}'(\psi_i' - \psi_3')} -$$
$$- \frac{A f_m^2}{\sigma_2 P_2 g} \overline{\left[\nabla(\psi_i' - \psi_3')\right]}$$

So that using Phillips' notation (1956) we have the following transformations:

$$(54) \quad [\overline{K}, K'] = \frac{p_2}{g}\left[\tilde{u}_1 \frac{\partial}{\partial y}\overline{(\tilde{u}_1' v_1')} + \tilde{u}_3 \frac{\partial}{\partial y}\overline{(\tilde{u}_3' v_3')}\right]$$

$$[\overline{P}, P'] = -\frac{f_m^2}{p_2 g \, \sigma_2}\overline{\widetilde{\psi_1' \psi_3'}(\tilde{u}_1, -\tilde{u}_3)}$$

$$[\overline{K}, \overline{P}] = \frac{f_m}{g}\overline{\tilde{\omega}_2(\tilde{\psi}_1 - \tilde{\psi}_3)}$$

$$[K', P'] = \frac{f_m}{g}\overline{\omega_2'(\psi_1' - \psi_3')}$$

$$[\overline{P}, Q] = -\frac{R}{C_p}\frac{f_m}{\sigma_2 p_2 g}\overline{\widetilde{H}_{2a}(\tilde{\psi}_1 - \tilde{\psi}_3)}$$

$$[P', Q'] = -\frac{R}{C_p}\frac{f_m}{\sigma_2 p_2 g}\overline{H_{2a}'(\psi_1' - \psi_3')}$$

$$[\overline{K}, \overline{F}] = \cdot p_2 \, k_m\left[\left(\frac{\partial C}{\partial p}\right)_1 \overline{\tilde{u}_1 \tilde{u}_4} + \left(\frac{\partial C}{\partial p}\right)_3 \overline{\tilde{u}_3 \tilde{u}_4}\right]$$

$$[K', F'] = p_2 \, k_m\left[\left(\frac{\partial C}{\partial p}\right)_1 \overline{v_1' v_4'} + \left(\frac{\partial C}{\partial p}\right)_3 \overline{v_3' v_4'}\right]$$

$$[\overline{K}, A] = \frac{A}{g}\left(\overline{\tilde{\zeta}_1^{\,2} + \tilde{\zeta}_3^{\,2}}\right)$$

$$[K', A] = \frac{A}{g}\overline{\left[(\zeta_1')^2 + (\zeta_3')^2\right]}$$

$$[\overline{P}, A] = A\frac{f_m^2}{\sigma_2 p_2 g}\left[\overline{\frac{\partial}{\partial y}(\tilde{\psi}_1 - \tilde{\psi}_3)^2}\right]$$

$$[P', A] = A\frac{f_m^2}{\sigma_2 p_2 g}\left[\overline{\nabla(\psi_1' - \psi_3')}\right]^2$$

THE DEVELOPMENT OF THE CIRCULATION

The first experiment to be denoted as Experiment I, does not include water vapor, and is similar to Experiment I by Huss (1967), except that lateral viscosity has been included. Like in the corresponding experiment mentioned above, the disturbance was found to grow initially at an exponential rate. Later on this growth ceased and the appearance of higher harmonics was observed.

In fig. (1) we observe the variations of the amplitudes of the first wave components of the stream function at the central latitude, as a function of time. The amplitude of the first component at both levels reached its first maximum after about 13 days, the numerical value attaining $9.3 \times 10^6 m^2/sec$ at 250 mb, almost half the value obtained by Huss in the corresponding experiments, which was $1.7 \times 10^7 m^2/sec$. As we shall frequently refer to Huss' corresponding first experiment we shall call it thereafter the "previous run", without any other specification.

After reaching the maximum the amplitude decreased for 5 days, then continued to rise, reaching a second maxima at the 25th day amounting to $1.42 \times 10^7 m^2/sec$ at the 250 mb level.

No pronounced oscillations as in the previous run were observed. After a minimum on the 27th day of $1.05 \times 10^7 m^2/sec$

at 250 mb and of 1.3×10^6 m^2/sec at the 750 mb level, the amplitudes continued to rise until the 35th day. Following this date the amplitudes at both levels remained more or less stable with 2.65×10^7 m^2/sec at the 250 mb level and 6.4×10^6 m^2/sec at 750 mb, retaining those values until the end of the run on the 42nd day. Generally speaking the latest values attained seemed to be half the average values of the previous run during the corresponding stages. The smoothing is due to the action of the lateral friction term, now introduced.

Fig.(2) shows us the amplitudes of the odd harmonic components of the disturbance at the central latitude of the upper reference level.

The component with wave number (I) initially imposed on the flow remains dominant throughout the run. Compared to the previous run, a considerable smoothing is observed - in the amplitudes of the shorter waves. Still, the components with odd wave numbers are much greater than those with even wave numbers. On the 10th day only the 3rd component exceeds 10^4 m^2/sec while the 5th has a value of about 10^2 m^2/sec. The 7th component reaches this value only on the 25th day.

On the 20th day the fundamental wave (no. I) has a minimum consisting of 6.4×10^6 m^2/sec while the 3rd harmonic, the value of $7 \cdot 10^5$ m^2/sec, the 5th a value of 7.5×10^4 m^2/sec and the 7th a value of 5.5×10^3 m^2/sec.

We observe that they are one or two magnitudes smaller than the fundamental wave. Thus, the noise level was considerably reduced and lowered in the present model compared with the previous run:

On the last day of the run the 3rd component attained the value of 2×10^5 m^2/sec, the 5th 3.2×10^5 m^2/sec and the 7th 3×10^4 m^2/sec.

Fig. 3 shows us the amplitudes of the various harmonic components of the disturbance with even wave numbers at the central latitude of the upper reference level.

The amplitudes of the even harmonics never exceeded the value of 10^4 m^2/sec and the highest value in the run was attained by the 2nd component on the 34th day; 4×10^3 m^2/sec. The even harmonics, amplitudes were one or two magnitudes smaller than the amplitudes of the corresponding odd components.

On the 42nd day, the 2nd harmonic attained 1.4×10^3 m^2/sec, the 4th attained 7×10^2 m^2/sec and the 6th 4×10^2 m^2/sec.

This indicates a drastic smoothing if we compare our values to those of the previous run, thus confirming our expectations as to the effect of the inclusion of the lateral eddy viscosity term.

The latitude pressure distribution of the poleward eddy momentum transports is shown for 4 selected days in fig. 6. The values of $u'v'$ must be antisymmetrical around the central latitude - therefore the poleward flux vanishes there.

On the 10th day the flux is consistently toward the central latitude at the 2 levels and at all latitudes. Absolute maximum values were of the order of 11.5 m^2/sec^2 compared to 20 m^2/sec^2 in the previous run for the corresponding period. On the 15th day maxima of 40 m^2/sec^2 were attained, the highest values during the entire run

On this date small regions in the extreme South and North were characterized by transports toward the boundaries.

On the 20th day the distribution of the fluxes was quite different indicating a negative transport in the south and positive transports in the north. Their maximum magnitude was 11.2 m^2/sec^2. In small regions in the extreme north and south, the flux was directed away from the boundaries in opposite direction of the bulk of the flux in each half of the atmosphere. Such an opposite transport appeared also in the central region.

On the 30th day the fluxes dropped to smaller magnitudes but the characteristic feature of positive transports in the southern half and negative ones in the northern half reappeared.

The maxima are 10.5 m^2/sec^2 at $j = 10$ at the upper level. The transports opposite in direction to the bulk of the flow disappeared along the lateral boundaries.

On the 40th day values increased again reaching 33.1 m^2/sec^2 at the upper level.

Transports in opposite directions are again observed at
the lower reference level at $j = 6\frac{1}{2}$ and $j = 9\frac{1}{2}$.

The change with time of the various components of the
specific kinetic energy is shown in fig. 9.

The zonal kinetic energy decreased at the upper reference
level from the value of 536 m^2/sec^2 on the first day to the
value of 387.5 on the 40th day. The decrease was accompanied
by small oscillations. A tendency of stabilization can be
perceived around the 42nd day, which is the last day of the
present run.

At the lower level a slight decrease of the zonal kinetic
energy is observed until the 22nd day, followed by a slight
increase. Towards the end of the run, a tendency towards
stabilization may be indicated.

At the upper level, the eddy kinetic energy increased
while oscillating and attained its highest maximum of 137 m^2/sec^2
on the 38th day.

The eddy kinetic energy at the lower level was very small.
It appears to increase somewhat with time and attains a value
of 10 m^2/sec^2 on the 37th day, thereafter stabilizing at this
value.

The total averaged kinetic energy decreased very slightly
during the formative stage from 282 m^2/sec^2 on the 16th day
and then more abruptly to 248 m^2/sec^2 on the 22nd day. After

this date the energy increases again, attaining a maximum
of 280 m^2/sec^2 on the 37th day. This is followed by almost
constant values and apparently a steady state has been ob-
tained.

The variation of the zonally averaged flow at 1000 mb
as a function of latitude and time is shown in figure 5.

The development was considerably slower than in the
previous experiment. A value of 4.20 meter/sec was observed
at the central latitude on the 16th day, and this was the
highest value of the entire run.

The boundaries between the central latitude and the
regions of the easterlies which developed were, relatively,
more smooth during the entire course of the integration,
being located in the South between $j = 4$ and $j = 5\frac{1}{2}$ and
in the North between $j = 10$ and $j = 12$.

The speeds in the belts of the easterlies and in the
belt of the westerlies were considerably lower than in the
previous run.

The maximum wind speed decreased from 4.20 m/sec at
the central latitude on the 16th day to 0.22 m/sec on the
22nd day, then rose again and reached a maximum on the 27th
day, of 3.71 m/sec, again decreasing to 1.60 m/sec on the 32nd
day and rising again to a local maximum of 3.65 m/sec on the
38th day. These variations might indicate a cycle

of 11 days at 1000 mb, but we cannot draw such a
conclusion from only 42 days of integration and it seems
that afterwards this clear-cut cycle disappears due to the
increasing effect of the eddy diffusion term, as it is seen
in the amplitude of the disturbance.

The highest speed of easterlies appears between the 36th
- 42nd days, reaching speeds not exceeding 2 m/sec (the
highest speed being 2.13 m/sec on the 38th day = the
same day on which the highest local maximum of 3.65 m/sec
was observed in the westerlies).

The local maxima of easterlies appear on the same days
as the maxima in the westerlies. Their intensities being
however lower.

Various energy transformations are shown in figures 7,
8, 8'.

The highest value of $\{\bar{P}, P'\}$ amounting to 4.2×10^{-5} kj m^{-2}
sec^{-1} cb^{-1} was attained on the 37th day. This was the third
maxima during the entire run, the first being observed on the
14th and the second on the 25th days, with values of $1.88 \times$
10^{-5} and 3.14×10^{-5} kj m^{-2} sec^{-1} cb^{-1} respectively. During
the course of the run the values were found to drop down to
0.12×10^{-5} on the 19th day. In this run much lower values
were attained than in the previous run.

The conversion of heat into zonal potential energy is

consistently positive and into eddy potential energy, con-
sistently negative.

The positive conversion in this experiment was larger
than the negative conversions.

Friction causes a reduction of kinetic energy. The
variations in the tranformation of kinetic energy into
friction are not exactly in phase with the other trans-
formations, attaining maxima on the 16th, 27th and 39th days.
Thus having a phase lag of two days relative to $\{\bar{P},\ P'\}$.
The absolute values are smaller, by a factor of 3 than the
energy gained by heating. Frictional losses are shown ac-
cording to a scale reduced by 10 compared to the other
transformations. Their values are much lower than those
obtained in the previous run. The highest value of $\{K, F\}$
was attained on the 39th day having a value of 7.5×10^{-6}
compared to 24×10^{-6}, the absolute maximum attained in the
previous run.

During this run most of the eddy kinetic energy was
transformed into kinetic energy. Oscillations that indicated
small negative values were obtained on the 22nd and the 33rd
day but the negative values were very small compared to the
dominant positive ones.

In fig. 8 the frictional losses of kinetic energy due
to lateral eddy viscosity are shown.

The values of these transformations are smaller than

the values of all other transformations taking part in the
energy exchanges.

Starting with 127×10^{-7} kj m^{-2} sec^{-1} on the first
day of the run $\{ \overline{K}, A \}$ decreased until the 15th day, when
it reached the values of 32×10^{-7} kj m^{-2} sec^{-1}. A
local maximum was attained on the 18th day, a second one on
the 29th day and values appear to become stable on the 40th
day, with 43×10^{-7} kj m^{-2} sec^{-1}. The values of the first
two maxima were 40×10^{-7} and 41×10^{-7} kj m^{-2} sec^{-1} res-
pectively.

The frictional losses of eddy kinetic energy rose slowly
from the first day to a maximum of 40×10^{-7} kj m^{-2} sec^{-1}
on the 16th day. A second maxima of 44×10^{-7} kj m^{-2} sec^{-1}
was observed on the 27th day, and a higher maximum of $63 \times$
10^{-7} kj m^{-2} sec^{-1} was reached on the 37th day. While in the
first half of the run, i.e. until the 24th day the values
of $\{ \overline{K}, A \}$ dominate, in the second half i.e.
from the 24th day until the end of the run on the 42nd day
the values of $\{ K', A \}$ dominate. Towards the end
of the run a tendency towards stabilization can be observed
in the values of both transformations.

The zonally averaged diabatic heating as a function
of latitude is shown in fig. 10 for the 10th, 20th, 30th and
40th days.

The magnitudes were considerably lower than in the previous
run and the distribution was also much smoother.

On the 10th day the heating was still very small, almost imperceptible.

On the 20th day it was not much higher, but on the 30th day the general pattern could be easily observed.

The region of most extreme heating was in the south around $j = 2$. Proceeding to the North, the values became negative between $j = 4$ and $j = 5$. No diabatic heating was obtained at the central latitude, due to the constraints of the model.

Small positive values were obtained however between $j = 8$ and $j = 11\frac{1}{2}$. Intense cooling was observed in the north with its highest value at $j = 14$.

No simplification of the distribution occurred on the 40th day - contrary to the previous run.

While the values were lower, the same pattern persisted, so that most of the heat was supplied to the atmosphere at the very low latitudes while the sink was located in the extreme north.

The zonally averaged zonal flow is shown in fig. 4 as a function of latitude and pressure for 4 selected days at intervals of 10 days.

The same tendencies as in the earlier run towards the formation of a "jet" at the central latitude at the formative stage of the run are observed. (The jet was slightly "split"). On the 10th day the velocity at p_1 at the central latitude

was 36.1 m/sec while the maxima located at $j = 6$, and $j = 11$ are 36.7 m/sec. A less pronounced similar effect was observed at the lower level. On the 20th day the splitting remained evident - the velocity at the central latitude was 37 m/sec and maxima of 40.1 m/sec were located at $j = 6$ and $j = 10$.

On the 30th day the splitting tended to disappear. The velocity at p_1 at the central latitude was 41.4 m/sec while the 2 maxima of 42.3 m/sec were observed near it at $j = 7$ and $j = 9$. On the 40th day a single well developed central jet could be observed with a speed of 48.2 m/sec . The development of the easterlies proceeded at a slower rate. On the 20th day easterlies were found slightly below 750mb level. Their lateral extent was constant during the run, not penetrating beyond $j = 4$ and $j = 12$.

On the 40th day easterlies penetrated up to the 500 mb level.

The maxima of the speeds of the easterlies did not exceed during the entire course of the run, the value of 2 m/sec. The highest maximum was attained by the westerlies on the 40th day reaching a value of 48 m/sec.

Description of the development in the second Experiment

The amplitude of the first harmonic of the stream function at the central latitude, at the two reference

levels is shown in fig. 12. The stage of initial growth was similar to the corresponding stage in experiment I until the 13th day. The maximum attained on the 13th day had a value of 9.8×10^6 m^2/sec at the 250 mb level, and of 6×10^6 m^2/sec at the 750 mb level. These maxima are almost half of the corresponding maximum values obtained on the 13th day in the previous run.

No small amplitude oscillations were observed in this experiment.

The pronounced variation, which may presumably be identified as an "index cycle" which appeared in the previous run - was also not present in this run, although one long period oscillation was observed, with a period of 10 days. This may perhaps be a remnant of the former index cycles, all later cycles having been obliterated by the strong effect of the lateral eddy viscosity term. The 18th day presents the lowest value of this oscillation, with 2.8×10^6 m^2/sec (at 250 mb and 1.9×10^6 m^2/sec at 750 mb). The minimum of the present run is approximately 1/3 of the corresponding values in the previous run.

The following minimum was observed on the 28th day, with 1.4×10^7 m^2/sec and 1.6×10^6 m^2/sec respectively at the 250 and 750 mb levels.

The 750 mb minimum on the 28th day is somewhat lower than the corresponding value at the beginning of the same cycle,

a detail that characterized also the first cycle in the
previous run.

From the 28th day on - our amplitudes depart from
the "index cycle" pattern which was typical of the previous
run. We observe a slow but constant growth at both levels
at a roughly exponential rate, until the 51th day of the
integration when the values attained were $5.0 \times 10^7 \ m^2/sec$
at the 250 mb level and $2.0 \times 10^7 \ m^2/sec$ at the 750 mb level.
From the 51st day until the end of the run, on the 65th day,
the amplitudes at both levels became more or less stabilized
at the values attained on the 51st day - indicating consider-
able smoothing of the first harmonic of the disturbance at
both levels. Yet, those stabilized values correspond roughly
to the mean amplitudes obtained at both levels in the previous
run.

In figs. 13,14,15,16 the change with time of the
amplitudes of the various harmonic components of the dis-
turbance at the central latitude of the upper reference level
are shown. Figs. 14 and 16 show the components with odd and even
wave numbers respectively in the previous run, while
figs. 13 and 15 show the corresponding components in the present
experiment.

In the previous run components with even wave numbers
attained higher values than those with odd wave numbers. In
the present run, a considerable smoothing was observed in the

case of both odd and even wave components. In this run the components with odd wave numbers also attained higher values.

Fig. 14 shows the components with odd wave number of experiment III of the previous run. The 3rd harmonic exceeds 10^3 m^2/sec on the 4th day, the 5th harmonic on the 8th day and the 7th harmonic on the 11th day.

In fig. 13 the corresponding odd wave number components of the present experiment are shown. Here the 3rd harmonic exceeds 10^3 m^2/sec on the 4th day, the 5th harmonic on the 9th day and the 7th harmonic on the 15th day.

In experiment III of the previous run, the 3rd harmonic attained a first maximum of 1.3×10^6 m^2/sec on the 16th day while in the present run on the same day the 3rd harmonic attained 3.1×10^5 m^2/sec. The same harmonic attained its highest value of 5.5×10^6 m^2/sec on the 51st day in the previous run, and it attained its highest value of 3.0×10^6 m^2/sec on the present run on the 56th day.

The 5th harmonic attained a first maximum of 2.1×10^6 m^2/sec on the 20th day in the previous run while in the present experiment its first maximum 9.5×10^4 m^2/sec is attained on the 22nd day. The highest value attained by the 5th harmonic in the previous run, 2.8×10^6 m^2/sec, was observed on the 54th day while in the present run the highest value of the same harmonic 6×10^5 m^2/sec was attained on the 60th day. The 7th harmonic attained a first maximum of 4.8×10^5 m^2/sec on the 22nd day in the previous run, while

in the present experiment the same harmonic had its first maximum on the 22nd day also, with a value of 9.2×10^4 m^2/sec. The highest value attained by the 7th harmonic, 8×10^5 m^2/sec, was observed in the previous experiment on the 48th day while in the present model the highest value of 2.8×10^5 m^2/sec was observed on the 56th day.

Fig. 16 shows the components with even wave number of Experiment III of the previous run, while fig. 15 shows the corresponding components of the present experiment.

We see that the higher harmonic components are more attenuated than the lower components. In the previous experiment the 2nd component attained a value of 10^6 m^2/sec at the first noticeable maximum on the 22nd day while in our experiment it attained a maximum of 6.5×10^5 m^2/sec on the 27th day. The highest value of 1.2×10^7 m^2/sec was attained by the 2nd component in the previous experiment on the 40th day, while the highest value in the present run was 3.5×10^5 m^2/sec.

In the previous experiment the 4th harmonic attained the first maximum and of 1.8×10^6 m^2/sec on the 22nd day while on the same day the same harmonic in our present experiment attained the value of 9.5×10^4 m^2/sec.

The highest value attained by the 4th harmonic in the previous experiment of 4.2×10^6 m^2/sec was observed on the 44th day, while in the present experiment the highest value was 6×10^5 m^2/sec and it was observed on the 55th day.

In the previous experiment the 6th harmonic attained
its first maximum 7.5 x 10^5 m^2/sec, on the 23rd day, while
in the present run it attained a first maximum of 4 x 10^4 m^2/sec
on the 26th day. It attained its highest value of 3.9 x 10^6
m^2/sec in the previous run on the 59th day. While in the
present run it attained its highest value of 1.2 x 10^5 m^2/sec
on the 57th day.

Thus again the effect of the lateral viscosity is strongly
marked.

The variation of the zonally averaged zonal component of
the wind at 1000 mb as a function of latitude and time is
shown in fig. 17.

The same fundamental pattern subsists, westerlies dom-
inating the central region, while the easterlies were con-
fined to the north and the south.

Speed maxima are lower than in the previous run and the
distribution differed considerably.

Maxima of the westerlies are observed in the present
model, on the 16th, 27th and on the 48th day. The index cycle
was no longer a prominent feature of the developing circulation
although traces of it may perhaps be detected during the
earlier stages of the run.

Between the maxima of the westerlies their speeds
go down to 25% of the peak values between the first two maxima,

and to 50% of the peak values between the second and the third maxima. The values of the maxima attained by the westerlies on the 16th, 27th, 48th and 64th days were 4.99 m/sec, 5.07 m/sec, 6.47 m/sec and 3.10 m/sec respectively. They are by 50% lower than the corresponding maxima obtained in the previous run.

Intensification of the easterlies in the south was practically in phase with the changes of the westerlies in the central belt.

All the three maxima of the easterlies in the north coincided in time with the maxima of the westerlies in the central belt. In the south only two maxima were observed, on the 16th and 48th day during which the westerlies also had reached maximum values. The first maximum of the easterlies in the north had a higher value than the corresponding maximum of the easterlies in the south. On the 16th day, the maximum speed attained in the north was located at $j = 13$ the extremal velocity was 1.65m/sec while the corresponding value in the south at $j = 3$ was 1.31 m/sec.

The second speed maxima in the north at the same latitude of $j = 13$ indicated a velocity of 2.06 m/sec while in the south the corresponding value at $j = 3$ (which was not a speed maximum) attained 3.53 m/sec.

The third speed maximum of the easterlies in the north was obtained at the same latitude of $j = 13$ on the 48th day with a velocity of 5.75 m/sec while in the south a simultaneous maximum was observed at $j = 3$ with 4.73 m/sec.

Compared with the previous experiment the values of the
easterlies were much lower.

A northward shift of the central belt is no longer ob-
tained in the present experiment although at the end of the
run such a tendency appeared to develop. Consequently all the
maxima in the westerlies were observed at the central latitude
$j = 8$ and only on the 64th day, one day before the conclusion
of the present run the local maximum of the westerlies was
located at $j = 9$.

An additional aspect of the structure of the zonal flow
is presented by the pressure latitude distribution of $\widetilde{u}$ for 4
selected days, as shown in fig. 18.

I have chosen the 4 days which were the more significant.
Some of the latest stages of the run were selected, as in
experiment I. They resembled the pattern already obtained in
that experiment.

After the 48th day – the velocity in the axis of the jet
reached 42.5 m/sec and on the 54th day, 31.2 m/sec. The cor-
responding values on the 60th day and 68th day were of 27.7
m/sec and 27.5 m/sec., respectively.

The most intense velocities in the easterlies in the
south were 4.7 m/sec on the 48th day, 4.0 m/sec on the 54th day,
3.5 m/sec on the 60th day and 2.8 m/sec on the 65th day. No
indication of an index cycle such as in the previous experiment
could be detected. In the North the easterlies pehetrated

vertically beyond the 500 mb level on the 48th day. On the other 3 days, chosen, they extended only to a limited extent beyond the 750 mb level. Also in the north the highest speeds were located near the surface. The largest speed in the easterlies in the north among those 4 days, amounted to -5.8 m/sec on the 48th day. The corresponding value on the 54th day was -4.3 m/sec.. These two values were higher than those attained by the easterlies in the south on the same days. On the 60th day, the easterlies in the north attained -2.5 m/sec and on the 65th day -2.2 m/sec., i.e., lower than the corresponding values in the south on the same dates.

On the 60th and 65th days, the vertical axis of the wind speed maxima in the belt of the westerlies tilted with height towards the south from $j = 9$ at 1000 mb to $j = 6$ at 250 mb on the 60 th day, and from $j = 9$ to $j = 5$ at the same levels on the 65th day. A small tilt of the axis towards the north from $j = 8$ at 1000 mb level to $j = 9$ on the 250 mb level was observed on the 54th day.

Fig. 19 shows us the patterns of the zonally averaged northward eddy transport of momentum. The same days quoted above were chosen. Here also, like in the previous experiment, large variations from one day to another were observed. On the 48th day, transports toward the south prevailed over the northern half of the region and a part of the southern one. Northward transports were observed, in the southern region, and at 250 mb in certain parts in the northern region. A

maximum of southward transports - 43.3 m^2/sec^2 was obtained
on the 48th day at the upper level at j = 10. The maximum
of the northward transport, 31.2 m^2/sec^2 at j = 5 on the same
day, was observed also at the upper level. On the 54th day the
pattern gains additional complexity. The northward positive
values extend now well into the northern half of the region,
attaining a maximum value of 43.0 m^2/sec^2 at the upper level
at j = 6. The southward negative values attain a maximum of
- 23 m^2/sec^2 at the upper level at j = 12. At the 750 mb
level on the same day the situation is reversed. In the northern
half a patch of positive northward values was observed with
a maximum value of 15.1 m^2/sec^2 at j = 10. In the southern
half of the region a patch of negative southward transports
was observed, with -15.9 m^2/sec^2 at j = 5. On the 60th day
the distribution resembles the pattern observed on the 54th
day. The southward transports attained at the upper level on
this day the maximum of -27.3 m^2/sec^2 at j = 12 and the
northward maximum of 43.8 m^2/sec^2 at j = 6.

The same pattern persisted on the 65th day. The north-
ward transports attained the higher value of 53.0 m^2/sec^2
at j = 5 and a maximum negative transport of -38.0 m^2/sec^2
at j = 10. At the 750 mb level the same inversed situation
was observed. A maximum northward transport of 12.8 m^2/sec^2
was observed at j = 12 while in the southern region a maximum
negative transport of -11.3 m^2/sec was obtained at j = 5.

The mean zonal heat balance for the same 4 representative
days is shown in fig. 20.

Two maxima in the sensible heat flux can be distinguished. One in the South was located on the 48th day (which is a maximum day), at $j = 3$. Then it shifted southward to $j = 2$ during the 3 additional representative days. The other in the north was located systematically at $j = 14$. This may have been a result of the fact that in the present model no clear cut index cycle was observed.

The net heating and cooling distribution in the present model has the general features of the low-index situation in the previous run, i.e., only two subregions are observed: heating taking place between the southern boundary and $j = 10$ for the 48th day, between the southern boundary and $j = 9$ for the 54th day, between the southern boundary and $j = 8\frac{1}{2}$ for the 60th and the 65th day. Thus the boundary between the two subregions shifts somewhat as time goes on. In the present numerical experiment, maximum heating was observed on the 48th day, at $j = 2$, amounting to 18.7×10^{-2} kj m^{-2} sec^{-1}. The most intense cooling on the same day was -21.5×10^{-2} kj m^{-2} sec^{-1} near the pole, at $j = 14$. This corresponded to observations which indicate a pronounced sink near the pole. On the 54th day the maximum of the heating attained the value of 24×10^{-2} kj m^{-2} sec^{-1} at $j = 2$ in the south and the maximum value of cooling of -23.5×10^{-2} kj m^{-2} sec^{-1} at $j = 14$ in the north. On the 60th day the maximum appeared at the same latitudes, of the corresponding values being 26.5×10^{-2} kj m^{-2} sec^{-1} and -23×10^{-2} kj m^{-2} sec^{-1}.

On the 65th day the maximum values were observed at the same latitudes attaining the values of 22.2×10^{-2} kj m^{-2} sec^{-1}

and $-21.5 \times 10^{-2} kj \ m^{-2} sec^{-1}$

Fig. 21 shows the march of the various kinetic energy components with time.

The variation of the energy of the zonal flow at the 250mb level did not vary periodically as in the previous run but was characterized by a slow but steady decrease. The only local maximum was observed on the 28th day. After this day, there was a slow, but continuous descent until the 42th day. After this day, the decrease became more intense until the 60th day on which a tendency towards stabilization began to be manifested. Starting from 533 m^2sec^{-2} the zonal flows energy decreased to 250 m^2/sec^2 on the 60th day stabilizing itself at this value until the end of the run on the 65th day. From the 53rd day onwards, the eddy kinetic energy at the 250 mb level became greater than the kinetic energy of the zonal flow at the same level.

At the 750 mb level the variations were less clear cut. the K_{750} component had a slight maximum on the 28th day, coinciding in time with a slight maximum in K_{250}. Another local maximum was observed on the 42nd day, and thereafter K_{750} decreased slowly until the end of the run. The energy of the perturbations exceeded that of the zonal flow at 750 mb from the 48th day and it increased slowly up to the 59th day where it appeared to stabilize itself around the value of 67.5 m^2sec^{-2}.

The mean total kinetic energy $\{\overline{K} + K'\}$ attained a small minimum on the 22nd day and a maximum on the 28th day. After a small decrease it began to rise from the 32nd day and grew steadily. Attaining a maximum value of $395.5\,m^2\,sec^{-2}$ on the 58th day, when a tendency towards stabilization could be observed, the values of the mean total kinetic energy oscillated around the value of $387.5\,m^2sec^{-2}$ until the end of the run on the 65th day.

Compared with the previous run the march of the various components of the kinetic energy is smoother with less oscillations and shows a tendency towards stabilization at the end of the run.

Fig. 22 shows us the transformation of zonal potential energy into eddy potential energy and the frictional losses. No cycle appears in the variation of $[\overline{P},P']$ with time. Its intensity was much lower compared to the previous run, attaining similar values only towards the end of the run. A first maximum of $2.2 \times 10^{-5}\,kj\,m^{-2}\,sec^{-1}$ was observed on the 14th day. A second maximum was observed on the 27th day, with the value of $0.45 \times 10^{-4}\,kj\,m^{-2}\,sec^{-1}$.

After a minimum on the 29th day continuous growth was observed, leading to a maximum of $0.95 \times 10^{-4}\,kj\,m^{-2}\,sec^{-1}$ on the 53rd day. From this day on the transformation decreased until the end of the run, reaching on the last day, the 65th day, the value of $0.73 \times 10^{-4}\,kj\,m^{-2}\,sec^{-1}$. The frictional losses of the eddies were quite small. They did not exceed $10^{-5}kjm^{-2}sec^{-1}$ until the 47th day of the integration. From this day on

a gradual increase of the frictional losses of the eddies was observed, reaching a maximum value of 27×10^{-5} kj $m^{-2}sec^{-1}$ on the 58th day. After that, a gradual decrease followed so that on the 65th day the value of 2.3×10^{-5} kj m^{-2} sec^{-2} was obtained.

The frictional losses of the zonal flow dominate those of the eddies until the 47th day. From that day on a gradual decrease was observed until the end of the run. two maxima of the [F,K] transformation on the 15th and 26th day lag one day behind the corresponding maxima of the $[\bar{P},P']$ transformation. On the 27th day the transformation reached the value of 1.0×10^{-5} kj m^{-2} sec^{-1} and on the 47th day 1.1×10^{-5} kj m^{-2} sec^{-1}. At the end of the run the intensity of the transformation became very small: 0.2×10^{-5} kj m^{-2} sec^{-1}. The area averaged precipitable water as a function of time is shown in fig. 23. The broken line corresponds to a constant value of 15 mm which is the average winter amount quoted by Peixoto (1958). The water content rose from the initial stage until it reached a maximum of 16.3 mm on the 23rd day. After this day, a tendency toward lower values appeared, with much smaller oscillations than in the previous model. No index cycle was observed and the slight oscillations superimposed on the general trend had variable periods. On the 49th day the water content reached the value of the winter average given by Peixoto and continued to decrease until the end of the run, when on the 65th day the water reached a value of 13.7 mm.

The area averaged precipitation and evaporation as a
function of time is shown in fig. 24. At the start of the
integration - no evaporation was observed, because of the
vanishing surface wind speed at 1000 mb. The evaporation
grew rapidly - while the precipitation started only on the
10th day. Until the 21st day precipitation was less than
evaporation. From the 21st day on the evaporation and the
precipitation had a similar distribution, their values being
close one to the other; the precipitation's values slightly
exceeding the evaporation values. A first maximum of the
precipitation was observed on the 16th day, with 0.5 mm/day.
A second maximum of the precipitation was observed on the
27th day, with 1.23 mm/day. Precipitation was slightly higher
than evaporation in the vicinity of the maxima while at the
vicinity of the minima the situation was reversed. After a
minimum of the precipitation on the 30th day, with 0.86 mm/day,
the precipitation values rose steadily with small oscillations
superimposed on the general trend until they reached the highest
value of the entire run on the 55th day with 2.91 mm/day. This
value is lower than the maximum obtained in the previous run,
amounting to 3.56 mm/day. The evaporation in the present model
on the same day was 2.77 mm/day. After the 55th day a trend
towards lower values was observed, again accompanied by small
oscillations on the 65th day. The precipitation reached the
value of 2.75 mm/day and the evaporation the value of 2.61 mm/day.

The latitudinal distribution of the relative humidity as
a function of time is shown in fig. 25.

During the first 14 days the relative humidity increased
constantly, over the entire region. On the 19th day some
general features which were retained during the whole course
of the run, became already evident. The extreme south beyond
$j = 2\frac{1}{2}$ was very humid, the humidity exceeding 90,. North of
$j = 3$ a belt of relatively dry air was located in which the
values occasionally went down to 70, and even less. The
smallest relative humidity values of 64, were obtained on the
41st day. A northward shift of the dry belt such as in the
previous run could hardly be detected. No irregularities in
the 90 humidity belt were observed in the present model,
while they were quite pronounced in the previous run, part-
icularly north of the dry belt. The dry belt remained in the
southern half of the region, and did not penetrate beyond the
central latitude.

The changes in the relative humidity within the dry
belt were quite pronounced during the early stages of the run,
but no indications of an index cycle were observed. Another
feature worth mentioning is the appearance of a small dry
region in the extreme north with values of 80%. This was ob-
served during the 43rd and the 48th days, at $j = 14\frac{1}{2}$. The region
in excess of 90, in the northern half was larger and more
compact, in the present model, with a high degree of uniformity.
In the extreme south the line of 90, values was quite uniform,
with few fluctuations. Towards the end of the run the humidity
was generally higher than in the previous model, the values
in the last 10 days of the run (after the 56th day) being
everywhere higher than 80,.

In fig. 27 the frictional losses of kinetic energy due to lateral eddy viscosity are shown.

Comparing the results in the present experiment (No. 2) with our first experiment some striking features are evident: the frictional losses of eddy kinetic energy through lateral eddy viscosity attain much higher values in the course of the run.

In this experiment harmonic components with high wave numbers had considerably higher amplitudes and thus the transformation $[K', A]$ was more intense. On the other hand, the frictional losses of zonal kinetic energy followed the same pattern as in the first experiment but during the last 20 days of the run (i.e., from the 45th to the 65th day) considerably lower values of $[\bar{K}, A]$ were obtained.

The $[K', A]$ transformation followed as mentioned above a different evolution in the present run exhibiting a totally different march in the last half of the present run.

Starting slowly from zero on the first day, $[\bar{K}', A]$ attained a first maximum of 46×10^{-7} kj m^{-2}sec^{-1} on the 16th day. A second maximum was observed on the 27th day, 58×10^{-7} kj m^{-2}sec^{-1}, much higher than the corresponding value of the same tranformation on the same day in the first experiment. After some small oscillations which lasted until the 37th day, the values of $[K', A]$ rose constantly and very rapidly to attain 231×10^{-7} kj m^{-2} sec^{-1} on the 59th day and from then until the end of the run on the 65th day its values oscillated around an average value of 215×10^{-7} kj m^{-2} sec^{-1}.

The frictional losses of zonal kinetic energy due to lateral eddy viscosity $\left[\overline{K}, A\right]$ started from a value of 127×10^{-7} kj m^{-2} sec^{-1} on the first day of the run and decreased steadily until the 15th day when the transformation attained a value of 31×10^{-7} kj m^{-2} sec^{-1}. A local maximum was obtained on the 19th day, a second one on the 29th day and a third one on the 43rd day, the corresponding values being 41×10^{-7}, 45×10^{-7} and 49×10^{-7} kj m^{-2} sec^{-1}.

From the 43rd day until the end of the run a gradual decrease is observed, the value of $\left[\overline{K}, A\right]$ declining to 12×10^{-7} kj m^{-2} sec^{-1} on the 64th day.

The zonally averaged poleward eddy flux of water vapor is shown in fig. 26.

On the 40th day of the run the values were very close to those observed in the real atmosphere by Peixoto (1958). On the other 4 representative days - due to the absence of an index cycle - a similar pattern was observed, with values almost double of Peixoto's values.

The largest poleward flux was located at the low levels, the maxima being a little south of the central latitude. On the 40th day, the maximum was 5.27 gm.m.kg^{-1}sec^{-1} obtained at j = 6. On the 48th day the maximum was 9.66 gm.m.kg^{-1}sec^{-1} at j = 7. On the 59th day the maximum was 11.60 at j = 5, on the 60th day it was 11.04 at j=5, and on the 65th day it was of 10.0 at j=5. We notice that towards the end of the run there is a tendency of the poleward fluxes to reach maxima in south.

Fluxes with inverse sign were located on the northern border of the region, and they appear on each representative day. The maxima at the upper level (the 250 mb level) were smaller by one order of magnitude than those located at the lower level, but they appear consistently at the same latitudes.

INTRODUCTION OF THE MATSUNO SCHEME

Introduction

Equations of a two level quasi-hydrostatic and quasi-geostrophic model were integrated again, this time using the Matsuno (Euler-Backward) two level time difference scheme instead of the centered time difference scheme (the leap-frog scheme) used in the first two experiments discussed above, one without and one with the introduction of lateral eddy viscosity.

This scheme has been shown to have a damping effect on high frequency waves (low-pass filter) but it is only conditionally stable.

Matsuno (1966) mentions that his scheme reduces the amplitudes of longitudinal horizontal waves in addition to those of gravity waves. As gravity waves were eliminated from our model by the geostrophic assumption, only the effect of the scheme on the longitudinal horizontal waves will be observed.

Experiment No. 3, was similar in all details to Experiment No. 1, mentioned above, without any lateral friction, but with time-differencing according to the Matsuno scheme instead of the leap-frog scheme. The integration was carried for 62 days.

The calculated distribution of the field variables was

compared with the results of Ex. No. 1 by Huss (1967) mentioned above and also with the two experiments already discussed in this report.

Smoothing of the field variables was observed in this experiment mainly during the last stages of the integration. The first 40 days of the 62 days integration showed no serious departure from the results of Huss's No. 1 Exp. (1967).

The Matsuno scheme is as follows: (Matsuno, 1966): We are given the partial differential equations :

$$\text{(I)} \quad \frac{\partial u_i}{\partial t} = F_i(u_j) \qquad (i,j = 1,2,\ldots N)$$

The F's involving finite differencing operators, then Matsuno's two level scheme may be written:

$$\text{(a)} \quad \begin{cases} u^{(z+1)^*} - u^{(z)} = F(u^z)\,\Delta t \\ \\ \text{(b)} \quad u^{(z+1)} - u^{(z)} = F(u^{(z+1)^*})\,\Delta t \end{cases}$$

where $u^{(z+1)^*}$ is an intermediate value in the calculations. Let us assume that equations (I) are of a pure oscillatory type, i.e. $\frac{\partial u_i}{\partial t} = i\,\omega_i\,u_i$ where ω_i is the frequency of the i-th component of normal modes. Let us consider a single component, and omit the subscript.

Defining $\Omega = \omega\,\Delta t$ the amplification factor for the

Matsuno scheme will be:

$$A = 1 + i\Omega - \Omega^2$$

and:

$$|A| = [1 - \Omega^2 + \Omega^4]^{1/2}$$

Thus the scheme is conditionally stable. u_i will be damped if $|\Omega| < 1$, neutral if $|\Omega| = 1$ and unstable if $|\Omega| > 1$. To obtain the value of Ω at which strongest damping occurs, we differentiate $|A|$

$$\frac{\partial |A|}{\partial \Omega} = \frac{-2\Omega + 4\Omega^3}{2(1 - \Omega^2 + \Omega^4)^{1/2}} = \frac{-\Omega(1 - 2\Omega^2)}{[1 - \Omega^2 + \Omega^4]^{1/2}} = 0$$

Thus $\omega_{crit} = \frac{1}{\sqrt{2}}$

In a meteorological problem, such as the problem under discussion, the modes of highest frequencies are normally assumed to be undesireable noise effects, generated by various processes. Any filtering device, introduced into the model either explicitly, or implicitly, should, therefore have the property of smoothing out the higher frequencies, and leaving the lower frequencies intact. Damping, if present, should therefore increase monotonously with frequency. This would not occur in the Matsuno scheme if Ω is allowed to increase beyond $\frac{1}{\sqrt{2}}$. Therefore, the scheme will be stable, and will also act like a high-cut filter, if the time step will be chosen so that: $\Delta t < \frac{1}{\sqrt{2}\,\omega_{max}}$,

ω_{max} being the highest frequency in the system.

It is easily seen that the scheme acts as a filter by eliminating $u^{(s+i)*}$ from the equations defining the scheme.

$$u^{(s+i)} - u^{(s)} = i\omega\left(u^{(s)} + i\omega u^{(s)}\Delta t\right)\Delta t = i\omega u^{(s)}\Delta t - \omega^2 u^{(s)}\Delta t^2 \cong$$

$$\cong \left(\frac{\partial u}{\partial t}\right)_{(s)}\Delta t + \left(\frac{\partial^2 u}{\partial t^2}\right)_{(s)}\Delta t^2$$

By comparing the resulting expression with the Taylor expansion we note that the scheme introduces a $\frac{1}{2}\left(\frac{\partial^2 u}{\partial t^2}\right)_{s}\Delta t^2$ term, which, in a way, acts like a diffusion term in time.

The Development of the Circulation

In fig. 29 the variations of the amplitudes of the first harmonic wave components of the stream function at the central latitude, at 250 mb and at 750 mb, as a function of time are shown. During the first 30 days of the integration, no serious departure from the results of Exp. 1 of Huss was observed.

The amplitude of the first component at both reference levels reached its first maximum on the 14th day, amounting to 1.5×10^7 m^2/sec at 250 mb. The evolution from now on until the 30th day was similar to that observed in the Experiment described by Huss, with a time-lag of two days.

On the 32nd day, the amplitudes at the upper level of reference were 2.7×10^7 m^2/sec, as compared with the 3.4×10^7 m^2/sec in Huss's experiment and 2.5×10^7 m^2/sec in the experiment with eddy-viscosity.

During the latest stages of the run no oscillations were observed. The dominating feature was a smooth and gradual rise of the amplitudes at both reference levels reaching on the 50th day values of 5.28×10^7 m^2/sec at the 250 mb level and 2.20×10^7 m^2/sec at the 750 mb reference level.

From the 50th day until the end of the run, on the 62nd day, the amplitudes remained about equal to the values of the 50th day. These stable values were twice as high as those observed in the experiment including lateral eddy viscosity, i.e. 2.65×10^7 m^2/sec at the 250 mb level and 6.4×10^6 m^2/sec at the 750 mb level (stabilization taking place already on the 42nd day of the run, with eddy viscosity). This appears to be due to the different smoothing involved in the two models.

Fig. (30) shows us the amplitudes of the odd harmonic components of the disturbance at the central latitude of the upper reference levels. The component with wave number (I) is dominant throughout the entire run - as in the earlier experiments. A prominent feature of the present run is that the magnitudes of the components with even wave numbers were extremely small. Thus the noise due to non-physical effects is eliminated by the use of the Matsuno scheme leaving the interactions between the odd wave number components which are mainly of physical nature.

The 3rd component exceeds 10^4 m^2/sec on the 6th day, the 5th on the 11th day and the 7th on the 19th day. Thus in the beginning this run exhibited the same features as those which were characteristic of Huss's experiment I.

The 3rd component attained a first maximum of 9.5×10^5 m^2/sec on the 17th day, and after a series of small oscillations stabilized itself from the 48th day onwards at a value of $2.5 \times 10^7 m^2/sec$.

The 5th component attained a first maximum of $10^6 m^2/sec$ on the 21st day and after a series of oscillations began to stabilize at the value of $3.5 \times 10^5 m^2/sec$.

The 7th component reached a maximum of $6.5 \times 10^4 m^2/sec$ on the 22nd day, then underwent a series of large-amplitude oscillations. Towards the end of the run the values oscillated between $10^5 m^2/sec$ and $2.0 \times 10^4 m^2/sec$. The amplitude of these oscillations decreased somewhat towards the end of the run. The amplitudes of the components were much larger, generally two or even three times larger than these observed in the experiment with lateral viscosity. Fig. 31 shows us the amplitudes of the various harmonic components of the disturbance with even wave numbers at the central latitude of the upper reference level. Here, as in the experiment with lateral eddy-viscosity, the amplitudes never exceeded a value of $10^4 m^2/sec$ and their magnitudes were the smallest in all the three experiments. On the 42nd day, for instance, the second component attained $7 \times 10^2 m^2/sec$, the 4th $4 \times 10^2 m^2/sec$ and the 6th $10^2 m^2/sec$. On the last day of the present run, the 62nd day, the 2nd component attained a value of 2.8×10^3 m^2/sec, the 4th $4 \times 10^2 m^2/sec$ and the 6th component attained $7 \times 10^2 m^2/sec$. This drastic damping of the even harmonics

which is more severe than in the corresponding experiment
with eddy-viscosity, is reflected by the high degree of sym-
metry between the northern and southern halves of the field
variables around the central latitude, which was conserved
perfectly until the end of the run.

The variation of the zonally averaged zonal flow is
shown in fig. 32 as a function of latitude and pressure for
4 selected days..

During the earlier stages of the run, i.e., until the
30th day the patterns were quite similar to those obtained in
Huss's experiment No. 1, including a tendency toward the
formation of a split jet. Thus on the 10th day the highest
velocities at the upper reference level 37.3 m/sec were located
at j = 11 and j = 5, while at the central latitude a value
of 35.7 m/sec was observed. On the 20th day no trace of the
splitting of the jet was observed and the highest velocity
within the single well-developed central jet was of 44 m/sec.
On the same day easterlies were observed at the lower boundary.
On the 30th day the central jet already had a maximum value
of 48.6 m/sec at the 250 mb level. The easterlies extended
now beyond the 750 mb level penetrating up to j= 5 in the
south and up to j = 11 in the north. On the 40th day the
central jet had become slightly weaker with a maximum velocity
of 45 m/sec.

The corresponding value of the maximum obtained in Huss's

experiment I, was of 38.7 m/sec. The easterlies had a similar extent as those of the 30th day.

On the 50th day further decrease in the velocities was observed with a very slight tendency towards splitting of the jet, the velocity at the central latitude at 250 mb being 30 m/sec, while at j = 9 and j = 7 it was 30.2 m/sec.

The extent of the easterlies was smaller, but they still penetrated a little beyond the 750 mb level.

On the 60th day of the run, the weakening of the velocities became even more pronounced, as well as the splitting of the jet. The velocity at the central latitude at 250 mb was 24.2 m/sec while the maxima of 26.6 m/sec were located at j = 10 and j = 6 .

The easterlies were found only below the 750 mb level, and their lateral extent was also reduced: they did not penetrate inward beyond j = 12 and j = 4.

The variation of the zonally averaged flow at 1000 mb as a function of latitude and time is shown in fig. 34. As could be inferred already from fig. 32, the development followed almost the same pattern as the corresponding distribution of Huss's experiment No. 1 until the 30th day, with slight changes and a time lag of 2 days.

The highest velocity was obtained at the central latitude on the 17th day amounting to 8.4 m/sec as compared to the

corresponding value of 9.8 m/sec observed in Huss's experiment on the 15th day.

The boundaries between the central region and the region of the easterlies were smoother in the present experiment and especially during the last stages of the run (days 40-61) the boundary line has few sinuosities.

The boundary line was located between j = 5 and j = 7 in the south and between j = 9 and j = 11 in the north.

After a first maximum of the surface wind speed at the central latitude on the 17th day, a minimum of 5.0 m/sec was observed on the 20th day, followed by another maximum of 8.2 m/sec on the 23rd day. This in turn was followed by a gradual decrease down to 3.3 m/sec on the 30th day. The next maximum of 5.7 m/sec was observed on the 43rd day.

Thereafter, until the end of the run a continuous decrease of the surface wind speed was observed, the westerlies at the central latitude decreasing down to 2.8 m/sec on the 62nd day.

Easterlies with values exceeding 2.5 m/sec were observed between the 16th - 58th day, except for the 26th day.

The highest velocity attained by the easterlies, 4.7 m/sec, was observed on the 43rd day simultaneous with a maximum in the westerlies.

Local maxima in the easterlies were observed on the 17th and 23rd days - at j = 3 in the south - also coinciding in time with maxima of the westerlies indicating a strong correlation

between the intensities of the easterlies and westerlies.

The latitude-pressure distribution of the poleward eddy
momentum flux is shown in fig. 33 for 4 characteristic days.

On the 10th day the transport was towards the central
latitude at both levels and resembled the pattern obtained
by Huss for the same day.

On the 20th day trends in opposite directions appeared at
the lower reference level.

The maximum values of the fluxes directed towards the
central latitude amounted to 23.0 m^2sec^{-2}, An additional local
maximum of 20.4 m^2sec^{-2} was observed further towards the center.
On the 30th day the values observed had increased and the
maximum magnitude was 48.8 m^2sec^{-2} . Trends in opposite direc-
tions were located in the extreme South and North with the flux
directed toward the boundaries.

On the 40th day the values dropped, the maximum observed
being 28.6 m^2sec^{-2}. At the lower reference level positive
transports extended over the whole northern half of the
region with a maximum of 4.3 m^2sec^{-2}.

Symmetrical negative transports appeared in the south.

A totally different distribution was observed on the
50th day. At the upper level in the north small negative
transports were observed, maxima having dropped to the smallest
value observed during the entire run, -8.3 m^2/sec^2 —
while at the lower reference level positive transports attained
values of 11.8 m^2/sec^2 at $j = 11$.

The positive values in the North extended beyond the 500 mb level. On the 60th day a similar distribution was observed. At high latitudes in the north, momentum transports reached $-25 \text{ m}^2/\text{sec}^2$. At the lower reference level positive transports were observed in the North and negative transports in the South with $\pm 9.9 \text{ m}^2/\text{sec}^2$. Their extent was more limited, and these fluxes remained below the 500 mb level. The change with time of the various components of kinetic energy is shown in fig. 36. The zonal kinetic energy at the upper level decreased from an initial value of $536 \text{ m}^2/\text{sec}^2$ to a value of $414 \text{ m}^2/\text{sec}^2$ on the 35th day. Then the values dropped more abruptly to reach $264 \text{ m}^2/\text{sec}^2$ on the 52nd day and appeared to become stable at a value of $248 \text{ m}^2/\text{sec}^2$ for the last days of the run.

At the lower level, $\overline{K}_{750}$ first increased slightly until the 25th day and then a gradual constant decrease was observed until the end of the run.

A reversed situation was observed in the case of the eddy kinetic energy. At the upper reference level, K'_{250} increased from zero to a maximum of $156 \text{ m}^2/\text{sec}^2$ on the 21st day. After that a sharp decrease down to $60 \text{ m}^2/\text{sec}^2$ on the 25th day was observed. From this day on K'_{250} increased rapidly. On the 47th day the kinetic energy of the eddies became equal to the kinetic energy of the zonal flow. A stable value of $378 \text{ m}^2/\text{sec}^2$ was attained on the 56th day. The kinetic energy of the eddies at 750 mb increased beyond the kinetic energy of the zonal flow at this level on the 44th day.

The total kinetic energy $\bar{K} + K'$ increased during the
formative stages of the run from 280 m^2/sec^2 on the first day
to 322 m^2/sec^2 on the 21st day of the run, decreasing down
to 269 m^2/sec^2 on the 29th day. After this day continuous
growth of the total kinetic energy up to the 52nd day was
observed. On this date a value of 345 m^2/sec^2 was observed with
little further change observed until the conclusion of the run.
Various energy transformations are shown in fig. 35.

The transform $\{\bar{P}.P'\}$ attained its first marked
maximum of 7.0 X 10^{-5} kj m^{-2} sec^{-1} on the 21st day and another
pronounced maximum of 7.40 X 10^{-5} kj m^{-2} sec^{-1} towards the end
of the run, on the 47th day. The values fluctuated during the
first half of the run, dropping occasionally down to 1.4 X 10^{-5}
kj m^{-2} sec^{-1}. During the second half of the run the transformation
increased up to the maximum of the 47th day mentioned above and
then a gradual decrease with a tendency towards stabilization
near the end of the run, was observed. The conversion of heat
into zonal potential energy, $\{\bar{Q}, \bar{P}\}$, was positive, its variations
being much smoother in the present run than in Huss's experiment.
It attained its maximum on the 50th day amounting to 6 X 10^{-5}
kj m^{-2} sec^{-1} thereafter decreasing gradually until the end of
the run. Conversion of heat into eddy potential energy $\{Q', P'\}$
was negative throughout, its magnitudes being much smaller than
those of $\{\bar{Q}, \bar{P}\}$. The largest magnitude -3.25 X 10^{-5} kj $m^{-2}sec^{-1}$
was observed on the 51st day.

The transformation of zonal and eddy kinetic energy into
friction are shown in Fig. 35.

After the 42nd day $\{K', F'\}$ exceeded $\{\overline{K}, \overline{F}\}$, the first increasing and the second decreasing in time from the beginning of the run, corresponding to the behaviour of K_{250} and K'_{250}. Towards the end of the run, however, each of those transformations seemed to stabilize at a constant value.

The zonally averaged diabatic heating as a function of latitude is shown in fig. 37 for 6 representative days. On the 10th day very small heating was observed. On the 20th day the region of most intense heating was located in the south at $j = 2$ with $8 \times 10^{-2} kj \ m^{-2} sec^{-1}$. From $j = 6$ up to the central latitude cooling was observed. Due to the nature of the model no diabatic heating could result at the central latitude. Small positive values were found between $j = 8$ and $j = 10$ and cooling is observed north of $j = 10$ with a maximum at $j = 14$.

On the 30th day the value of maximum heating dropped to $6.4 \times 10^{-2} \ kj \ m^{-2} \ sec^{-1}$ and the zone of negative values in the South extended from $j = 4\frac{1}{2}$ to $j = 8$. On the 40th day the heating became more intense with maximum of $12 \times 10^{-2} kj \ m^{-2} sec^{-1}$. On the 50th day the most extreme values of cooling and heating during the entire run were observed amounting to $\pm 162 \times 10^{-2} \ m^{-2} sec^{-1}$. The zone of negative values in the south disappeared so that the entire southern half was a region of heating while the entire northern half was a region of cooling.

The same pattern persists until the end of the run, the

value of the maximum heating in the south at $j = 2$ dropping
to 14.1×10^{-2} kj m^{-2} sec^{-1} on the 60th day. We notice that
in all field variables a tendency of attenuation and smoothing
towards the end of the run can be observed.

In figs. 38, 39, 40 the zonally averaged meridional
velocities V_d at 250 mb in cm sec^{-1} and their variation
with latitude and time is shown. The mean meridional flow
was obtained from the computed values of the vertical velocity
at 500 mb. The values of the lower information level are
equal in magnitude but opposite in sign to those of the 250 mb
upper level.

Fig. 38 presents the values obtained in Exp. No. 1 with
eddy-viscosity. Until the 6th day a single Ferrel cell was
observed; from this day on, the familiar distribution of 3
cells in vertical planes emerged, with a central Ferrel cell,
surrounded by 2 direct Hadley cells.

On the 15th day values of -29 cm sec^{-1} were observed in
the center of the Ferrel cell at the central latitude. This
distribution persisted until the end of the run on the 42nd
day. The first maximum was obtained on the 15th day, a second
maximum was obtained on the 21st day, the values obtained at
the central Ferrel cell being -35 cm sec^{-1} and the third and
last maximum was observed on the 36th day with -41 cm/sec at
the central latitude.

Two points are perhaps worth being mentioned. First - the
3 cellular character persisted almost during the entire run,
except during the first 6 formative days.

Second - the maximum mean meridional velocity values
obtained in Exp. No. 1 were only about half those obtained
previously by Huss in 1965 when no lateral viscosity was
introduced. The positive values in the Hadley cells did not
exceed 3 cm sec^{-1} at most.

Fig. 39 corresponds to Exp. No. 2, including also eddy-
viscosity, in which water-vapor was introduced as an additional
field-variable.

Again until the 7th day only the indirect Ferrel cell
appeared, occupying all the region. In this experiment no
symmetry around the central latitude was expected once pre-
cipitation began.

As in Exp. I the familiar 3 cellular pattern persisted
until the end of the run. A first maximum in the central Ferrel
cell was obtained on the 15th day at the central latitude,
with -33 cm/sec, a second maximum on the 26th day, with -60 cm/sec,
and a third on the 48th day with -60 cm/sec. This was also ob-
served on the 51st day at the same latitude. From the 51st day
on, the values of the mean meridional velocity decreased, drop-
ping to a minima of -37 cm/sec on the 67th day, at the central
latitude (in the Ferrel cell). Until the 40th day the Southern
Hadley cell was larger than the Northern one, the highest
values rising up to 10 cm/sec at $j = 3$. From the 40th day on,
the northern Hadley cell became more prominent, with a maximum
velocity of +21 cm/sec on the 48th day. This was followed by
a decline until the end of the run on the 65th day. While the
values observed in this run were higher than the corresponding
values in Exp. 1, no marked asymmetry developed.

Fig. No.40 shows the pattern obtained in Experiment
No. 3, with the Matsuno time differencing scheme. In this
experiment a striking feature emerges immediately, the
persistence of the 3 cellular structure from the beginning
of the run until the end on the 62nd day. A first maxima
of -40 cm/sec was observed on the 15th day at $j = 7$ and
$j = 9$ in the central Ferrel cell. Another maximum, the
highest attained in the run, was observed on the 22nd day,
with a value of -65 cm/sec at the central latitude.

Another local maximum was observed on the 42nd day with
-44 cm/sec at the central latitude and the following, last
one, was observed on the 52nd day, with -43 cm/sec at the
central latitude. From this day until the end of the run the
magnitudes of the mean zonal meridional velocity in the central
Ferrel cell decreased, reaching on the 62nd day -32 cm/sec at
the central latitude.

The positive values in the Hadley cells never exceeded
17 cm/sec, a value attained on the 38th day. It appears thus
that the use of the Matsuno scheme results in a meridional
circulation which most closely resembles the meridional
distribution in the atmosphere, for all three experiments
described here.

In figs 41, 42, the time averaged mean geostrophic
poleward flux of sensible heat at 500, for exp. No. 1
and Exp. No. 2 is shown.

The units are in 10^{10} kj sec^{-1} cb^{-1}.

In fig. 43 the observed time averaged mean geostrophic poleward flux of sensible heat at 500 mb is given, as obtained by Mintz (1955) from daily circumpolar synoptic charts (in the Northern Hemisphere, in winter).

As the size of the grid interval used in our model is 444 km, it roughly corresponds to 4 degrees at 45°N.

Bearing this in mind, as well as the limitations of the model, the two figures can be compared . In Exp. I, the two maxima of the sensible heat flux were located at $j = 10$ and $j = 6$ respectively, with values of 3.3 X 10^{10} kj sec^{-1} cb^{-1}.

The values decreased symmetrically towards the south and the north down to 0.26 X 10^{10} kj sec^{-1} cb^{-1} at $j = 14$ and $j = 2$. At the central latitude, i.e., at $j = 8$ a value of 2.9 X 10^{10} kj sec^{-1} cb^{-1} was observed.

Fig. 42 shows the corresponding distribution obtained in Exp. No. 2. The mean geostrophic poleward flux of sensible heat at 500 mb, was time averaged between the 30th and the 60th days of the integration.

Due to the introduction of water vapor no symmetry around the central latitude was observed. A single maximum was observed at $j = 9$ of 4.5 x 10^{10} kj sec^{-1} cb^{-1}, higher by 50.% than the corresponding maximum in Exp. No. 1 .

Values decreased more sharply towards the north than towards

the south, down to a value of 0.21 X 10^{10} kj sec^{-1} cb^{-1} at
j = 14 and of 0.27 X 10^{10} kj sec^{-1} cb^{-1} at j = 2 .

Fig. 43 shows us the time-averaged mean poleward eddy
flux of sensible heat at 500 mb as observed by Mintz.

This is a wintertime average (Jan-Feb 1949). We notice
a single maximum of 3.41 X 10^{10} kj sec^{-1} cb^{-1} at 55° N.

The decrease toward the north is not more rapid than the
decrease towards the south.

In broad outline quite a good correspondence with Mintz's
observational values was obtained. It appears that in Exp. No.II
the heat flux was somewhat overestimated.

Exp. I gave realistic magnitudes but, due to the nature of
the model, presented two symmetrical maxima.

In fig. 44 the kinetic energy losses due to the use of
Matsuno's time differencing scheme are shown.

These losses were computed at the end of each day of the
integration between the 23rd and 24th time steps following the
formula:

$$ (\overline{K} + K')_{(\tau+1)} - (K, P)_{(\tau)} \Delta t - (K, F)_{(\tau)} \Delta t - (\overline{K} + K')_{(\tau)} = \text{RESIDUAL MATSUNO} $$

Until the 15th day the scheme is taking energy out from the
model, but during the 16-18th days and also during the period
of the 20th to the 26th day the model is gaining energy from
the scheme's application . The values were fluctuating between
0.3 - 0.6 m^2/sec^2 per day. Towards the end of the run this rate
decreases and negative values are again occasionally observed.
It is to be stressed that in order to gain further insight - a

much more detailed analysis is to be effectuated.

Yet, even this simple analysis shows that Matsuno's scheme has, as a rule, a damping effect, and on the whole is causing kinetic energy losses.

As an illustration we have computed daily changes of the total kinetic energy and received values, the magnitude of which was of the same order as the values above multiplied by the number of time steps per day.

C O N C L U S I O N S

Two smoothing techniques were applied in our model.

The results lead us to the conclusion that the Matsuno scheme (Euler-backward scheme) appears to give better results.

The second order diffusion term, which was first included in the model was very effective in damping waves.

The damping of the short wave lengths prevented accumulation of energy at those scales - thus stabilizing the solution - and preventing non linear instability.

Yet, the results seem to indicate that larger wave lengths were also damped. Thus, in the first experiment, no significant development was observed after the 40th day, while in the second experiment (which included a humidity field) - a steady state was attained after the 60th day. The choice of a constant coefficient of lateral diffusion ($A = 10^9$ $cm^2sec^{-1} = 10^5$ m^2sec^{-1} in our case) which is quite common in the numerical experiments simulating the general circulation, is derived from some large-scale turbulence theories by Richardson, Batchelor and Kolmogoroff.

Theory and observation indicate that the lateral diffusion coefficient has a strong dependence on the vertical coordinate, and changes also with latitude and season. As pointed out by R.F. Murgatroyd (1969) these values can range from $2 \times 10^5 - 20 \times 10^6 m^2 sec^{-1}$ depending on height, latitude and season.

Therefore a more refined and **differentiated** smoothing would be obtained if different coefficients of diffusion would be employed at the different levels of the model.

Our results, derived from the use of the second order diffusion term of the Fickian type - just open the question of the practical upper limit of any long-term numerical integration - which uses diffusion or diffusion-like terms for smoothing.

An upper-limit of several weeks (up to 60 days) imposes itself, as it seems that afterwards no significant changes can occur.

In our third experiment the Matsuno time differencing scheme was used, acting implicitly as a smoothing device.

It introduced a diffusion -like second term in time, but it had a more selective damping action - filtering mainly the high frequency waves - provided Δt is chosen so that the scheme will remain computationally stable.

As pointed by Y. Kurihara (1965) this gives a relation between Δt and the shortest wavelength we can treat.

An even more highly selective damping would presumably result with the use of a 3-level time-differencing scheme as pointed out by Kurihara (1965). This scheme is known under the name of the Modified Euler Backward Iteration.

In the third experiment, the results after a 62 days

integration show again a typical smoothing effect - and the development reached a steady state at the end of the integration period.

However in this experiment, a more realistic distribution of the field variables was obtained - and they had a higher degree of symmetry around the central latitude, which was conserved until the final stages of the integration.

Another feature was, that even-wave numbers components of the disturbance at the central latitude were highly damped. Our experiments point out that the numerical value for the eddy diffusion coefficient, 10^5 $m^2 sec^{-1}$, was somewhat too large. A confirmation of our results can be seen in A. Grammeltvelt's (1969) results for the primitive equations. He shows that using the Euler Backward time-differencing method for his model gives a decrease in available energy which corresponds to the use of the leap frog time differencing scheme with an eddy viscosity coefficient of $K = 3.6 \times 10^4$ m^2/sec.

The introduction of a more refined vertical resolution (i.e., with more vertical levels) together with more refined smoothing devices like variable eddy-diffusion coefficients - or more sophisticated time-differencing schemes - may promote more extended and physically significant long-term numerical integrations.

R E F E R E N C E S

Arakawa, A., 1966: Computational Design for Long-Term
Numerical Integration of the Equations of
Fluid Motion: Two Dimensional Incompressible
Flow. Part I. J. Comput. Phys. 1, 119-143.

Batchelor, G.K., 1950: The Application of the Similarity
Theory of Turbulence to Atmospheric Diffusion.
Quart. J.R. Met. Soc. 76, 133-146.

Csanady, G.T., 1969: Diffusion in an Ekman-Layer. J. Atm.
Sc. 26, 414-426.

Davidson, B., J.P. Friend and H. Seitz, 1966: Numerical
Models of Diffusion and Rainout of Stratospheric
Radioactive Materials. Tellus 18, 301-315.

Defant, A., 1921: Die Zirkulation der Atmospheren der
Gemassigten Breiten der Erde. Geog. Annal. 3,
209-266.

Döös, B.P., 1956: Automation of 500 mb Forecasts through
Successive Numerical Map Analyses. Tellus 8, 76-81.

Fischer, G., 1965: A Survey of Finite-Difference Approximations
to the Primitive Equations. Mon. Weath. Rev. 93, 1-10.

Gerrity, J.P., 1967: A Physical-Numerical Model for the
Prediction of Synoptic-Scale Low Cloudiness.
Mon. Weath. Rev. 95, 261-282.

Grammeltvelt, A., 1969: A Survey of Finite-Difference Schemes
for the Primitive Equations for a Barotropic
Fluid. Mon. Weath. Rev. 97, 384-404.

Houghton, D., A. Kasahara and W. Washington, 1966: Long
        Term Integration of the Barotropic Equation by
        the Lax-Wendroff Method. Mon. Weath. Rev. 94,
        141-150.

Huss, A., 1965: Numerical Studies of Planetary Circulations
        in a Model Atmosphere. Final Report under Contract
        AF-EOAR-64-76. Dept. of Met. Hebrew University,
        Jerusalem.

Huss, A., 1967: Numerical Studies of Planetary Criculations
        in a Model Atmosphere. Final Report under Contract
        AF-EOAR 65-89. Dept. of Met. Hebrew University,
        Jerusalem.

Koo-Chen-Chao, 1957: Smoothing Effect of the Turbulence Term
        in Objective Analysis and Numerical Prediction.
        Acta Met. Sinica, 28, 319-322, translated by
        AFCRL. -68-0289, Trans. No. 5, May 1968.

Kurihara, Y., 1965: On the Ure of Implicit and Iterative
        Methods for the Time Integration of the Wave Equation.
        Mon. Weath. Rev. 93, 33-46.

Leith, C.E., 1965: Numerical Simulation of the Earth's
        Atmosphere. Methods in Comput. Phys. 4, 1-28.

Lilly, D.K., 1965: On the Computational Stability of
        Numerical Solutions of Time-Dependent Non-Linear
        Geophysical Fluid Dynamics Problems. Mon. Weath.
        Rev. 93, 11-26.

Machta, L., 1954: Some Airborne Measurements of Atomic
        Debris. Bull. Amer. Met. Soc. 35, 493.

Machta, L., 1965: Some Aspects of Simulating Large Scale
        Atmospheric Mixing. Tellus 18, 355-362.

Matsuno, T., 1966: Numerical Integration of the Primitive
          Equations by a Simulated Backward Difference
          Method. J. Met. Soc. Japan, 44, 76-84.

Matsumoto, S., 1960: A Numerical Experiment Using Five-
          Level Geostrophic Model. Proc. Int. Sym. Numerical
          Weath. Prediction, Tokyo, 557-574.

Malkus, J.S. and G. Witt, 1959: The Evaluation of a Convective
          Element: A Numerical Method. The Atmosphere and Sea
          In Motion. B. Bolin, Ed., N.Y. Rockefeller Institute
          Press, 425-439.

Mintz, Y., 1955: Final Computation of the Mean Geostrophic
          Flux of Angular Momentum and of Sensible Heat in
          the Winter and Summer 1949. Final Report under
          contract AF(19)122-48. Dept. of Met. U.C.L.A. Art.5.

Mintz, Y., 1958: Design of Some Numerical General Circulation
          Experiments. Bull. Res. Counc. Israel 7G, 67-114.

Miyakoda, K., 1959: The Method of Numerical Time Integration
          of Vorticity Equation Involving Frictional Term.
          J. Met. Soc. Japan, 37, 10-21.

Murgatroyd, P.J., 1969: Estimations from Geostrophic Trajectories
          of Horizontal Diffusivity in the Mid-Latitude Troposphere
          and Lower Stratosphere. Quart. J. R. Met. Soc.95,40-63.

Phillips, N.A., 1956: The General Circulation of the Atmosphere:
          A Numerical Experiment. Quart. J.R.Met.Soc.82,123-164.

Phillips, N.A., 1959: An Example of Non-Linear Computational
          Instability. The Atmosphere and Sea in Motion, B.Bolin,
          Ed. N.Y. Rockefeller Inst. Press, 501-504.

Priestley, C.H.B., R.A. Mc Cormick and F. Pasquill, 1958: Turbulent Diffusion in the Atmosphere. W.M.O. Tech. Note, No. 24.

Priestley, C.H.B., 1959: Turbulent Transfer in the Lower Atmosphere. Univ. of Chicago Press, p. 130.

Richardson, L.F., 1926: Atmospheric Diffusion Shown on a Distance Neighbour Graph. Proc. R. Soc. Series A.110 709-737.

Shuman, F., 1955: A Method of Designing finite Difference Smoothing Operators to Meet Specifications. Tech. Memorandum J.N.W.P. Unit No. 7.

Smagorinsky, J., S. Manabe, and J. Holloway, 1965: Numerical Results from a 9 Level General Circulation Model of the Atmosphere. Mon. Weath. Rev. 93, 727-768.

Sutton, O.G., 1955: Atmospheric Turbulence. Methuen's Monographs on Physical Subjects. London.

Taylor, G.I., 1921: Diffusion by Continuous Movements. Proc. London. Math. Soc. Ser. 2, Vol. 20, 196-212.

Wien, Nielsen, A., and H. Sigtryggson, 1957: Experiments in Numerical Forecasting, Using Space-Smoothed Fields. Tellus 9, 296-312.

Williams, R.T., 1963: On the Inclusion of Lateral Friction in Numerical Prediction Models. Manuscript. U.C.L.A.
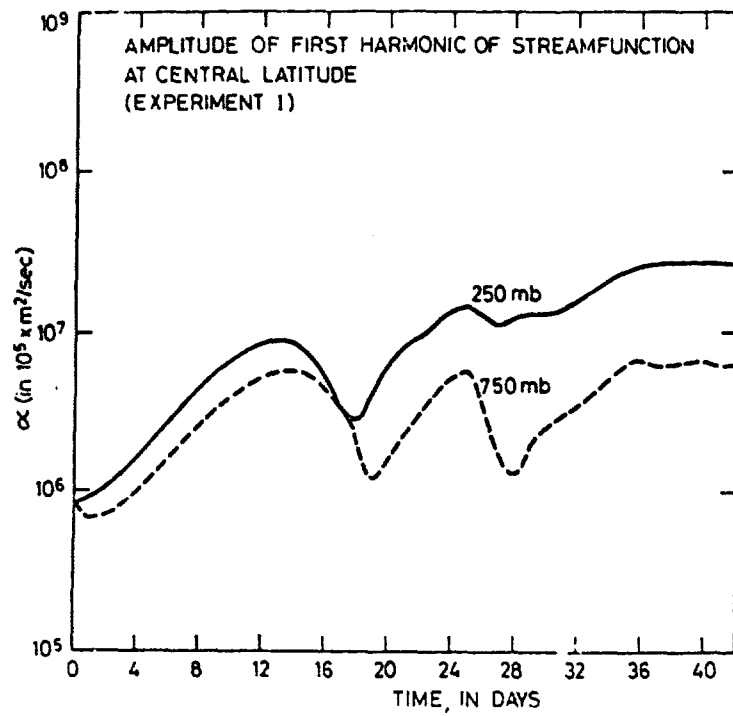
Fig. 1. Amplitudes of the first harmonics of the stream
function at the central latitude, at 250 mb and
750 mb. In m/sec.
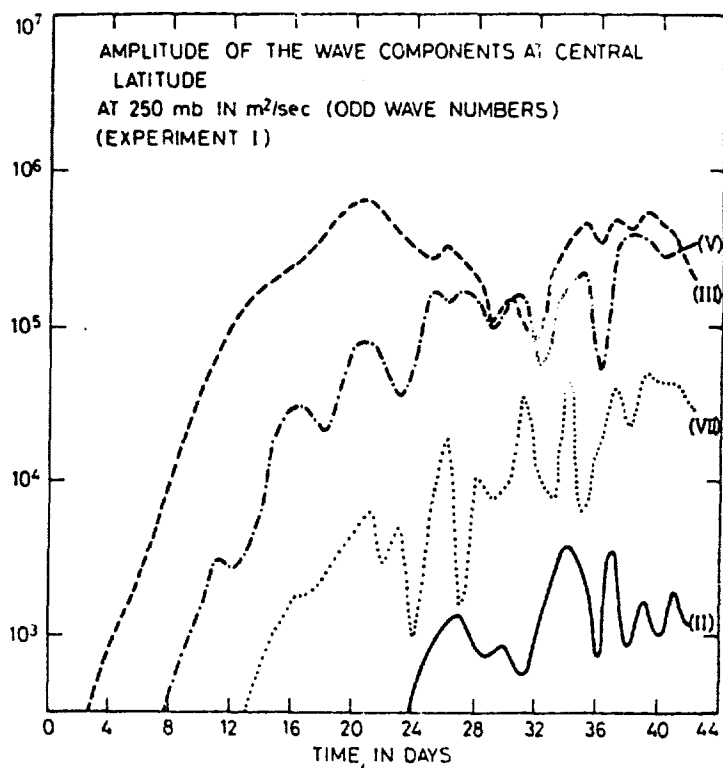
Fig. 2. Amplitudes of the odd wave numbers harmonics of the stream function at the central latitude, at the 250 mb level. In m^2/sec.
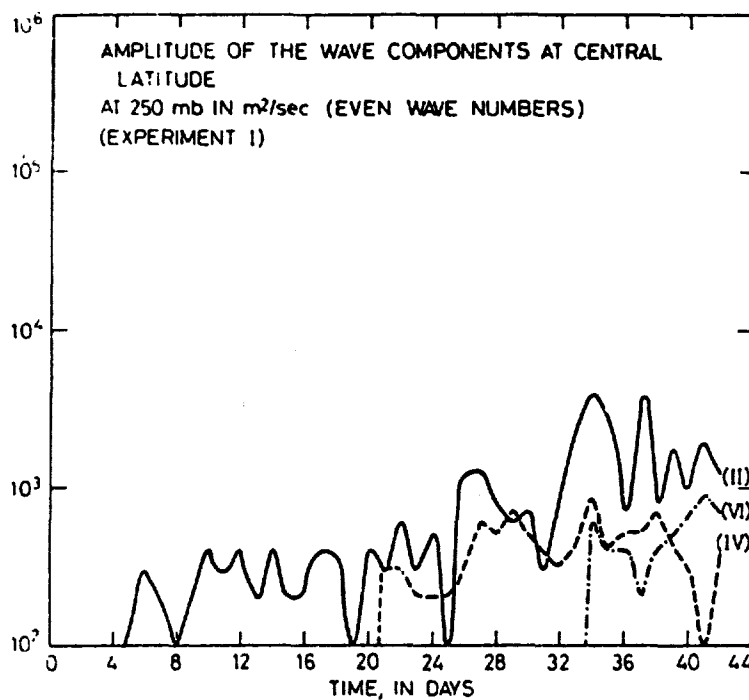
Fig. 3. Amplitudes of the even wave number harmonics
of the stream function at the central latitude,
at the 250 mb level in m^2/sec.
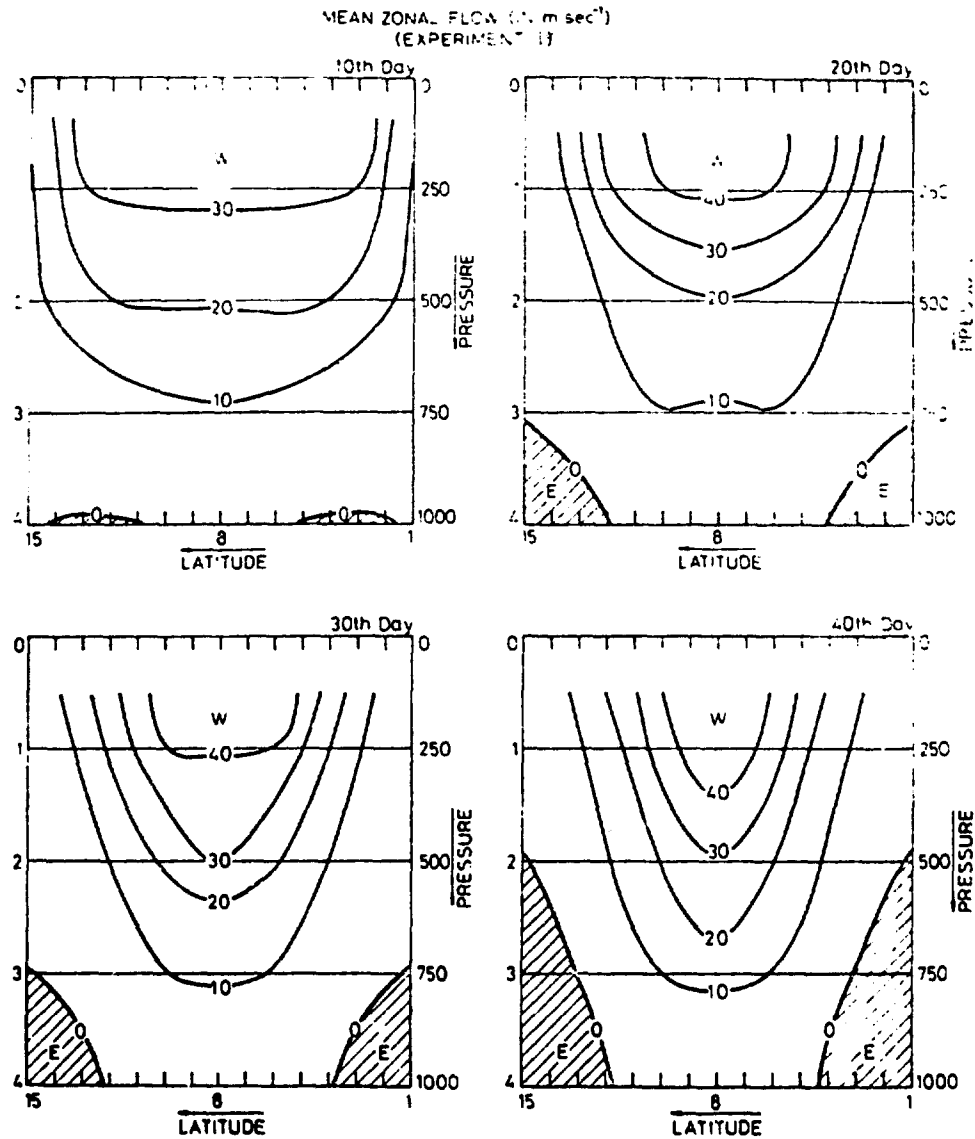
Fig. 4. The latitude pressure distribution of the zonally
averaged flow $\bar{u}$, on the 10th, 20th, 30th and
40th days of the integration.
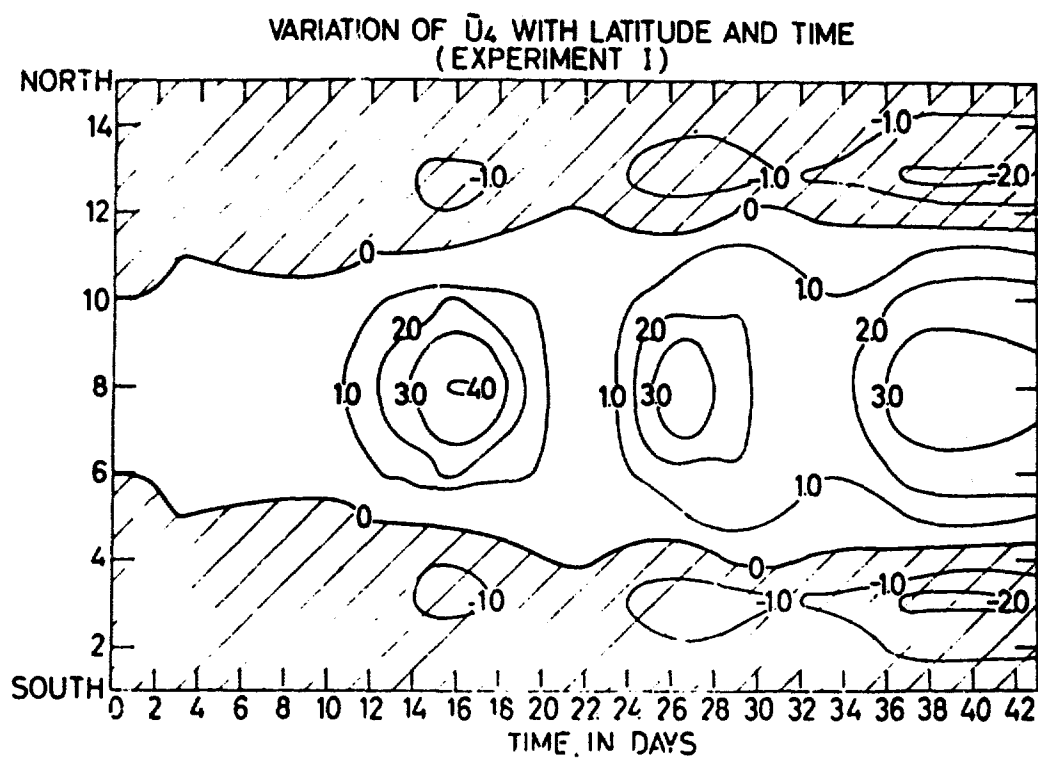
Fig. 5. The zonally averaged flow at 1000 mb as a function of latitude and time.

POLEWARD MOMENTUM FLUX (IN m²/sec²)
(EXPERIMENT I)
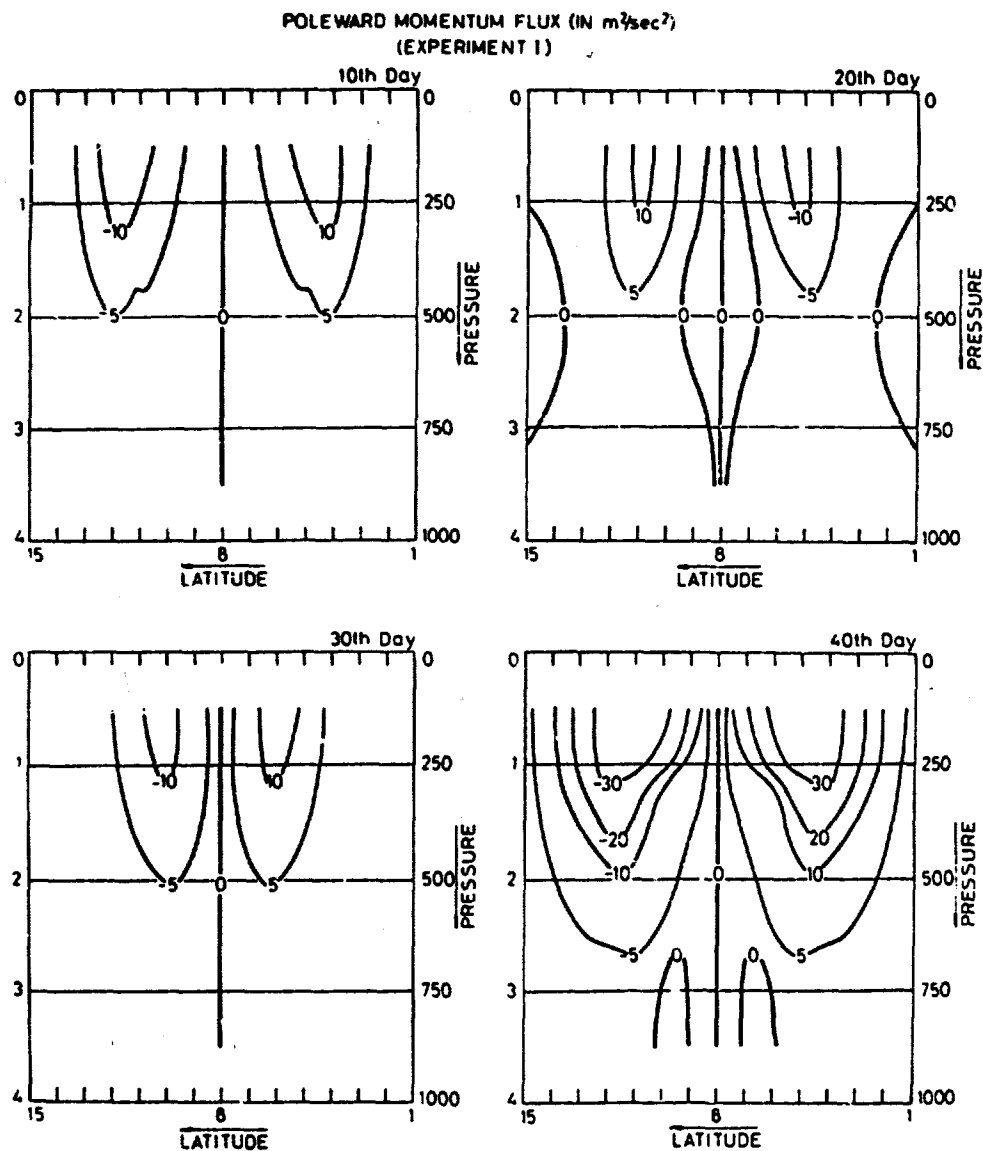
Fig. 6. The latitude pressure distribution of the zonally averaged
northward eddy transport of momentum in m²/sec² on the 10th,
20th, 30th and 40th days of the integration.
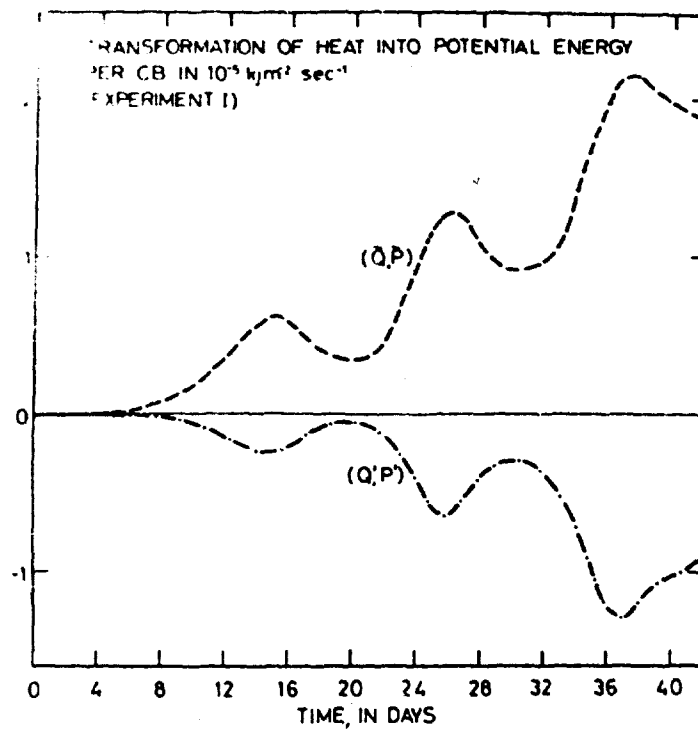
Fig. 7. Area and pressure averaged energy transformations as a function of time.
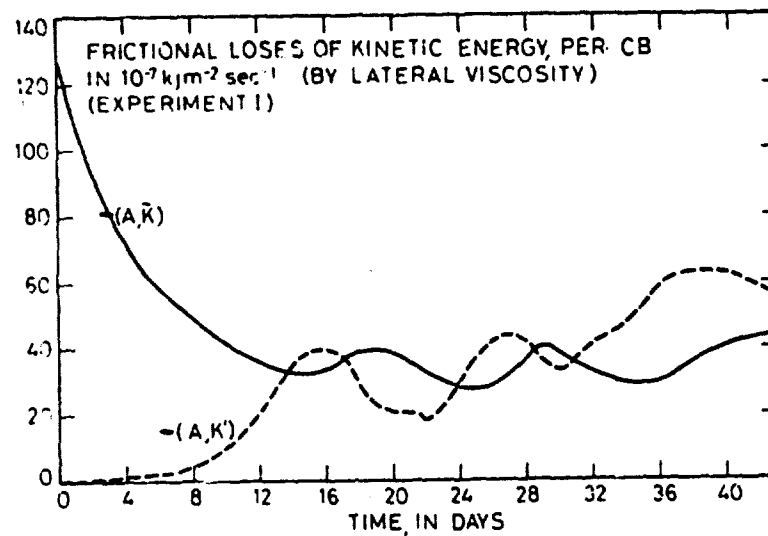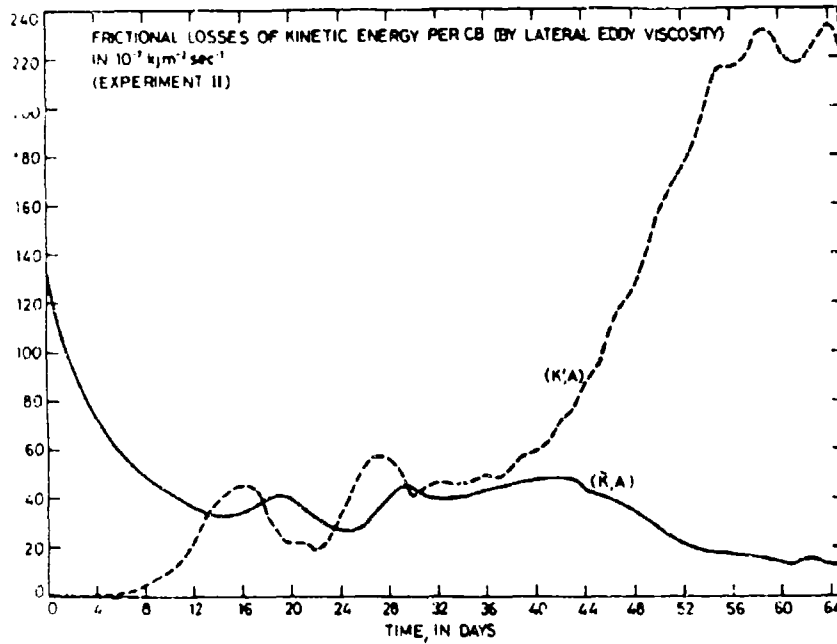

Fig. 8. The area averaged transformation of frictional losses of kinetic energy by lateral eddy viscosity as a function of time in
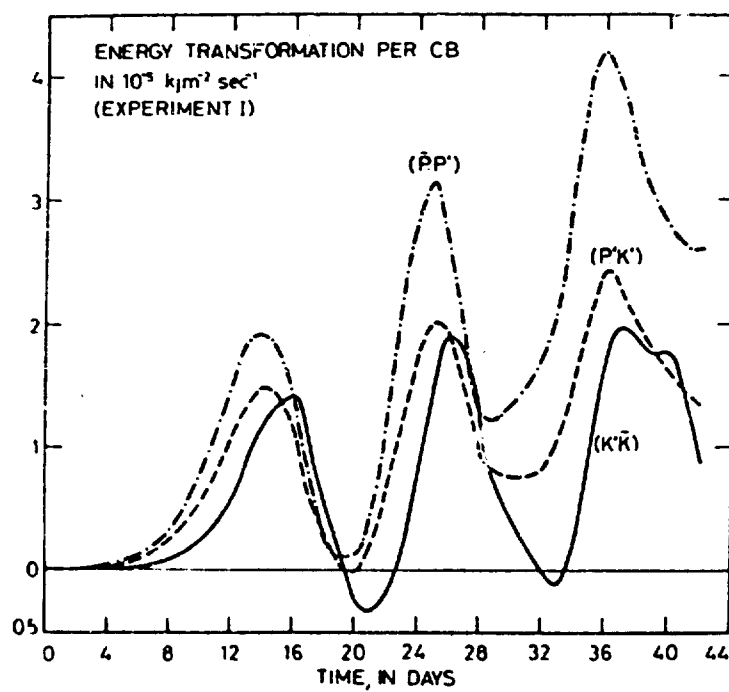
$$10^{-7} Kj \, m^{-2} sec^{-1}$$

Fig. 8. Area and pressure averaged energy transformations as a function of time, in 10^{-7} kj m^{-2} sec^{-1}.
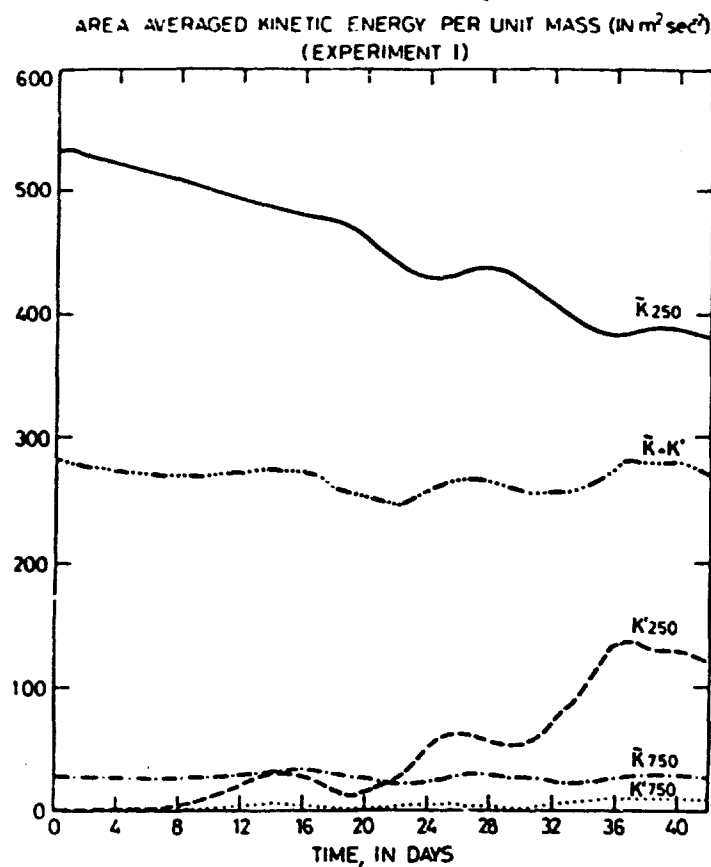
Fig. 9. Area averaged values of the kinetic energy of the
zonal flow, the eddies and of the total kinetic
energy in m^2/sec^2 as a function of time.
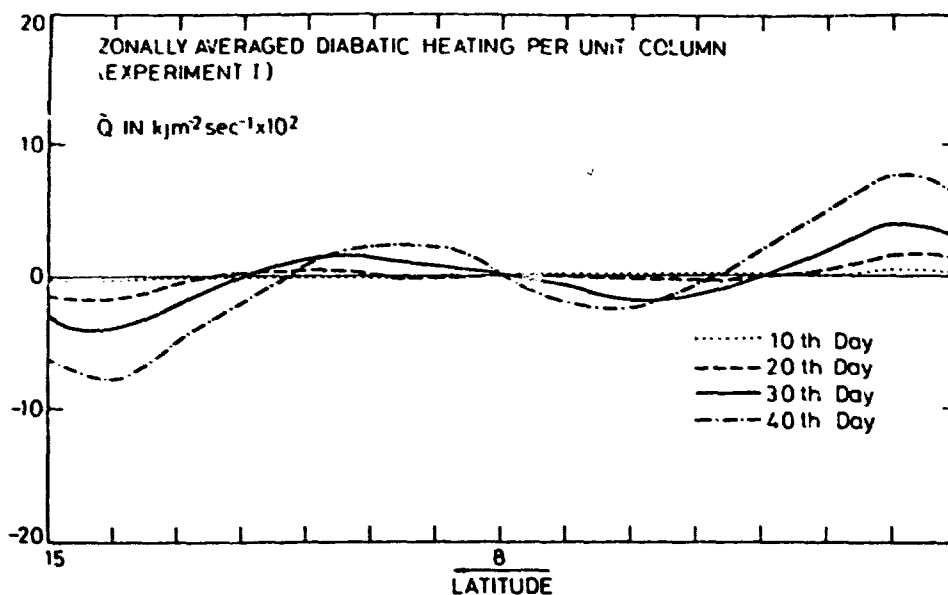
Fig. 10. Zonally averaged influx of sensible heat into unit
column, in kj m^{-2} sec^{-2}x10^2 on the 10th, 20th, 30th and
40th days of the integration.
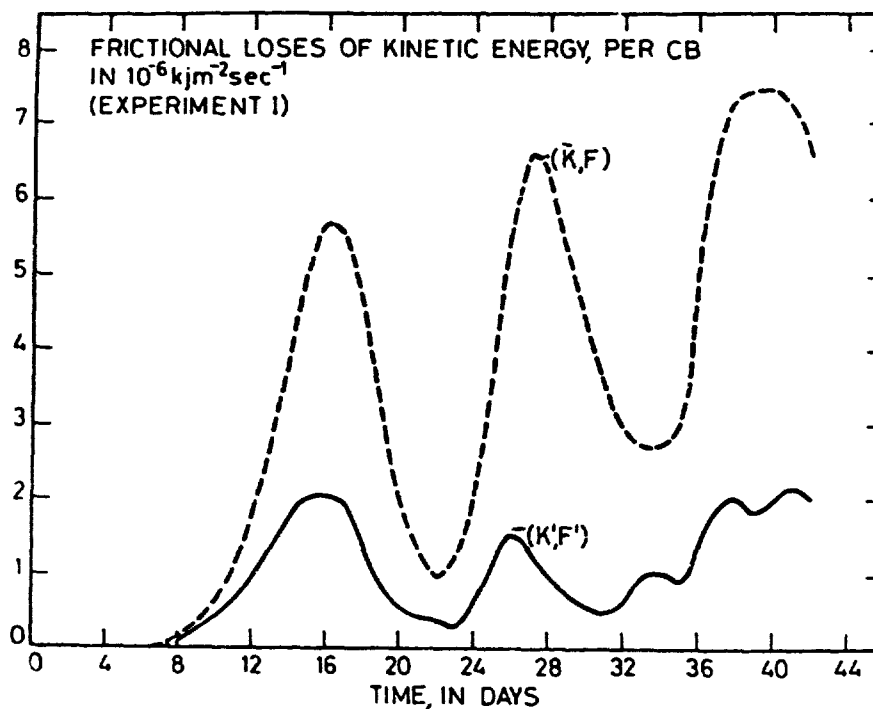
Fig. 11. Frictional losses of kinetic energy as a function
of time.
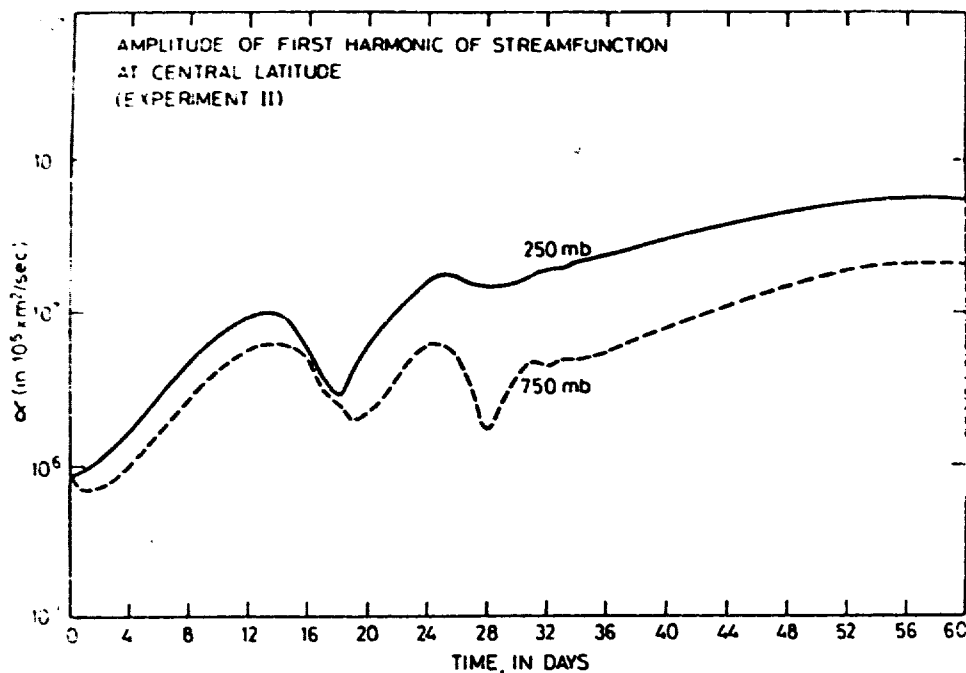
Fig. 12. Amplitudes of the first harmonics of the stream
functions at the central latitude at 250 mb and 750 mb.
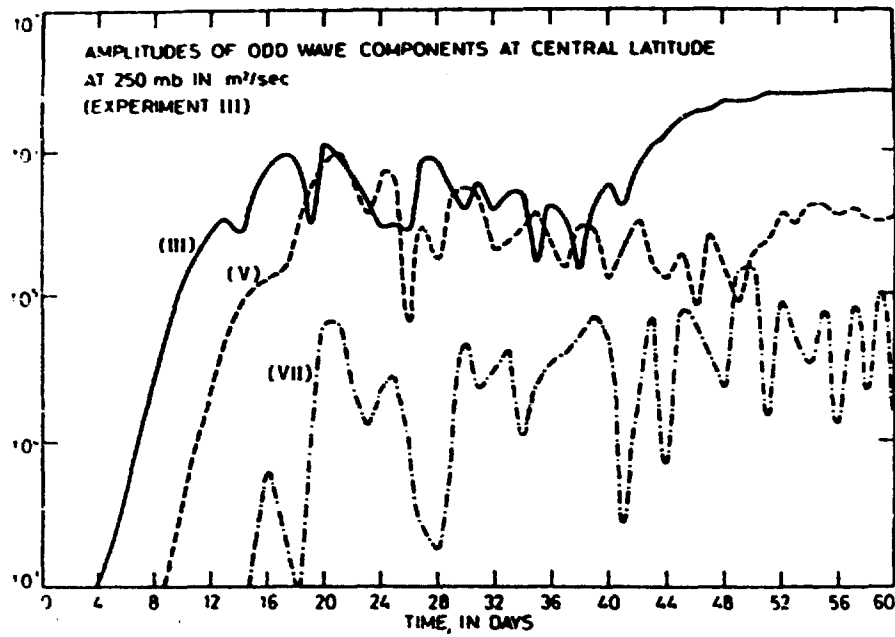In m^2/sec.
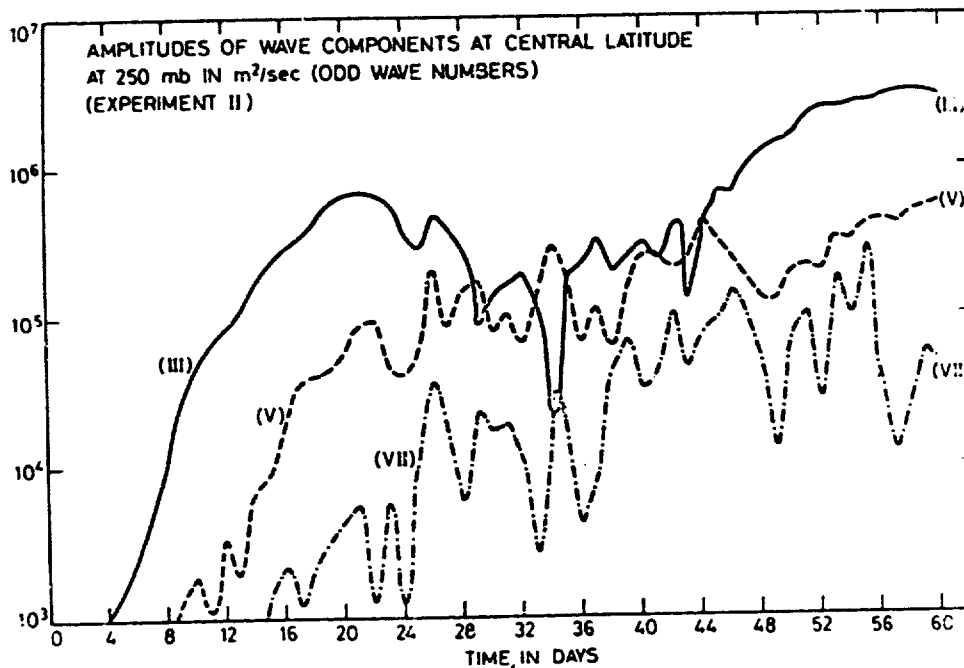
Fig. 13. Amplitudes of the odd wave numbers
harmonics of the stream function at the central
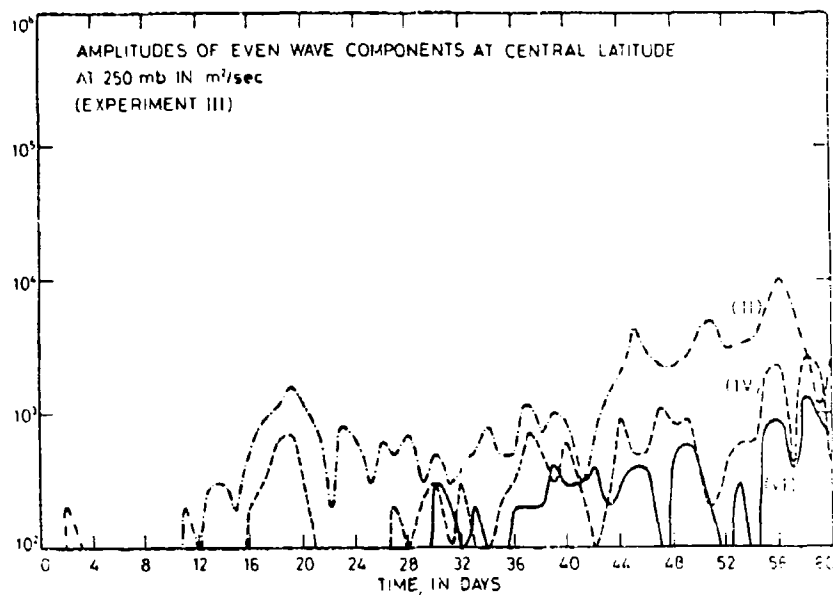latitude, at the 250 mb level in m^2/sec.
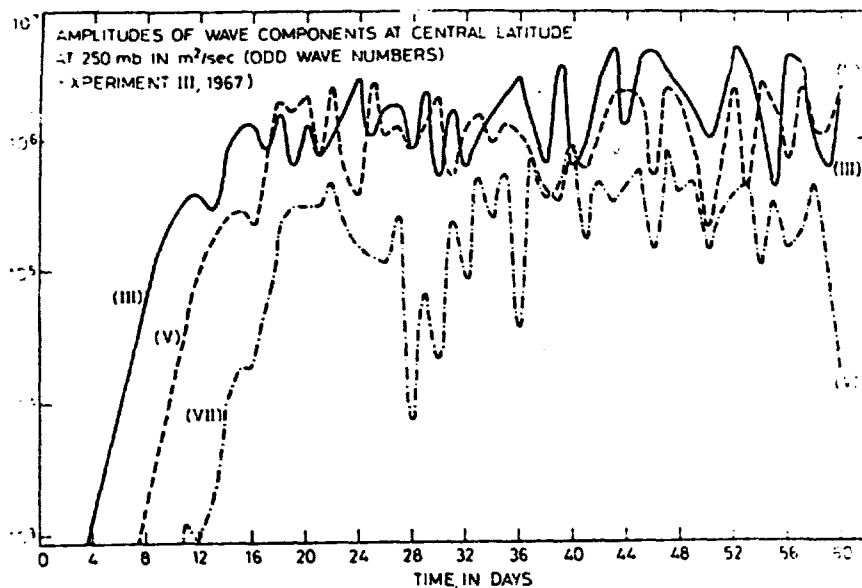
Fig. 14. Amplitu s of the odd wave numbers harmonics of
the st am function at the central latitude at
the 250 mb level. In m^2/sec. Exp. III, 1967.
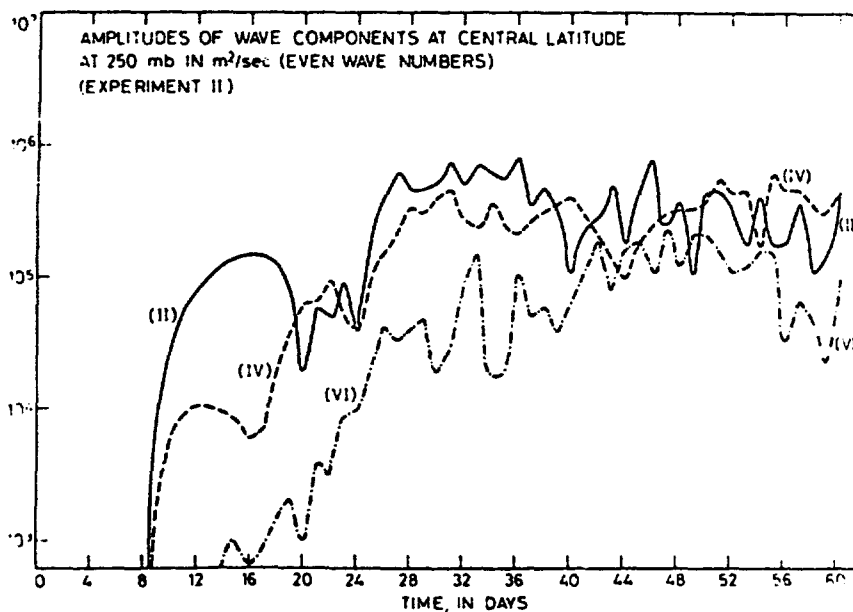
Fig. 15. Amplitudes of the even wave numbers harmonics of the
stream function at the central latitude at 250 mb level.
In m^2/sec.

AMPLITUDES OF WAVE COMPONENTS AT CENTRAL LATITUDE
AT 250 mb IN m²/sec (EVEN WAVE NUMBERS)
(EXPERIMENT III, 1967)
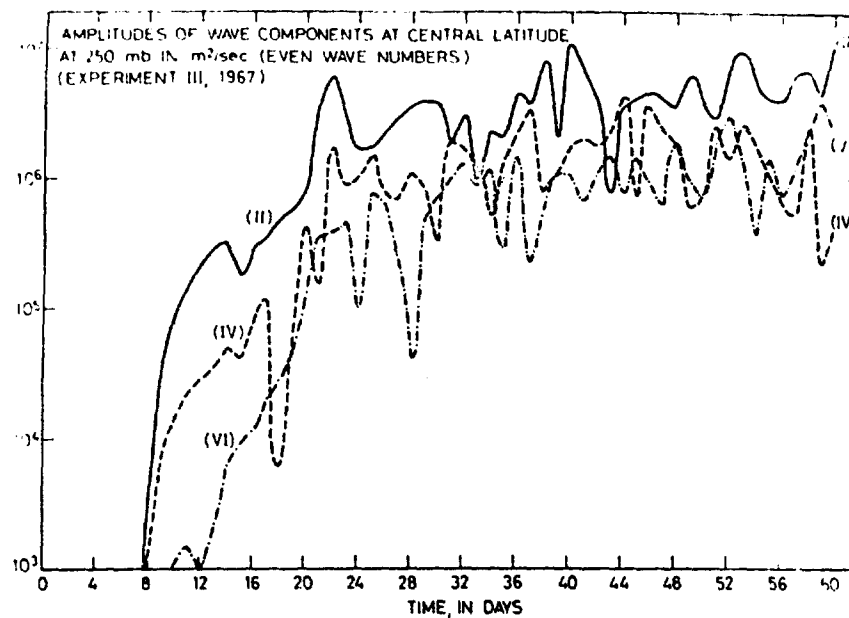
Fig. 16. Amplitudes of the even wave numbers harmonics of the stream
function in m^2/sec (Exp. III. 1967).
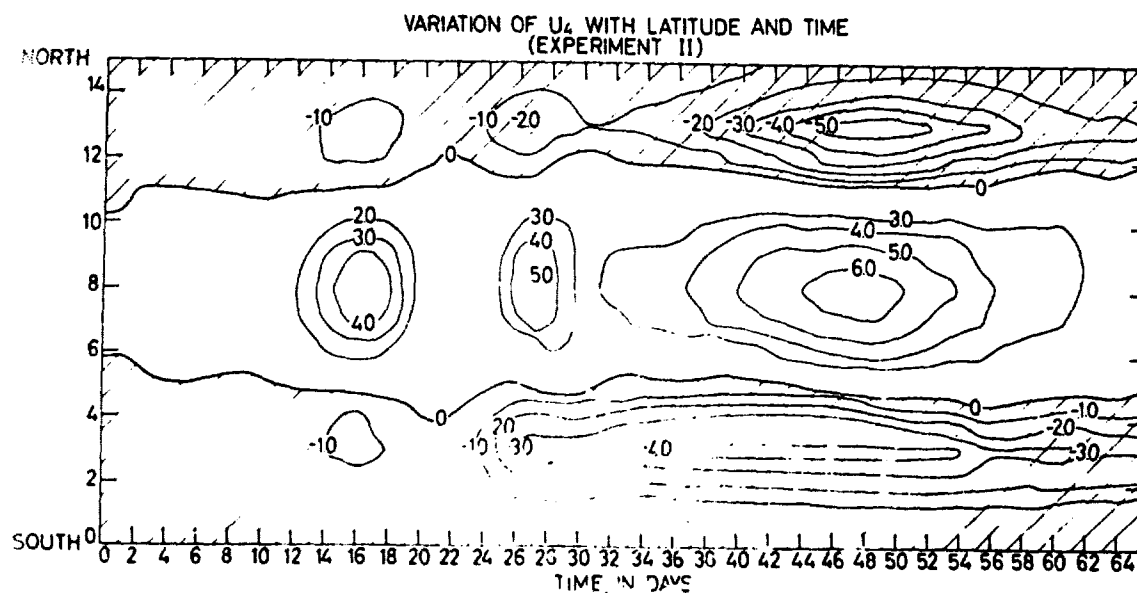
VARIATION OF U_4 WITH LATITUDE AND TIME
(EXPERIMENT II)

Fig. 17. The zonally averaged flow at 1000 mb as a function of latitude
and time.

MEAN ZONAL FLOW (IN m.sec⁻¹)
(EXPERIMENT II)
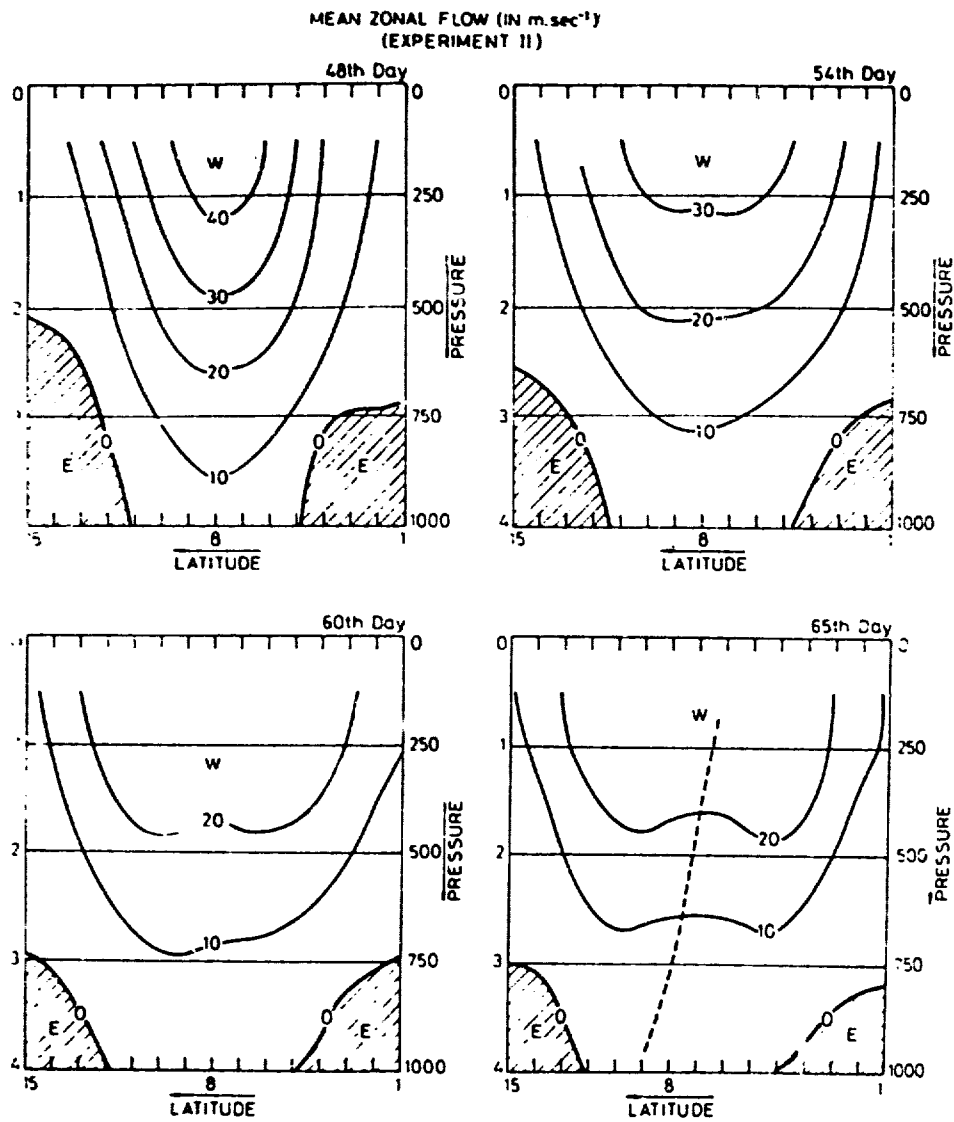
Fig. 18. The latitude pressure distribution of the zonally averaged
flow $\tilde{u}$ on the 48th, 54th, 60th and 65th days of the inte-
gration.

POLEWARD MOMENTUM FLUX (IN m²/sec²)
(EXPERIMENT II)
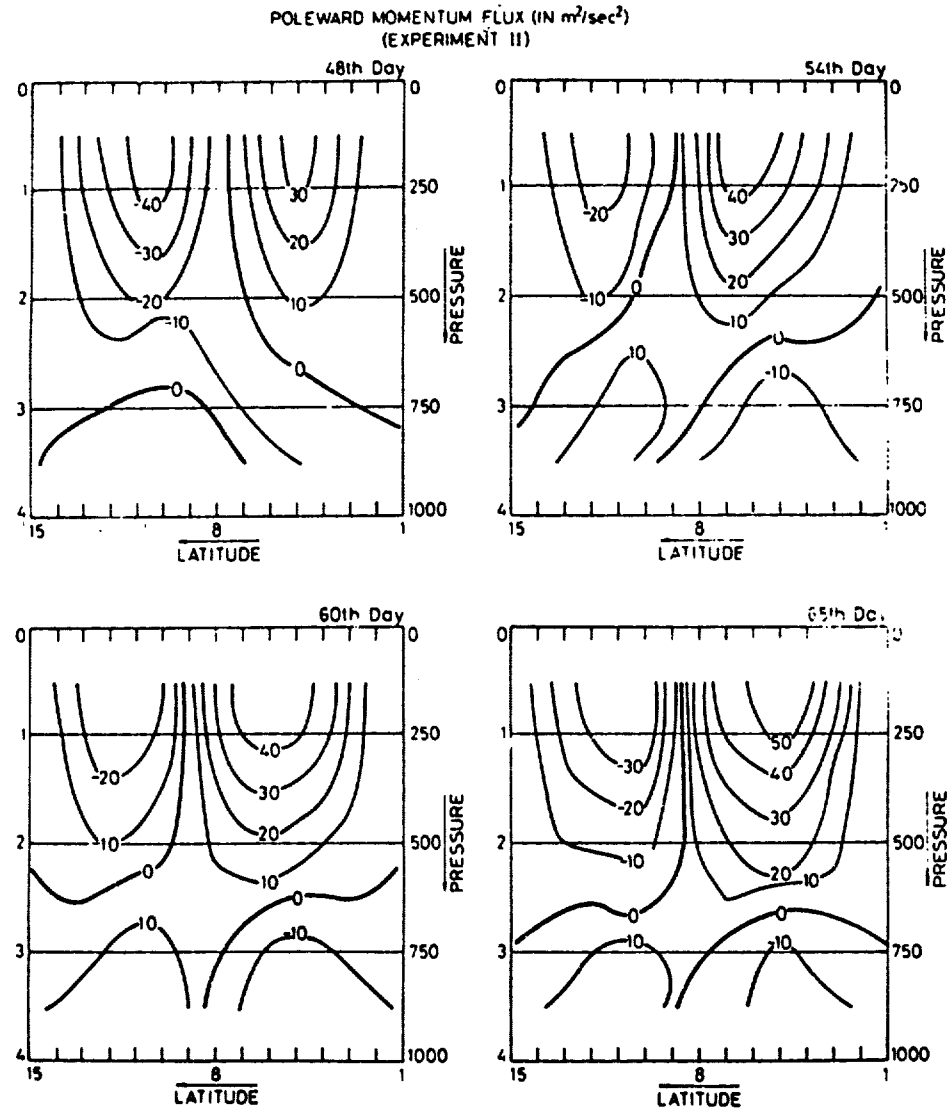
Fig. 19. The latitude pressure distribution of the zonally
averaged poleward eddy transport of momentum, in
m²/sec² on the 48th, 54th, 60th and 65th days of
the integration.
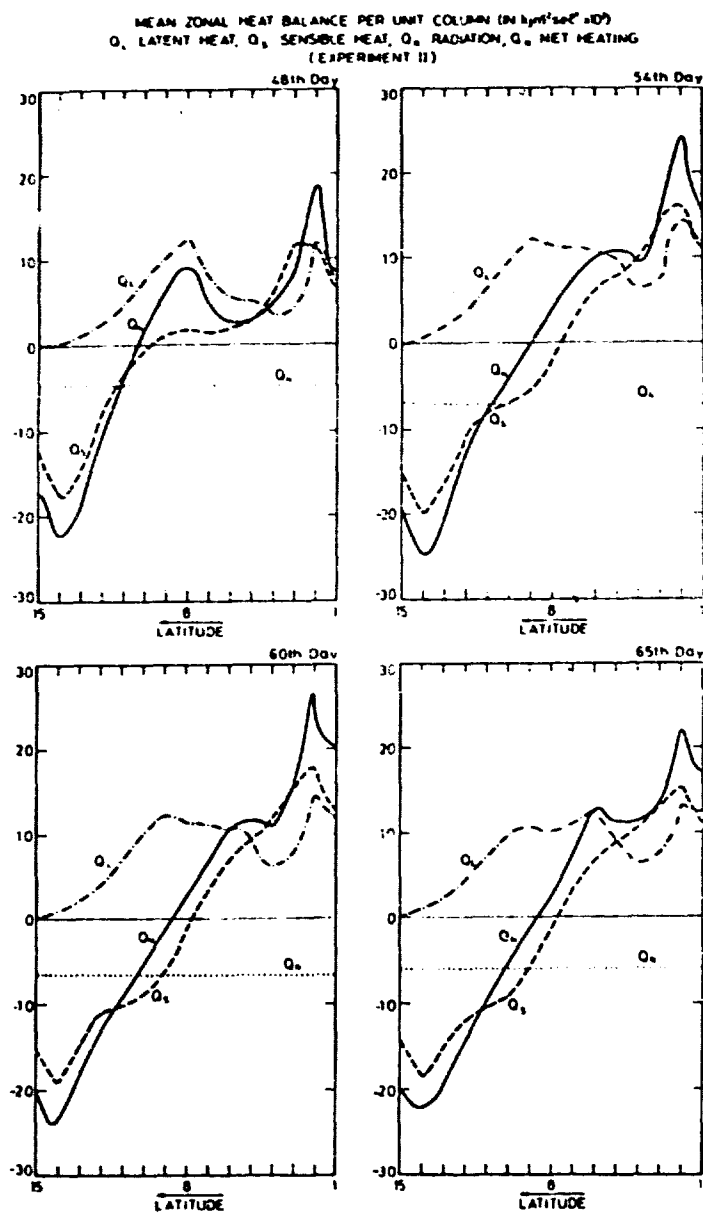
Fig. 20. Zonally averaged heat balance components per
unit column on the 48th, 54th, 60th and 65th days of
the integration.

AREA AVERAGED KINETIC ENERGY PER UNIT MASS (IN $m^2 sec^2$)
(EXPERIMENT II)
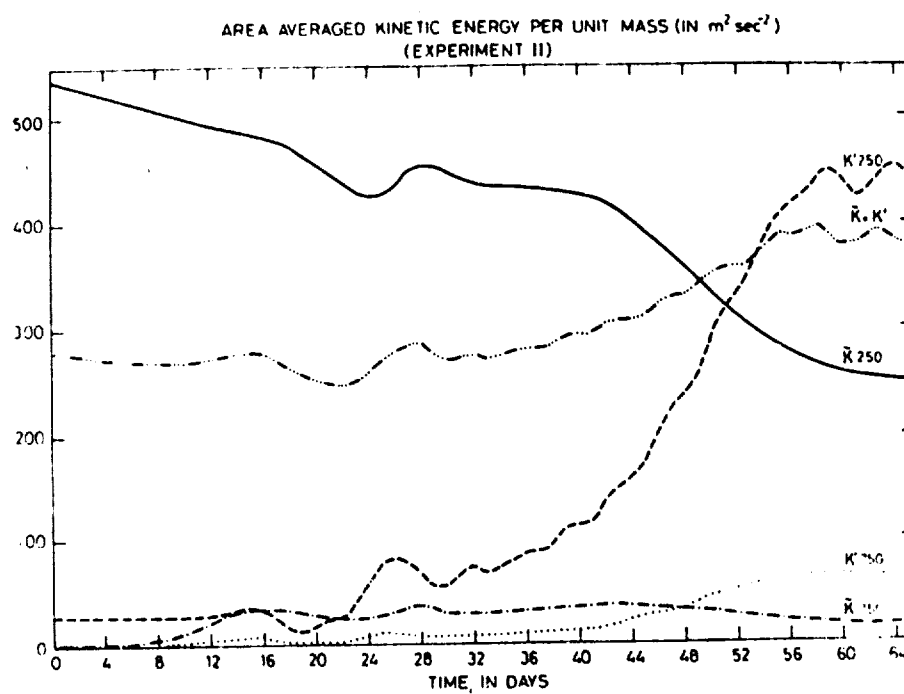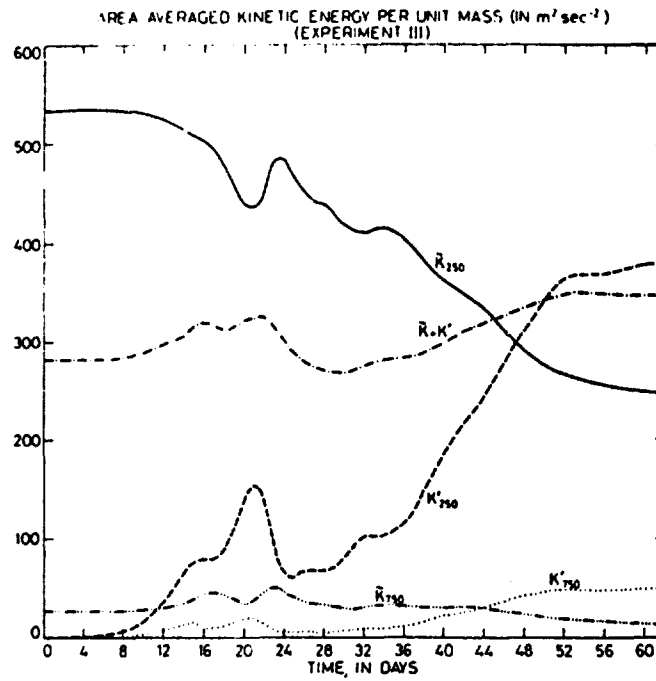

Fig. 21.   Area averaged values of the kinetic energy of the
zonal flow, the eddies, and of the total kinetic
energy, in m^2/sec^2 as a function of time.
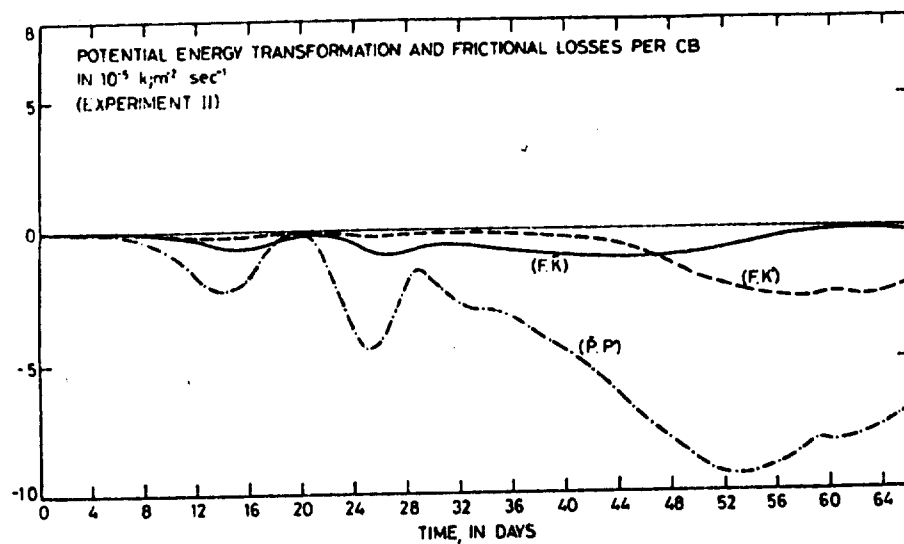
Fig. 22. The area averaged transformation of zonal potential
energy into eddy potential energy and of the frictional
losses, as a function of time
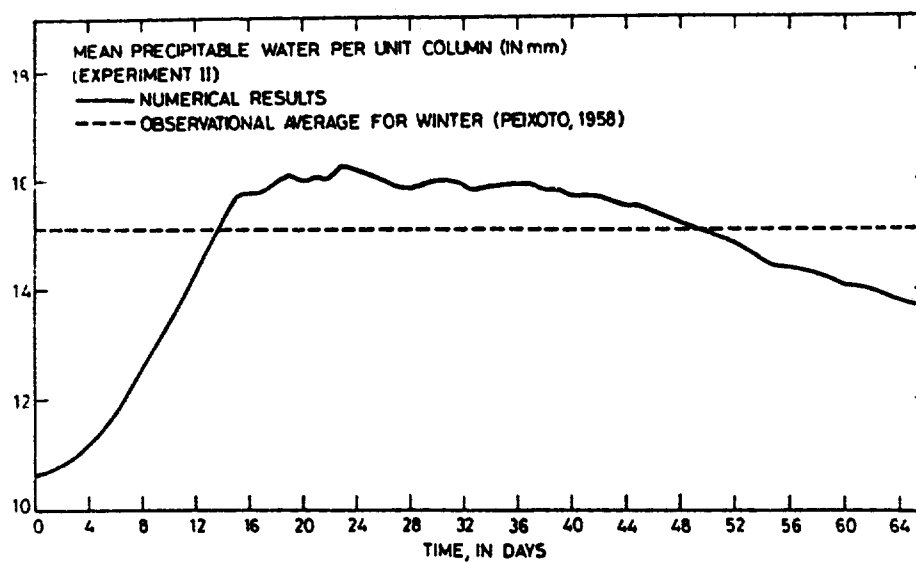
Fig. 23. Area averaged precipitable water content per unit
column in run Ⅱ, as a function of time.
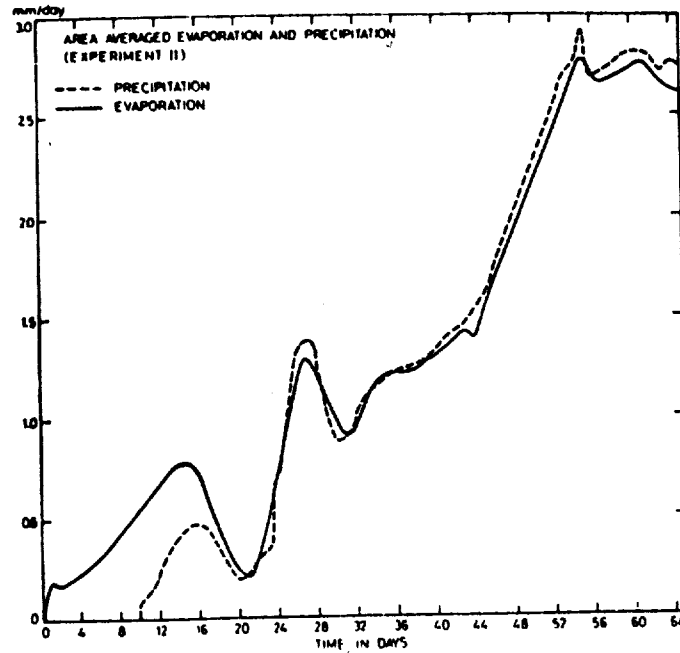
Fig. 24. Area averaged precipitation (dashed line) and
evaporation (solid line)in mm per day,   as a
function of time.
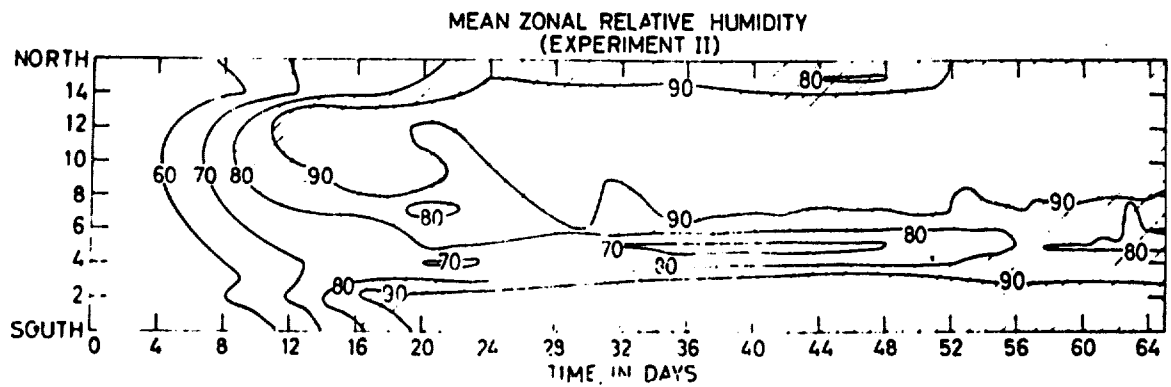
Fig. 25. Zonally averaged relative humidity as a function of
latitude and time.
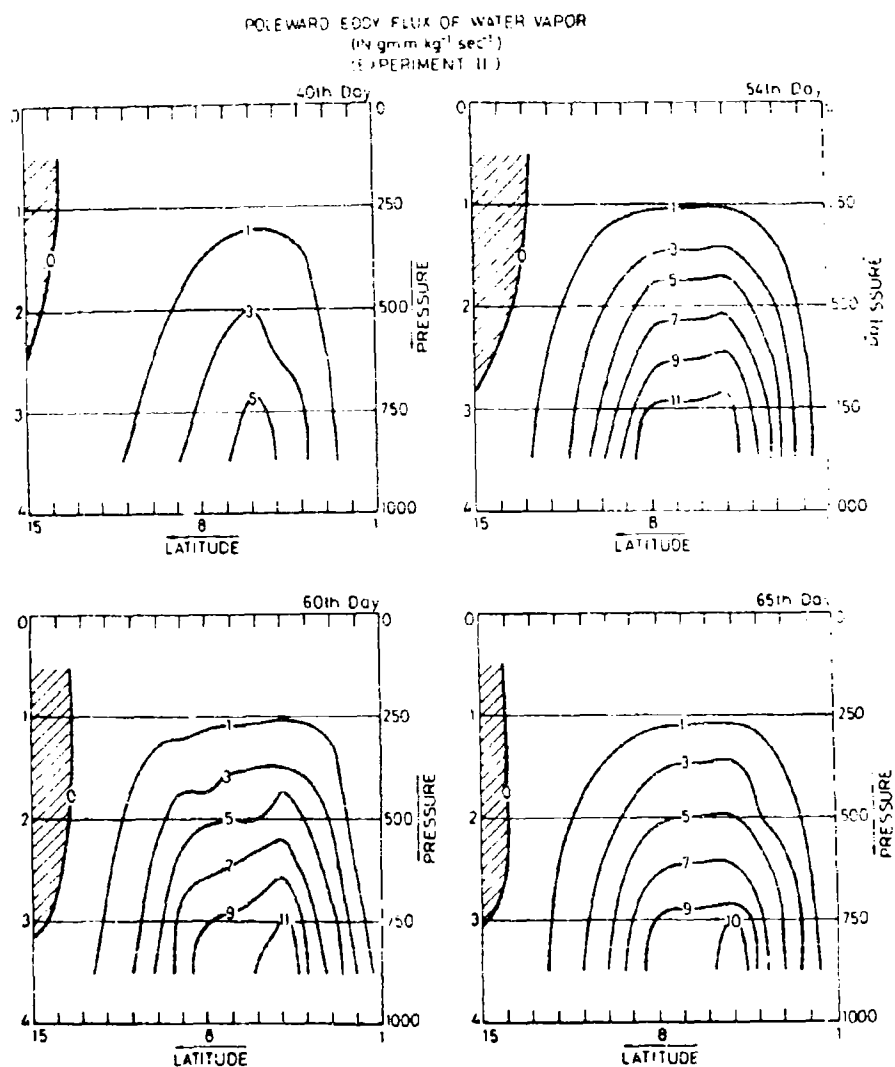
Fig. 26. The latitude pressure distribution of the zonally averaged
poleward eddy flux of water vapor in gm.m.kg^{-1}.sec^{-1} on the
40th, 54th, 60th and 65th days of the integration.

Fig. 27. The area averaged transformation of frictional losses of kinetic energy by lateral eddy viscosity as a function of time in $10^{-7} \text{kjm}^{-2} \text{sec}^{-1}$.
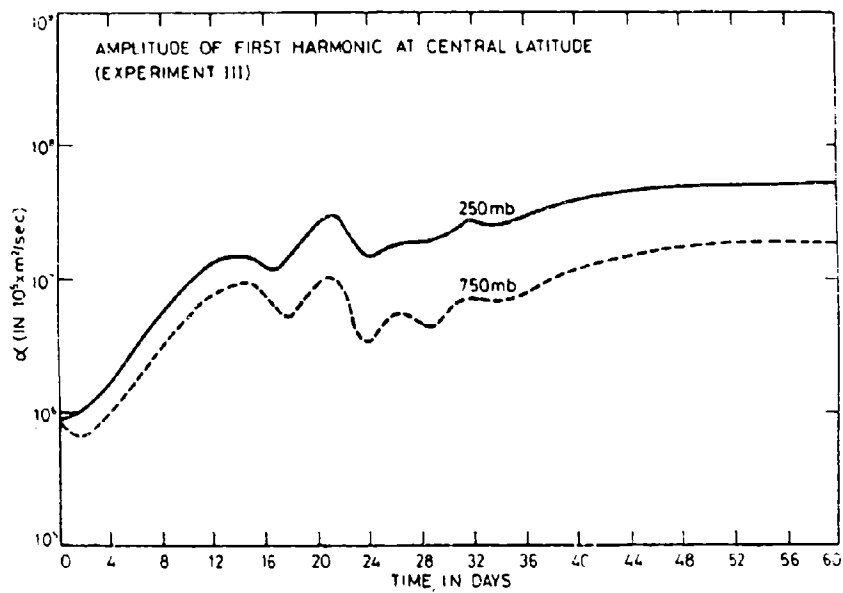
Fig. 29. Amplitudes of the first harmonics of the
          streamfunction at the central latitude at 250 mb
          and 750 mb. In m²/sec.

Fig. 30. Amplitudes of odd wave numbers harmonics of the stream function at the central latitude at 250 mb level. In m²/sec.

Fig. 31. Amplitudes of the even numbers harmonics of the stream
function at the central latitude at 250 mb level in
m^2/sec.
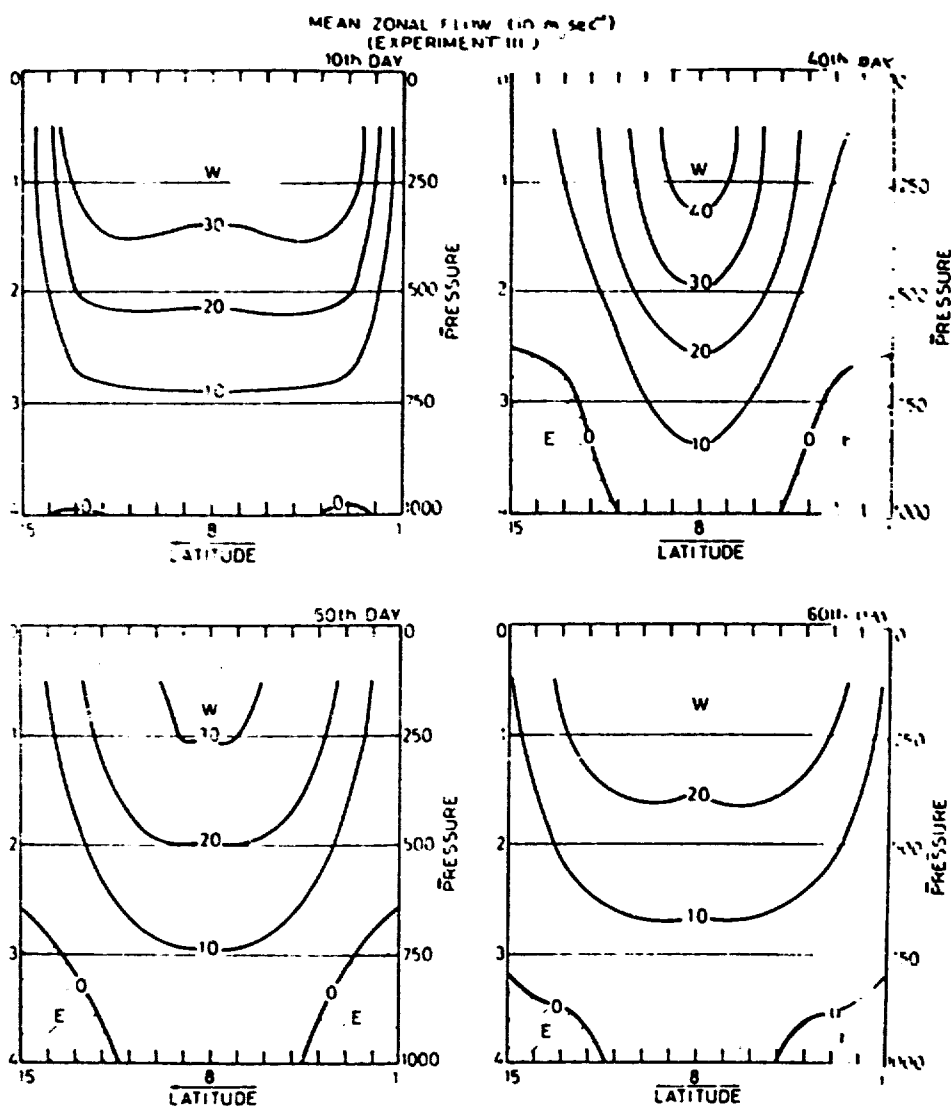
Fig. 32. The latitude pressure distribution of the zonally
averaged flow $\bar{u}$ on the 10th, 40th, 50th and 60th
day of the integration.
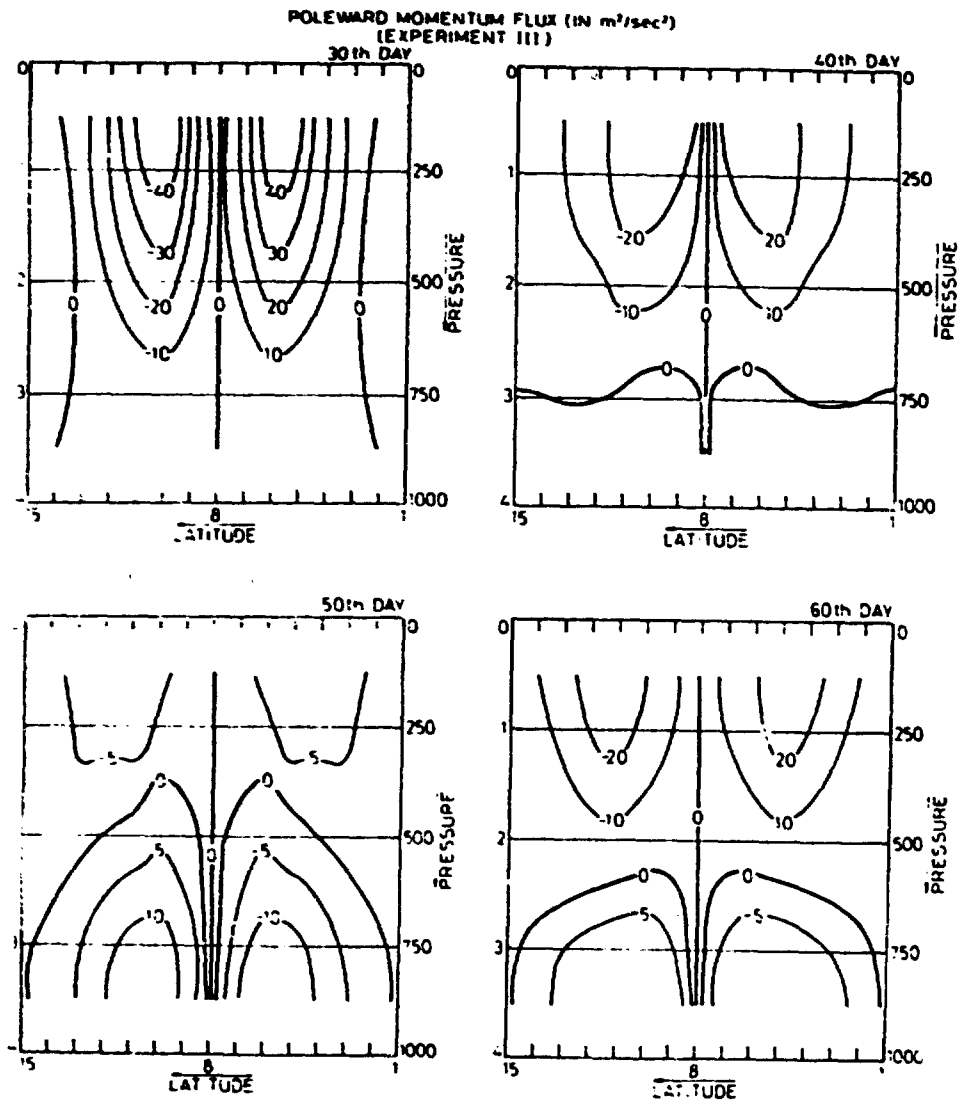
Fig. 33. The latitude pressure distribution of the zonally averaged northward eddy transport of momentum in m^2/sec^2 on the 30th, 40th, 50th and 60th days of the integration.
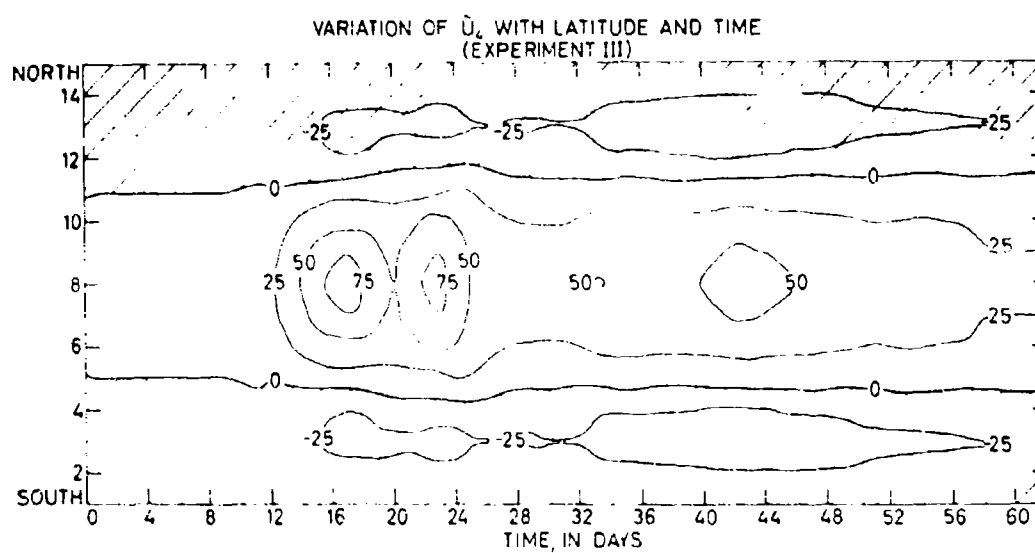
Fig. 34. The zonally averaged flow at 1000 mb as a
function of latitude and time.
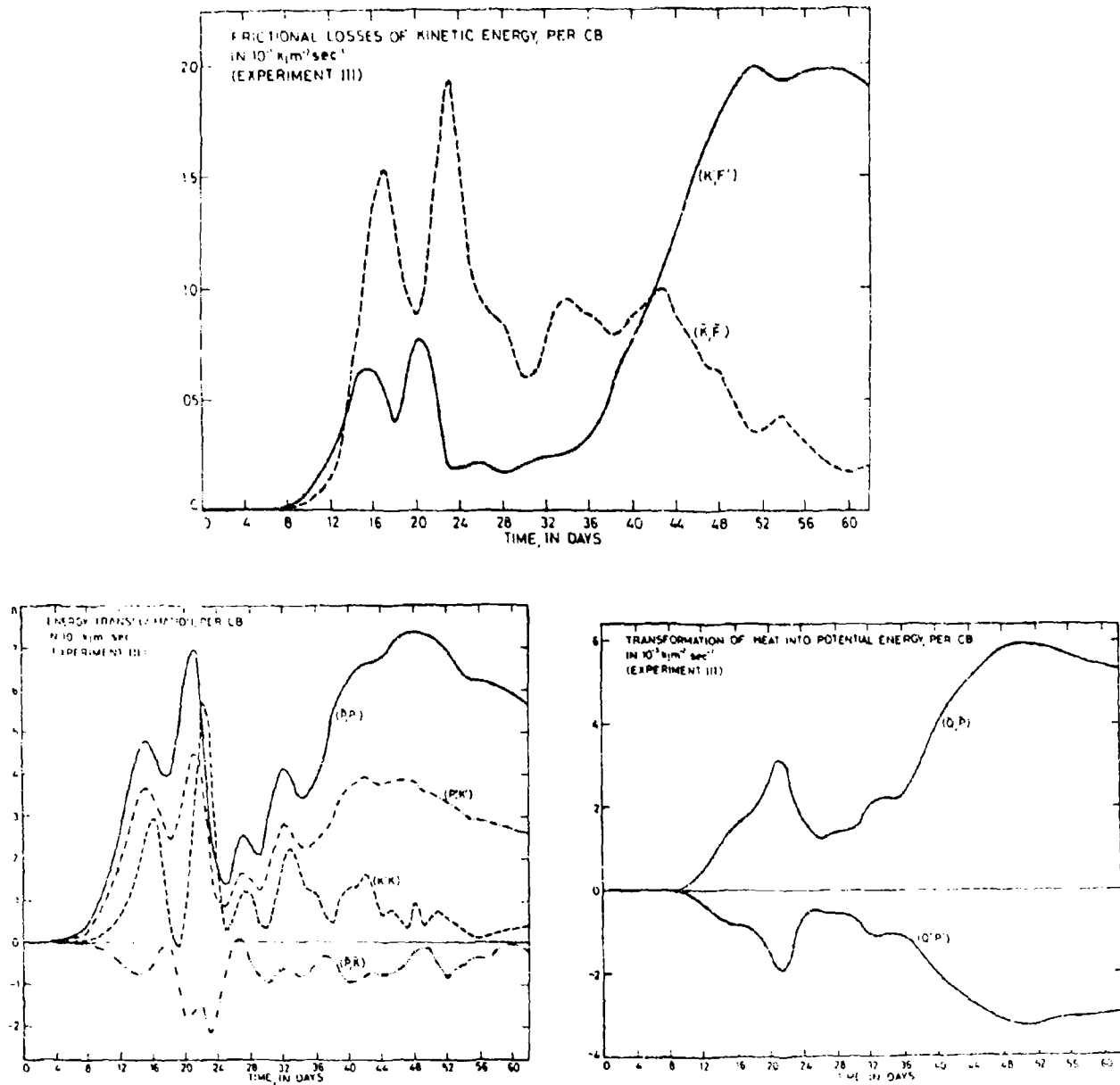
Fig. 35. Area and pressure averaged energy transformations
including frictional losses as a function of time.

Rig. 36. Area averaged values of the kinetic energy of
the zonal flow, the eddies and of the total
kinetic energy, in m²/sec² as a function of time.
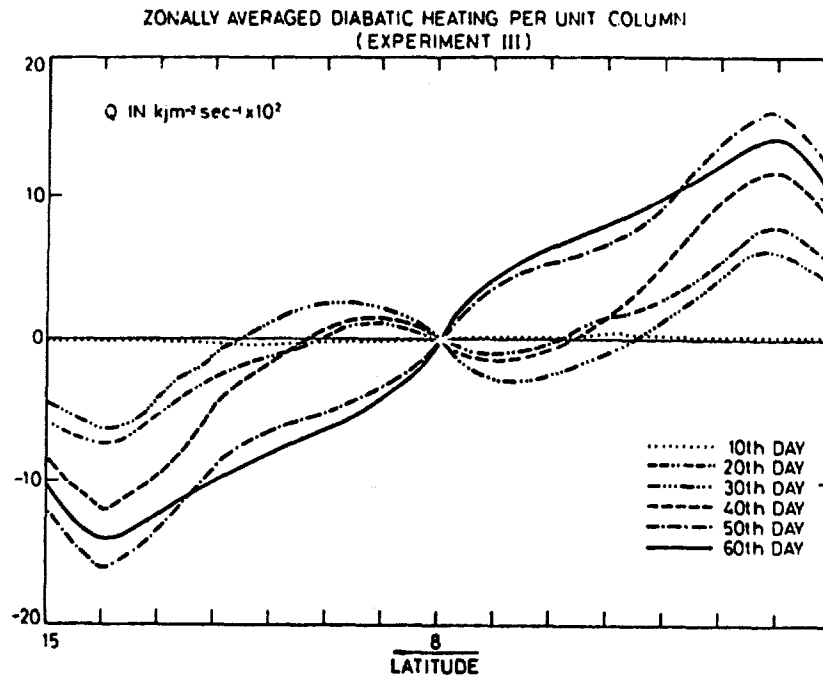
Fig. 37. Zonally averaged influx of sensible heat into unit
column in kjm^{-2}sec^{-1} x 10^2 on the 10th, 20th, 30th,
40th, 50th and 60th days of the integration.

VARIATION OF $\bar{V}_{d,l}$ (IN cm sec^{-1}) WITH LATITUDE AND TIME (EXP. I)

Fig. 38.   The zonally averaged meridional velocity at 250 mb in cm.sec^{-1} (Exp. I).
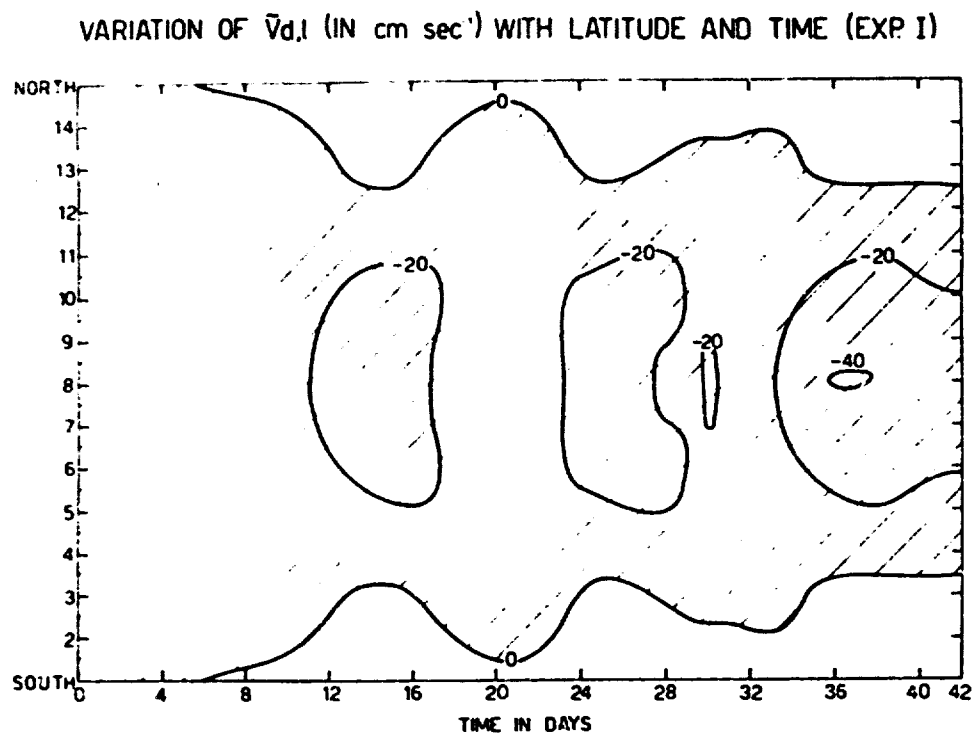
VARIATION OF $\bar{V}$d,I (IN cm sec⁻¹)WITH LATITUDE AND TIME (EXP II)

Fig. 39. The zonally averaged meridional velocity at 250 mb in
cm.sec^{-1}(Exp.II).
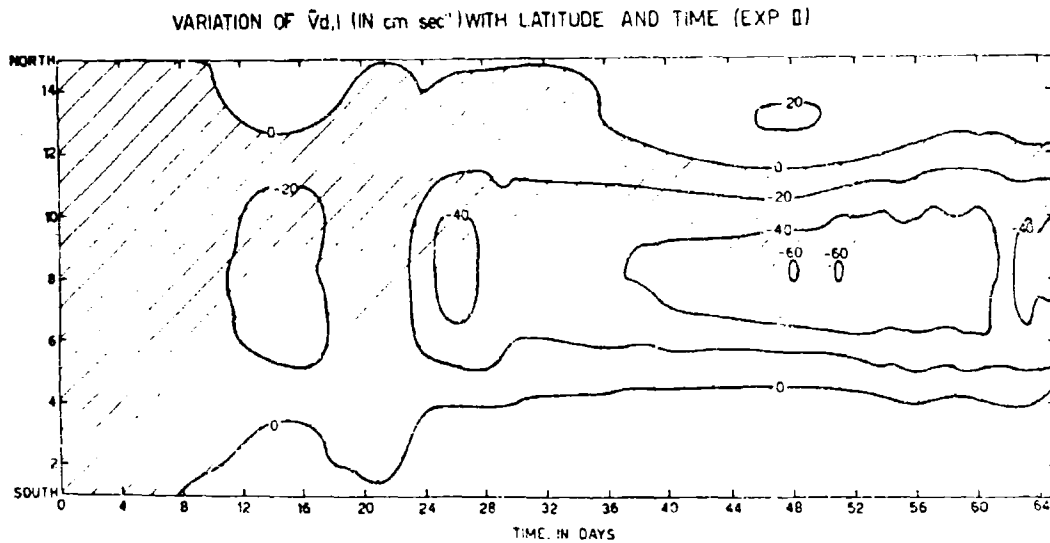
VARIATION OF V̄d,ı (IN cm sec⁻¹) WITH LATITUDE AND TIME (EXP. III)
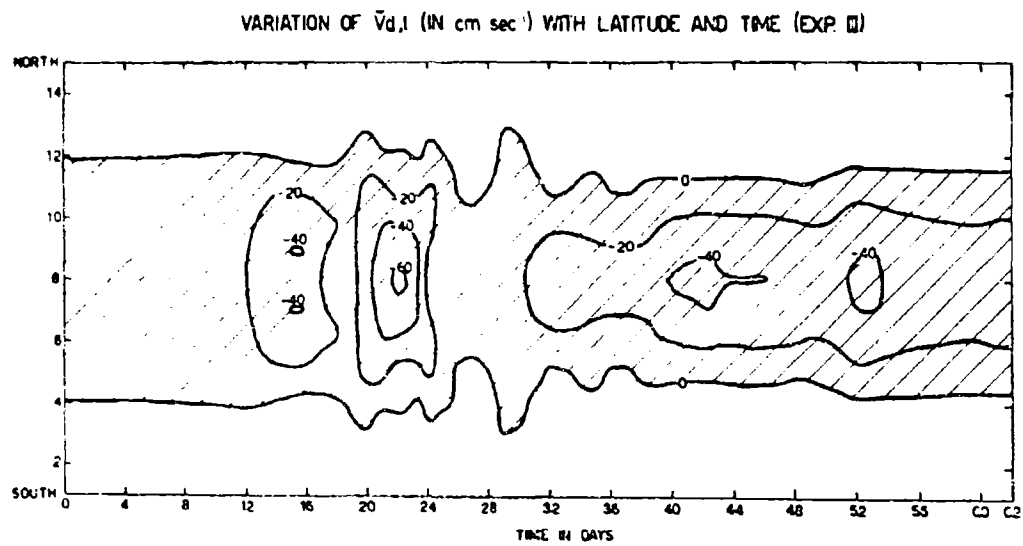
Fig. 40. The zonally averaged meridional velocity at 250 mb in
cm.sec^{-1}(Exp.III).
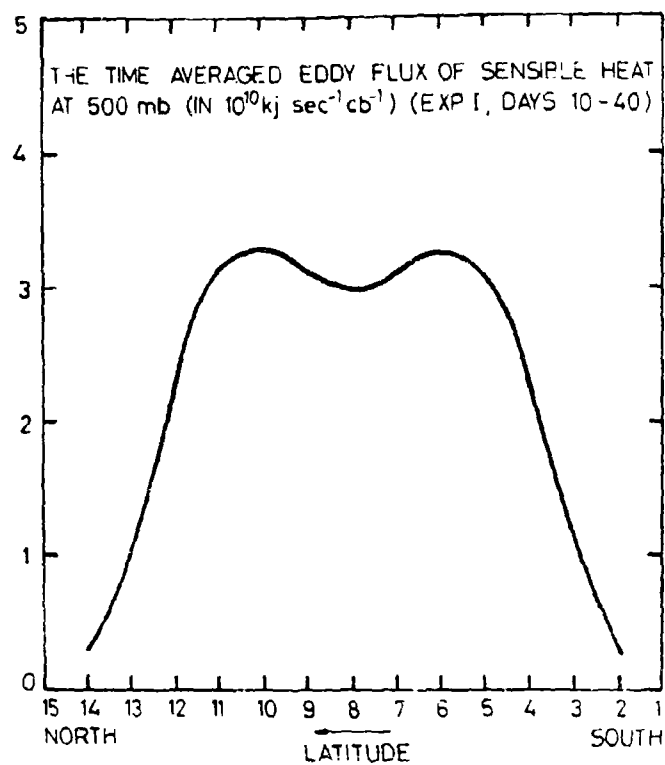
Fig. 41. The time averaged mean geostrophic poleward flux of sensible heat at 500 mb. Exp. No. 1.
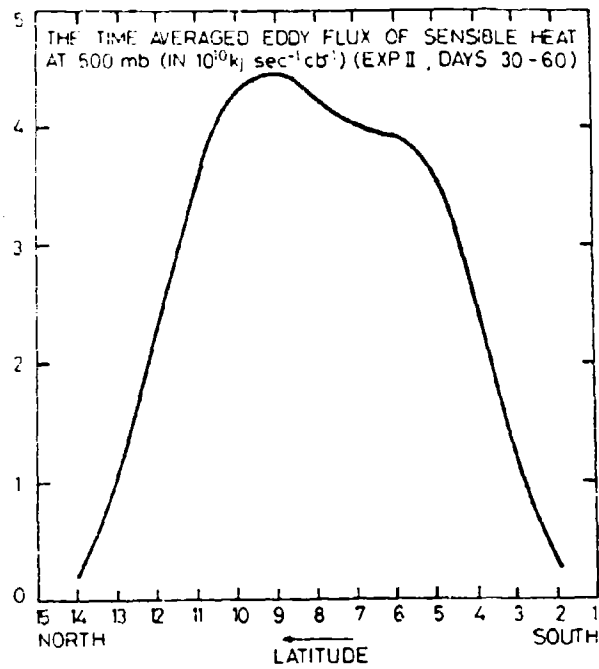
Fig. 42. The time averaged mean geostrophic poleward flux of
sensible heat at 500 mb. Exp. No. 2.
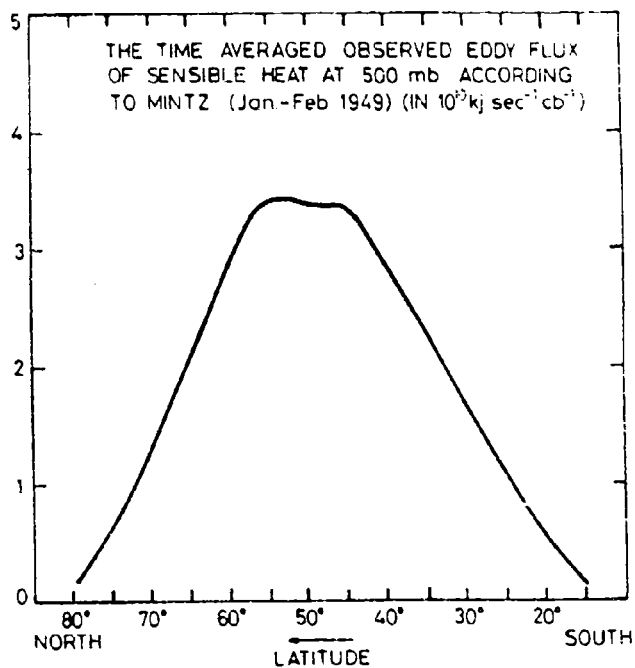
Fig. 43.   The time averaged observed mean geostrophic poleward
flux of sensible heat at 500 mb -according to Mintz.
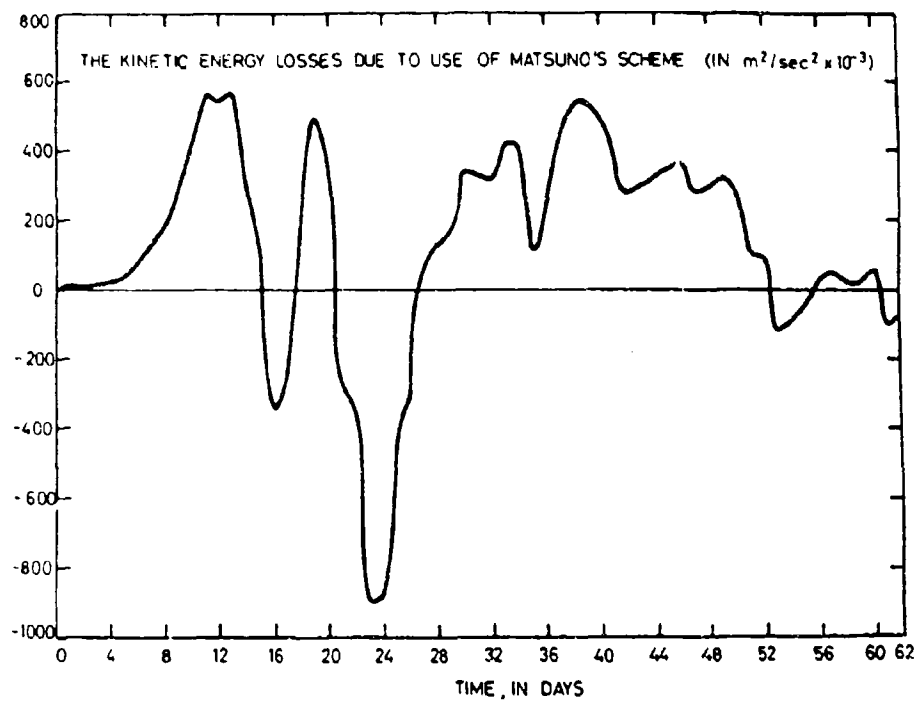
Fig. 44. The kinetic energy losses due to the use of Matsuno's time differencing schemes.

AN INTEGRATION OF A THREE-LEVEL QUASI-GEOSTROPHIC MODEL OF THE ATMOSPHERE WITH CONSTANT AND PRESSURE DEPENDENT STATIC STABILITY

by

A. Huss and M. Segal

ABSTRACT

The evolution of general circulation patterns has been studied by means of a three-level quasi-geostrophic model.

Two experiments were performed. In the first experiment static stability remained constant with height, while in the second it varied with height.

The results were compared to those obtained in a two level model experiment, with similar features, and also with distributions obtained from observational data.

The distribution of the various field variables, were found to be similar to those in the two-level model experiment, however their magnitudes were found to be as a rule higher in the present experiment.

Magnitudes of several variables, including wind velocities, were unrealistically high in the last stages of integration in the second experiment.

I. INTRODUCTION

General circulation patterns were studied by means of
a 3-level quasi-geostrophic and quasi-hydrostatic model. The
features of the model are the same as those adopted in the two-
level model described by Huss (1967). The initial conditions,
boundary conditions, differencing scheme etc. will be described
in the following.

In the two-level model the thermodynamic energy equation
was only applied at the 500 mb level, while in the present experi-
ment the thermodynamic energy equation was applied at two levels,
the 333 mb and the 667 mb levels. The application of the thermo-
dynamic energy equation at two levels instead of one, leads to a
better definition of the vertical p-velocity in the model-
atmosphere.

No release of latent heat and no lateral viscosity were
introduced into the model.

The influx of heat per unit column was formulated in the
same manner, as adopted by Staff Members of Electronic Computation
Center, Japan Meteorological Agency (1965). According to this
formulation the influx of heat per unit column was made proportional
to the temperature difference at the ocean-air interface and to the
geostrophic wind-speed at this level - which was taken as 1000 mb.

Static stability is a function of the spatial coordinates and
time. However in quasi-geostrophic models, as shown for instance by
Wiin-Nielsen (1959), the static stability should be assumed to
vary only in the vertical. Among the models in which the above
assumption was introduced we may mention those of Staff Members of
Electronic Computation Center, Japan Meteorological Agency (1965),
Murakami(1964) and Cressman (1963).

Two different experiments are described in this paper. In the first experiment, the static stabilities at 333 mb and 667 mb were assumed to be equal to the 500 mb static stability of the standard atmosphere. Thus in this experiment, the static ability is lower at 333 mb and higher at 667 mb, than the corresponding values in the standard atmosphere. In the second experiment the standard atmospheric stabilities are assumed at 333 mb and 667 mb.

II. THE STRUCTURE OF THE MODEL

The x,y, p system of spatial coordinates is adopted.
The 0, 167, 333, 500, 667, 833 and 1000 mb levels are indicated
by the subscripts 0,1,2,3,4,5 and 6 respectively. The vorticity
equation, from which the evolution of motion is deduced, was
applied at p_1, p_3 and p_5, while the thermodynamic energy equation
was applied at p_2 and p_4.

The coriolis parameter f was taken as the constant
$f = 10^{-4}$ sec^{-1}, except where its y derivative, β , appeared. The
Rossby parameter, β , was taken as the constant $\beta = 1.6 \times 10^{-11} m^{-1} sec^{-1}$.

The streamfunctions at p_1, p_3 and p_5 are related to the
geopotential, ϕ , by means of the expression

$$\psi = \phi/f \tag{1}$$

Thus the quasi-geostrophic approximation is adopted, with

$$V_g = K \times \nabla \psi \tag{2}$$

$$\zeta = \nabla^2 \psi \tag{3}$$

K = unit vertical vector

$V_g = V$ = geostrophic wind.

The thermodynamic energy equation can be written:

$$\left(\frac{\partial}{\partial t} + \vec{V}\cdot\nabla\right)\frac{\partial\varphi}{\partial p} + \omega\frac{\partial\varphi}{\partial p}\cdot\frac{\partial \ln\theta}{\partial p} = H\frac{1}{c_p T}\cdot\frac{\partial\varphi}{\partial p} \qquad (4)$$

with: $\omega = \frac{dp}{dt}$, the vertical p-velocity

θ = the potential temperature

H = the heat added to unit mass in unit time.

c_p = the specific heat at constant pressure = $1004 \; kj.t^{-1}deg^{-1}$

The hydrostatic equation is given by means of the streamfunction as :

$$\frac{\partial\psi}{\partial p} = \frac{1}{f}\frac{\partial\varphi}{\partial p} = -\frac{RT}{f p} \qquad (5)$$

with : R = the gas constant = $287 \; kj.t^{-1}deg^{-1}$

The static stability, b , which is assumed to be a function of the pressure only, is given by:

$$b = \frac{\partial\psi}{\partial p}\cdot\frac{\partial \ln\theta}{\partial p} \qquad (6)$$

The constants λ_i i=2 and i = 4 are defined as:

$$\lambda_i = \frac{1}{b_i}\left(\frac{f}{\Delta p}\right)^2 \qquad (7)$$

with Δp =333 mb.

In terms of the streamfunction (4) is written:

$$\frac{\partial}{\partial t}\frac{\partial \psi}{\partial p} + (\nabla \frac{\partial \psi}{\partial p})\cdot \mathbf{V} + \frac{\omega b}{7} = -\frac{R}{f\cdot C_p}\cdot \frac{H}{p} \qquad (8)$$

By applying equation (8) at p_2 and p_4, and replacing the pressure derivatives by centered differences, the following expressions for ω_2' and ω_4 are obtained:

$$\omega_2 = \lambda_2 \frac{\Delta p}{7}\left[\frac{\partial}{\partial t}(\psi_1 - \psi_3) - H_2\frac{R}{7C_p} + \mathbf{V}_2\cdot \nabla(\psi_1 - \psi_3)\right]$$

$$\omega_4 = \lambda_4 \frac{\Delta p}{7}\left[\frac{\partial}{\partial t}(\psi_3 - \psi_5) - H_4\frac{R}{2fC_p} + \mathbf{V}_4\cdot \nabla(\psi_3 - \psi_5)\right] \qquad (9)$$

The frictional stress is assumed to be dependent on surface wind and the pressure, according to the expression

$$\tau = C(p)\, k_m\, W_6 \qquad (10)$$

with Km = mean surface stress coefficient

$\mathbf{V}_6$ = geostrophic surface wind

The pressure dependence of C(p) is defined by:

$$C(p) = \frac{p^2}{p_0^2} \qquad (11)$$

The amount of sensible heat entering unit column of the
atmosphere at 1000 mb from the lower boundary (assumed to
represent an ocean surface) was expressed by:

$$Q_s = A_s \, V_s \, (T_g - T_s) \qquad (12)$$

with : V_s = the wind-speed at the surface

T_s = the temperature of the air, near the
surface.

T_g = the temperature of the underlying
surface.

A_s = Constant.

The influx of sensible heat was assumed to become distributed
instantaneously and homogenously throughout the whole column of
air. Thus the influx of sensible heat per cb is given by:

$$H = \frac{g}{p_6} \, Q_s \qquad (13)$$

Radiation losses were assumed to be constant throughout the whole
region. Thus, because of a symmetric choice of conditions, the
structure of the model equations, and by assuming that an
instantaneous heat balance was maintained at each instant of time in
the integration, zero net outgoing radiation results.

Applying the vorticity equation at the three reference
levels p_1, p_3 and p_5, while using $\omega_0 = \omega_6 = 0$ as a boundary condition
for ω, leads to:

$$\left(\frac{\partial}{\partial t} + V_1 \cdot \nabla\right)\left(f + f_1\right) - \frac{f\omega_2}{\Delta p} + gK_m\left(\frac{\partial c}{\partial p}\right)_1 f_6 = 0$$

$$\left(\frac{\partial}{\partial t} + V_3 \cdot \nabla\right)\left(f + f_3\right) + \frac{f(\omega_2 - \omega_4)}{\Delta p} + gK_m\left(\frac{\partial c}{\partial p}\right)_3 f_6 = 0$$

$$\left(\frac{\partial}{\partial t} + V_5 \cdot \nabla\right)\left(f + f_5\right) + \frac{f\omega_4}{\Delta p} + gK_m\left(\frac{\partial c}{\partial p}\right)_5 f_6 = 0 \quad (14)$$

The wind velocity at p_2 and p_4 was expressed by means
of the values at the two adjacent information levels:

$$V_2 = \frac{V_1 + V_3}{2}$$

$$V_4 = \frac{V_3 + V_5}{2} \quad (15)$$

Because of the quasi-geostrophic assumption we obtain:

$$V_2 \cdot \nabla(\psi_1 - \psi_3) = V_1 \cdot \nabla(\psi_1 - \psi_3) = V_3 \cdot \nabla(\psi_1 - \psi_3)$$

$$\quad (16)$$

$$V_4 \cdot \nabla(\psi_3 - \psi_5) = V_3 \cdot \nabla(\psi_3 - \psi_5) = V_5 \cdot \nabla(\psi_3 - \psi_5)$$

Eliminating ω_2 and ω_4 between (9) and (14), while using (16) leads
to the final form of the prediction equation, in terms of the poten-
tial vorticites, at the three information levels p_1, p_3 and p_5:

$$\frac{\partial q_1}{\partial t} = -V_1 \cdot \nabla q_1 - v_1 \beta - gK_m\left(\frac{\partial c}{\partial p}\right)_1 f_6 - \lambda_2 H_2 \cdot \frac{R}{f c_p}$$

$$\frac{\partial q_3}{\partial t} = -V_3 \cdot \nabla q_3 - v_3 \beta - gK_m\left(\frac{\partial c}{\partial p}\right)_3 f_6 + \lambda_2 H_2 \cdot \frac{R}{f c_p} - \lambda_4 H_4 \frac{R}{2f c_p}$$

$$\quad (17)$$

$$\frac{\partial q_5}{\partial t} = -V_5 \cdot \nabla q_5 - v_5 \beta - gK_m\left(\frac{\partial c}{\partial p}\right)_5 f_6 + \lambda_4 H_4 \frac{R}{2f c_p}$$

where the potential vorticities, q_1, q_3 and q_5 are defined by the

following diagnostic equations:

$$q_1 = \zeta_1 - \lambda_2(\psi_1 - \psi_3)$$

$$q_3 = \zeta_3 + \lambda_2(\psi_1 - \psi_3) - \lambda_4(\psi_3 - \psi_5)$$

(18)

$$q_5 = \zeta_5 + \lambda_4(\psi_3 - \psi_5).$$

The following averages are used in various computations:

$$(\widetilde{}) = \frac{1}{X}\int_0^X (\ ) \, dx$$

$$(\overline{}) = \frac{1}{Y}\int_0^Y (\ ) \, dy$$

(19)

where x is the length in the lateral extent of the rectangular region and y its north-south extent .

Let the subscript N and S denote the northern and southern boundaries respectively. With this notation the boundary conditions were written:

$$\left(\widetilde{\frac{\partial \psi'}{\partial y}}\right)_N = \left(\widetilde{\frac{\partial \psi'}{\partial y}}\right)_S = 0$$

(20)

$$v_N = v_S = 0$$

(21)

In the x-direction cyclical continuity of the field variables is assumed.

The boundary conditions for the potential vorticity will be discussed later.

For computing the zonally averaged meridional velocity, the following requirement is made:

$$\tilde{v}_{d,S} = \tilde{v}_{d,N} = 0 \tag{22}$$

where $\tilde{v}_d$ is the zonally averaged meridonal divergent component of the wind.

The zonally averaged meridional divergent velocity is derived from the zonally averaged equation of continuity:

$$\frac{\partial \tilde{v}_d}{\partial y} = - \frac{\partial \tilde{\omega}}{\partial p} \tag{23}$$

The hydrostatic equation (5) can be written as

$$d\varphi = - \frac{RT}{f} d\ln p \tag{24}$$

The application of finite differencing at p_2 and p_4 leads to:

$$T_2 = \frac{f}{R(\ln p_3 - \ln p_1)} (\varphi_1 - \varphi_3) \tag{25}$$

$$T_4 = \frac{f}{R(\ln p_5 - \ln p_3)} (\varphi_3 - \varphi_5)$$

Assuming the Standard Atmosphere lapse rate between 667 mb and the lower boundary:

$$T_6 = T_4 \left(\frac{p_6}{p_4} \right)^{0.19} = T_4 \left(\frac{3}{2} \right)^{0.19} \tag{26}$$

Integrating (24) between p_5 and p_6:

$$\psi_5 - \psi_6 = \frac{R}{f} \int_{p_5}^{p_6} \frac{1}{p} T_4 \left(\frac{p}{p_4}\right)^{0.19} dp = \frac{R}{f} \cdot \frac{T_4}{(p_4)^{0.19}} \int_{p_5}^{p_6} p^{-0.81} dp =$$

$$= \frac{R}{f} \cdot \frac{1}{0.19} \cdot \frac{T_4}{(p_4)^{0.19}} \left[p_6^{0.19} - p_5^{0.19} \right] \tag{27}$$

This equation gives the relation between the streamfunction at p_6 and p_5 by means of the temperature at p_4.

The finite difference form of the Jacobian term:

The finite difference scheme for the advective terms in the prognostic equations was the scheme suggested by A. Arakawa (1966). By using this scheme and appropriate boundary conditions, not only the area integral of the Jacobian vanishes, but also the advective process described by the finite-difference of the Jacobian does not leadto a fictitious generation of mean energy and mean square potential vorticity.

Denoting by $\tilde{J}$ the finite difference Jacobian, and i and j as indices increasing along x and y direction, and by J the total number of grid points along the y direction, the Arakawa analogue of the Jacobian at inner points will be:

$$\tilde{J}(\psi, q)_{i,j} = \frac{1}{12\,\Delta s^2} \left[(\psi_{i+1,j} - \psi_{i-1,j})(q_{i,j+1} - q_{i,j-1}) - (\psi_{i,j+1} - \psi_{i,j-1}) \right.$$

$$\cdot (q_{i+1,j} - q_{i-1,j}) + \psi_{i+1,j}(q_{i+1,j+1} - q_{i+1,j-1}) - \psi_{i-1,j}(q_{i-1,j+1} - q_{i-1,j-1})$$

$$- \psi_{i,j+1}(q_{i+1,j+1} - q_{i-1,j+1}) + \psi_{i,j-1}(q_{i+1,j-1} - q_{i-1,j-1})$$

$$+ q_{i,j+1}(\psi_{i+1,j+1} - \psi_{i-1,j+1}) - q_{i,j-1}(\psi_{i+1,j-1} - \psi_{i-1,j-1}) \tag{28}$$

$$\left. - q_{i+1,j}(\psi_{i+1,j+1} - \psi_{i+1,j-1}) + q_{i-1,j}(\psi_{i-1,j+1} - \psi_{i-1,j-1}) \right]$$

and on the boundaries :

$$\frac{1}{2}J(\psi,q)_{i,0} = \frac{1}{12(\Delta S)^2}\left[(2\psi_0 - \psi_{i,1} - \psi_{i-1,1})q_{i+1,0}\right.$$

(29a)

$$-(2\psi_0 - \psi_{i-1,1} - \psi_{i,1})q_{i-1,0} + (\psi_{i+1,1} - \psi_{i-1,1})q_{i,1}$$

$$(\psi_0 - \psi_{i,1})q_{i+1,1} + (\psi_{i,1} - \psi_0)q_{i-1,1}\right]$$

$$\frac{1}{2}J(\psi,q)_{i,J} = \frac{1}{12(\Delta S)^2}\left[(\psi_{i,J-1} + \psi_{i+1,J-1} - 2\psi_J)q_{i+1,J}\right.$$

$$+(\psi_{i-1,J-1} + \psi_{i,J-1} - 2\psi_J)q_{i-1,J} - (\psi_{i+1,J-1} - \psi_{i-1,J-1})q_{i,J-1}$$

(29b)

$$-(\psi_{i,J-1} - \psi_J)q_{i-1,J-1} - (\psi_J - \psi_{i,J-1})q_{i+1,J-1}\right]$$

where ψ_0 and ψ_J are the constant values of ψ on the southern and northern boundaries respectively, and ΔS is the grid interval.

The scheme for calculating the new values of the potential vorticity on the boundaries .

The Jacobian term on the boundary is given by (29a) and (29b).

For the frictional term, we introduce the Laplacian on the boundaries in the following way:

$$\frac{1}{2}\zeta_{i,0} = \frac{1}{(\Delta S)^2}\left(\psi_{i,1} - \psi_0\right)$$

(30)

$$\frac{1}{2}\zeta_{i,J} = \frac{1}{(\Delta S)^2}\left(\psi_J - \psi_{i,J-1}\right)$$

The surface velocities required for the calculation of the diabatic heating are defined on the boundaries:

$$|V|_{i,0,6} = \frac{1}{\Delta S}\left|\psi_{0,6} - \psi_{i,1,6}\right|$$

(31)

$$|V|_{i,J,6} = \frac{1}{\Delta S}\left|\psi_{J,6} - \psi_{i,J-1,6}\right|$$

The calculation of the new values of the potential vorticity
on the boundaries, is done by applying the above boundary condi-
tions with equation (17).

The finite difference form of the equations

In order to perform the calculations, equations (17)
and (18) have to be re-written in finite difference form.

Centered finite differences replace the time-derivatives
appearing in (17):

$$\left(\frac{\partial q}{\partial t}\right)_{i,j,\tau} = \frac{q_{i,j,\tau+1} - q_{i,j,\tau-1}}{2\Delta t} \tag{32}$$

The finite difference approximation for the advection
term is given by (28).

The Laplacian of the streamfunction will be approximated as:

$$\nabla^2 \psi = \frac{1}{(\Delta S)^2} \nabla^2 \psi_{i,j} = \frac{1}{(\Delta S)^2}\left(\psi_{i+1,j} + \psi_{i-1,j} + \psi_{i,j+1} + \psi_{i,j-1} - 4\psi_{i,j}\right) \tag{33}$$

Thus the equation (17) will be approximated by:

$$q_{1,i,j,\tau+1} = q_{1,i,j,\tau-1} + 2\Delta t\left\{J(\psi_1, q_1)_{i,j,\tau} - \frac{\psi_{i,i+1,j,\tau} - \psi_{i,i-1,j,\tau}}{2\Delta S}\beta - \right.$$

$$\left. - g K_m\left(\frac{\partial c}{\partial p}\right)_1 \frac{1}{(\Delta S)^2} \nabla^2 \psi_{i,j,\tau-1} - \frac{2R}{fc_p} H_{2,i,j,\tau-1}\right\}$$

$$q_{2,i,j,\tau+1} = q_{2,i,j,\tau-1} + 2\Delta t\left\{J(\psi_2, q_2)_{i,j,\tau} - \frac{\psi_{i,i+1,j,\tau} - \psi_{i,i-1,j,\tau}}{2\Delta S}\beta - \right.$$

$$\left. - g k_m\left(\frac{\partial c}{\partial p}\right)_3 \frac{1}{(\Delta S)^2} \nabla^2 \psi_{i,j,\tau-1} + \frac{2R}{fc_p} H_{2,i,j,\tau-1} - \right. \tag{34}$$

$$-\frac{\gamma_+ R}{2f_{\circ}\rho} H_{4,i,j,\tau-1} \Big\}$$

$$q_{5,i,j,\tau+1} = q_{5,i,j,\tau-1} + 2\Delta t \Big\{ \overline{J}(\psi_5,q_5)_{i,j,\tau} - \frac{\psi_{5,i+1,j,\tau}-\psi_{5,i-1,j,\tau}}{2\Delta s}\beta$$

$$-g K_{m} \Big(\frac{\partial \omega}{\partial p}\Big)_5 \nabla \psi_{6,i,j,\tau-1} + \frac{\gamma_+ R}{2f_{\circ}\rho} H_{4,i,j,\tau-1} \Big\}$$

and the diagnostic equations (18) by:

$$q_{1,i,j,\tau} = \frac{1}{(\Delta s)^2} \nabla \psi_{1,i,j,\tau} - \lambda_2 (\psi_{1,i,j,\tau} - \psi_{3,i,j,\tau})$$

$$q_{3,i,j,\tau} = \frac{1}{(\Delta s)^2} \nabla \psi_{3,i,j,\tau} + \lambda_2 (\psi_{1,i,j,\tau} - \psi_{3,i,j,\tau}) -$$

$$- \lambda_4 (\psi_{3,i,j,\tau} - \psi_{5,i,j,\tau})$$

$$q_{5,i,j,\tau} = \frac{1}{(\Delta s)^2} \nabla^2 \psi_{5,i,j,\tau} + \lambda_4 (\psi_{3,i,j,\tau} - \psi_{5,i,j,\tau}) \tag{35}$$

The energy transformations

The notations and the methods which are used for obtaining the energy transformations are the same as described by Huss (1967) for the two level model experiment. However in the present experiment energy transformations must be computed separately for the lower half of the atmosphere, and the upper half of the model atmosphere, and the corresponding values for the two layers are averaged. Energy transformations are computed per unit column; as follows :

$$\{\tilde{K},K'\} = \frac{p_0}{g} \Big[\overline{\tilde{u}_1 \frac{\partial}{\partial y}(\overline{u_1'v_1'})} + \overline{u_3 \frac{\partial}{\partial y}(\overline{u_3'v_3'})} + \overline{u_5 \frac{\partial}{\partial y}(\overline{u_5'v_5'})} \Big]$$

$$\{\tilde{P},P'\} = -\frac{\gamma_2}{\Delta p g} \Big[\frac{1}{b_2} \overline{\tilde{v_1'}\psi_1'(\tilde{u}_1 - \tilde{u}_3)} + \frac{1}{b_4} \overline{\tilde{v_3'}\psi_5'(\tilde{u}_3 - \tilde{u}_5)} \Big]$$

$$\{\tilde{K},\tilde{P}\} = \frac{f}{g} \Big[\overline{\tilde{\omega}_2(\tilde{\psi}_1 - \tilde{\psi}_3)} + \overline{\tilde{\omega}_4(\tilde{\psi}_3 - \tilde{\psi}_5)} \Big]$$

$$\{K',P'\} = \frac{f}{g} \Big[\overline{\omega_2'(\psi_1' - \psi_3')} + \overline{\omega_4'(\psi_3' - \psi_5')} \Big] \tag{36}$$

$$\{\tilde{P},\tilde{Q}\} = -\frac{R\tilde{f}}{C_p \Delta p \tilde{q}}\left[\frac{1}{b_2}\overline{\tilde{H}_2(\tilde{\psi_1}-\tilde{\psi_3})} + \frac{1}{2b_4}\overline{\tilde{H}_4(\tilde{\psi_3}-\tilde{\psi_5})}\right]$$

$$\{P',Q'\} = -\frac{R\tilde{f}}{C_p \Delta p \tilde{g}}\left[\frac{1}{b_2}\overline{H'_2(\psi'_1-\psi'_3)} + \frac{1}{2b_4}\overline{H'_4(\psi'_3-\psi'_5)}\right]$$

$$\{\tilde{K},\tilde{F}\} = \frac{P_6}{3}K_m\left[\left(\frac{\partial c}{\partial p}\right)_1\overline{\tilde{u}_1\tilde{u}_6} + \left(\frac{\partial c}{\partial p}\right)_3\overline{\tilde{u}_3\tilde{u}_6} + \left(\frac{\partial c}{\partial p}\right)_5\overline{\tilde{u}_5\tilde{u}_6}\right]$$

$$\{K',F'\} = \frac{P_6}{3}K_m\left[\left(\frac{\partial c}{\partial p}\right)_1\overline{\tilde{v}'_1\tilde{v}'_6} + \left(\frac{\partial c}{\partial p}\right)_3\overline{\tilde{v}'_3\tilde{v}'_6} + \left(\frac{\partial c}{\partial p}\right)_5\overline{\tilde{v}'_5\tilde{v}'_6}\right]$$

The ω equation

The diagnostic equation for the vertical velocity ω, is derived by eliminating time-derivatives from the potential-vorticity equations and the thermodynamic energy equations:

Equations (9) can be written as :

$$\frac{\partial}{\partial t}(\psi_1-\psi_3) = J(\psi_1,\psi_3) + \omega_2\frac{f}{\Delta p \lambda_2} + H_2\frac{R}{f C_p}$$

$$\frac{\partial}{\partial t}(\psi_3-\psi_5) = J(\psi_3,\psi_5) + \omega_4\frac{f}{\Delta p \lambda_4} + H_4\frac{R}{2f C_p} \tag{37}$$

By using (17) and (18) we obtain the following equations:

$$\frac{\partial}{\partial t}\nabla^2(\psi_1-\psi_3) - 2\lambda_2\frac{\partial}{\partial t}(\psi_1-\psi_3) + \lambda_4\frac{\partial}{\partial t}(\psi_3-\psi_5) = -J(\psi_1,q_1) + J(\psi_3,q_3)$$

$$-\beta(v_1-v_3) - gK_m\left[\left(\frac{\partial c}{\partial p}\right)_1 - \left(\frac{\partial c}{\partial p}\right)_3\right]\nabla^2\psi_6 + \frac{R}{f C_p}\left[-2\lambda_2 H_2 - \frac{1}{2}\lambda_4 H_4\right]$$

$$\frac{\partial}{\partial t}\nabla^2(\psi_3-\psi_5) - 2\lambda_4\frac{\partial}{\partial t}(\psi_3-\psi_5) + \lambda_2\frac{\partial}{\partial t}(\psi_1-\psi_3) =$$

$$= -J(\psi_3,q_3) + J(\psi_5,q_5) - \beta(v_3-v_5) - gK_m\left[\left(\frac{\partial c}{\partial p}\right)_3 - \left(\frac{\partial c}{\partial p}\right)_5\right]\nabla^2\psi_6 + \frac{R}{f C_p}\left[\lambda_2 H_2 - \lambda_4 H_4\right] \tag{38}$$

Eliminating $\frac{\partial}{\partial t}(\psi_3 - \psi_5)$, $\frac{\partial}{\partial t}(\psi_1 - \psi_3)$, $\frac{\partial}{\partial t}\nabla^2(\psi_1 - \psi_3)$
and $\frac{\partial}{\partial t}\nabla^2(\psi_3 - \psi_5)$ by means of (37) we obtain the final form of the
diagnostic equations for ω:

$$\nabla^2 \omega_2 - 2\lambda_2 \omega_2 + \omega_4 \lambda_2 = \frac{\Delta P}{f}\lambda_2 \Big[2\lambda_2 J(\psi_1, \psi_3) - \lambda_4 J(\psi_3, \psi_5) +$$

$$+ J(q_1, \psi_1) - J(q_3, \psi_3) - \beta(v_1 - v_3) - g k_m \Big[\Big(\frac{\partial c}{\partial p}\Big)_1 - \Big(\frac{\partial c}{\partial p}\Big)_3 \Big] \nabla^2 \psi_6 - \tag{39}$$

$$- \nabla^2 J(\psi_1, \psi_3) - \frac{R}{f C_p} \nabla^2 H_2 \Big]$$

$$\nabla^2 \omega_4 - 2\lambda_4 \omega_4 + \omega_2 \lambda_4 = \frac{\Delta P}{f}\lambda_4 \Big[2\lambda_4 J(\psi_3, \psi_5) - \lambda_2 J(\psi_1, \psi_3) +$$

$$+ J(q_3, \psi_3) - J(q_5, \psi_5) - \beta(v_3 - v_5) - g k_m \Big[\Big(\frac{\partial c}{\partial p}\Big)_3 - \Big(\frac{\partial c}{\partial p}\Big)_5 \Big] \nabla^2 \psi_6 -$$

$$- \nabla^2 J(\psi_3, \psi_5) - \frac{R}{2 f C_p} \nabla^2 H_4 \Big]$$

III. EXPERIMENT I

The static stabilities at p_2 and p_4 were assumed to be both equal to the Standard Atmospheric value at p_3. The duration of experiment I was 31 days.

Fig. 1 shows the variation of the amplitudes of the first harmonics of the streamfunctions at the central latitude, at 167, 500 and 833 mb, as a function of time.

In the first 10 days an almost exponential increase in amplitudes is observed. During this period the magnitudes of the amplitudes at 833 mb and at 500 mb are almost equal. Following this initial increase, a sharp decrease in amplitudes was observed and on the 12th day the amplitudes reached local minima of 57×10^5 m^2/sec at 833 mb, 95×10^5 m^2/sec at 500 mb and 157×10^5 m^2/sec at 167 mb. After attaining these minima (the only pronounced minima of the entire run) the amplitudes grew rapidly until the 16th day. Thereafter and up to the end of the run, a general trend of slow increase in amplitudes was observed, accompanied by small oscillations.

The variation of the zonally averaged zonal component of the wind, at 1000 mb, as a function of latitude and time is shown in Fig. 2. Except for the last days of the run, the boundaries separating easterlies from westerlies were located in the south, between $j = 4$ and $j = 5$, and in the north, between $j = 11$ and $j = 12$. The maximum intensity of the westerlies was obtained always at the central latitude. The first maximum, observed on the 12th day, had a value of about 10 m/sec, and was accompanied by low values of the amplitude of the disturbances in the streamfunctions. Other dominant maximum-velocities were attained on the 18th, 22th and 30th days. The last one had a value of 15 m/sec - the highest value observed during the entire run. The highest speed of the easterlies, - 6 m/sec, was observed on the 18th and on the 30th day . Maxima of surface wind velocities were larger than those observed in the two levels model experiment. Thus frictional energy losses, and the influx of sensible heat from the

surface, being dependent on surface wind velocity, could attain larger maximum values than in the case of the two level model.

The zonally averaged zonal flow as a function of latitude and pressure for 3 selected days is shown in Fig. 3. On the 13th day the region of easterlies extended to j=5 at the south and to j=11 at the north, and penetrated somewhat beyond p_5. The maximum values of westerlies were attained at the central latitude. The velocity at p_1 at the central latitude was 55 m/sec, while at p_3 and p_5 the corresponding velocities were 26 m/sec and 13 m/sec respectively.

On the 21st day the distribution and intensity of easterlies remained almost the same as on the 13th day. At the upper levels a split "jet" had developed with two maxima north and south of the central latitude. The velocity at p_1, at the central latitudes was 32 m/sec, while the maximum velocity at this level, 37 m/sec, was located between j=5 and j =6 and between j=10 and j=11. The splitting of the jet at p_3 was less pronounced, while at p_5 no such feature was observed. Compared with the 13th day, the intensity of the westerlies had decreased, the decrease being most pronounced at the central latitudes.

On the 31st day the northern and southern regions of easterlies were considerably smaller in lateral extent and height, compared with correpsonding regions observed on the 21st day. Easterlies were also observed between j=7 and j=9, penetrating somewhat beyond p_5. The speed of the easterlies was very low and did not exceed -1 m/sec. No slight easterlies of this nature appeared on the days preceeding the 31st day.

A very pronounced splitting of the belt of the westerlies, with two maxima at about j=5 and j=11, was observed at all levels. The velocity at p_1 at the central latitude was 22 m/sec, compared with a velocity of 42 m/sec at j=5 and j=11. The maximum values

at P_3 were 24 m/sec, while at the central latitude a value of only 1 m/sec was observed.

The mean poleward flux of momentum on the 10th and on the 20th days as a function of latitude and pressure is presented in Fig. 4.

On the 10th day two well-defined regions were observed in the northern and southern halves of the model-atmosphere, with positive flux in the south and negative flux in the north, having identical magnitudes at symmetrical location with respect to the central latitude. At p_1 the maximum positive and negative values, of 182 m^2/sec^2, were observed at j=5 and j=11 respectively, compared with maximum values of 10 m^2/sec^2 at p_3 and 9 m^2/sec^2 at p_5. Thus, momentum was transported predominantly at the upper layers.

On the 20th day broad regions of momentum transports towards the southern and northern boundaries (the highest value at p_1 being 163 m^2/sec^2) were observed in the south and north respectively. Positive momentum transports were observed in a relatively narrow region south side of the central latitude, while corresponding negative momentum transports were observed north of it . In these regions transports were less intense. On the 20th day as well as on the 10th day most of the momentum was transported in the upper layers.

Various energy transformations are shown in Fig. 5 . The energy transformations $\{\tilde{p}, p'\}$ and $\{p', \kappa'\}$ were both consistently positive during the entire run. The changes of one of these transformations were parallel to those of the other . Except for the first 12 days, the differences between the values of these transformations were quite large. Thus only part of the total amount of zonal potential energy which was converted into eddy potential energy, was transformed into kinetic energies of eddies. The highest values of $\{\tilde{p}, p'\}$ and $\{p', \kappa'\}$ amounting to 43.2 x 10^{-5} $kjm^{-2}sec^{-1}cb^{-1}$ and 19.2x$10^{-5}kjm^{-2}sec^{-1}cb^{-1}$ respectively were observed on the 30th day. The average values of $\{\tilde{p}, p'\}$

and $\{ p', \kappa' \}$ were considerably higher compared with those obtained in the two levels experiment.

During most stages of the run the $\{ \kappa', \tilde{\kappa} \}$ transformation was lower than the $\{ \tilde{p}, p' \}$ and $\{ p', \kappa' \}$ transformations. Negative values of $\{ \kappa', \tilde{\kappa} \}$ were observed several times during the run.

The conversion of heat into zonal potential energy was consistently positive, while conversion of heat into eddy potential energy was consistently negative. The numerical values of the first transform were slightly larger than those of the second transform. Thus available potential energy appears to increase somewhat due to heating.

The frictional losses of zonal kinetic energy were small, with a maximum of $32 \times 10^{-5} kjm^{-2}sec^{-1}cb^{-1}$. The frictional losses of eddy kinetic energy increased with time and reached a value of 11.3×10^{-5} $kj.m^{-2}sec^{-1}cb^{-1}$, at the end of the run.

The change with time of the various components of the kinetic energy is shown in Fig. 6. At each level the kinetic energy of the eddies increased in general with time. Normally a situation of this nature was accompanied by a decrease of the kinetic energy of the zonal flow. However, no balance was observed and a steady increase in the total averaged kinetic energy took place. At the two upper levels the kinetic energy of the eddies exceeded the zonal kinetic energy from about the 18th day, while at p_5 this was the case already from the 12th day on. Following these dates an increase in the kinetic energy of the eddies and a decrease in kinetic energy of the zonal flow was observed at all levels.

The total averaged kinetic energy had a value of about 330 m^2/sec^2 during the formative stages of the run, and rose to 1040 m^2/sec^2 at the end of the run.

Fig. 7 represents the distribution of the zonally averaged diabatic heating per unit column, for the 13th, 21st and 31st days. Due to the structure of the equations and the initial conditions, the distribution is antisymmetrical around the central latitude. On each of those three

selected days, the southern half of the region gained heat, while the northern half lost heat.

On the 13th day heating has a maximum value of 0.05 $kjm^{-2}sec^{-1}$ at j=3, and cooling the negative corresponding value at j=13. The magnitude of the heat influx was considerably larger on the 21st and 31st days. The maximum value on the 21st day was 0.29 $kjm^{-2}sec^{-1}$, and on the 31st day 0.35 $kjm^{-2}sec^{-1}$. These values are about twice the maximum values obtained in the two level model experiment.

The latitude-pressure distribution of the poleward flux of sensible heat is shown for 3 selected days in Fig. 8. Positive values predominated. On the 13th day, the negative sensible heat flux values were observed at the upper level near the southern and northern boundaries; however, the magnitudes were very small.

On the 21st day the negative values disappeared, and a very pronounced intensification of flux took place. A maximum value of 72×10^2 $kjsec^{-1}cb^{-1}$ was observed at p_4 at j=8, while at p_2 two maxima of 50×10^2 $kjsec^{-1}cb^{-1}$ were observed at j=7 and j=9.

Further intensification of sensible heat flux values was observed at p_2 on the 31st day, and a maximum value of 210 $kjsec^{-1}cb^{-1}$ was located at j=8.

IV. EXPERIMENT II

       The amplitudes of the first harmonics of the disturbances
at the central latitude, at the three reference levels, as a function
of time, are shown in Fig. 9 . Broadly speaking, the variation
of the amplitudes at the three reference levels was similar.

       During the formative stages, the familiar pattern observed
in Experiment I was repeated ; a steady, nearly exponential growth
at the three levels, with only a small decrease within the first day.
The first maximum was attained on the 13th day, amounting to
128×10^5 m^2/sec at 833 mb, 193×10^5 m^2/sec at 500 mb and 133×10^5
m^2/sec at 167 mb. From now on up to the end of the run the amplitudes
oscillated . These oscillations at the different pressure levels were
not in phase. However, the dates at which extremal values appeared
at the different levels, did not vary by more than a day or two.

       Low amplitudes were observed at the three levels approximately
on the 23rd, 31st, 39th, 46th and 51st days. The lowest value
at p_5 was obtained on the 45th day, amounting to $52 \times 10^5 m^2/sec$; at p_3
on the 46th day, amounting to 70×10^5 m^2/sec and at p_1 on the 39th day
amounting to 77×10^5 m^2/sec. On the whole the amplitudes at the two lower
levels had the same order of magnitude as those observed in experiment I.
However, the average   amplitude at the upper level was smaller
in the present experiment, due to the greater stability at this level.

       Fig. 10 represents the mean zonal wind at 1000 mb, as
a function of latitude and time. During the first 31st days the
distribution and intensity of surface wind were similar to those observed
in experiment I. Thereafter, the region of westerlies narrowed and
disappeared entirely at about the 36th day. Unitl the 45th day easterlies
prevailed at all latitudes, having a maximum of -5 m/sec at the central
latitude . The familiar distribution of surface wind reappeared at
about the 45th day.

The first three maxima of westerlies were observed on the 16th, 23rd, and 31st days, reaching values of 13 m/sec, 8 m/sec and 15 m/sec respectively. The intensification of the westerlies was accompanied by an intensification of the easterlies flanking them and by a reduction of the amplitude of the disturbance at p_5 .

The distribution of wind was similar to that observed in the two-level model experiment (except for the period where easterlies became dominant throughout the entire region), but wind speeds were somewhat larger in the present experiment.

The latitude-pressure distribution of $\tilde{u}$ for 5 selected days, is shown in fig. 11. On the 13th day surface easterlies were observed in the south and in the north regions, penetrating close to the lateral boundary beyond p_5. The highest velocity in the easterlies was observed at j=3 and j=13, with values of -5 m/sec. The westerlies prevailing over most of the region, are characterized by smaller vertical wind shears at the lower layers compared with those at the upper layers. The maximum velocity at p_1 is 47 m/sec, observed at the central latitude. A similar pattern was observed on the same day in Experiment I.

On the 21st day the distribution and intensity of the easterlies remained almost unchanged. A slight splitting in the westerlies was observed at p3, without appearing at p_1 and p_5. The westerlies were almost equal to those in the previously described day. Compared with the same day in experiment I, the wind had a similar distribution but somewhat higher velocities.

On the 31st day a considerable intensification and extension of easterlies was observed ; laterally they were found to prevail beyond j=5 and j = 11 and vertically they had penetrated somewhat beyond p_3. Maximum easterly velocities were attained near the surface at j=3 and j= 13, with -8 m/sec.

The westerlies also intensified, reaching values of 67 m/sec and 30 m/sec respectively at p_1 and p_3 at the central latitude.

On the 39th day easterlies were found to prevail throughout a shallow layer near the surface, with an upward bulge penetrating vertically up to p_4 in the central part of the region.

The westerlies were split, with two maxima of 75 m/sec and 14 m/sec located at j=6 and j=11 at p_1 and p_3 respectively.

The vertical wind shear in the upper layers was extremely large compared with the shear observed in the previous days.

On the 53rd day no easterlies were any longer observed at the central latitudes. They recovered their normal spatial distribution, with quite a small intensity, not exceeding -3 m/sec.

Compared with the 39th day considerable intensification of westerlies was observed, the velocity at the central latitude at p_1 rising beyond 95 m/sec.

On the whole the wind velocities at the upper layers were larger than those observed in the two-level experiment.

A three-level model, by its very nature, enables a vertical resolution of the vertical shear. In the present experiment a strong shear was generated in the upper layer and a weak shear in the lower layer.

The latitude- pressure distribution of the poleward eddy momentum transport is shown in fig. 12 for a number of selected days. On the 13th day the northward flux was contained within the southern half of the region, and the southward flux, with symmetrical magnitudes around the central latitude, in the northern half. The most intense momentum fluxes of $\pm$ 79 m^2/sec^2 were observed at p_3, j=5 and j=11. Highest values of momentum transport at p_1 were observed at j=4 and j=12, amounting to 72 m^2/sec^2.

The pattern on the 31st day remained almost the same as that on the 13th day, but considerable amplification took place. The largest transports positive and negative, were located at j=5 and j=11 at all the levels with magnitudes of 135 m²/sec², 144 m²/sec² and 57 m²/sec² at p_1, p_3 and p_5 respectively.

On the 53rd day the pattern became quite complex, with strips of negative values alternating with strips of positive values. The maximum intensities were located in the upper levels. Somewhat similar patterns ,with about the same intensities were also obtained in the case of the two level model at some stages of the integration.

The energy transformations are presented in Fig. 13. Compared with experiment I the values of $\{\hat{P}, P'\}$ and $\{P', K'\}$ were generally lower. The magnitudes of these two transformations during most stages of the integrations differed while the pattern of their variation with time was similar. Low values of the transformations were accompanied by low values of stream function disturbances.

During the first 23 days the values of $\{\hat{P}, P'\}$ and $\{P', K'\}$ are quite low . During the following days a steady increase both in $\{\hat{P}, P'\}$ and $\{P', K'\}$ was observed . On the 27th day the maxima of 20.4x 10^{-5} kjm^{-2}sec^{-1} and 15.2 x 10^{-5}kjm^{-2}sec^{-1} respectively were observed, followed by a decrease to quite low values. However, toward the end of the run the transformations increased again attaining their highest values during the entire run on the 58th day: 30 x 10^{-5}kjm^{-2} and 21x10^{-5}kjm^{-2}sec^{-1} respectively. Negative values of both transforms were observed between the 35th and 37th days.

The $\{k',\breve{K}\}$ transformation as in Experiment I, was occasionally
negative. Towards the end of the run large-amplitude fluctuations of
this transformation were observed. Generally speaking, the magnitudes
of the transformations were quite similar to the corresponding values
in the two level model.

The conversion of heat into zonal potential energy was
consistently positive, while the conversion of heat into eddy poten-
tial energy was almost always negative, except that during some
stages of the run this transformation vanished.

Except for the first 20 days, the values of the first
transformation were considerably larger than those obtained for the
second one. In the two-level model, and in Experiment I, both trans-
formations had almost the same absolute magnitudes.

The maximum value of $\{\tilde{Q}, \tilde{P}\}$ was observed on the
29th day, amounting to 19.2 x 10^{-5} kjm^{-2}sec^{-1}. On the same day $\{Q', P'\}$
had its minimum value, amounting to -3.8x10^{-5} kjm^{-2} sec^{-1}.

It will be noticed that, as has been observed also in the two
previous experiments, maximum values of $\{\tilde{Q}, \tilde{P}\}$ were generally
accompanied with minimum values of $\{Q', P'\}$

The $\{\tilde{K}, \tilde{F}\}$ values were quite small; moreover, during
some stages, this transformation became negative. Such negative
values occurred during the days in which surface easterlies were
observed at all latitudes.

The frictional losses of eddy kinetic energy did not exceed
7.2 x 10^{-5} kjm^{-2} sec^{-1}. Compared with the corresponding period in
Experiment I their values were found to be lower, but still larger than
those observed with the two level model.

The march of the various kinetic energy components with time is
shown in Fig. 14. $\tilde{K}$ values decreased slightly

during the first 21st days. Thereafter a noticeable growth
was observed, up to 2453 m^2/sec^2 on the 57th day. K'_{167} values
were consistently lower than $\widetilde{\mathcal{K}}_{167}$ values, as was also
observed in Experiment I. Their magnitudes were lower than during
the corresponding period in Experiment I. On the other hand K'_{167}
values were higher in the present experiment.

At p_3 the kinetic energy of the eddies exceeded during some
stages the zonal kinetic energy, however toward the end of the run
$\mathcal{R}_{500}$ again exceeded K'_{500} .The maximum of $\widetilde{\mathcal{K}}_{500}$
amount to 160 m^2/sec^2 (the initial value of $\widetilde{\mathcal{K}}_{500}$ was 146 m^2/sec^2.
The maximum of K'_{500} observed on the 30th day, amounted
to 219 m^2/sec^2. Compared with experiment I the $\widetilde{\mathcal{K}}_{500}$ average values
obtained in the present experiment, were about the same, while K'_{500}
values were considerably lower.

Except for the first 19 days, the kinetic energy of the
eddies at p_5 exceeded the zonal kinetic energy. Its highest value of
120 m^2/sec^2, was observed on the 29th day, while the maximum value of
the kinetic energy zonal flow amounting to 45 m^2/sec^2, was observed
on the 31st day. The average magnitude of both quantities was similar
to that observed in Experiment I.

The area averaged kinetic energy, including all components,
increased from the initial value of 328 m^2/sec^2 to 1175 m^2/sec^2 at the
end of the run. In the present experiment the rate of increase in total
kinetic energy was larger than during the corresponding period in
experiment I. On the 31st day total averaged kinetic energy was almost
twice the value observed in Experiment I.

The zonally averaged diabatic heating, as a function of la-
titude, for 6 selected days, is shown in fig. 15. Except for the 31st
day the heating values were quite moderate, and their maxima were
between 0.07 $kjm^{-2}sec^{-1}$ to 0.16 $kjm^{-2}sec^{-1}$. Similar maxima are obser-
ved in the two-level model experiment. On the 31st day the maximum

was 0.35 $kjm^{-2}sec^{-1}$. Generally, the magnitudes of both heating and cooling were seen to be of the same order of magnitude as those obtained by Clapp (1961) for the winter period.

Fig. 16 represents the poleward flux of sensible heat as a function of latitude and pressure for 5 selected days. On the 13th day sensible heat flux had negative values near the northern and southern boundaries; however the absolute magnitudes were small compared with the positive values around the central latitude, where a maximum value of 42×10^2 kjm $sec^{-1}cb^{-1}$ was obtained at p_4. Intensification and spreading of negative values was observed on the 21st day, positive values were dominant at the lower levels, while negative values dominanted at the upper levels.

A similar distribution was observed on the 31st day. However, the region with negative values contracted. A maximum value of 44×10^2 kj-$sec^{-1}cb^{-1}$ was obtained at p_4, at j=8 ,compared with 24×10^2 kj $sec^{-1}cb^{-1}$, observed at p_2 at j=3.5 and j=12.5.

On the 39th day positive values prevailed almost throughout the whole regions, but the magnitude of the flux at p_2 was considerably smaller than that at p_4. On the 53th day most values were positive. Maximum values were obtained at p_2.

Generally, the variation of the sensible heat flux at p_4 was small, compared with pronounced changes observed at p_2.

Fig. 17 shows the time-averaged zonal flow (for the 38th-60th days). Except for a slight splitting at p_3 the westerlies had one maximum, at the central latitude. The most intensive velocity of the westerlies was observed at p_1. At the central latitude the velocity reached 90 m/sec, compared with a 17 m/sec velocity at p_3. Easterlies were observed at the edge of the southern and northern regions, their intensity being low, not exceeding -2.2 m/sec.

The vertical shear of the wind velocity was very pronounced in the upper half of the model atmosphere, as compared with the lower half.

In the representation of the zonal wind distribution
in the northern hemisphere, by Mintz (1954), based on real data,
the jet is situated around $30^{\circ}N$ in the winter, and its highest
intensity of 40 m/sec is found at 200 mb. Likewise, easterlies
are observed at northern latitudes with maximum intesity of
-5m/sec. Thus the jet intensity in our experiment is about
twice that of the real atmosphere, while the easterlies are less
pronounced.

Fig. 18 represents a time-averaged eddy momentum
transport. The values were positive over the southern half
region, and negative over the northern half. The flux had extre-
mal values of ± 48 m^2/sec^2 at $j = 5$ and $j = 11$, at p_1. The
maximum values at p_3 amounted to $8 m^2/sec^2$, and were observed at
the same latitudes. The momentum transport at p_5 was very
small .

The poleward momentum flux in winter as estimated
by Holopainen (1967) has its maximum of 66 m^2/sec^2 at 250 mb
and is located at $30^{\circ}N$.

Fig. 19 shows a time average of the poleward flux of
sensible heat, as a function of latitude and pressure. Positive
values prevailed almost throughout the whole region. The
values at p_2 and p_4 had similar magnitudes. The sensible heat
flux maxima were observed at the central latitude, with
18 $kj\text{-}sec^{-1}cb^{-1}$ and 15 $kj\ sec^{-1}\ cb^{-1}$ at p_2 and p_4 respectively.
The values of sensible heat flux decreased gradually toward
the northern and southern boundaries.

V . CONCLUSIONS

Two numerical experiments dealing with the evolution of atmospheric general circulation patterns were performed by means of a 3-level quasi-geostrophic and quasi hydrostatic model. In the first experiment static stability was assumed to be constant with height, while in the second experiment it varied in the vertical. These experiments were compared to earlier experiments with a two level model.

The resulting patterns of the various field variables showed a certain resemblance to those of the earlier experiments; however magnitudes of field variables were generally larger .

The amplitude of the disturbances in the streamfunctions at the central latitude on the upper level were smaller in Experiment II, than the corresponding amplitudes in Experiment I, due to the greater stability at this level in the second experiment.

The distribution of the zonal surface wind was generally similar in both experiments to that observed in the two level model experiment. However, wind speeds were somewhat larger in the present two experiments.

The time averaged zonal speeds in the westerlies in the upper layers were considerably higher in Experiment II than values observed in real atmosphere.

The distribution of eddy fluxes of momentum was occasionally quite unrealistic, and varied considerably from day to day. A time averaged distribution for 23 days , in the case of experiment II, showed pronounced negative eddy momentum flux in the northern region.

The transformations of zonal potential energy into eddy potential energy, and from eddy potential energy to eddy kinetic energy, had a similar pattern of variation with time, in both

experiments. Low values of these transformations were accompanied by low values of the streamfunction disturbance.

Due to more intensive surface wind speeds, transformations of heat into potential energy, and frictional losses were higher than those observed in the earlier experiment.

In both experiments a steady increase in the total averaged kinetic energy was observed, due to the fact that there was no balance between kinetic energy of zonal flow, and kinetic energy of the eddies.

The magnitudes of the zonally averaged diabatic heating were generally higher in Experiment I than those observed in Experiment II. The magnitude of both heating and cooling were seen to be of the same order of magnitude as those in the real atmosphere during winter.

REFERENCES

1. Arakawa, A., 1966: Computational Design for Long-Term Numerical
                Integration of the Equations of Fluid Motion:
                Two-Dimensional Incompressible Flow. Part I. J. Comput.
                Phys. 1, 119-143.

3. Clapp, P.F., 1961: Normal Heat Sources and Sinks in the Lower Tropos-
                phere in Winter. Mon. Wea. Rev. 89, 147-162.

3. Cressman, George, P. 1963: A Three-level Model Suitable for Daily
                Numerical Forecasting. U.S. Weather Bureau,
                National Meteorological Center, Technical Memorandum
                No. 22.

4. Holopainen, E.O., 1967: On the Meridional Circulation and the Flux
                of Angular Momentum Over the Northern Hemisphere.
                Tellus 19, 1-13.

5. Huss, A., 1967: Numerical Studies of Planetary Circulations in a Model
                Atmosphere. Final REport, USAF Grant Af EOAR 65-89.

6. Mintz, Y., 1954: The Observed Zonal Circulation of the Atmosphere.
                Bull. Amer. Meteor. Soc. 35, 208-214 (33,46).

7. Murakami, T., 1964: Multiple-Level Model for the P- and S-Coordinates.
                J. Met. Soc. Japan, Ser. 2, 42, 1-12.

8, Staff Members of Electronic Computation Center, 1965:
                72-hr Baroclinic Forecast by the Diabatic Quasi-
                Geostrophic Model. J.Met.Soc.Japan. Ser.2,43, 246-261.

9. Wiin-Nielsen, A., 1959: On Certain Integral Constraints for the Integra-
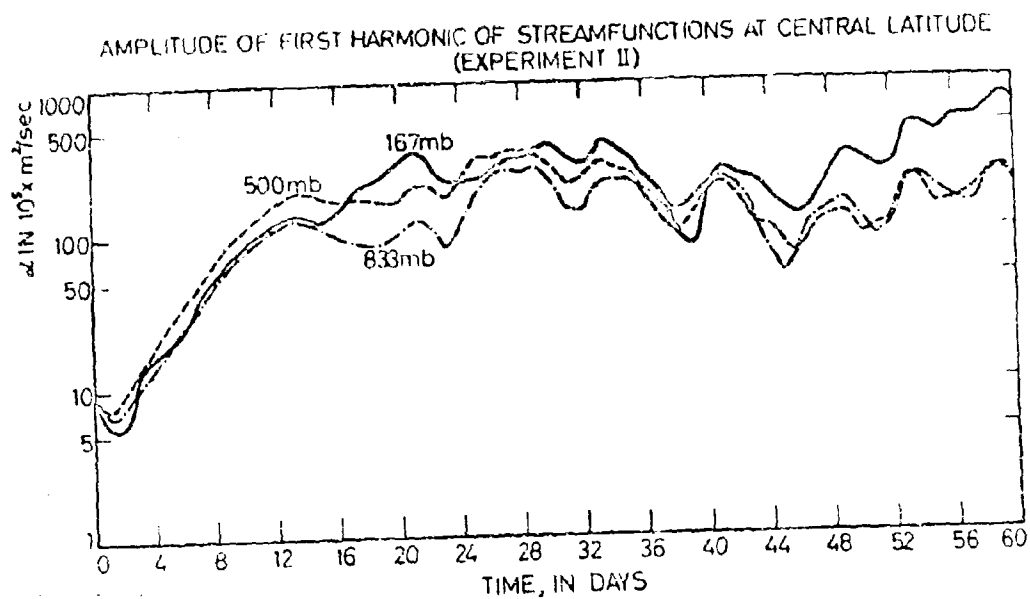   tion of Baroclinic Model. Tellus 11, 45-59.
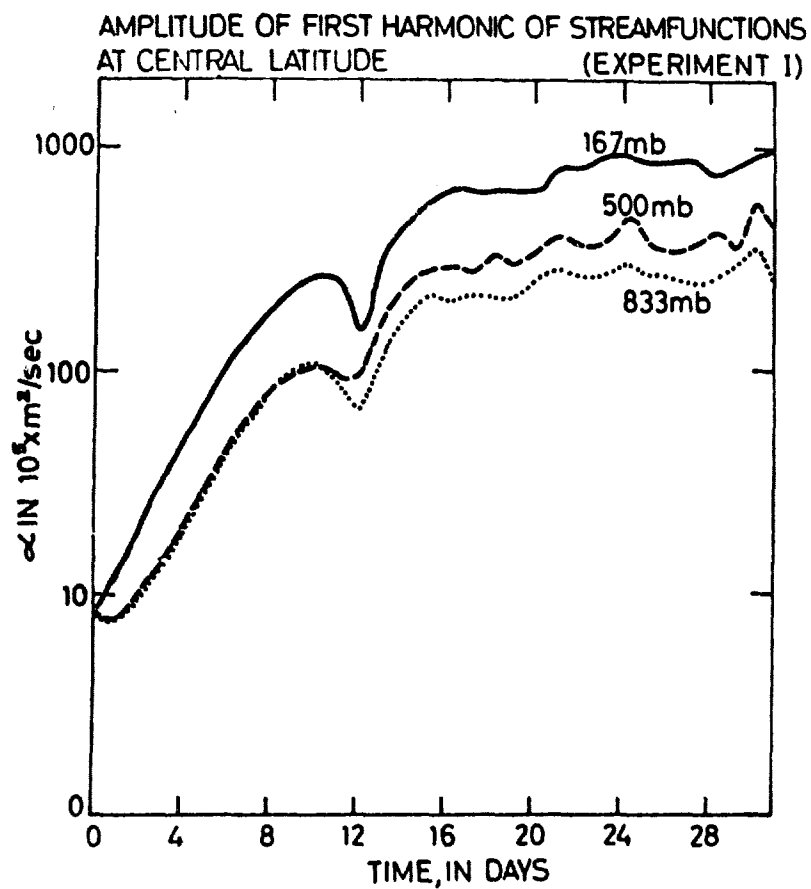
Fig. 1. Amplitudes of the first harmonics of the stream-functions
at the central latitude at 167, 500 and 833 mb.
In m^2/sec. Experiment I.

Fig. 2. The zonally averaged flow at 1000 mb as a function of latitude and time. Experiment I.
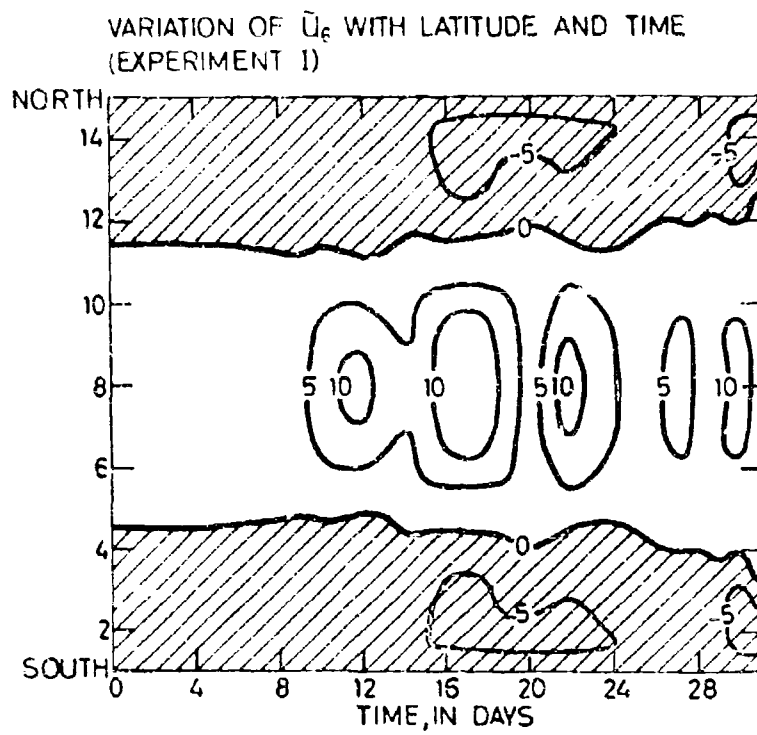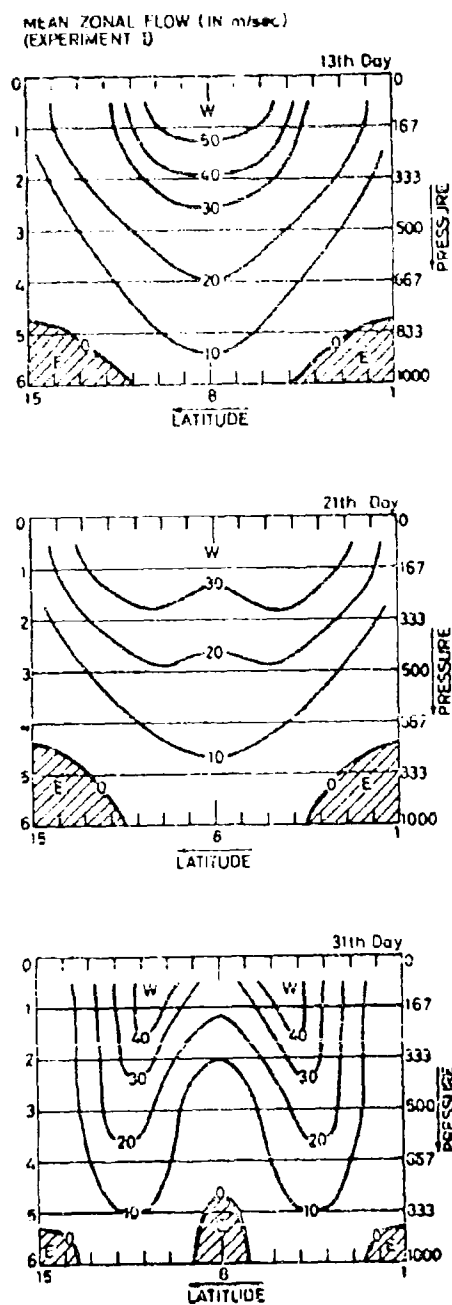
MEAN ZONAL FLOW (IN m/sec)
(EXPERIMENT I)

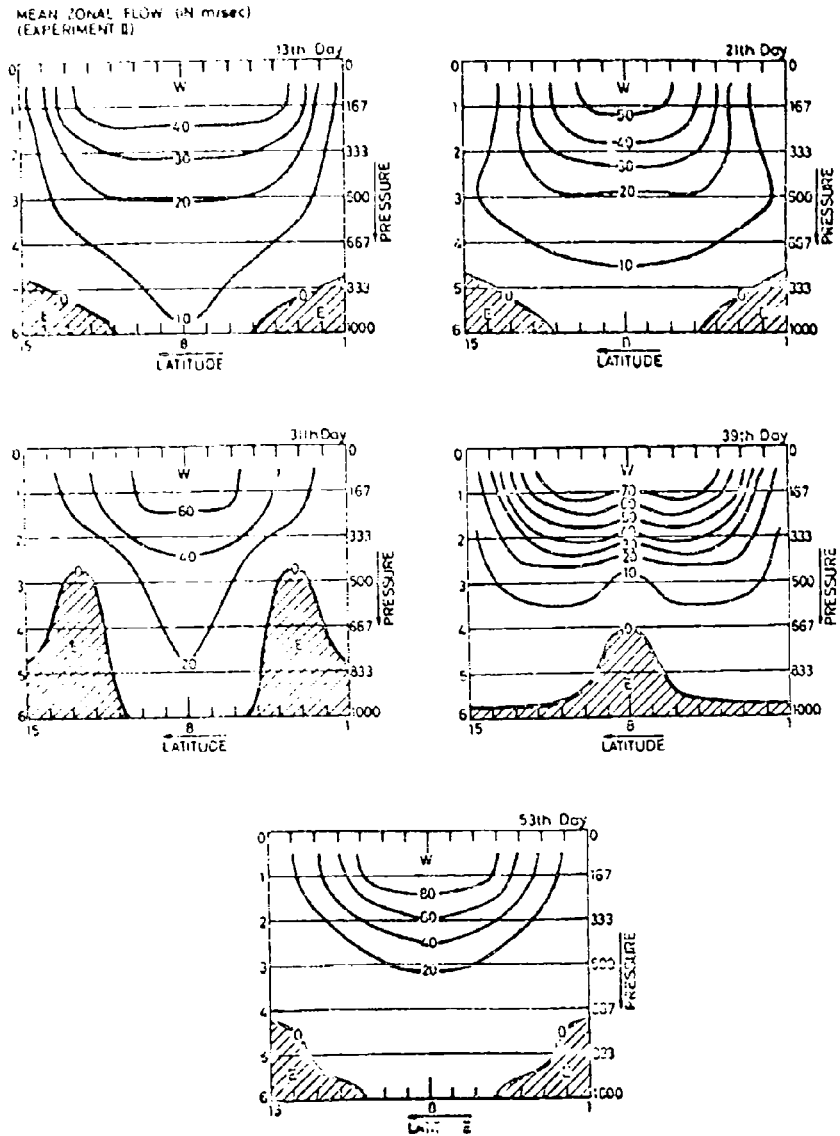

Fig. 3. The latitude-pressure distribution of the zonally averaged
flow, $\overrightarrow{U}$, on the 13th, 21st and 31st days of the integration.
Experiment 1.
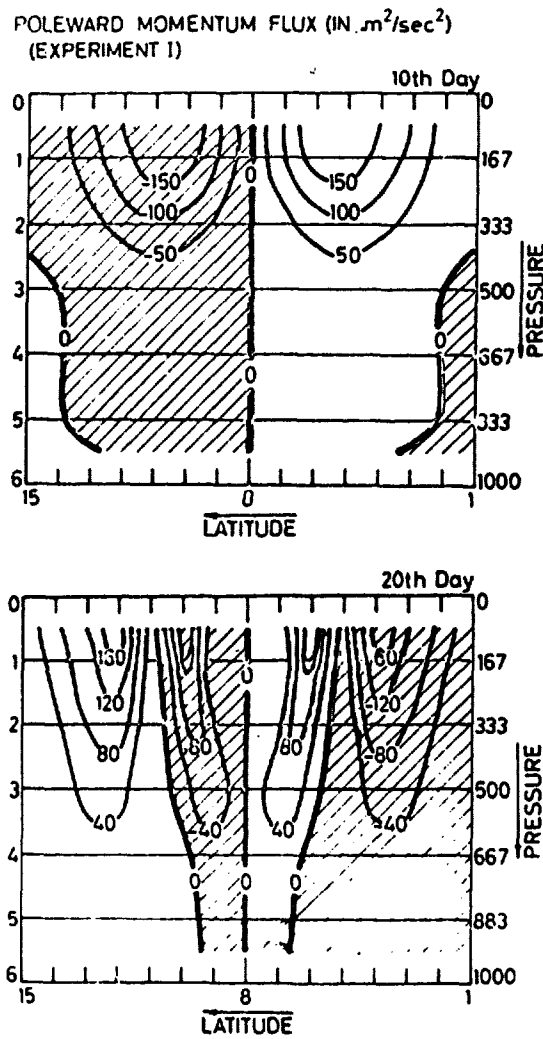
POLEWARD MOMENTUM FLUX (IN .m²/sec²)
(EXPERIMENT I)

Fig. 4.   The latitude-pressure distribution of the zonally averaged
northward eddy transport of momentum, in m²/sec², on the 10th
and 20th days of the integration. Experiment I.
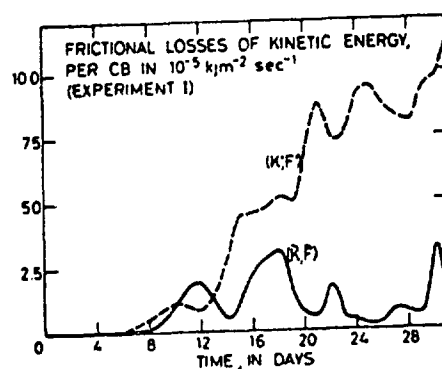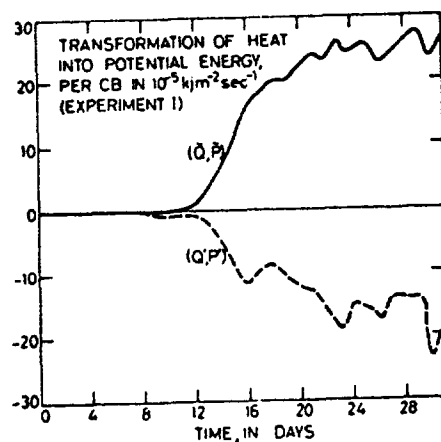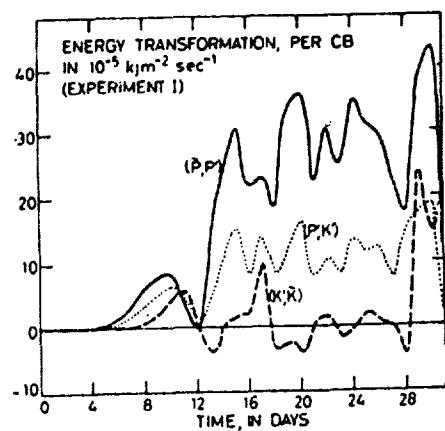
Fig. 5. Area and pressure averaged energy transformations, including frictional losses, as a function of time. Experiment I.

Fig. 6. Area-averaged values of the kinetic energy of the zonal flow, the eddies, and of the total kinetic energy, in m^2/sec^2, as a function of time. Experiment I.

ZONALLY AVERAGED DIABATIC HEATING PER
UNIT COLUMN   (EXPERIMENT I)

$\bar{Q}$ IN $kjm^{-2}sec^{-1}\times 10^{2}$

———— 13th Day

— — — 21th Day

·········· 31th Day

LATITUDE
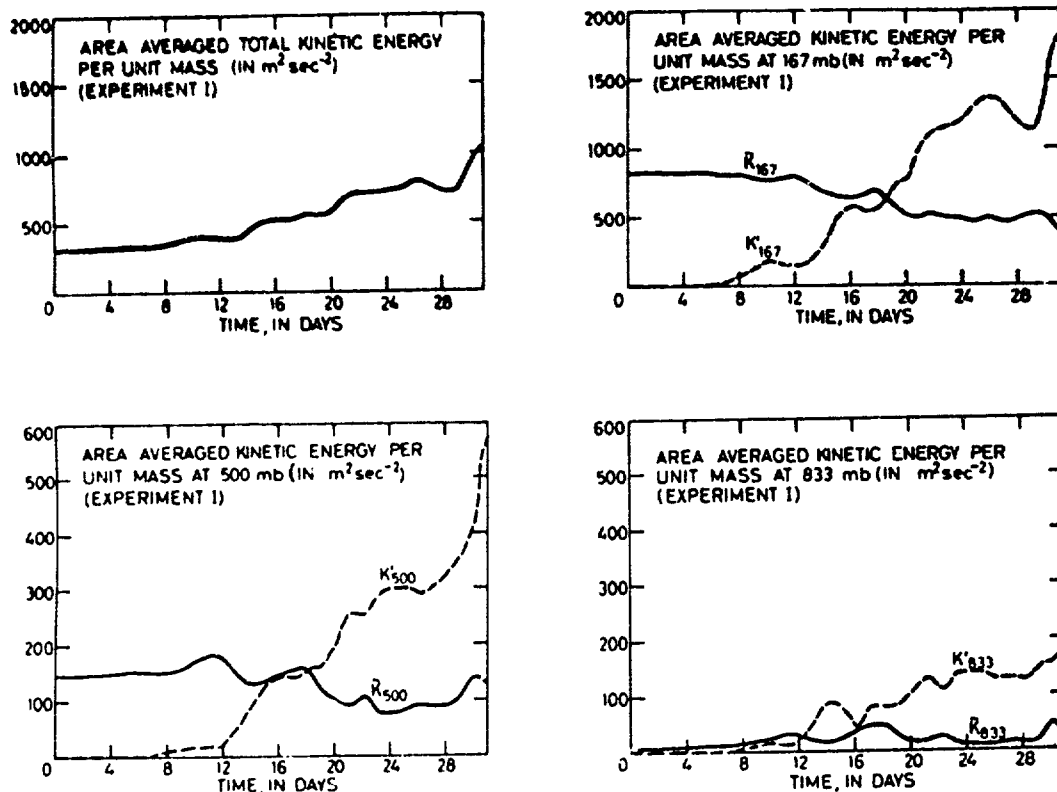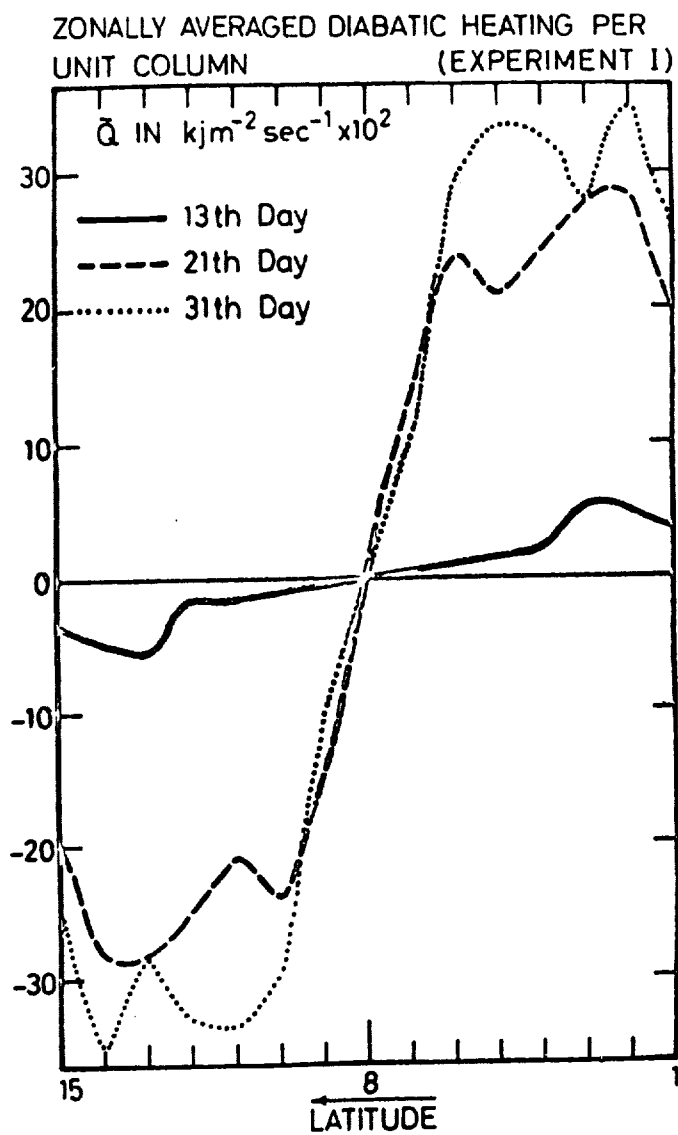
Fig. 7. Zonally averaged influx of sensible heat into unit
        column in $kjm^{-2}sec^{-1}\times 10^{2}$, on the 13th, 21st and 31st days
        of the integration. Experiment I.

POLEWARD FLUX OF SENSIBLE HEAT
(IN kj sec⁻¹ cb⁻¹ x 10⁻¹) (EXPERIMENT I)
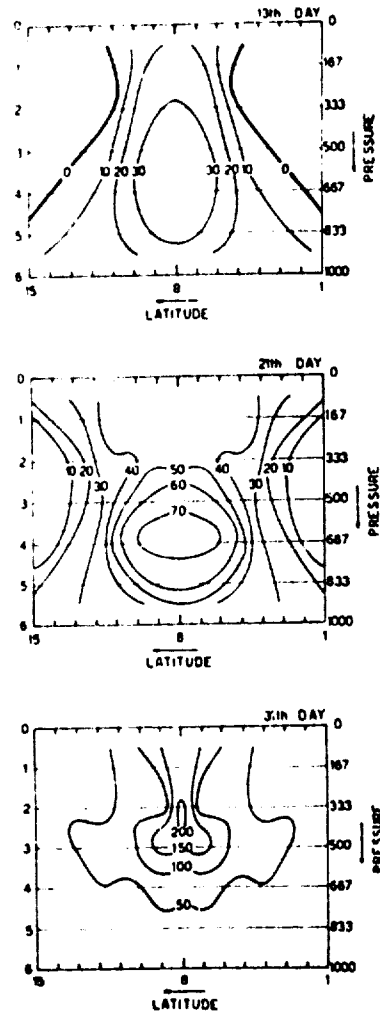
Fig. 8. The latitude-pressure distribution of the zonally averaged poleward flux of sensible heat in kj $sec^{-1}cb^{-1} \times 10^{-2}$, on the 13th, 21st, and 31st days of the integration. Experiment I.

AMPLITUDE OF FIRST HARMONIC OF STREAMFUNCTIONS AT CENTRAL LATITUDE
(EXPERIMENT II)

Fig. 9. Amplitudes of the first harmonics of the stream-functions
at the central latitude at 167, 500 and 833 mb in m^2/sec.
Experiment II.

VARIATION OF $\bar{u}_3$ WITH LATITUDE AND TIME
(EXPERIMENT II)
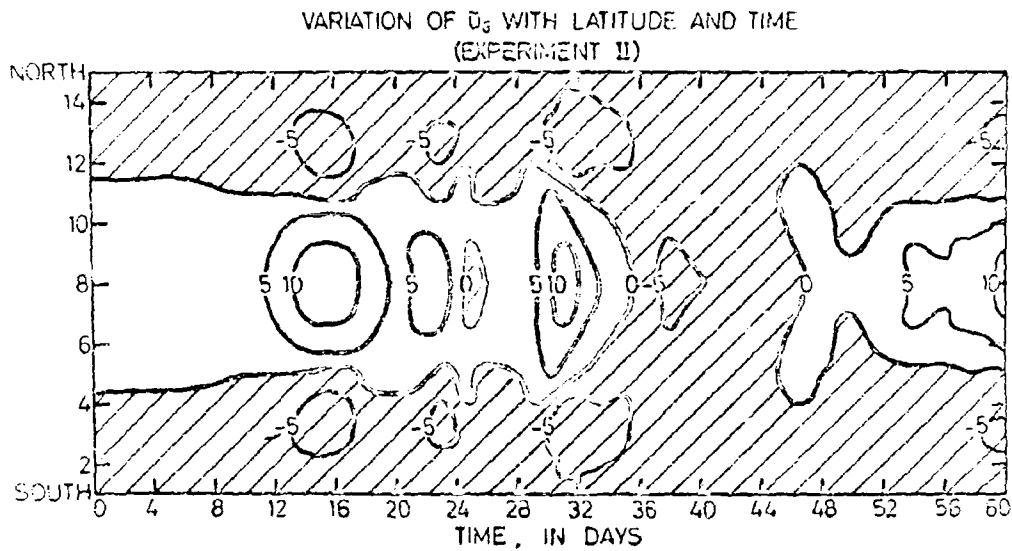
Fig. 10. The zonally averaged flow at 1000 mb as a function of
latitude and time. Experiment II.

Fig. 11.   The latitude-pressure distribution of the zonally
averaged flow, $\widetilde{u}$, on the 13th, 21st, 31st, 39th and
53rd days of the integration. Experiment II.
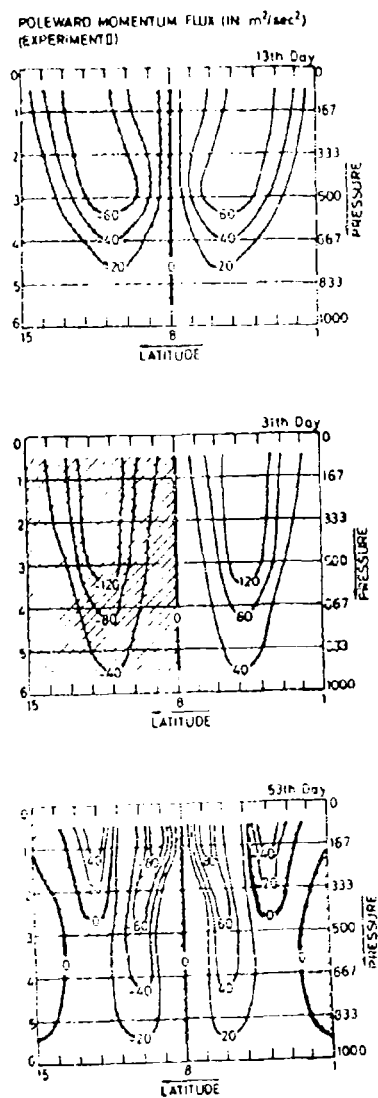
Fig. 12. The latitude-pressure distribution of the zonally
averaged northward eddy transport of momentum in
m^2/sec^2, on the 13th, 31st and 53rd days of the integration.
Experiment II.
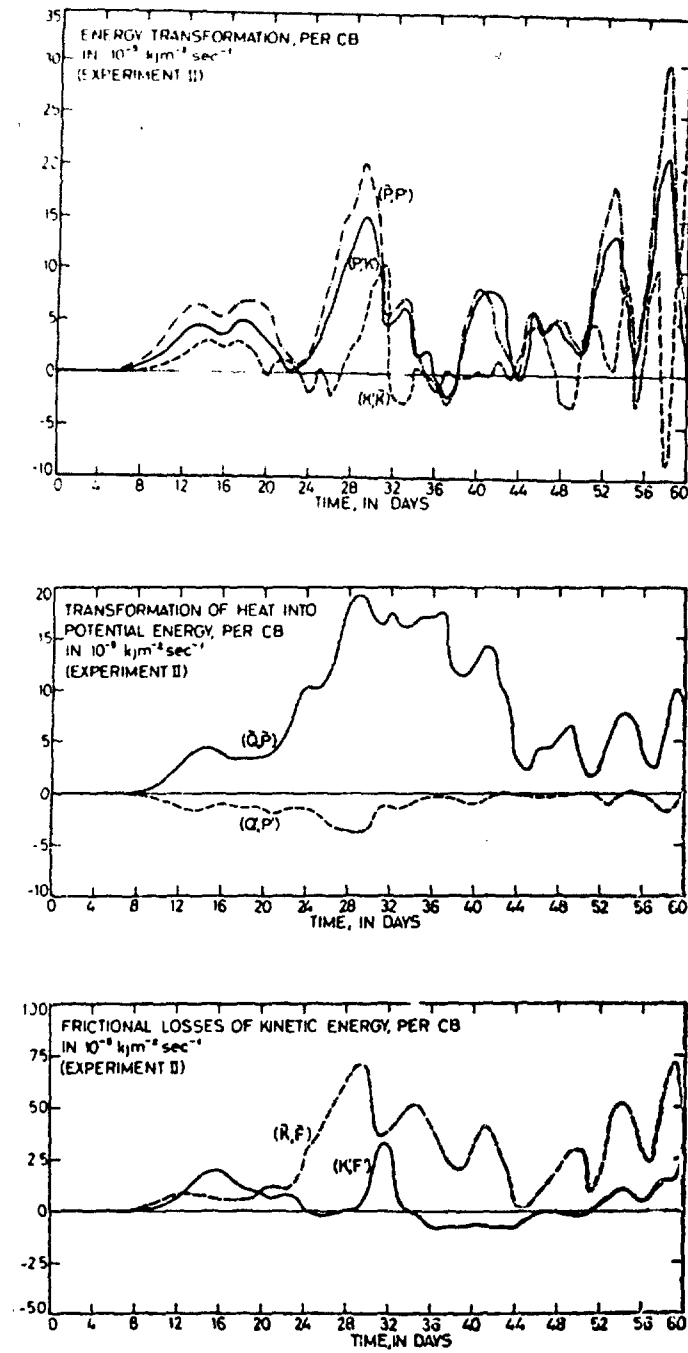
Fig. 13. Area and pressure averaged energy transformations,
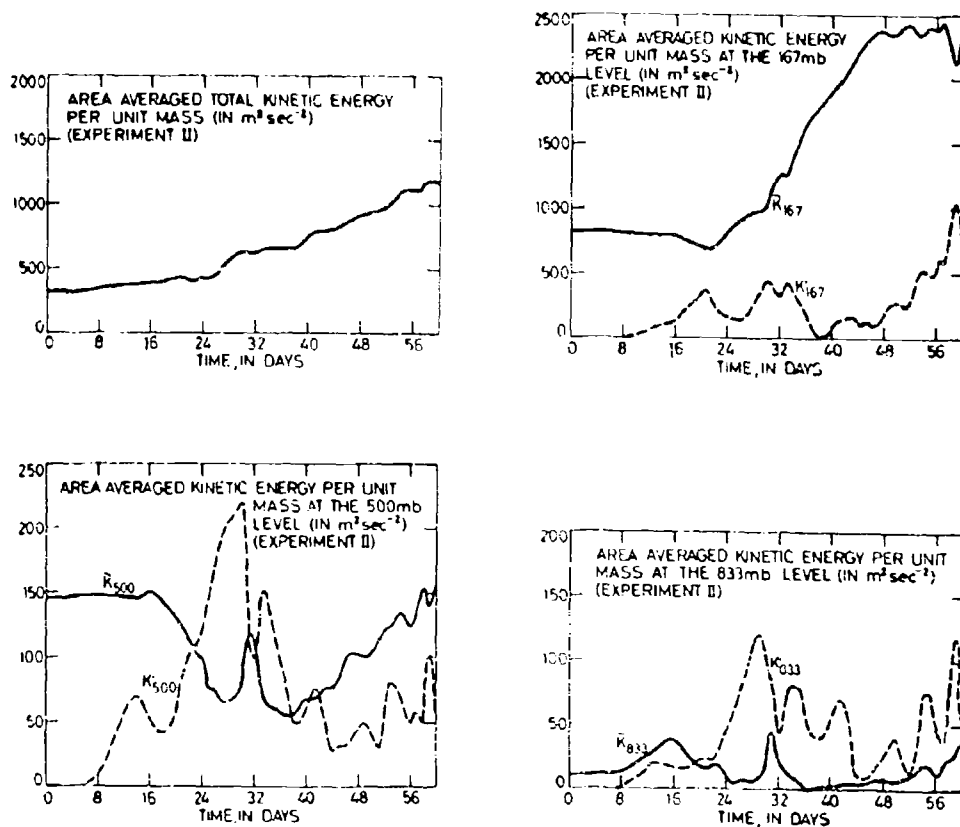including frictional losses, as a function of time.
Experiment II.

Fig. 14. Area-averaged values of the kinetic energy of the zonal
flow, the eddies, and of the total kinetic energy, in
m^2/sec^2, as a function of time. Experiment II.

ZONALLY AVERAGED DIABATIC HEATING PER UNIT
COLUMN   (EXPERIMENT II)
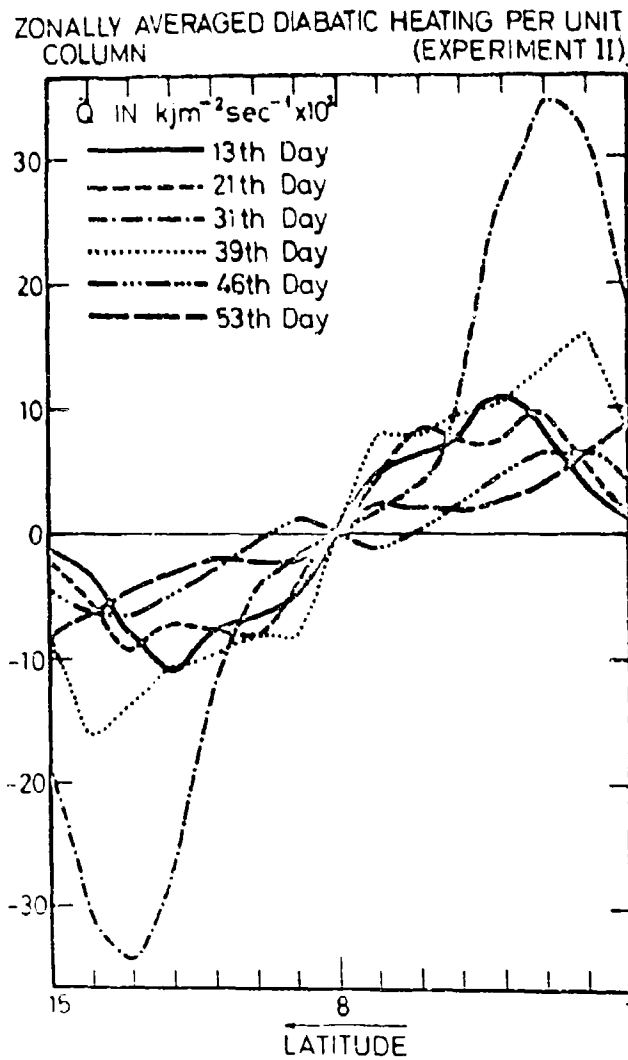
Fig. 15.   Zonally averaged influx of sensible heat into
unit column, in $kjm^{-2}sec^{-1}X10^2$ on the 13th, 21st,
31st, 39th, 46th and 53rd days of the integration.
Experiment.II.

Fig. 16. The latitude-pressure distribution of the zonally
averaged poleward flux of sensible heat, in
$kjsec^{-1}cb^{-1}x10^{-2}$, on the 13th, 21st, 31st, 39th
and 53rd days of the integration. Experiment II.

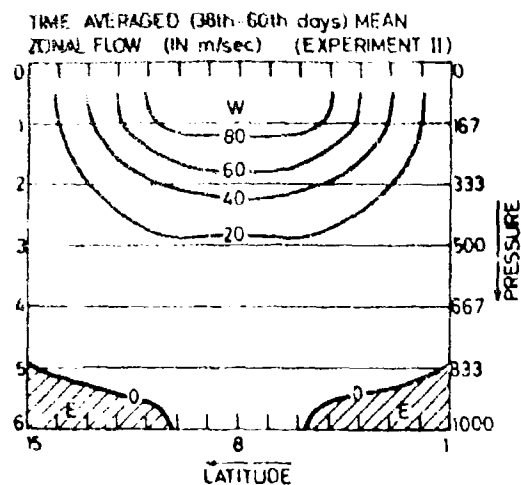TIME AVERAGED (38th-60th days) MEAN
ZONAL FLOW (IN m/sec) (EXPERIMENT II)

Fig. 17. Time averaged (38th-60th days) latitude-pressure
distribution of the zonally averaged flow. Experiment II.

TIME AVERAGED (38th-60th days) POLEWARD
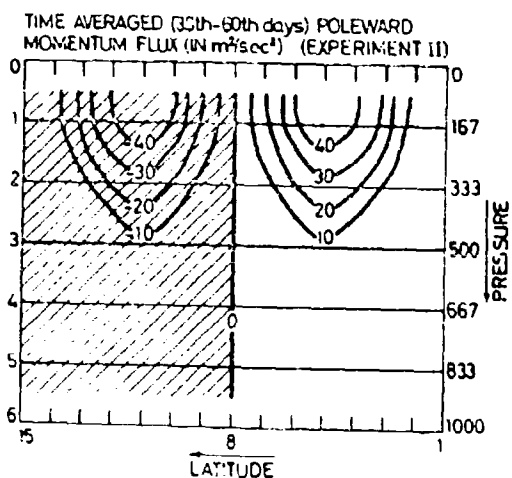MOMENTUM FLUX (IN m²/sec²) (EXPERIMENT II)

Fig. 18. Time averaged (38th-60thdays) latitude-pressure distribution
of the zonally averaged northward eddy transport of momentum, in
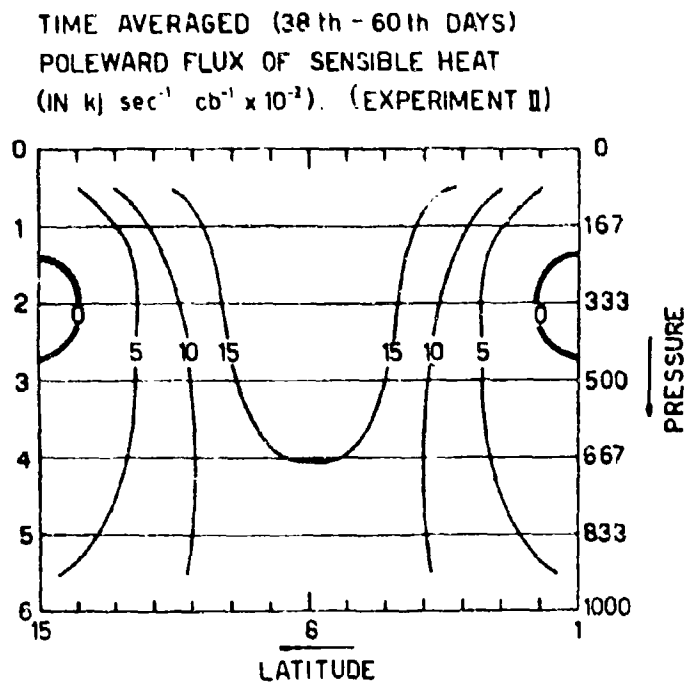m^2/sec^2. Experiment II.

TIME AVERAGED (38 th - 60 th DAYS)
POLEWARD FLUX OF SENSIBLE HEAT
(IN kj sec^{-1} cb^{-1} x 10^{-2}). (EXPERIMENT II)

Fig. 19. Time averaged (38th-60th days) latitude-pressure distribution of the zonally averaged poleward flux of sensible heat, in kjsec^{-1}cb^{-1}x10^{-2}. Experiemnt II.

MODEL INVESTIGATION OF THE TIME DEPENDENT
DISTRIBUTION OF RADON

A. Huss and M. Segal
Department of Meteorology, Hebrew University
Jerusalem

and

G. Assaf
Isotope Research Department, Weizmann Institute
of Science, Rehovot

Abstract

A three-level quasi-geostrophic model of the atmosphere has been used to obtain a three dimensional time dependent radon distribution.

Several experiments were performed in which radon was introduced at the lowest level. The sources were distributed uniformly - either over the whole region, or over one half of the total region. The distribution of radon was observed to respond quite realistically to the large scale atmospheric flow, and particularly to the convergence-divergence patterns, i. e. to the distribution of the vertical components of the motion.

Introduction

Studies of trace elements in the atmosphere are concerned as
a rule with two domains, that of the large scale processes and that of small
scale phenomena, i. e. tracers have been widely applied to the study of prob-
lems of stratospheric and tropospheric mixing (Hunt and Manabe, 1968,
Machta 1966 and others), and to the study of the mean residence time of
aerosols (for example several papers reviewed by Junge, 1963). In these
studies synoptic-scale disturbances were treated as large-scale eddies and
their detailed structure was not taken into account. On the other hand the
scavenging of tracers and their transport in the boundary layer were treated
by several investigators (Greenfield, 1957, Gat and Assaf, 1968 and others),
under the assumption that synoptic features are large-scale phenomena. Only
in a few studies dealing with trace elements (Danielsen, 1968) was the syn-
optic scale, including its variations in time and space, considered as the scale
of interest.

A scale analysis (Assaf, 1969) assuming steadiness and uniform-
ity, indicated that the radon distribution is sensitive to the divergence regime
and might be used as a measure of the vertical wind on the synoptic scale. How-
ever, these are very strong assumptions, if we bear in mind that the mean
life of radon is of the same order of magnitude as the period of synoptic oscil-
lations. Moreover, changes in the source distribution may become quite im-
portant, particularly once we are dealing with the effects due to ocean-continent
contrasts. The aim of this paper is to substantiate this approach by studying
the response of the radon distribution to different source distributions and to
different patterns of atmospheric motions.

It was realized that it would be easier, in the first step in this
direction, to make use of a rather simple and crude numerical model, rather

than to advect the radon by an observed real distribution of winds. As the simplest possible model adequate for our purpose, a three-level quasi-hydrostatic and quasi-geostrophic model was chosen. This model generated a streamline field at 3 levels, and vertical velocities at 2 levels. Needless to say, the model does not provide a very accurate analogue of the general circulation of the atmosphere, nor was it intended to do so. Several import-ant dynamical processes were disregarded, such as small-scale convection and diffusion. The aims of the experiment were not to obtain at this stage realistic three-dimensional distributions of radon, but to observe how radon, introduced at the lower boundary of the model, would react to a time-dependent circulation - and in particular, what its schematic distribution would look like in regions where horizontal divergence or convergence respectively dom-inate.

The Model

The calculation of the velocities required to transport the radon were obtained by means of a three level quasi-hydrostatic and quasi-geostro-phic general circulation model incorporating diabatic heat sources and surface friction, whose details will be described elsewhere (see third article in this report) and which resembles in many respects the model constructed by Phillips (1956). The prognostic equations were applied at three pressure levels 167, 500, 833 mb, to be denoted by indices 1, 3 and 5. The predicted values were the potential vorticities from which the geopotentials at the three reference levels (proportional to the streamfunctions) were derived by means of an inversion procedure. From the streamfunctions the rotational component of the horizontal wind was obtained. The potential vorticity in the model is advected horizontally only by the rotational component of the wind, while no advection in the vertical is assumed.

The initial conditions correspond to a baroclinically unstable zonal westerly flow, constant at each level, with a small perturbation superimposed

upon it. At the lower boundary the velocity is assumed to vanish. As time
went on a jet stream developed in the upper level of the model atmosphere,
and easterlies were generated in the lower layers in the north and in the
south. Lows and highs evolved at the surface, and became displaced to the
north and to the south respectively. Thus, the model was capable of genera-
ting some of the basic features of the general circulation of the atmosphere.

It was considered essential to introduce vertical advection of
radon. The model allows a diagnostic computation of the vertical p-velocity,
ω , at 333 mb and 666 mb, denoted as levels 2 and 4. These velocities
were used to advect radon vertically. ω was assumed to vanish at p = 0
and at p = 1000 mb. Thus it is not required to specify the radon concentra-
tion at the top or at the bottom of the model atmosphere. It is quite obvious
that the introduction of vertical advection required that the horizontal advec-
tion should be not only due to the rotational component of the wind, but also
due to the divergent component, in order that the total mass of the material
advected should be conserved (except for decay processes). The divergent
components were obtained by relaxation from the ω - distribution.

The prognostic equation for concentration of radon was:

$$\frac{\partial c}{\partial t} = - \frac{\partial}{\partial x}(uc) - \frac{\partial}{\partial y}(vc) - \frac{\partial}{\partial p}(\omega c) - \lambda c + S , \tag{1}$$

in which: c = concentration in atoms per ton,

  x, y - the horizontal coordinates

  u, v - the horizontal components of wind,

  p - pressure,

  ω - dp/dt,

  λ - the decay constant,

  S - the source constant.

The horizontal velocity components were split into:

$$u = u_g + u_d \; ; \qquad\qquad v = v_g + v_d \; . \qquad\qquad (2)$$

The rotational components u_g, v_g were obtained from the quasi-geostrophic stream-function, while the divergent components u_d, v_d were obtained by means of

$$u_d = \frac{\partial \chi}{\partial x} \; ; \quad v_d = \frac{\partial \chi}{\partial y} \; ; \quad \nabla^2 \chi = -\frac{\partial \omega}{\partial p} \; , \qquad\qquad (3)$$

from a velocity potential.

Equation (1) is applied at levels 1, 3 and 5, and the derivatives are approximated by finite differences. To avoid mathematical instability centered time differences replace the time derivatives and the decay term was evaluated at time step $\tau - 1$.

Using a rectangular grid with identical increments in the x and y direction $(\Delta x = \Delta y)$, the following equations are obtained:

$$\frac{c_{ij1}^{\tau+1} - c_{ij1}^{\tau-1}}{2\Delta t} = J(\psi, c)_{ij1}^{\tau} - \lambda c_{ij1}^{\tau-1} - Q_{ij2}^{\tau} - \nabla \cdot (v_d c)_{ij1}^{\tau} \, ,$$

$$\frac{c_{ij3}^{\tau+1} - c_{ij3}^{\tau-1}}{2\Delta t} = J(\psi, c)_{ij3}^{\tau} - \lambda c_{ij3}^{\tau-1} + (Q_{ij2}^{\tau} - Q_{ij4}^{\tau}) - \nabla \cdot (v_d c)_{ij3}^{\tau} \, ,$$

$$\frac{c_{ij5}^{\tau+1} - c_{ij5}^{\tau-1}}{2\Delta t} = J(\psi, c)_{ij5}^{\tau} - \lambda c_{ij5}^{\tau+1} + Q_{ij4}^{\tau} - \nabla \cdot (v_d c)_{ij5}^{\tau} + S \, ,$$

$$(5)$$

where τ, i and j identify the discrete values in time, x and y, and

$$Q_{ij_2}^{\tau} = \frac{c_{ij_3}^{\tau} + c_{ij_1}^{\tau}}{2 \times 33.3} \omega_{ij_2}^{\tau} ;$$

$$Q_{ij_4}^{\tau} = \frac{c_{ij_3}^{\tau} + c_{ij_5}^{\tau}}{2 \times 33.3} \omega_{ij_4}^{\tau} ;$$

$$\Delta p = 33.3 \, cb .$$

(6)

Cyclical continuity was assumed in the x direction. The vertical advection and the divergence term were neglected at the northern boundaries. These boundaries were treated from the point of view of the dynamics involved, as "solid" walls. Time increments of 1 hour, space increments of 444 km, and a grid size of 15 x 15 points were used.

The source at level 5, introduced into the atmosphere 1100 atoms per ton per sec., which is equivalent to 0000 atoms per m^2 per sec. Two different source distributions were used: (a) A uniform distribution over the whole region. (b) A uniform distribution over the western half of the region defined as the "continent", while the eastern half, without sources, was defined as an "ocean". A third numerical integration (c) was carried out with the same source distribution as (b) but with different initial conditions.

In (a) and (b) radon was introduced on the 10th day of the dynamic experiment, while in (c) it was introduced on the 16th day.

Results and Discussion

The radon distribution was allowed to evolve between the 10th day and the 23rd day and between the 16th day and the 23rd day of the circulation experiment for cases (a), (b) and case (c) respectively. 3 days were selected for a detailed analysis: the 14th, the 18th and the 22nd days. These days are characterized by different distributions of the vertical velocity. Fig. 1 to 6 show the radon distribution at levels 5 and 3, superimposed on the vertical wind field at level 4 on the corresponding days.

On the 14th day the circulation is characterized by well defined centers of the convergence and divergence. The area with $|\omega| > 10^{-4}$ cb/sec is quite extensive. The developing circulation up to this stage, acting on an initially uniform concentration introduced at day 10, results in a rather regular distribution of radon. The iso-concentration lines of radon are roughly parallel to the lines of constant vertical wind, and the maxima of the radon concentrations at levels 5 and 3 coincide with the maxima of upward vertical wind. This regular pattern is most pronounced in experiment (a) where the source is uniformly distributed over the total region, but even in experiment (b), where the center of the convergence is located over the "ocean", i.e. over the region which does not introduce radon into the air, tongues of radon are directed towards this center.

Day 18 has a different distribution of vertical velocities, with two separate cells of relatively small magnitudes of the vertical wind. The area over which $|\omega| > 1.0^{-4}$ cb/sec is very small, and in one of the cells does not exceed 0.3×10^{-4} cb/sec. As a result horizontal transports become dominant, as can be seen from the elongation of the iso-concentration curves of radon due to the zonal flow.

Day 22 is again characterized by relatively high magnitudes of the vertical wind. Here again the correspondence between the vertical wind and the radon concentration is quite remarkable. Fig. 7 presents the distribution of radon in experiment (c) superimposed on the radon distribution in experiment (b). The correspondence between the two is indicative of the short "memory" of radon; its distribution is almost unaffected by the prevailing flow pattern at the moment at which radon is introduced first into the model atmosphere.

The meridional distribution of the zonally averaged concentration of radon is shown in Figs. 9 - 14. A pronounced correlation with the vertical velocity was observed on the days with strong ascent and descent of air Thus on days 14 and 22 the zonally averaged vertical wind at level 4 has a strong effect on the zonally averaged distribution of radon. The distribution observed on day 18 on the other hand, was quite erratic.

Fig. 15 gives the ratio between the total radon content of the western half of the region and the total content of the eastern half. In experiment (a), where the source is uniformly distributed, the fluctuations reflect the changes in the convergence-divergence patterns generated by the model. In experiment (b), with the sources located in the western half of the region, the trends are somewhat similar to those in experiment (a), but the ratio is obviously lower. The relative amounts of radon at different levels at the end of the integration period (23rd day) are presented in table 1, in the form of percentages.

Level Exp.	1 (833 mb)	3 (500 mb)	1 (166 mb)
(a)	89	9	2
(b)	85	12	3

Summary

The preliminary numerical experiments, described above, generated time dependent radon distributions, which show that the radon distribution responds to large scale patterns of the vertical wind, as well as to those of horizontal flow. This correspondence was quite pronounced in the case of a well-defined cellular distribution of ω . In our model the maximum vertical p-velocity generated did not exceed $\pm\ 2\ \times\ 10^{-4}$ cb/sec. Danielsen's analysis (1966) resulted in values up to $\pm\ 5\ \times\ 10^{-4}$ cb/sec. It seems reasonable to suppose that velocities of this magnitude will have an even more marked effect on the radon distribution Advection by small-scale motion will modify the distributions generated by synoptic-scale flow. However, it is quite difficult to incorporate such effects into present-day numerical models. The results obtained so far are schematic, and it is planned to repeat the calculations with more realistic general circulation models. Small scale effects could be introduced parametrically In any case, the results, presented above, raise the possibility, that observed distributions of radon in the free atmosphere may help us in the identification of the synoptic-scale patterns of vertical motions.

References

1.   Assaf G., 1969· Emanated Products as a Probe of Atmospheric
      Transport, to be published, Tellus

2.   Danielsen E. F., 1968: Stratospheric-tropospheric Exchange based
      on Radioactivity, Ozone and Potential Vorticity, J. Atmos. Sci. 25,
      502-518.

3.   Danielsen E. F., 1966: Research in Four-Dimensional Diagnosis
      of Cyclonic Storm Cloud Systems· (I) AFCRL 66-30, (II) AFCRL
      66-849.

4.   Hunt G. B. and S. Manabe, 1968: Experiments with Stratospheric
      General Circulation Model II. Large Scale Diffusion of Tracers in
      the Stratosphere, Mon. Weath.Rev. 96, 503-538.

5.   Gat J.R. and Gad Assaf. 1968; Atmospheric Bi ^{212}· Measurements
      and some Geophysical Applications, Science, 159, 977-979.

6.   Greenfield S.M., 1957: Rain Scavenging of Radioactive Particulate
      Matter from the Atmosphere J. Met, 14, 115-125.

7.   Junge. C. E., 1963: Air Chemistry and Radioactivity, Academic
      Press N. Y.

8.   Machta L., 1966: Some Aspects of Simulating large Scale Atmospheric
      Mixing, Tellus, 18, 365-362.

9.   Phillips, N. A., 1956: The General Circulation of the Atmosphere.
      A Numerical Experiment. Quart. J. R. Met. Soc., 82, 123-164.

Figure Captions

Figs 1 - 6 :   The distribution of radon and of the vertical velocity.

- - - -   lines of constant concentration of radon at 833 mb.

- . - -   lines of constant concentration of radon at 500 mb.

————--   lines of constant vertical velocity.

Hatched areas are regions of rising air. Cross-hatched areas are regions with $\omega > 10^{-4}$ cb/sec.   M and m refer to maximum upward and downward flow.

The heavy vertical line in Figs. 2, 4 and 6 indicates the boundary between the region containing sources of radon (on the left) and the region without sources.

Fig. 1:   Day 14,   Experiment a.
Fig. 2:   Day 14,   Experiment b.
Fig. 3:   Day 18,   Experiment a.
Fig. 4:   Day 18,   Experiment b.
Fig. 5:   Day 22,   Experiment a.
Fig. 6:   Day 22,   Experiment b.

Fig. 7:   The zonally averaged zonal component of the velocity, as a function of latitude and altitude, in m sec^{-1}. The center of the diagram models the 45° latitude. Hatched areas correspond to easterly flow.

Fig. 8:   The distribution of radon on the 22nd day in Experiments (b) and (c).

————→   lines of constant concentration of radon in Exp. (b) at 833 mb.

————   lines of constant concentration of radon in Exp. (b) at 500 mb.

- - - -   lines of constant concentration of radon in Exp. (c) at 833 mb.

- - - -   lines of constant concentration of radon in Exp. (c) at 500 mb.

Fig. 9 - 14:   The zonally averaged vertical velocity and the zonally averaged radon concentration as a function of latitude.

————   vertical velocity.   - - - - radon concentration in Exp. (a)

- .- .- .-   radon concentration in Exp. (b).

Fig. 15:   The ratio between the total radon content of the western half of the region to that of the eastern half of the region, for experiments (a) and (b), as a function of time.
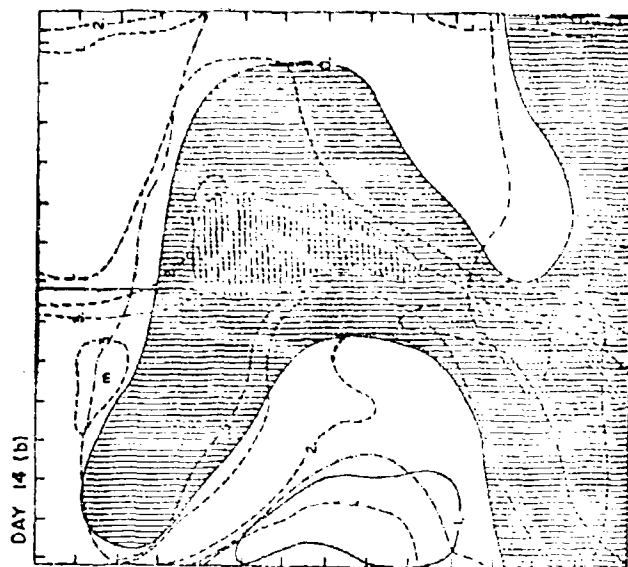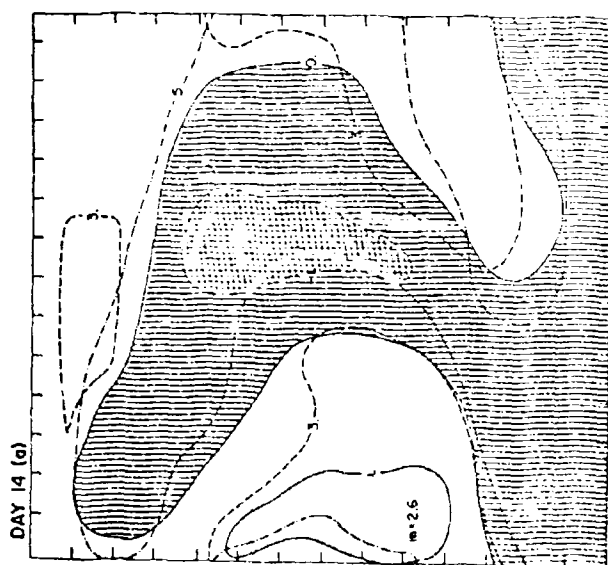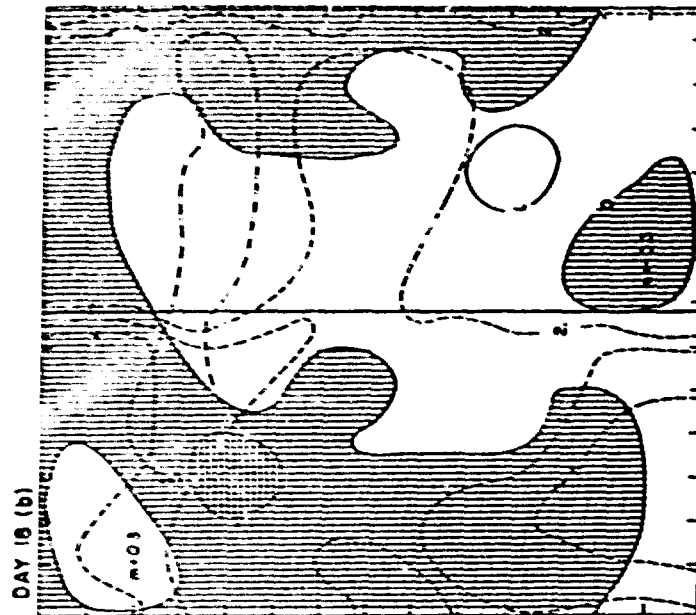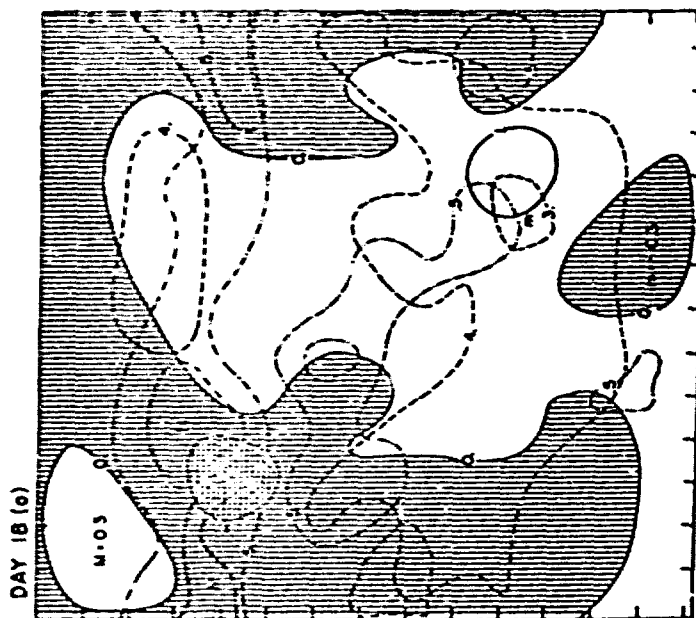
DAY 14 (b)
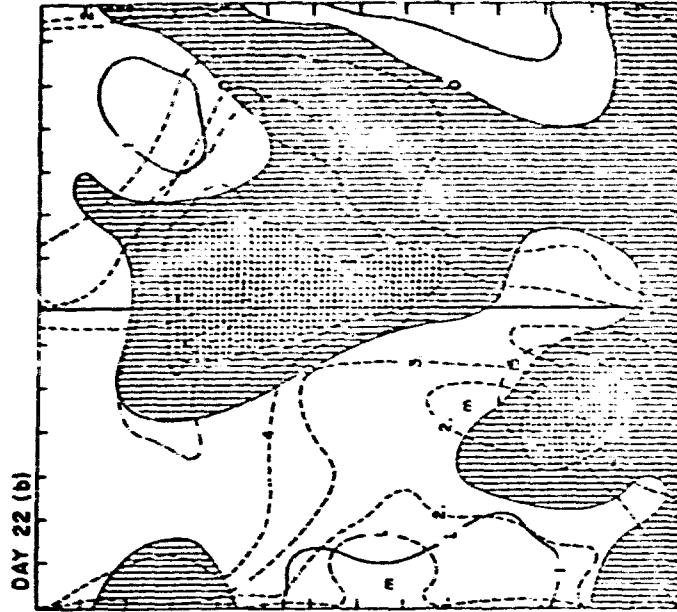
Fig. 2

DAY 14 (a)

Fig. 1

DAY 18 (b)
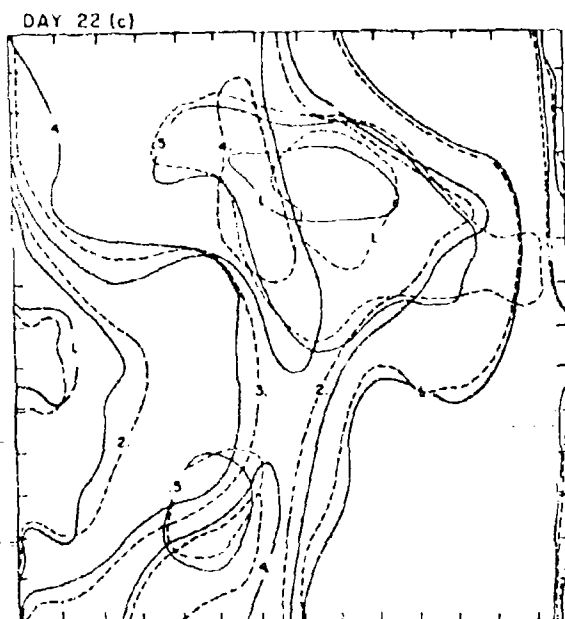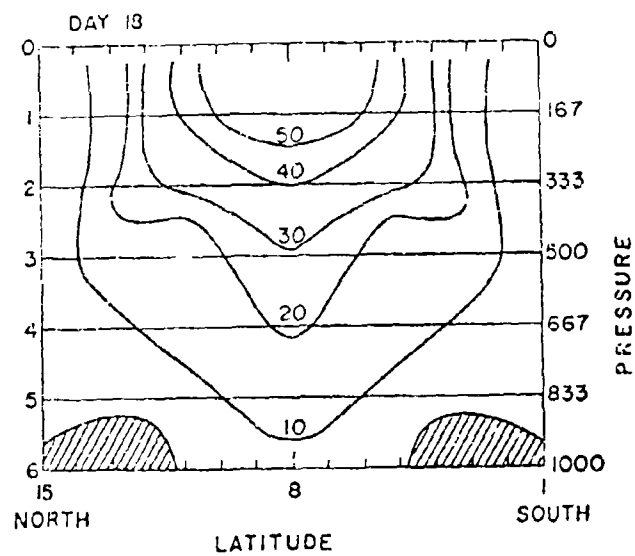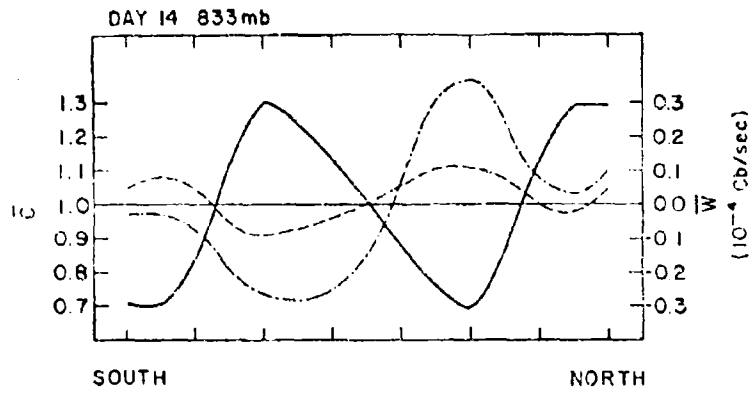
Fig. 4

DAY 18 (o)

Fig. 3

DAY 22 (b)

Fig. 6

DAY 22 (a)

Fig. 5

Fig. 7

Fig. 8

Fig. 9

Fig. 10

Fig. 11

DAY 13   500 mb.

SOUTH   NORTH

Fig. 12

DAY 22   833 mb.

SOUTH   NORTH
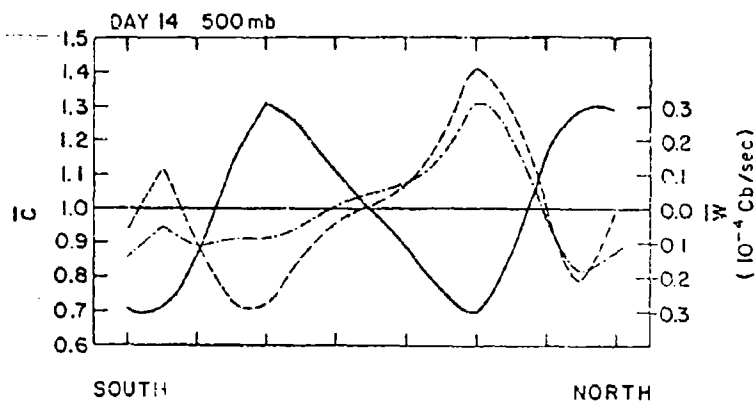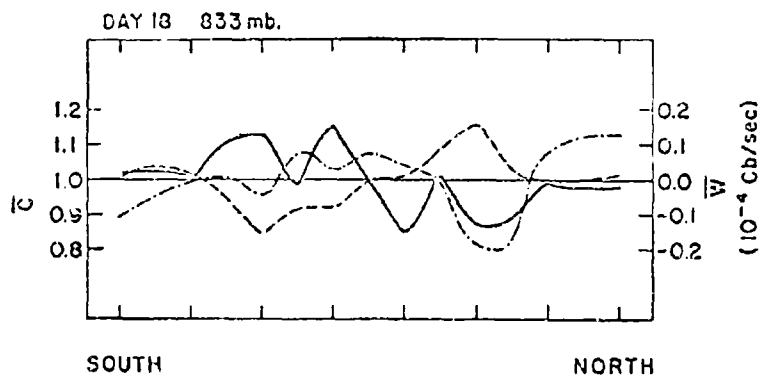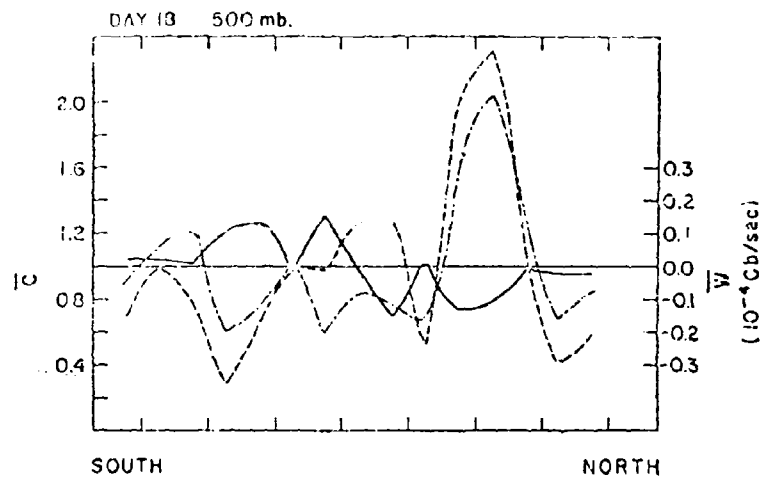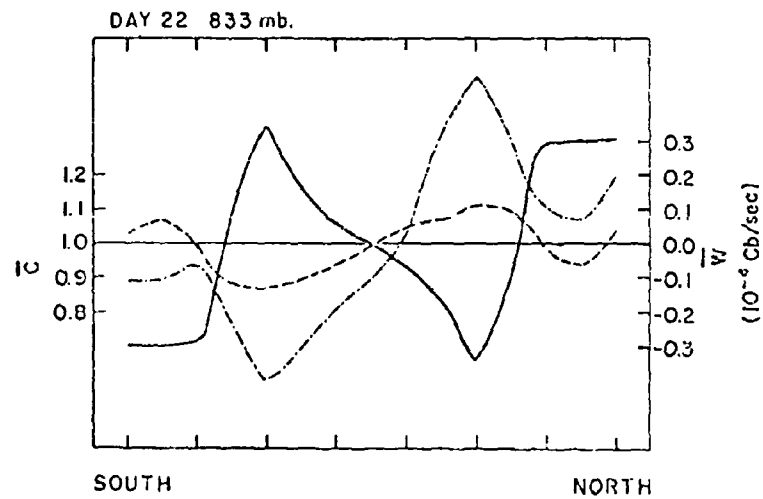
Fig. 13
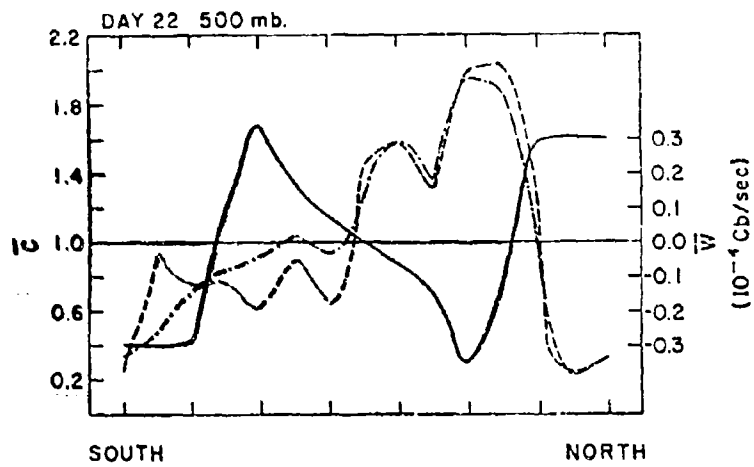
Fig. 14

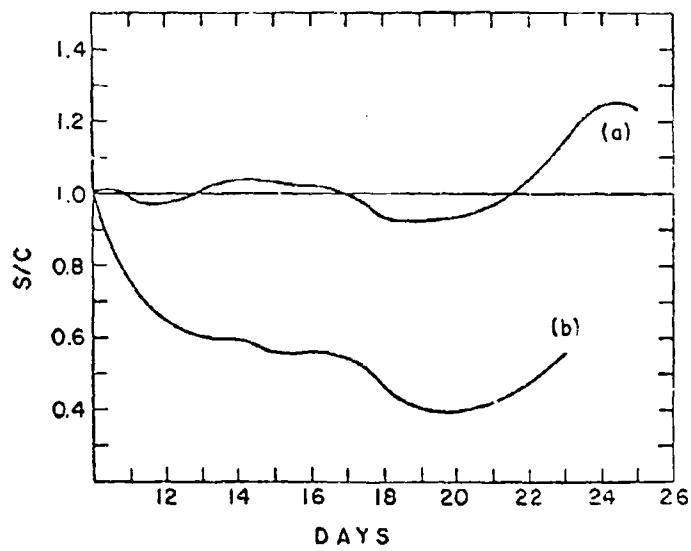Fig. 15

DOCUMENT CONTROL DATA - R & D

Security classification of title, body of abstract and indexing annotation must be entered when the overall report is classified

1. ORIGINATING ACTIVITY (Corporate author)	2a. REPORT SECURITY CLASSIFICATION
Hebrew University of Jerusalem Jerusalem, Israel	UNCLASSIFIED
	2b. GROUP

3. REPORT TITLE

Numerical Studies of Planetary Circulations in a Model Atmosphere

4. DESCRIPTIVE NOTES (Type of report and inclusive dates)

Scientific.   Final.

5. AUTHOR(S) (First name, middle initial, last name)

Abraham Huss

6. REPORT DATE	7a. TOTAL NO. OF PAGES	7b. NO. OF REFS
March 1970	233	66

8a. CONTRACT OR GRANT NO	9a. ORIGINATOR'S REPORT NUMBER(S)
AF EOAR 67-46	
b. PROJECT NO	
8604-04	
61445014	9b. OTHER REPORT NO(S) (Any other numbers that may be assigned this report)
d. 681310	

10. DISTRIBUTION STATEMENT

This document has been approved for public release and sale; its distribution is unlimited.

11. SUPPLEMENTARY NOTES	12. SPONSORING MILITARY ACTIVITY
	Air Force Cambridge Research Laboratories (CRHD) L G Hanscom Field, Bedford, Mass 01730

13. ABSTRACT   A sequence of numerical experiments was performed modelling general features of the planetary circulation over a limited region. In the first experiment the results obtained from a primitive equation 2 level model are compared with the results of a geostrophic 2 level model. The equations were integrated over a β -plane with two lateral walls in the north and in the south. In the second experiment the results of a 3 level geostrophic model are compared with those of a 2 level geostrophic model. In the third experiment the smoothing effects of a lateral viscosity term are investigated and compared with the smoothing effect of the Matsuno approximation, of the time derivative. In the 4th experiment the spread of radon in a model atmosphere is investigated schematically, the source of the radon being located in the lower boundary.

DD FORM 1473

KEY WORDS	LINK A		LINK B		LINK C	
	ROLE	WT	ROLE	WT	ROLE	WT
General Circulation						
Primitive Equation Model						
Lateral Viscosity						
Matsuno Scheme						
Harmonic Analysis of the Geopotential Field						
Release of Latent Heat						
Transport of Radon						